Developments and perspectives on robust nano- and micro-structured binder-free electrodes for bi-functional water electrolysis and beyond

Sundaram Chandrasekaran[a], Mahima Khandelwal[b], Fan Dayong[a], Lijun Sui[c], Jin Suk Chung[d], RDK Misra[e], Peng Yin[f], Eui Jung Kim[d], Woong Kim[b], Aravindan Vanchiappan[g], Yongping Liu[a]*, Seung Hyun Hur[d]*, Han Zhang[f] and Chris Bowen[h]**

((Optional Dedication))

[a] Assoc. Prof. Sundaram Chandrasekaran, Asst. Prof. Fan Dayong, and Prof.Yongping Liu,
Guangxi Key Laboratory of Electrochemical and Magneto-chemical, Functional Materials, College of Chemistry and Bioengineering, Guilin University of Technology, Guilin, 541004 P.R. China.
Email: yes.chandrasekaran@gmail.com, chandru@glut.edu.cn, liuyp624@163.com

[b] Dr. Mahima Khandelwal, and Prof. Woong Kim,
Department of Materials Science and Engineering, Korea University, Seoul 02841, Republic of Korea.

[c] Dr. Lijun Sui,
Shanghai Key Laboratory for R&D and Application of Metallic Functional Materials, Institute of New Energy for Vehicles, School of Materials Science and Engineering, Tongji University, Shanghai 201804, P.R. China.

[d] Prof. Jin Suk Chung, Prof. Eui Jung Kim, and Prof. Seung Hyun Hur,
School of Chemical Engineering, University of Ulsan, Nam-gu, Daehakro 93, Ulsan 680-749, South Korea.
Email: shhur@ulsan.ac.kr

[e] Prof. RDK Misra,
College of Engineering Metallurgical, Materials and Biomedical Engineering, University of Texas at El Paso, Texas 79968, USA.

[f] Dr. Peng Yin, and Prof. Han Zhang,
Key Laboratory of Optoelectronic Devices, Systems of Ministry of Education and Guangdong Province, College of Physics and Optoelectronic Engineering, Shenzhen University, Shenzhen 518060, China.

[g] Asst. Prof. Aravindan Vanchiappan,
Department of Chemistry, Indian Institute of Science Education and Research (IISER), Tirupati 517507, India.

[h] Prof.Chris Bowen,
Department of Mechanical Engineering, University of Bath, BA2, 7AY, Bath, UK.
Email: c.r.bowen@bath.ac.uk

Keywords: binder-free electrodes, free-standing electrodes, HER, OER, water splitting

Abstract

The development of robust nano- and micro-structured catalysts on highly conductive substrates is an effective approach to produce highly active binder-free electrodes for energy conversion and storage applications. As a result, nanostructured electrodes with binder-free designs have abundant advantages that provide superior electrocatalytic performance; these include more exposed active sites, large surface area, strong adhesion to substrates, facile charge transfer, high conductivity, high intrinsic catalytic activity, and fine-tuning of its electronic nature through nanostructure modification. Notably, the interface chemistry of an electrocatalyst plays a significant role in their optimized electrocatalytic activity and stability. This review provides an overview of recent progress in nano- and micro-structured catalysts, such as one, two, and three-dimensional catalysts as binder-free electrodes for electrocatalytic water splitting *via* the hydrogen evolution reaction and oxygen evolution reaction, and beyond. Furthermore, this review focuses on the current challenges and synthesis strategies of binder-free electrodes, with a focus on the impact of nanostructure on their functional property relationships and enhanced bi-functional electrocatalytic performance. Finally, an outlook for their future advances in energy conversion and storage is provided.

1. Introduction

Energy conversion and storage *via* electrocatalysis has led to significant developments in recent decades, in part due to advances in catalyst design at the nano- and micro-scale level. This growth in research activity has been vital for the realization and development of alternative energy technologies based on electrochemical reactions such as water splitting, metal-air batteries, and fuel cells.[1-7] Typically, bi-functional electrocatalytic reactions such as the hydrogen evolution reaction (HER) and oxygen evolution reaction (OER) are the core mechanisms for the conversion of chemical energies and storage systems.[8] Precious metals such as platinum (Pt), ruthenium (Ru), and iridium (Ir) are ideal electrocatalysts for the HER and OER, but they are expensive. Thus, there is a need for high-throughput and scalable manufacturing processes to create a new generation of low-cost, efficient, and highly durable electrocatalysts; this

represents a significant challenge for the large-scale execution of electrochemical energy technologies.

Electrocatalytic energy conversion reactions are complex since there is an interaction between the solid catalyst, electrolyte, gas, liquid-phase reactants, and products.[8-10] Traditional electrodes, that are typically fabricated by drop-casting methods using glassy carbon (GC), binders (e.g. Nafion), and conductive additives (e.g. carbon black), exhibit several unfavorable reactions which block charge transfer through the increased resistance of the electrocatalyst-substrate interface, reduce the number of active sites and limits the mass transfer rate; which results reduced catalytic activity and stability (**Figure 1a**).[11-13] As a result, there is a need to optimize the choice of material and conductive additives to deliver high-performance electrocatalytic systems. Thus, the electrochemical reactivity of the conductive substrate is a key feature in selecting a substrate for electrochemical applications. An ideal substrate should be able to easily access the electrochemical reactivity; however, this can be a challenge since the overall behaviour depends not only on the properties of the substrate but is also on the choice of liquid electrolyte, voltage range, temperature, gas purge, and other operating conditions.[14-18]

In particular, the high-throughput scalable manufacture of inexpensive, efficient, and highly durable electrocatalysts that can operate in harsh conditions represents a significant challenge for the large-scale execution of electrochemical technologies, as outlined in **Scheme 1**. Consequently, there is a need for new electrode materials that are both highly electro-active and demonstrate robust stability. In this context, the direct growth of nano- and/or micro-scale structures is regarded as an important approach for the manufacture of 1D, 2D, and 3D catalyst/electrode interfaces.[2, 19-22] These types of catalysts often exhibit superior activity compared to bulk materials due to their unique combination of structural, morphological, electronic, charge transfer rate, and chemical surface properties. The size and dimensions of the nano- and/or micro-structured catalyst can be used to regulate the amount of low-coordinated sites on the catalyst surface, which can control the binding strength of the reactant and enhance a specific catalytic reaction.[2, 23-27] To fully exploit these features, there is a need for scalable preparation methods to manufacture binder-free electrodes and their heterostructures in high-quality form at a low cost. At present, energy conversion is restricted to a restricted number of materials and their composites, and several new binder-free electrodes are being developed for renewable energy applications, such as H_2 and O_2 generation.

This review, therefore, aims to provide new directions and opportunities for these intriguing new materials. While there have been excellent reviews on binder-free electrodes (for instance, *see* Ref.[28-36]), they have an emphasis on either one or a limited number of systems for energy conversion and storage applications. The study of binder-free nano- and/or micro-structured catalysts and electronic structure engineering through the use of a range of substrate materials offers exciting prospects to design innovative materials with superior multi-functionality and is of interest for future directions in the field of energy conversion and storage research. They also are attractive candidates for next-generation energy conversion and storage applications. The successful application of binder-free nano- and micro-structured materials relies on a better understanding of their structural and functional properties and their role in system performance. Therefore, a comprehensive review and discussion on recent advances in binder-free nano- and micro-structured materials should examine the influence of the substrate material and the potential to modify the electronic structure, exposed active sites, conductivity, and porosity by tailoring their structure. In this review, we overview and analyze the current challenges on the synthesis strategies to create binder-free electrodes and focus on the impact of nano- and micro-structure and their functional property relationships and enhanced bi-functional electrocatalytic performance such as the HER and OER, and beyond. We believe that this overview of the latest research data is crucial for advancing novel binder-free electrode materials, given the vast number of combinations that can arise in the short term.

2. Dimensionality of nano- and micro-structured catalysts

Nanostructured materials having dimensions in the 1 to 100 nm range were initially classified based on the chemical composition and atomic arrangement, such as the crystallite morphology and/or atomic structure of the material, and this concept was then extended by Skorokhod *et al.*[37] Later, Pokropivny and Skorokhod[38] classified nanomaterials based on the dimensionality of the nano- and micro-structures in the category of 0D, 1D, 2D, and 3D systems. Interestingly, nanostructure control over dimensions and the composition of structures makes it possible to tailor/fine-tune material properties to specific applications.[39-43] Nanoparticles (NPs), fullerenes, nanodots, and quantum dots (QDs), all fall under the category of 0D nanostructured materials.[44, 45] 1D materials include nanoneedles, nanotubes, nanorods, nanofibers, nanowires, nanoribbons, and nanobelts.[46] These materials are a few nanometers in

breadth and a few micrometers in length in 1D. Meanwhile, 2D nanostructures are one-atom or few atoms thick-layered materials with two dimensions that lie beyond the nanoscale size range, which includes nanoplates, nanoflakes, nanosheets, nanoprisms, nanowalls, and nanodisks.[8] Finally, 3D materials consist of all three dimensions beyond the nanoscale size range and have emerged as an exciting class of nanomaterial. Numerous interesting morphologies appear under the category of 3D nanostructured materials, which include dendritic structures, microcubes, hierarchical structures, and micro flowers.[2] Nanomaterials (0D, 1D, 2D, and 3D) have found a wide range of applications due to their unique characteristics such as precise control over size, shape, porosity, morphology, and interface structure to promote electrical conductivity, abundant electrochemical active sites, facile charge transfer, and mass transport. Applications include bio-sensing, bio-medicine, photocatalysis, electronic devices, CO_2 reduction reaction (CO_2RR), supercapacitors, batteries, and electrocatalysis.[47-54] However, the practical use of nanomaterials in powder form is restricted by the cost of large scale production and the complex fabrication processes used to create the electrodes, which influences the performance of several energy conversion and storage systems, especially in electrocatalysis (**Figure 1a**, for more details *see* section 3). In this context, the direct growth of nano- and micro-scale structures is regarded as an important approach for the manufacture of 1D, 2D, and 3D catalyst/electrode interfaces. Hence, significant research effort has been dedicated to the fabrication of different dimensional electrocatalysts with controlled 1D, 2D, and 3D morphologies with regulated size and shape on a variety of conductive substrates, such as Ni, Fe and Cu foams to form robust binder-free electrodes for high performance electrocatalytic reactions.[55-59] Interestingly, directly grown multi-dimensional electrocatalysts at the nanoscale on a range of current collectors, namely substrates, and will benefit from a strong adhesion with the current collector to avoid catalyst delamination, limited active sites and charge transfer blockage to enhance catalytic reactions(**Figure 1b-d)**.[9, 60-64]

3. Key prospects, insights, and the dynamic properties of nano- and micro-structured binder-free electrocatalysts and their direct impact on electrochemical reactions

Water splitting has become one of the most important technologies to produce hydrogen (H_2) in high purity form. Water splitting includes two half-reactions, namely the cathodic HER and anodic OER.[8, 65] Generally, the electrocatalytic performance and

activity are highly sensitive to local reaction conditions and is largely valued by the energy required for adsorption/desorption of reaction intermediates and the rupture/creation of chemical bonds. Hence, the conventional powder form of precious metals such as Pt/C for the HER and RuO_2 or IrO_2 for the OER are considered ideal electrocatalysts.[66] In addition, several non-precious 1D, 2D, and 3D nano- and micro-structured powder catalysts such as MoS_2, WS_2, Ni_3S_2, $NiCo_2S_4$ are also of interest for the HER and OER reactions.[54, 67-74]

However, for commercial purposes and practical applications, the catalysts need to provide continuous gas evolution (*i.e.*, H_2, O_2) at a high current density (~1 A cm^{-2} with stability for a few thousands of hours), and the use of these powdery nanocatalysts coated on the current collector (typically glassy carbon; GC) is limited by the complex fabrication process and deterioration in electrocatalytic performance and stability.[55, 64, 75, 76] Meanwhile, an inappropriate optimization/use of binders may lead to an increase of resistance, inhibit mass and charge transport and bury the real active sites, as shown in **Figure 1a**., to reduce the overall catalytic activity. In addition, the low electrical conductivity of several powder based nanocatalysts necessitates the use of conductive additives (*e.g.,* carbon black). Under OER conditions and at high potential, the carbon-based conductive additives may be etched or are prone to oxidize, which limits the overall performance and stability. Importantly, the low adhesive force between the substrate (e.g. GC) and catalytically active phase results in low mass-loading of catalysts (>1 mg cm^{-2}), which reduces the number of exposed catalytically active sites for electrocatalytic reactions. As a result, powdery nanocatalysts cast on conductive substrates often result in low current densities and requires high overpotentials for both HER and OER for a few dozens of hours, with the possibility of delamination from the substrate during large-current and/or long-term electrocatalysis.

To address these challenges, and inspired by the advantages of the nano- and micro-structured architectures, researchers have integrated a range of nano- and micro-structures with substrates to optimize the electrocatalytic performance from the laboratory scale to the commercial level.[28],[55],[77],[78-81] These have included foams (Ni, Fe, and Cu), stainless steel (SS), foils (Cu, Ti, and Al), Si wafer, transparent conductive substrates (ITO and FTO) and carbon-based materials such as graphene foam (GF), highly oriented pyrolytic graphite (HOPG), carbon cloth (CC), carbon paper (CP), carbon fibers (CF), carbon nanotubes (CNTs), and GC.

Usually, electrode-based electrochemical reactions are known to occur at a three-phase electrochemical interface that consists of an electrocatalyst, conductive support, and the electrolyte. The three-phase main steps during the electrode reaction are shown in **Figure 1b and Figure 2;** these include (i) mass transfer (*i.e.,* transfer of ions/molecules from the bulk electrolyte to the electrocatalytic surface), (ii) electron transfer from the substrate to electrocatalysts surface and (iii) electrocatalytic surface reaction employing adsorption of ions/molecules, charge transfer, reconstruction of molecules, rupture/creation of chemical bonds, and desorption of reaction intermediates/products at the active sites surface.[76, 82-84] For an easier understanding, the effect of powder based nanocatalysts and nano- and micro-structured binder-free electrocatalysts on electrocatalytic activity is compared and discussed from two main perspectives such as electron transfer and mass transfer (**Figure 2**). As shown in **Figure 1 and Figure 2**, engineering the dimensionality of nano- and micro-structured catalysts on a conductive substrate has been widely employed as an effective strategy to improve catalytic performance. In addition, the inherent properties of catalysts/support interface energetics/kinetics include,

(i) As shown in **Figure 2a**, nano- and micro-structured catalysts on conductive substrate encourage fast electron transfer at the substrate-catalyst interface and catalyst-electrolyte interface to enhance the catalytic activity. A strong coupling between the substrate and catalyst can inject or withdraw electrons from the in-situ grown nanocatalyst, and thus modify the interfacial resistance. In fact, the interface resistance between the conductive substrate and metal catalyst is smaller than that of the semiconductor or insulating catalyst. However, the electrocatalytic properties of semiconducting binder-free electrocatalysts have been improved by the reduction of interfacial resistance, through optimization of size and/or thickness at the nanoscale or formation of catalyst-catalyst interfaces.

(ii) In a 1D, 2D, and 3D nano- and micro-structured binder-free electrodes, the catalyst can be uniformly deposited on a range of substrates. This can provide structural stability, controlled morphology, and avoids the aggregation of the catalyst during electrocatalytic reactions. Appropriate 1D, 2D, and 3D nano- and micro-structure engineering on a catalyst surface can alter the surface electronic structure and bond strength between reaction intermediates (by hydrogen bonding, van der Waals interaction, and electrostatic interactions) and active sites, which

directly effects on the interface adhesion force and thereby improve mass transfer for catalytic reactions.

(iii) As shown in **Figure 2b**, nano- and micro-structured binder-free catalyst electrodes can influence channel size and the exposure of active sites to the reactant. The reduced size and thickness of 1D, 2D, and 3D nano- and micro-structured binder-free electrodes offer abundant exposed active sites that are available to access reactants; hence the catalytic reaction rate enhances per electrode. In addition, the electron transfer overpotential reduces by the presence of short paths for electron transfer and small resistances at the catalyst-support interfaces, which results in high current densities at relatively a small low overpotential.

(iv) The interaction between the 1D, 2D, and 3D nano- and micro-structured binder-free catalyst surface and the interfacial water in an inner Helmholtz plane (IHP), influences the bond strength between 1D, 2D, and 3D nanocatalysts and reaction intermediates (*i.e.,* breakdown/creation of chemical bonds, and intermediates stabilization) and proton concentrations, and hence effects on the activity and reaction mechanism **(Figure 2c)**. It is worth noting that interfacial water accommodates the transfer of charges through the electric double layer, which may facilitate water dissociation to influence activity.[85, 86]

(v) The pore channels made by catalytic 1D, 2D, or 3D nano- and micro-scale building blocks ensure a smooth supply of electrolyte and help remove H_2 and O_2 bubbles to increase mechanical stability, and reduce mass transfer overpotential for HER/OER. Furthermore, the strong adhesion of the catalyst to the electrode surface offers high structural stability and outstanding electrocatalytic activity for practical applications.

In addition, the use of binder-free electrodes has additional distinctive physical advantages such as: (i) they can be used as a direct electrode material for a range of electrochemical reactions and can minimize the number of processing steps, (ii) binder-free electrodes avoid the need for insulating polymer binders and conducting carbon additives, (iii) the catalyst can be uniformly deposited on a range of substrates with a favourable architecture (nanowires/plate/pillar arrays; 3D porous architecture) that provide an open porous structure and a large electroactive surface area to facilitate the

diffusion of electrolyte ions (H^+/OH^-) to the electroactive sites and fast reaction kinetics.[56-58, 87]

In summary, binder-free nano- and micro-structured electrodes provide control of (i) the dimensionality of catalysts (controlled *via* fabrication conditions), (ii) engineering of the catalytic surface chemistry (e.g., structure, defect, doping, chemical composition effects), (iii) the nano- and micro- structure of catalysts (size and thickness at nanoscale), (iv) the electron transport path (electrical conductivity effect, catalysts-substrate effect, and catalyst-catalyst effect) and (v) the catalysts-electrolyte interplay, (intermediates/products and active sites) which have a significant role on electrocatalysis, which controls the performance of 1D, 2D, and 3D nano- and micro-structured binder-free electrodes for electrocatalytic reactions. Based on the above-mentioned inherent properties, in the following sections, we will present recent progress in understanding how the above-discussed parameters influence the catalytic performance from the basis of the design of 1D, 2D, and 3D nano- micro-structured binder-free electrodes, to realizing robust water splitting with current challenges and future perspectives.

4. Fabrication of nanostructures on binder-free electrodes

In light of the above considerations, binder-free electrodes have attracted significant interest.[55-58, 79, 83, 87] Nano- and micro-scale catalysts directly grown on a range of substrates are superior to powder based electrocatalysts as they provide structural stability, controlled morphology, uniformity, and significantly enhanced electrocatalytic activities; details in this regard are summarized in **Table 1 and Scheme 2**. In the following sections, we discuss the controlled fabrication of 1D, 2D, and 3D nano- and micro-structured catalysts on a variety of substrates.

4.1 Nickel foam (Ni foam or NF)

Nickel foam (NF) is the most widely employed 3D porous metal substrate for the growth of a range of dimensional nano- and micro-structured materials due to its large surface area, high conductivity, and attractive mass-transport properties.[87, 88] Previously, a large number of nano- and micro-structured materials with different morphologies and dimensionalities have been grown directly on NF, which includes transition metal oxides/hydroxides,[89-91] sulfides,[92-96] selenides,[97, 98] phosphides, [99, 100] phosphates,[101, 102] nitrides,[103, 104] layered double hydroxides [105] and their composites with carbon-based materials.[106, 107] Numerous synthetic strategies have

been explored, including chemical, electrochemical, and physical methods to synthesize a wide range of nano- and micro-structured materials on 3D porous NF to employ as a binder-free electrode for electrocatalytic water splitting reactions.[87, 88, 100] For example, Wang *et al*.[92] described the growth of hierarchically porous Ni_3S_2 nanorod arrays on HCl treated NF by a direct hydrothermal treatment. The strong interaction between the electrocatalysts (Ni_3S_2) and acid-treated current collector (NF), led to improved electron transport and long-term stability of the electrocatalyst. It has been observed that the NF not only acts as a current collector for the growth of electrocatalysts, but it also serves as a source of Ni since it facilitates the unidirectional diffusion of Ni ions from its surface towards the solution.[87, 88] In addition, a range of nickel sulfide crystal structures have been grown on NF with a variety of morphologies that depend on the ratio of nickel and sulfur, which includes NiS, Ni_3S_2, NiS_2, Ni_3S_4, Ni_9S_8, and Ni_7S_6.[88, 92, 108-110] A significant effect of electrocatalyst morphology and crystal growth has been observed on electrocatalytic reactions. Yang *et al.*[101] used a solvothermal phosphatization strategy for the *in-situ* growth of vertically grown 2D amorphous $FePO_4$ nanosheets on NF ($FePO_4$/NF) for efficient water splitting. Gupta *et al.*[90] reported on the solvothermal synthesis of binder-free flower-shaped Co_3O_4 nanostructure electrode directly grown on NF. In addition to hydrothermal and solvothermal approaches, an electrodeposition method was also employed to synthesize a range of dimensional cobalt oxides and hydroxides nanostructures on NF for alkaline and neutral medium-based electrocatalytic water splitting.[91] The intrinsic conductivity of any electrocatalysts is further improved by transition metal doping into the crystal host lattice.[93, 94] For example, Sun *et al*.[93] reported Fe doped Ni_3S_2 particles with a high Fe content (~11.8%) grown on an NF by a hydrothermal treatment. To improve the intrinsic conductivity of Ni_3S_2/NF nanowire arrays, Mo-doping has been employed by Du *et al.*[111] Recently, as shown in **Figure 3(i)**, Yu *et al.*[112] established the fabrication of Ni nanodots (~2 nm) on NF (NiNDs@NF) *via* the electrodeposition method. The subsequent drying of NiNDs@NF in air, resulted in the formation of a binder-free NiO/NiNDs@NF electrode with highly porous structure, abundant exposed active sites, and enhanced electrical conductivity.

The formation of binary and ternary transition metal-based electrocatalysts is also of interest. In this regard, Chen *et al.*[113] prepared nanorod arrays of the ternary transition metal Fe-Co-Ni dichalcogenide on NF *via* the hydrothermal method. The precursors of Na_2S, $FeSO_4 \cdot 7H_2O$, $Co(NO_3)_2 \cdot 6H_2O$, urea, sodium citrate dihydrate

($Na_3C_6H_5O_7 \cdot 2H_2O$) were used for synthesis, whereas bare NF was employed as the Ni source, as presented in **Figure 3(ii)**. As a consequence, the electronic properties were enhanced. Similarly, Huang *et al.*[114] utilized a Fe doping strategy to improve the electronic properties of a CoNi (oxy)hydroxide nanorod array catalyst *via* two hydrothermal processes. In brief, in the first hydrothermal process, the CoNi-OH nanorod arrays were uniformly grown on the NF at 120 ℃ for 12 h, as shown in **Figure 3(iii)**. Later, a $Fe(NO_3)_3$ solution of different concentrations (10, 20, and 30 mM) was mixed with CoNi-OH/NF to prepare Fe-CoNi-OH-*x* (*x* = 10, 20, and 30) *via* a second hydrothermal method at 60 ℃ for 6 h. The unique nanorod array structure of Fe-CoNi-OH-*x* exhibited a high electrical conductivity and increased electrocatalytic active sites. Wang *et al.*[115] prepared vertically grown binary porous $CoFe_2O_4$ nanomesh arrays on NF ($CoFe_2O_4$ NM-As/Ni) *via* a hydrothermal approach followed by high-temperature calcination at 680 ºC in air. As a consequence of the nanomesh structure and temperature effect, the $CoFe_2O_4$ NM-As/Ni exposed numerous pores leading to a large specific surface area and electrochemical active sites. Furthermore, it has been observed that the vertical growth of $CoFe_2O_4$ NM-As/Ni minimized the degree aggregation, which led to an enhanced conductivity. Typically, the catalytic performance of any binder-free nanostructures can be enriched by heterojunction formation, which leads to unique electronic properties at the interface, interfacial charge polarization, and bonding with reaction intermediates. In this regard, Guan *et al.*[105] fabricated a hierarchical structure of CoNi/$CoFe_2O_4$ on an NF as an efficient binder-free electrode material for overall water splitting, as shown in **Figure 4(i)**. The unique hierarchical structure, the CoNi/$CoFe_2O_4$/NF binder-free electrode exhibits abundant exposed electrochemical active sites and enhanced electron transport with an open channel for the release of gas bubbles. Liang *et al.*[116] used a uniform magnetic field as a one-step chemical-deposition method to prepare a robust Ni_xFe_{1-x} alloy (core)–ultrathin amorphous oxyhydroxide (shell) nanowire array on NF (denoted as Ni_xFe_{1-x}–AHNAs), and they are shown in **Figure 4(ii)**. This approach enhanced the catalytic activity, and the electrodes with altered Ni/Fe ratios were prepared by simply changing the molar ratio of the Ni precursor compared to the Fe amount.

In addition, the temperature-controlled phosphorization, sulphurization, and selenization growth of dissimilar nanostructures on NF followed by hydrothermal, solvothermal, and solution methods are of interest to fine-tune the catalytic properties of binder-free nano- and/or micro-structures.[92-99, 117-119] For example, Shen *et al.*[117]

demonstrated the growth of bi-functional electrocatalyst of porous molybdenum phosphide (MoP) nanoflakes on NF (**Figure 5(i)**). Typically, the growth of MoP nanoflakes on NF involved a two-step process, namely the growth of MoO_2 nanoflakes on NF by hydrothermal treatment, followed by a phosphorization treatment. The direct phosphorization of bare NF was performed using a solvothermal approach to achieve a nickel phosphide nanorods/nickel (Ni_2P nanorods/Ni) electrode by utilizing red phosphorous as a phosphorous source.[99] As shown in **Figure 5(ii)**, by using thermal phosphorization, Zhang *et al.*[120] prepared $Ni_{12}P_5$-Ni_2P polymorphs on NF, where phosphorization was achieved using thermally as-prepared $Ni(OH)_2$/Ni/NF with NaH_2PO_2 at 300 °C for 120 min under Ar gas. As shown in **Figure 5(iii)**, to expose more active sites and high stability, Duan *et al.*[121] prepared P doped $Ni_3S_2/CoFe_2O_4$ arrays on NF (P-$Ni_3S_2/CoFe_2O_4$/NF) *via* a two-step hydrothermal treatment and subsequent phosphorization. As a consequence, the P-$Ni_3S_2/CoFe_2O_4$/NF was in the form of micrometer-sized flowers, where several nanosheets were assembled to form the flower-like architectures.

Effort has also been made to combine different transition-based nano- and micro-structures with carbon-based materials to enhance the conductivity of bi-functional binder-free electrocatalysts.[106, 107, 122] In this regard, Guan *et al.*[122] prepared a terephthalic-acid (TPA) induced binder-free NiCoP-carbon nanocomposite (NiCoP-C(TPA)) film on conductive NF. The as-obtained NiCo(TPA)/NF electrode was subsequently carbonized at 500 °C for 3 h under an Ar atmosphere (2 °C min^{-1}) for enhancing crystallinity and integrating the carbon material in the NiCo bimetallic compound. Finally, NiCo-C(TPA)/Ni foam electrode material was phosphorized with NaH_2PO_4 to achieve a NiCoP-C(TPA)/NF. Similarly, a 3D porous $NiSe_2$/Ni hybrid electrocatalyst was fabricated by direct thermal selenization (at 450 to 600 °C for 1 h under Ar gas) of NF using selenium powder.[97] The direct growth of the $NiSe_2$ catalyst on an NF provided good electrical conductivity and led to the formation of a porous structure of $NiSe_2$ on the NF surface. Notably, the morphology of the as-grown $NiSe_2$ catalyst on NF was controlled by different growth temperatures. The conductivity and active sites were further enhanced by the formation of a composite structure ($NiSe_2$-anchored N, S-doped graphene/NF) using the CVD grown N, S-doped graphene.[123] Jiang *et al.*[104] created a mesoporous Fe_2Ni_2N nanoplate array (NPAs) on NF by nitridation (under an NH_3 atmosphere at 380 °C) of a hydrothermally prepared NiFe LDHs nanoplates/NF. As a consequence, the Fe_2Ni_2N nanoplates exhibited a large

electrochemical active surface area. To date, research effort has been dedicated to the growth of different dimensional metal oxides on NF as a binder-free electrode; however, to enhance the physicochemical properties, they have subsequently undergone a high or low temperature assisted sulphurization, selenization, phosphorization, and nitridation process to convert them into high purity sulphides, selenides, phosphides and nitrides for water splitting reactions.[124-128] Examples include, $FeCo_2S_4$ nanosheets,[125] $Co_{0.75}Ni_{0.25}Se$ nanorods,[126] 3D mesoporous rose-like $Ni_{0.76}Fe_{0.24}Se$ microspheres,[127] Co-Ni-P nanowires,[129] hierarchical NiFeP micro flowers,[130] 2D NiCoFe phosphate nanosheets,[131] 3D Ni-Co sulfoxide nanosheet arrays,[132] nanosheets of Ni_3N,[133] and Ni_3S_2@$Co(OH)_2$ heterostructures[134] supported on NF.

4.2 Copper foam (Cu foam or CF)

In a similar way to NF, copper foam (CF) is a widely used current collector substrate for the direct growth of a range of nano- and micro-structured materials due to its 3D conductive framework and microporous structure. Recently, Xing *et al.*[135] prepared Cu_xO nanowire array (NWs)/CF through oxidation followed by calcination of the CF. As a consequence of the NWs and calcination effect, the conductivity of Cu_xO NWs/CF was highly enriched (**Figure 6(i)**). A vapour ammonization strategy has been utilized by Zhang *et al.*[136] to fabricate an N-modified 3D Cu foam. Initially, a piece of CF was placed on a porous SiO_2 griddle of a glass steamer and then inserted into a 100 mL Teflon vessel, at the bottom of which 5.0 mL of NH_3 solution was added, then the ammonization was performed at 100 °C for 12 h; these are shown in **Figure 6(ii)**. In addition, compared to bare NF, the Cu foams are stable in acidic media, which makes this substrate more viable for the HER and OER in an acidic or alkaline medium. In this regard, Sun *et al.*[137] demonstrated the fabrication of Cu_3P nanowire arrays on commercial porous CF by a two-step process that served as high-performance HER electrocatalysts in acidic media. In the first step, a $Cu(OH)_2$ NW precursor was directly grown on the CF ($Cu(OH)_2$ NW/CF) by wet chemical synthesis that was carried out at room temperature. In the second step, the $Cu(OH)_2$ NW/CF precursor was treated with NaH_2PO_2 at 300 ºC with a heating rate of 2 ºC min^{-1} for 1 h under Ar to obtain Cu_3P NW/CF (phosphidation reaction). The unique architecture of the electrocatalyst on the CF allowed good adhesion of the electrocatalyst and rapid electron transport. Later, Chen *et al.*[138] reported similar electrocatalysts Cu_3P nanoarrays on CF formed through a topotactic phosphorization method and found that they provided a large electrochemical active surface area for electrocatalytic water splitting in a basic

medium; as shown in **Figure 6(iii)**. Similarly, using a solution method followed by phosphidation of $Cu(OH)_2$ NWs/CF with $Co(NO_3)_2.6H_2O$ and NaH_2PO_2, Doan *et al.*[139] prepared a hierarchical hybrid of an O-doped Co_2P layer on CuO nanowires on a CF substrate, as shown in **Figure 6(iv)**.

Zou *et al*.[140] reported on a highly efficient bi-functional electrocatalyst that consists of a Cu cluster coupled with an amorphous cobalt sulfide supported on a CF (Cu@CoS_x/CF). The amorphous nature of the Cu@CoS_x film was observed by HR-TEM and SAED images which were further supported by XRD analysis. Furthermore, a detailed structural analysis on the oxidation state/coordination of the Co and Cu atoms in Cu@CoS_x film was performed by X-ray absorption near edge structure (XANES) and extended X-ray absorption fine structure (EXAFS) analysis, which revealed the presence of sub-nanometric Cu metal clusters in Cu@CoS_x. The synergistic effect between the Cu clusters and CoS_x was revealed by the experimental results and theoretical calculations. In addition, several Ni-based electrocatalysts have been directly grown on a CF as bi-functional electrocatalysts.[141, 142] Asiri *et al*.[141] reported the fabrication of a Ni_3Se_2 film on a CF (Ni_3Se_2/CF) through an electrochemical deposition method which operated as an outstanding bi-functional electrocatalyst in a strongly alkaline medium. Recently, Streb *et al*.[143] presented a one-step synthesis of non-precious metals and mixed metal oxide nanostructures on a commercial macroporous CF by employing the hydrothermal treatment of $Co(NO_3)_2.6H_2O$ and $K_8[SiW_{11}O_{39}].13H_2O$ at 150 °C for 8 h; this is shown in **Figure 7**. This mixed metal oxide electrocatalyst was designed to enhance the electrical conductivity, achieve a large electrochemical active surface area, and provide an excellent catalytic activity, structural stability, and durability. In addition, Tang *et al*.[144] presented a simple and facile approach for the fabrication of forest-like NiCoP@Cu_3P heterostructure immobilized on a CF (NiCoP@Cu_3P/CF). During the synthesis of the NiCoP@Cu_3P/CF hierarchical structure, $Cu(OH)_2$ nanowires were first synthesized by chemical oxidation of the CF. In the second step, NiCo-LDH@$Cu(OH)_2$/CF nanosheets were synthesized by the hydrothermal route, which were subsequently phosphorized using NaH_2PO_2 and heated to 300 °C for 1 h under an N_2 atmosphere at a heating rate of 5 °C min^{-1}. The TEM analysis revealed a rough and porous surface on the NiCoP@Cu_3P/CF electrocatalyst. Recently, Jiang *et al*.[145] reported on the formation of an intermetallic Co_3Mo NPs supported on a nanoporous Cu surface (Co_3Mo/Cu), where the intrinsic activity of intermetallic Co_3Mo and hierarchical nanoporous Cu

skeleton provided rapid electron-transfer and mass-transport pathways. Notably, several research groups have reported on the use of a Cu-based electrocatalysts with different 1D, 2D and nanostructures to improve water splitting performance.[140, 146-149]

4.3 Stainless steel sheet (SS or SSM)

Until now, we have discussed 3D foams (Ni and Cu) as the supporting material for the growth of nano- and micro-structured materials which were employed as binder-free high-performance electrocatalysts for water splitting reactions and other electrocatalytic processes. In addition to 3D foams, a stainless steel (SS)-based supporting material has attracted attention for the direct growth of a variety of nano- and micro-structured materials for enhanced HER/OER performance.[150-155] For example, Todoroki *et al.*[150] demonstrated the synthesis of Ni-Fe hydroxide nanofiber/Ni-Fe oxide hetero-layered nanostructures on a 316 SS substrate by employing a simple electrolysis process. During the initial stage of electrolysis (2 h), the formation of Ni-Fe hydroxide nanofibers was observed using scanning transmission electron microscopy (STEM) analysis, which upon an increase in electrolysis time to 5 h resulted in the growth of heterostructure layers. As the electrolysis time was further increased, a dense nanofiber structures were observed on the upper layer, as seen in **Figure 8**. Their study presented a simple and effective route to fabricate ternary NiFeSe on a SS mat (SSM) (NiFeSe/SSM).[156] The as-obtained NiFeSe/SSM was found to be highly catalytically active, which was thought to be due to the direct binding of NiFeSe to the SSM through strong covalent bonding during selenization; this resulted in the low charge-transfer resistance and high durability against gas bubbles produced during operation at high current densities. This synthetic strategy directed a new route for the surface engineering of conductive substrates. In other work, nickel (II) sulphide (NiS) 2D nanosheets with a thickness of 10 nm and length of 200 nm were directly grown on SS meshes *via* a facile hydrothermal approach.[151] Recently, Wehrspohn *et al.*[154] demonstrated the fabrication of CNTs on a SS (CNT/SS) and employed it as an electrocatalyst. The interfacial interaction between CNTs and the SS support layer was found to be the governing factor in enhancing the surface area and achieving excellent conductivity for rapid electron/charge transfer at the 3D CNT/SS electrode. The interfacial interactions were identified by X-ray tomography and focused ion beam techniques. In the search for cost-effective bi-functional electrocatalytic materials for water splitting, the direct modification of SS has been explored as a binder-free electrode material for water electrolysis in acidic and alkaline media. In this regard,

surface oxidation has been performed either chemically or electrochemically for a variety of SS substrates, which have been utilized as a bi-functional electrode for water splitting.[157-160] In addition to the chemical and electrochemical modification of SS substrate, Xue *et al*.[161] proposed the design of a cellular SS with high electrochemical active surface area and mechanical properties through selective laser melting (SLM). The optimum pore size and electrochemical active surface area with an interconnected 3D porous network were achieved *via* the SLM technique, which resulted in high catalytic activity.

4.4 Foils

4.4.1 Copper foil (Cu foil or CF or CFl)

Another class of conductive substrates that have been employed widely for the fabrication of a 3D electrode are metallic foils, in particular Cu, Ti, and A.[162] They are often used to fine-tune the electrocatalytic performance by structural, electronic, and chemical composition engineering strategies. For example, Chen *et al.*[163] described the *in-situ* growth of crystalline Cu-based nanowire arrays, namely $Cu(OH)_2$, CuO, Cu_2O, and CuO_x on a Cu foil (CFl), and exploited the as-grown electrocatalysts for OER catalytic activity. In their work, the Cu foil served as a source of Cu-ion, which upon an oxidation treatment using a mixture containing NaOH and $(NH_4)_2S_2O_8$ led to the formation of a deep blue $Cu(OH)_2$ film on the CFl surface $Cu(OH)_2$/CFl. The as-prepared $Cu(OH)_2$/CFl films were calcined under different experimental conditions, which resulted in the formation of self-supported black CuO, orange Cu_2O, and dark brown CuO_x nanostructures on the CFl. The morphologies of the various resultant copper oxide/CFl films were characterized by SEM, as seen in **Figure 9(i)**, which demonstrated the formation of nanowire arrays in all samples. However, the examination of microscopic images revealed a rougher surface in the case of Cu_2O and CuO_x nanowires, as compared to $Cu(OH)_2$ and CuO nanostructures. Recently, Hussain *et al.*[164] reported on the construction of higher-dimensional CuO nanostructures on CFl by employing a wet chemical approach to form a binder-free electrocatalyst. The chemically controlled growth of CuO nanostructures resulted in the formation of controlled morphologies, namely nanosheets, nanocubes, nanoflowers, and nano leaves; these are shown in **Figure 9(ii)**. It is worth noting that the electrocatalytic performance of the different dimensional CuO nanostructures was found to be highly dependent on the electrochemical active surface area. Among the different morphologies of CuO nanostructures grown on Cu foil, CuO nanoflowers exhibited an

excellent intrinsic contact between the catalysts and substrate, which is beneficial for facile electron transport. Similarly, using the hydrothermal method, Wang *et al.*[165] prepared heterostructured hierarchical CuO@ZnCo LDH/CFl using a precursor of CuO NW/CFl. In brief, a precursor of CuO NW/CFl was prepared *via* a solution method, followed by thermal annealing of $Cu(OH)_2$/CFl at 180 °C for 1 h. Furthermore, the hydrothermal method was conducted using $Co(NO_3)_2 \cdot 6H_2O$, $Zn(NO_3)_2 \cdot 6H_2O$, NH_4F, and urea with CuO NW/CFl at 120 °C for 4 h to achieve a CuO@ZnCo LDH/CF. After the hydrothermal reaction, the XRD pattern exhibited several new diffraction peaks assigned to a typical ZnCo-LDH in CuO@ZnCo-LDH/CFl (**Figure 9(iii))**. Microscopic images of CuO@ZnCo LDH/CFl revealed that the smooth surface of the CuO NW was uniformly covered with dense ZnCo LDH, thereby indicating a core-shell structure of CuO@ZnCo LDH was formed. Recently, Wei *et al.*[166] reported on the formation of a dendritic structure, the FeN_3 phase grown on a CFl (Ni:Fe = 7.5:2.5/CFl) by electrodeposition for use as a binder-free electrode. In addition, La-doped CuO,[167] and 3DGraphene/g-C_3N_4/Cu_3P[168] electrocatalysts have been fabricated on CFl as binder-free electrodes for water splitting reactions.

4.4.2 Titanium foil (Ti foil or Ti)

Similar to Cu foil, Ti foil/mesh/plate has also been widely employed for the direct growth of nanostructured electrocatalysts for water splitting reactions due to its cost-effectiveness, lightweight, superior conductivity, excellent chemical, thermal, and mechanical stabilities, and good corrosion resistance. These characteristics are favourable for immobilization of the catalyst on a conductive titanium substrate with an open porous structure that is beneficial for facile electron/ion transport and easy escape of gas bubbles. A wide variety of nanostructured electrocatalysts such as oxides, hydroxides, chalcogenides, phosphides, and borides had been deposited directly on conductive Ti plate/mesh/foil through a chemical and electrochemical deposition for water splitting reactions.[169-178] For example, Sun *et al.*[169] demonstrated the growth of nickel diselenide ($NiSe_2$) nanoparticles on a conductive titanium plate substrate ($NiSe_2$/Ti) at room temperature through electrodeposition. The electrodeposition process on a Ti plate was performed at a potential of –0.45 V *vs.* SCE using an aqueous solution of $NiCl_2.6H_2O$ (0.065 M), SeO_2 (0.035 M), and LiCl (0.2 M) electrolyte. The as-grown electrocatalyst on the Ti plate was employed as a highly efficient and durable binder-free electrode in an alkaline medium. Similarly, the electrodeposition of Co-doped $NiSe_2$ nanoparticles on a conductive Ti plate was demonstrated by the same

group.[170] In contrast, Ma *et al*.[173] demonstrated a template-free hydrothermal strategy for the fabrication of 3D hierarchical MoS_2 micro-flowers on a microporous titanium mesh as a binder-free electrode exhibiting favourable structural features for high electrocatalytic activity. The hydrothermal treatment process was performed at 210 °C for 12 h, containing a titanium mesh and ammonium heptamolybdate, and thiocarbamide as the precursors for Mo and S, respectively. The conductive substrate Ti mesh served as a template for the growth of self-assembled hierarchical micro-flowers from MoS_2 nanosheets. Similarly, Wang *et al.*[174] examined the controlled synthesis of 1D porous and interconnected FeP nanorod-like structures on a Ti plate using a facile hydrothermal method, followed by calcination. Due to the synergistic effect of the porous nature of the FeP nanorods and the conductive Ti substrate, the as-fabricated binder exhibited more exposed active sites. Recently, Ding *et al.*[172] prepared nanoporous Zn-doped Co_3O_4 sheets with single-unit-cell-wide lateral surfaces for efficient electrochemical water splitting. The formation of nanoporous Zn-doped Co_3O_4 sheets with a unit-cell-thick sheet (NPCoO-UCSs) initially involved the growth of Zn-doped α-$Co(OH)_2$ nanosheets on a titanium foil by a hydrothermal route. Eventually, nanosheets were treated with NaOH and $NaBH_4$ to introduce porosity and reduce their thickness. Morphological analyses showed the presence of nanopores with < 10 nm in diameter, which resulted in a number of ligaments within the lateral surface in sheets; these are shown in **Figure 10**. The as-formed nanoporous Zn-doped Co_3O_4 benefitted from the presence of additional oxygen vacancies, thereby providing an ultrahigh catalytic activity and durability. As an alternative approach, Sun *et al.*[175] demonstrated the fabrication of a self-supported 3D Co-B@CoO nanoarray on a Ti mesh for water splitting under alkaline conditions. The fabrication of 3D Co-B@CoO nanoarray on a Ti mesh involved the *in-situ* formation of Co-B NPs (10-35 nm in diameter) on the surface of the CoO NWs array on the Ti mesh by $NaBH_4$ treatment under alkaline pH conditions at room temperature. The high catalytic activity of the 3D bi-functional electrocatalyst was attributed to the high loading of catalyst and large electrode thickness.

4.4.3 Aluminum foil (Al foil)

In recent years, efforts have been made for the utilization of Al foil as a substrate for the growth of electrocatalysts to enhance HER and OER performance.[179, 180] For example, Liu *et al.*[179] reported on the enhancement in the catalytic activity of 2D MoS_2 towards HER by making an exposed and activated basal plane of monolayer 2H MoS_2

via an ultrathin alumina mask (UTAM)-assisted ion beam etching (IBE). UTAM was obtained by two-step anodization of Al foils, which was later transferred to a substrate with as-grown monolayer MoS_2 (**Figure 11**). Recently, a new strategy was presented for the growth of tungsten and phosphorous co-decorated Ni-based alloy (NiWP) on anodic aluminum oxide (AAO) sacrificial substrate for OER performance.[180] For the growth of NiWP, the AAO template was first sensitized by treatment with a small concentration of $SnCl_2$ and $PdCl_2$ solutions. Thereafter, the sensitized AAO sheets were treated with the salts of Ni, W, and P, and sodium citrate at 80 °C for 2.5 h, which was later treated with NaOH to remove the AAO. The as-obtained free-standing NiWP electrocatalyst film was used as a binder-free electrode for high-performance catalysis.

4.5 Si wafer/SiO_2 substrate

Recently, Wang *et al.*[181] revealed the large-scale bottom-up synthesis of CoO nanosheets with a thickness of ~2.8 nm *via* an ionic layer epitaxy (ILE) method. During the ILE process, a monolayer of ionized amphiphilic oleyl sulfate surfactants at the water-air interface acted as a flexible template to direct the growth of CoO crystallization underneath by the electrostatic and covalent interactions between the precursor ions and functional groups on the amphiphilic molecules. For electrochemical measurements, the as-obtained 2D CoO nanosheets were directly transferred on a rigid Si wafer substrate. Shin *et al.*[182] used an atomic layer deposition (ALD) technique for the direct preparation of crystalline Ni_3S_2 thin films on a SiO_2 substrate. For the preparation of Ni_3S_2, bis(1-dimethylamino-2-methyl-2-butoxy) nickel (II) [$Ni(dmamb)_2$], and H_2S were used as the source materials for Ni and S, respectively. The as-obtained wafer-scale Ni_3S_2 layers on a non-conductive SiO_2 substrate suggest a potential as a binder-free electrode for large scale applications. Moreover the growth of transition metal nanostructures on a Si or SiO_2 substrate are of interest, usually, the carbonaceous materials have been grown on the native SiO_2 of a Si wafer.[183] In addition, as shown in **Figure 12**, Goldoni *et al.*[183] fabricated multi-walled carbon nanotube (CNTs)-based electrodes on Si wafers for water splitting reactions. After the growth of CNTs on a Si wafer, the CNTs were decorated with Pd, Ni, and Co metals *via* thermal evaporation. The decoration of a thin layer of metals on CNTs provided a high surface area and high electrical conductivity, which led to the maximum electrochemical reactivity at the electrode/electrolyte interface.

4.6 Carbon-based substrates

4.6.1 Graphene foam (GF or 3DGF)

A variety of soft and rigid substrates have been explored for the fabrication of binder-free electrode materials as robust bi-functional electrocatalysts for water splitting reactions. Recently, 3D graphene structures such as graphene foam (GF or 3DGF) and graphene aerogels (GA) have attracted considerable attention as self-supported substrates and/or current collectors for the growth of electrocatalysts. They have also been used as a catalyst due to their large surface area, porous structure, short ion/electron transport paths, and abundant electrocatalytic active sites. For example, Khojin *et al.*[184] examined the fabrication of 3D structured transition metal dichalcogenide (MoS_2) on a graphene film as a binder-free electrocatalyst for HER by employing the CVD method. The MoS_2/3DGF exhibited large active sites and high charge transfer due to the low contact resistance between graphene and MoS_2 toward active edge sites and optimum hydrogen binding energy is owing to the presence of graphene. N-doped GF was prepared by Qiao *et al.*[185] by the electrochemical expansion of carbon fiber paper followed by N_2 plasma treatment. The self-supported N-doped GF electrocatalyst exhibited abundant active sites, large electrochemical active surface area, and enhanced mass/electron transport within the graphene framework. Li *et al.*[186] reported on a self-supported bi-functional electrode for overall water splitting based on $CoS_{1.097}$/N-doped GF (NGF). The uniform decoration of $CoS_{1.097}$ NPs on a 3D-NGF was achieved by a two-step process involving hydrazine-induced foaming followed by thermal treatment at different temperatures (650-950 ºC); this is shown in **Figure 13**. Thermal treatment of the $CoS_{1.097}$/NGF composite at a range of temperatures played a crucial role in achieving a high electrocatalytic activity. Notably, the composite thermally treated at 750 ºC ($CoS_{1.097}$/NGF-750) exhibited a highly porous structure with super-hydrophilic properties. In addition, using a two-step process involving hydrothermal treatment followed by a low-temperature phosphatization, Jian *et al.*[187] prepared nickel-iron phosphide (NiFe-P) nanosheets on a 3D porous GF. The unique architecture of the NiFe-P nanosheets on a porous 3DGF resulted in a high surface area, conductivity, and stable structure. Similarly, other transition metal phosphides such as urchin-like cobalt-chromium phosphides and star-like molybdenum phosphides have also been grown on a 3D GF for water splitting reactions.[188]

4.6.2 Highly oriented pyrolytic graphite (HOPG)

In addition to the utilization of flexible GF, graphite sheets have also been employed as a self-supported substrate for the growth of a variety of nano- and micro-structured

materials for electrocatalysis due to their highly conducting network structure, the presence of meso-/macro-pores, and a large specific surface area (SSA).[189-194] The HOPG is a highly pure and well-ordered form of synthetic graphite. In this regard, Wang *et al.*[189] demonstrated the growth of self-supported graphene (SSG) on a flexible graphite sheet (SSG-FGS) *via* electrochemical intercalation. The $Co(OH)_2$ particles were subsequently deposited on SSG-FGS ($Co(OH)_2$/SSG-FGS) using a microwave-polyol method, as outlined in **Figure 14(i)**. The unique electrode structure ($Co(OH)_2$/SSG-FGS) consisted of FGS as a current collector and SSG as conducting channels to allow $Co(OH)_2$ to provide fast electron transfer. Meanwhile, the unique electrode assembly avoids the use of binders and inhibits the aggregation of graphene layers, which helps to achieve a high catalytic performance. In other work, a fascinating electrode design strategy was adopted for H_2 generation using Ni/$Ni(OH)_2$ on graphite.[190] The generation of a Ni/$Ni(OH)_2$ interface on graphite (Ni/$Ni(OH)_2$/graphite) was achieved using an electrochemical dual-pulse plating method with sequential galvanostatic and potentiostatic pulses. The as-fabricated Ni/$Ni(OH)_2$/graphite electrode exhibited an enhanced surface area on the graphite substrate, thereby facilitating a rapid charge transfer rate. In addition to the fabrication of these catalysts on a graphite electrode, amorphous nickel-iron (oxy)hydroxide nanosheets (NiFe) have been deposited on an exfoliated graphite foil (EG) substrate by a facile electrodeposition route, as seen in **Figure 14(ii)**.[191] The combined effect of the NiFe(oxy)hydroxide material and carbon (EG) substrate provides a hierarchical structure, high electrical conductivity, and a large surface area. Such an electrode architecture can accelerate ion transport and diffusion of gas bubbles, which provides a strong interaction between the catalyst and substrate and ensure good stability. Recently, Kim *et al.*[195] prepared solid–electrolyte interphase (SEI) layers of 21 m lithium bis(trifluoromethanesulfonyl)imide on HOPG electrode at −2 V *vs*. Ag/AgCl *via* electrodeposition, as shown in **Figure 14(iii)**. As a consequence of defect optimization, the catalytic performance was improved. In addition to the fabrication of oxides and hydroxides on a graphite substrate, other materials such as sulfides, selenides have also been deposited directly on a graphite electrode.[192, 193] For example, Irzhak *et al.*[193] deposited a thin film of WSe_x on a graphite electrode for HER activity in acid. Recently, N and S co-doped graphene (SNG) has been attached to a conductive graphite foam (SNG@GF) by a drop-casting method, followed by *in-situ* annealing.[194] XPS analysis revealed the presence of 7.22 and 1.34 at.% of N and S in the SNG, respectively.

However, the N and S peaks became weaker in SNG@GF with the prominence of pyrrolic-N (68.6%) compared with SNG (56.2%). A higher content of pyrrolic-N and pyridinic-N is beneficial to activate the adjacent carbon in the carbon framework for water splitting reactions. Furthermore, SNG@GF exhibited a robust interconnected structure which provided an improved interaction at the electrode/electrolyte interface.

4.6.3 Carbon cloth (CC)

Carbon cloth (CC) is one of the most flexible and conductive 3D self-supporting substrates for fabricating electrocatalysts for water splitting reactions. Extensive effort has been made in constructing different dimensional nano- and micro-structured materials, such as transition metal oxides, sulfides, phosphides, selenides, nitrides, doped systems, and composites with carbonaceous materials of various morphologies on self-supported CC substrate as a binder-free robust electrode for bi-functional electrocatalytic water splitting.[196-211] For example, Wang *et al*.[196] reported on the *in-situ* decoration of porous tungsten carbide NPs on CC (WC_x@CC) as a self-supported electrode for HER activity using CVD. An enhanced electrocatalytic performance results from the porous electrode structure and improved mass transport in both parallel and vertical directions to the substrate, with more accessible catalytically active sites. Pu *et al*.[203] examined the construction of a flexible electrode based on nickel diphosphide nanosheet arrays on CC (NiP_2/CC) by the phosphidation reaction of $Ni(OH)_2$ nanosheet. Later, the same research group presented a facile strategy for the fabrication of Co_2P QDs integrated with N, P co-doped carbon (Co_2P@NPC) on CC (Co_2P@NPC/CC).[198] To construct the flexible and binder-free electrode of Co_2P@NPC/CC, a solution of phytic acid (PA) and aniline was first electrodeposited on a CC. Thereafter, the polyaniline (PANI)-PA/CC precursor was immersed in a solution of $Co(NO_3)_2.6H_2O$ to immobilize the Co^{2+}, followed by calcination at 800 °C for 2 h under an H_2 atmosphere (**Figure 15**). The integration of N and P co-doped carbon framework inhibits the aggregation of Co_2P NPs and provides additional electrochemical active sites, enlarged surface area, and low charge transfer resistance. Sun *et al*.[200] attempted to enhance the catalytic performance of CoP by Mn doping through electrodeposition on a conductive CC substrate. Chu *et al*.[197] reported the formation of 0D-2D $CoSe_2$/$MoSe_2$ heterostructure by selenization of $CoMoO_4$ nanosheets integrated on a CC. The unique hierarchical heterostructure that consists of 0D $CoSe_2$ nanoparticles uniformly decorated on the $MoSe_2$ nanosheets facilitated the reaction kinetics and resulted in enhanced structural stability and accessible

catalytically active sites. Similarly, Chen *et al.*[204] established the integration of a high-performance $CoMoS_4$ nanosheet array on flexible CC support ($CoMoS_4$ NS/CC). The $CoMoS_4$ NS/CC was obtained by employing topotactic conversion of the Co(OH)F nanosheet array on CC (Co(OH)F NS/CC) in an $(NH_4)_2MoS_4$ solution *via* anion exchange reaction.

Recently, a facile two-step hydrothermal method was used to prepare uniform nanotube arrays of bimetallic iron-cobalt sulfide ($FeCo_2S_4$ NTA/CC) with tunable morphology, where the Co/Fe ratio and sulfidation concentration was varied to obtain a range of samples.[211] Initially, a precursor of Fe-Co nanowire arrays on CC (Fe-Co-NWA/CC) was prepared using $Fe(NO_3)_3 \cdot 9H_2O$, $Co(NO_3)_2 \cdot 6H_2O$, NH_4F, and urea in distilled water by a hydrothermal method at 120 °C for 24 h. The precursor Fe-Co-NWA/CC was then transferred into a $Na_2S \cdot 9H_2O$ solution for the second hydrothermal treatment (120 °C for 8 h). During synthesis, the control experiments using a range of $Na_2S \cdot 9H_2O$ concentrations of 0.01 M, 0.05 M, 0.2 M were executed, as shown in **Figure 16**. As a consequence, the optimized $FeCo_2S_4$ NTA/CC exhibited a well-defined hollow nanotube structure with highly exposed active sites. Qu *et al.*[205] fabricated a robust NiCoPS/CC electrode by a three-step process. The first step involves the formation of $NiCo_2O_4$ NWs on a conductive CC substrate *via* hydrothermal treatment, which is followed by the sulfidation of $NiCo_2O_4$ NWs in the second step using vaporized S powder. Finally, the as-obtained NiCoS nanowires were allowed to undergo a phosphorization reaction using NaH_2PO_2 as a phosphorous precursor at 400 °C under an Ar atmosphere. Liu *et al.*[207] presented the rational design of hierarchical nanoflakes of flower-like Ni_3FeN electrocatalyst on CC *via* electrodeposition, which was followed by ammonization of the NiFe precursor at 400 °C under an NH_3 atmosphere to obtain interlaced Ni_3FeN sheets, as shown in **Figure 17**. Interestingly, a transition in morphology was observed from nanoflakes to a 3D porous nano framework with a large surface area, which is beneficial for the electrocatalytic process. Recently, Guo *et al.*[209] reported on the precise control over the morphology of a cobalt-phosphorous-boron (Co-P-B) electrocatalyst on a CC (Co-P-B/CC) substrate by controlling the temperature using an electroless plating technique. Co-P-B/CC electrodes with a range of morphologies, namely nanothorns, nanoflowers, and microplates were obtained at 20, 30, and 40 °C, respectively, which was employed as a working electrode for water splitting reactions. Compared to the other electrodes, the Co-P-B/CC electrode with a nanoflower morphology exhibited a large electrochemical active surface area, low

charge-transfer resistance, and high electrical conductivity. In addition, different transition non-noble metals, transition metal oxides, dichalcogenides, and alloys have been integrated with a carbonaceous material to improve the electrocatalytic activity due to the large surface area, structural stability, and electrical conductivity of carbon materials.[208] For example, Hu *et al.*[210] obtained the direct growth of CNTs@$CoS_xSe_{2(1-x)}$ on CC by the CVD method. In order to integrate the multi-walled CNTs on the CC, a ZIF-67 precursor was directly grown on CC (CC/ZIF-67) in the presence of melamine at 800 °C for 1 h under H_2 (10 sccm) and Ar flows (90 sccm); this resulted in the formation of CC/CNTs@Co. Afterward, the CC/CNTs@Co was subjected to sulfurization/selenization reactions at different molar ratios using CVD to attain CNTs@$CoS_xSe_{2(1-x)}$. The incorporation of Se led to the creation of a polarized electric field, and the hierarchical structure of the electrocatalyst revealed an improved mechanical strength. Jeon *et al.*[208] prepared a sea-grape-like MoS_2/graphene 3D heterostructure on CC. Initially, graphene was grown on the CC substrate with a sea-like grape morphology (Gr/CC) using Ni electrodeposition and CVD at high temperatures. Thereafter, the MoS_2 was deposited on Gr/CC using a two-zone CVD (MoS_2/Gr/CC), resulting in a 3D heterostructure.

4.6.4 Carbon paper (CP)/Carbon fiber paper (CFP)

Carbon paper (CP)/carbon fiber paper (CFP) is another porous 3D self-supporting substrate that has been widely employed for the growth of a variety of electrocatalysts. The surface texture of carbon fiber accelerates the nucleation and growth of the catalyst, thereby providing a strong interaction between catalyst and support. A range of dimensional nanostructures such as nanoparticles, nanobelts, nanosheets, nanoplates, nano-octahedra, nanoflowers, and 3D heterostructures have been directly grown on CP/CFP for water splitting reactions.[212-226] For example, Zhao *et al.*[215] fabricated a $NiSe_2$ NWs/CFP by a two-step process involving the formation of $Ni_2(CO_3)(OH)_2$ on CFP ($Ni_2(CO_3)(OH)_2$/CFP) followed by the thermal selenization using selenium powder; see **Figure 18(i)**. In addition, other morphologies such as 0D nanoparticles of $NiSe_2$[221] and lamellar $CoSe_2$ nanosheets[219] have been grown on CP as a robust binder-free electrode by employing a one-step solvothermal method. Recently, Tian *et al.*[227] used electric-field assisted in-situ hydrolysis of two isomeric MOFs (FJI-H25Fe and FJI-H25FeCo). The subsequent FeCo-oxyhydroxide nanosheets exhibited a highly crystalline nature, as shown in **Figure 18(ii)**. In addition, Wang *et al.*[214] demonstrated the facet-dependent catalytic activity of $Co_{1-x}S$ nanosheet arrays (110

orientation) grown on a 3D CFP. The binder-free $Co_{1-x}S$/CFP electrode was achieved by a one-step electrodeposition method. Interestingly, the highly oriented exposed (110) facets of $Co_{1-x}S$ improved the porous structure and conductivity, which led to the generation of more catalytically active sites for efficient charge transfer. Ye *et al*.[223] fabricated metal-ion (Fe, V, Co, and Ni)-doped MnO_2 ultrathin nanosheets on a CFP by facile and effective anodic co-electrodeposition method. Ni-doped MnO_2 ultrathin nanosheets with a thickness of ~5 nm were deposited on the surface of the CFP, which exhibited several distinctive features such as being binder-free, ease of control of the catalyst loading level, and providing strong adhesion between the catalytic active material and CFP substrate. These features were beneficial for achieving a high catalytic performance towards OER.

Similarly, Hu *et al*.[217] created a range of morphologies of Zn-Co mixed sulfide (Zn-Co-S) nanostructures such as nanosheets, nanoplates, and nanoneedles on CFP by a two-step wet chemical synthesis, which involved hydrothermal treatment followed by a thermal sulfidation technique. Among the different Zn-Co-S nanostructures formed, the 1D Zn-Co-S nanoneedle decorated on a CFP binder-free electrode exhibited an enhanced electrochemical active surface area with abundant catalytically active sites and faster reaction kinetics. Other mixed metal sulfides, such as $Mo_{1-x}Co_xS_2$ nanosheets, have also been anchored on CFP as a self-standing and efficient bi-functional electrocatalyst for overall water splitting.[218] Phosphides have also been grown directly on a CFP as an efficient and low-cost HER electrocatalyst using an aqueous H_2SO_4 electrolyte.[224, 225] Heteroatom-doped carbon (N, S co-doped carbon) (NSC) films have also been grown on conductive CFP (CFP@NSC) as a self-supported electrode by electrodeposition of 2-amino-5-mercapto-1,3,4-thiadiazole, followed by pyrolysis.[226] As a result of the strong interaction between the NSC and CFP, the CFP@NSC electrode has abundant catalytic active sites, and the architecture of the electrode provided substantial channels for efficient electron and mass transfer.

4.6.5 Carbon nanofibers (CNFs)/Carbon nanotubes (CNTs)

Carbon nanofibers (CNFs) and CNTs have also been employed as substrate materials for the growth of different nano- and micro-structural materials due to their excellent conductivity, outstanding mechanical strength, favourable structure, good corrosion resistance, and large specific surface area. These characteristics provide efficient mass and electron transport to enhance electrocatalytic activity.[213, 228-237] Wang *et al*.[228] prepared PtNi nanoparticles (NPs) immobilized on 3D CNF mats (PtNi/CNFs) using

an electrospinning method and followed by carbonization. CNFs provide distinctive advantages as a support material, including removing the need for polymer binders and providing a strong interaction between the NPs and CNFs. PtNi NPs of several nm in size were uniformly dispersed on the surface of the CNFs, and the NPs were embedded in the carbon, layers which were found to be conducive to providing long-term durability. Similarly, the WO_{3-x} catalyst was synthesized on carbon nanofiber mats (CFM) by electrospinning and followed by carbonization.[231] In addition Liu *et al*.[232] presented the rational design of phosphorus-doped $NiCo_2S_4$ grown on a CNTs embedded CNF (P- $NiCo_2S_4$@CNT/CNF) by a two-step process which includes the preparation of CNT/CNF using co-electrospinning of a polyacrylonitrile (PAN) and CNT dispersion, which is followed by the peroxidation and carbonization; this is shown in **Figure 19(i)**. The CNTs were used to enhance the electrical conductivity of the 3D CNF network, which accelerated electron transfer to the active material. Thereafter, $NiCo_2S_4$ was grown perpendicularly on the CNT/CNF template by hydrothermal treatment ($NiCo_2S_4$@CNT/CNF), which provided more catalytically active sites. Finally, the as-resulted $NiCo_2S_4$@CNT/CNF material was doped with phosphorous *via* a phosphidation reaction at 300 ºC for 1 h (2 ºC min^{-1}) under an N_2 atmosphere. The P-doping in $NiCo_2S_4$@CNT/CNF improved the electronic structure of the $NiCo_2S_4$. Meanwhile, thin MoS_2 nanosheets grafted Co-N-C flakes (CoNC@MoS_2) have been grown *via* an electrospinning technique.[233] The unique hierarchical architecture of the binder-free electrode of CoNC@MoS_2/CNF imparted favourable flexibility and sufficient electrical conductivity for electrochemical reactions. Recently, Kulandaivel *et al*.[230] demonstrated the growth of 2D NbS_2/MoS_2 ultra-thin vertical nanosheets on CNFs with a high aspect ratio by a CVD approach, as shown in **Figure 19(ii)**. The designed heterostructure served as a viable electrocatalyst due to the presence of active edges and sulfur sites, which act in accelerating charge transfer towards the electrolyte. The use of a CNF substrate is not only limited to the growth of transition metal NPs, metal oxides, sulfides, selenides, and heterostructures on CNFs. Carbon hybrids with metal NPs have also been coated on carbon fibers as a flexible and binder-free water-splitting catalyst.[234] For example, Fan *et al*.[234] attained the integration of transition metal-based NPs (Ni-Fe, Ni-Mo) in an N-doped carbon, and it was found that synergistic effects between the bimetallic elements and N-doping led to improve the conductivity of the electrode.

4.7 Glassy carbon electrodes (GCE)

To date, a variety of nano- and micro-structured catalytic materials have been drop cast on a glassy carbon electrode (GCE) with the aid of a polymeric binder, such as Nafion, for a variety of electrochemical reactions.[238] However, this can lead to the catalyst layer peeling off/delaminating, which leads to poor conductivity and a deterioration in catalytic performance. Hence several researchers have realized binder-free nanostructures directly grown on a GCE for enhanced catalytic electrochemical properties.[239-241] In this regard, using the metal chloride salts of $FeCl_2 \cdot 4H_2O$ and $CoCl_2 \cdot 6H_2O$ and a supporting electrolyte of 0.5 M KCl, Sakita *et al*.[242] prepared binder-free CoFe//LDH/GCE electrode *via* a pulse electrodeposition method. To realize an optimal binder-free electrode, the deposition time was varied from 1 to 60s. As shown in **Figure 20**, Hasan *et al*.[243] proposed the electroless deposition of silver particles onto a GCE surface without the use of a capping agent or external triggers such as current, pressure, or temperature. In brief, the GCE surface was initially treated by potential cycling in Ar- saturated 0.1 M H_2SO_4 from 0 V to +1.0 V at a scan rate of 100 mV s^{-1}. Next, the GCE was kept in equal volumes of $AgNO_3$ and NaOH solution and taken into a glass cell for 24 h at room temperature under dark conditions. This led to the natural deposition of Ag particles onto the GCE surface. Shervedani *et al*.[244] prepared a graphene/Nile blue nanostructure on GCE, where further Pt decoration was conducted to enhance the electrochemical performance. In addition, Noorbakhsh *et al*.[245] used an electrodeposition strategy to fabricate cobalt oxide nanostructure on a GCE (CoO_xNS/GCE). Fascinatingly, these methodologies avoid the use of a Nafion binder for the adhesion of the catalyst to the GCE, which also results in enhanced activity.

4.8 Transparent conductive substrates

4.8.1 Indium Tin Oxide (ITO)

Transparent conductive substrates, in particular indium tin oxide (ITO), have served as a high stability non-carbon support for transition metal NPs.[246, 247] NPs supported on an ITO substrate exhibited high mass activity for catalytic reactions, and ITO has been utilized as a support material that demonstrated outstanding stability under acidic conditions and oxidizing environments. For example, Mustain *et al*.[246] deposited Pt on an ITO support by galvanic displacement of a Cu layer, which resulted in the formation of small Pt NPs (~5 nm) on ITO, estimated from TEM measurements. Furthermore, XPS revealed a strong interaction between the Pt and ITO support, which resulted in facile electron transfer between the Pt and Sn surface and imparting high activity and

stability to the Pt/ITO. In addition, the deposition of Pt NPs on ITO has been exploited for electrocatalytic processes.[247-249] The immobilization of metallic NPs on a porous ITO electrode has been employed for Ir and Ru.[250] In addition, Lebedev *et al*.[250] demonstrated a facile solution method for the immobilization of small and narrowly distributed Iridium NPs (1.5 nm) on a conductive ITO support (Ir_{NPs}-ITO) for water oxidation under acidic conditions. The as-obtained Ir_{NPs} – ITO electrocatalyst was found to be highly active and stable towards OER, despite having a low Ir loading (4.1 wt.%). High-angle annular dark-field scanning transmission electron microscopy (HAADF-STEM) showed the presence of spherical crystallites of Ir NPs on the ITO support (1.5 ± 0.2 nm); these are shown in **Figure 21**. High-resolution microscopic data, in combination with XPS, revealed the formation of a core-shell structure where the core remained metallic (Ir_{NPs}), while the outer layer was amorphous (Ir-oxo-hydroxide). The formation of Ir-oxo-hydroxide was found to be crucial for enhanced activity and stability of the electrocatalyst.

4.8.2 Fluorine-doped Tin oxide (FTO)

Transparent fluorine-doped tin oxide (FTO) has also been widely employed as a working electrode for the direct immobilization of a range of electrocatalysts such as metal oxides, layered double hydroxides, sulfides, selenides, and phosphides. Different methods have been adopted for the immobilization of various nano- and micro-structured materials on FTO, such as hydrothermal, solvothermal, and electrochemical deposition.[251-254] For example, Bogdanoff *et al.*[251] reported on α-Mn_2O_3 electrodes prepared by galvanostatic deposition of $MnOOH_x$ films with a varied thickness on a conductive FTO glass substrate, followed by annealing for 1 h under air at 773 K. The as-synthesized α-Mn_2O_3 was found to have a large electrochemical active surface area and good electrical conductivity. In addition, a unique, robust, and highly efficient bi-functional nickel phosphite ($Ni_{11}(HPO_3)_8(OH)_6$) electrocatalyst with excellent structural features has been electrophoretically deposited on FTO for water splitting. The as-deposited $Ni_{11}(HPO_3)_8(OH)_6$ catalyst on the FTO exhibited outstanding activity and stability for OER and HER under alkaline conditions.[252] Recently, Lee *et al*.[253] reported on CoP_2 NPs formed on an nm-thick Pt-coated FTO (CoP_2/Pt/FTO) substrate by employing a two-step physicochemical method. In the first step, the Pt layer with 50 nm thicknesses (50Pt) was deposited on an FTO substrate *via* sputtering, which was followed by electrodeposition of a CoP_2 layer (CoP_2/Pt/FTO); see **Figure 22(i)**. As a consequence, the conductivity has been enhanced. Nur *et al*.[254] reported on the

fabrication of a binder-free bi-functional electrocatalyst based on nickel-iron layered double hydroxide (NiFeLDH) functionalized cobalt oxide (Co_3O_4) NWs. This interesting approach resulted in the formation of a core-shell structure that consisted of Co_3O_4 NWs covered with NiFeLDH nanosheets. As shown in **Figure 22(ii),** the fabrication of core-shell structure on the FTO substrate was carried out in two steps. In the first step, the hydroxide phase of cobalt was deposited on the FTO substrate, which was subsequently converted into cobalt oxide by performing thermal annealing at 500 ^oC for 4 h. In the second step, a NiFeLDH nanosheet functionalization was performed on the cobalt oxide nanostructure by an electrodeposition technique. The surface modification of Co_3O_4 NWs with NiFeLDH nanosheets resulted in the generation of abundant catalytically active sites, increased the oxygen defects, and enhanced electronic conductivity.

4.9 Summary and Perspectives

Binder-free electrodes have been established as a simple, economical, and versatile fabrication technology for a range of 1D, 2D, and 3D nano- and micro-structured materials as active materials in water splitting. In this regard, several effective fabrication techniques have been exploited to prepare robust binder-free nano- and micro-structured electrodes; these are outlined in **Table 1**. From the controlled fabrication viewpoint, we have overviewed the fabrication strategies for creating active materials consisting of 1D, 2D, and 3D nano- and micro-structured materials, including nanorods, nanotubes, nanowires, nanoplates/flakes, nanosheets, and hierarchical structures. Typically, their fabrication conditions are relatively mild (e.g., room temperature) and do not require elevated temperatures or ultrahigh pressures that can reduce structural integrity or alter the composition of the deposits and substrates. Moreover, the fabrication of binder-free electrodes and their 1D, 2D, and 3D morphological tuning does not require advanced instruments and sophisticated operations.

Binder-free nano- and micro-structured electrodes can integrate robust active materials onto current collectors, a feature that removes the need for binders and conductive additives, which eases electrode fabrication. In addition, binder-free electrodes offer facile tunability with regard to chemical composition, crystal phase, and surface morphology of the deposited materials *via* changing *in-situ* and/or using *ex-situ* depositing conditions, and tailoring of the type of solvent, precursor composition, pH of the reaction medium, surfactant, and reaction temperature. The fabrication of binder-

free electrodes can also direct the growth of active components onto user-designed shapes/patterns in electrically conductive regions with a high mass loading. In addition, the preferred deposition of active materials with preferred dimensions at ion-accessible locations ensures the high utilization efficiency of the active materials.

However, binder-free electrode materials prepared at low temperatures are typically poorly crystalline, and some are defect rich or fully amorphous. Post-thermal treatments after fabrication are commonly needed to improve the crystalline nature of deposits and fine-tune the physical, mechanical strength, crystal structures, functionality concentration, or porous structure. However, transforming metal oxides into the corresponding sulfides, selenides, phosphides, and nitrides through temperature-controlled heat treatment strategies is an alternative approach. However, this post-thermal conversion usually involves high temperatures with can lead to challenges when using thermally unstable compounds and loss of active sites, porosity, or active materials morphology, which is critical for charge transport. Thu,s optimal fabrication conditions are highly preferred to fine-tune the surface morphology, chemical composition, surface area, porosity, conductivity, and exposed active sites of the active materials.

5 Impact of nanostructure properties on bi-functional electrocatalytic water splitting

It is well known that water splitting is one of the basic production units of hydrogen (H_2). In general, the overall water splitting reaction is centered on two half-reactions, which are,

For HER; $4H^+ + 4e^- \rightarrow 2H_2$ (1)

For OER; $2H_2O \rightarrow O_2 + 4H^+ + 4e^-$ (2)

Overall: $2H_2O \rightarrow 2H_2 + O_2$; $\Delta E = -1.23$ V (3)

Understanding the water splitting reaction enables a facile way to screen a new robust catalyst.[75, 255, 256] Under a standard temperature and pressure, a free energy of +237.2 kJ mol^{-1} per mol of H_2 is required for the conversion of one water molecule into hydrogen and oxygen. However, to expand the gases produced, extra work ($T\Delta S^0$) is required, with this respect the enthalpy change is +286 kJ mol^{-1} per mol of H_2 (*i.e.,* $\Delta H^0 = \Delta G^0 + T\Delta S^0$). These values are equivalent to a reversible electrolysis cell potential at standard conditions is of $\Delta E^0_{rev,298} = 1.23$ V, and a thermoneutral cell potential of $\Delta E^0_{th,298} = 1.48$ V (*i.e.,* heat is not required or lost) for water splitting. In an ideal water splitting system, the $T\Delta S^0$ is provided by an external supply. Hence, in an

ideal electrochemical water splitting cell, the use of a 1.23 V external voltage is sufficient to initiate the splitting of water. For practical use, splitting of water is less efficient and requires external voltage above the minimum value of 1.23 V. Thus, overpotentials are vital to initiate rapid charge transfer rates for the break/formation of reaction intermediates and products on the electrocatalyst active surface **(**for more details *see* **Section 3)**. It has been realized that efficient 1D, 2D, and 3D nano- and micro-structured electrocatalysts on conductive supports can effectively reduce these overpotentials to reach several hundred to thousands of mA cm^{-2} for practical applications.

In addition, the different dimensionality of electrocatalysts with a controlled morphology is of importance due to their distinctive features, such as high specific surface area (SSA) and abundant electrochemical active sites. These characteristics make them viable catalytic candidates to provide high electrocatalytic activity.[257] Moreover, the range of morphological electrocatalysts provides channels for the rapid transportation of electrolyte ions. In addition, the surface morphology and crystallinity of the directly grown nano- and micro-sized catalyst strongly depends on the conductive substrate, which can have a strong influence on electrocatalytic performance.[16, 28, 211] The presence of an open and porous structure on the substrate results in a high catalyst loading capacity and can allow it to act as a current collector to facilitate rapid transportation of electrolyte ions at the interface of electrode/electrolyte or to penetrate inside the electrode/catalyst surface, with a positive impact on the overall electrochemical water-splitting performance.[258] The different dimensional nano- and micro-structural materials are endowed with improved conductivity, electron mobility, and optimal defects, which consequently lead to enhanced electrocatalytic performance compared to their bulk counterparts.[257] It is worth highlighting that the presence of defects in nano- and micro-structured materials are responsible for inducing electrochemical active sites, which are crucial for modulating the performance of electrocatalytic processes due to the modulated electronic and surface properties of these materials.[259, 260] Active sites for different electrochemical reactions are induced by specific defect types as a result of specific reactant binding energy for each electrochemical reaction.[47, 259] The use of conductive substrates can also improve stability during operation in harsh conditions and corrosive environments due to the improved release of gas bubbles from the electrode surface.

6. Hydrogen evolution (HER) and oxygen evolution reactions (OER) on binder-free electrodes

The development of low-cost, highly efficient, and stable self-supported bi-functional electrocatalysts can reduce the complex synthesis process of catalysts for many electrochemical energy conversion devices; this is essential for their eventual commercialization. It is well known that the morphologies of catalysts and the choice of electrode substrate plays an important role in their HER and OER performance, which can be significantly enhanced with the increase of effective electrode surface areas in nanostructured systems.[16, 30] In the context of binder-free planar film electrodes, binder-free nanostructured electrodes exhibit not only superior catalytic activity but also improved stability due to a rapid release of gas bubbles from the electrode surface; this is summarized in **Table 2–Table 4**.[8, 28] In this regard, in the upcoming sections, we will overview current approaches to enhance the HER and OER performances of 1D, 2D, and 3D binder-free nano- and micro-structures for a variety of conductive substrates.

6.1 HER/OER performance on 1D nano- and micro-structured binder-free electrodes

Binder-free 1D nanostructured electrocatalysts such as metal oxides, hydroxides, phosphides, nitrides, and metal chalcogenides with different stoichiometry and polymorphs have been widely studied as alternative robust HER and OER catalysts to noble metals.[8, 111, 113, 211] These nanomaterials have been engineered to exploit the number of active sites for optimal HER/OER performance. Unusually, due to their improved intrinsic electrical conductivity, several 1D transition metal oxides, hydroxides, and their composites are being widely investigated.[261-264] In addition, 1D transition metal sulfides, phosphides, and nitrides offer highly exposed active sites for robust electrocatalytic reactions.[107, 265, 266] Due to their unusual geometric and morphologic features, 1D binder-free nanostructures have additional properties, such as accelerated charge transfer and inhibition of agglomeration. For example, as shown in **Table 2**, 1D binder-free electrocatalysts including Ni_3S_2, MoS_2, CoPi, WN, CoN, NiCoS, and their composites are attractive candidates for electrochemical water splitting due to their excellent intrinsic conductivity, rich catalytic activity, porosity, and superior electrochemical stability when used in HER/OER.[266-269] Fine-tuning the surface morphology, chemical composition, porosity, and conductivity of bi-functional electrocatalysts into a wide range of nanostructures, such as nanotubes, nanorods, and

nanowires improved the physical properties of the electrocatalysts through increasing the number of exposed active sites and assisting in the diffusion of reactants in the electrolyte. In particular, the meso-/macro-porous features of the catalysts can act as diffusion channels for the electrolyte to connect to the active sites.

6.1.1 Impact of exposed active sites

Among the several transition metal sulfides, MoS_2, WS_2, FeS_2, CoS_2, and NiS_2 are particularly renowned as promising low-cost catalysts for the HER.[2, 270] For example, Guo *et al*.[271] prepared a cost-effective lawn-like NiS_2 nanowire array (NWs) on a flexible CFP electrode via sulfurization of $Ni_2(CO_3)(OH)_2$ for bi-functional HER and OER uses. As a result of the structural features and more exposed active sites, the NiS_2 NWs/CFP requires small overpotentials of ~165 and 246 mV for the HER and OER, respectively, to provide a current density of 10 mA cm^{-2} in 1.0 M KOH. The resultant symmetric two-electrode alkaline water electrolyzer needed a cell voltage of 1.59 V to attain a 10 mA cm^{-2} water-splitting current density. Due to the 1D binder-free structural features, Ni_3S_2 nanowires (NWs) grown on NF revealed a low overpotential of ~81 and ~317 mV to achieve a water-splitting current density of 10 mA cm^{-2} for electrocatalytic HER and OER, respectively, in 1.0 M KOH, along with 30 h of long-term stability.[272] In addition, theoretical predictions of template-grown MoS_2 nanowires (NWs) on Au(755) surfaces provide both low kinetic barriers (~0.49 eV on the Mo edges) for H_2 evolution and high active site density.[273] Remarkably, the HER activity has been maintained through the substitution of an Au(755) substrate with non-noble metals, such as Ni(755) and Cu(755). In addition, extensive attention has been focused on self-supported pyrite-phase CoS_2 with metallic conduction and long-term stability in both acidic and alkaline conditions.[274-276] For example, a MOF-derived self-supported flexible hollow nanoarray of CoS_2 nanotubes (NTA's) with high surface area and hierarchical pores revealed an excellent bi-functional electrocatalytic performance in terms of a small onset potential, high current density, and excellent stability in alkaline condition.[140] During overall HER/OER testing, the CoS_2 nanotube required a cell voltage of 1.67 V to attain a current density of 10 mA $cm^{-2,}$ and a steady current could be maintained for 20 h. As shown in **Figure 23 (i),** due to the well-defined hollow nanotube arrangement and more exposed and abundant active sites, a $FeCo_2S_4$ NTA/CC grown by a template-free method can accelerate charge transfer for outstanding electrocatalytic OER performance with a low overpotential of ~317 mV at

a current density of 100 mA cm^{-2}, a small Tafel slope of ~36 mV dec^{-1}, and good durability during alkaline water electrolysis.[211] A high electrochemical active surface area for $NiCo_2S_4$ nanoneedles has been achieved by 3D printing on SS.[277] Due to the high conductivity and high loading of catalyst, large enhancements in electrochemical OER performance were obtained with a low Tafel slope of ~38.7 mV dec^{-1} and overpotential of ~226 mV at 10 mA cm^{-2} in alkaline media. $Cu(OH)_2$ and CuO nanostructures were directly grown on a Cu mesh and demonstrated an extraordinary electrocatalytic performance toward OER in an alkaline electrolyte.[278]

Using a plasma-assisted nitridation method, Ren *et al.*[279] fabricated self-supported porous WN NW arrays on CC (WN NW/CC, **Figure 23(ii)**). The as-prepared WN NW/CC displayed a low overpotential of 130 mV *vs*. RHE at 10 mA cm^{-2} and a small Tafel value of 59.6 mV dec^{-1} in 1.0 M KOH, producing a superior HER current density compared to Pt foil (~200 mV *vs*. RHE). In a similar approach, vertically aligned CoTe and NiTe NA's were grown on Ni foams (named as CoTeNR/NF and NiTeNR/NF) via a facile hydrothermal method for overall water splitting.[280] As a consequence of more exposed active sites, the CoTeNR/NF catalyst required a low overpotential of ~350 mV to provide 100 mA cm^{-2} during the OER, and for the HER, a ~202 mV overpotential was required to produce 10 mA cm^{-2} in an alkaline condition (**Figure 24**); this performance was higher than NiTeNR/NF. A detailed DFT analysis revealed that the active sites of CoTeNR/NF for OER arise from the in situ generated CoOOH species on CoTeNR/NF during the OER process, and they proposed a new HER activity evaluation criteria via H_2O adsorption energy, H_2O dissociation barrier, and H_2/OH^- desorption energy as indicators. In addition, the Fe@Ni nanofiber electrode exhibited excellent activity and stability toward OER and HER, with overpotentials as low as ~230 and ~55 mV to attain a current density of ~10 mA cm^{-2} in an alkaline solution, respectively.[281] Moreover, when assembled into a two-electrode arrangement for overall water splitting, a cell voltage of only 1.53 V is needed to drive a current density of 10 mA cm^{-2}.

For the metal phosphides, the hydrogen adsorption free energy, which is closely linked to the intrinsic catalytic activity, is often either too strong or too weak. In this regard, by utilizing the hydrothermal method and low-temperature phosphorization, Zheng *et al.*[282] prepared maize-like CoP nanorod arrays (NRA) on NF. Due to the abundant active sites, the unique architecture of CoP NRA exhibited a remarkable catalytic performance for the HER, with a low overpotential of ~130 mV *vs.* RHE at

10 mA cm^{-2} and a small Tafel slope of 59 mV dec^{-1} in 1.0 M KOH, which demonstrated excellent stability. Theoretical investigations *via* DFT calculations delivered new insights into the reaction mechanism and the nature of the active site in this process. It showed that dense active sites and a high phosphorization degree on these maize-like CoP NRA's could increase the HER performance in terms of low adsorption energy and free energy. Yang *et al*.[283] reported on a topotactic assembly method for in-situ growth of CoP nanowire arrays (NWAs) on CC using a phosphidation treatment of a Co(OH)F/CC precursor. The CoP/CC nanowire arrays exhibited a high HER catalytic activity in a wide range of pH from 0 to 14 with excellent stability. Remarkably, the CoP NWA exhibited a high density of active sites, estimated as 7.77×10^{17} sites/cm^2, and as a result, it achieved a small Tafel slope of 30.1 mV dec^{-1} in 0.5 M H_2SO_4 and 42.6 mV dec^{-1} in 1.0 M KOH. In addition, other metal phosphides, such as FeP NW on a Ti plate,[284] and Cu_3P NW on a CF,[13] were also produced by similar preparation methods, in which the corresponding transition-metal hydroxide/oxy-hydroxides were rehabilitated to corresponding transition-metal phosphides *via* a low-temperature phosphidation reaction. Recently, an urchin-like $Co_{0.8}$-$Mn_{0.2}$-P NWA which was supported on a CC provided a high HER activity in both acidic and alkaline media.[285] In 0.5 M H_2SO_4, this free-standing electrode only requires an overpotential of 55 mV to attain 10 mA cm^{-2}. Similarly, it only requires an overpotential of 61 mV to reach 10 mA cm^{-2} in 1.0 M KOH. Furthermore, this electrocatalyst exhibited superior stability after 1000 cycles of cyclic voltammetry testing and 24 h in an *i-t* test. Such an excellent electrocatalytic performance was accredited to the synergistic effect between the Co and Mn atoms, which offer more exposed active sites. However, the exposed active sites can be further enriched by the synergistic effect of heterojunction formation, conductivity enhancement, creation of defects, edge sites, and the inclusion of metalloids, which all provide positive effects to the binder-free electrode-based electrocatalytic systems.

6.1.2 Effect of intrinsic conductivity enhancement

Freestanding electrocatalysts with high electrical conductivity typically exhibit fast catalytic reaction kinetics owing to reduced charge-transfer resistance, which assists in improving the overall efficiency of the catalytic process.[286] Notably, several 1D electrocatalysts such as metal chalcogenides, oxides/hydroxides, and metal nitrides have high electrical conductivities and robust performance in acid and alkaline media.[35, 287] In this regard, Cheng *et al*.[288] prepared (100) facet exposed bimetallic nanofibers

of NiMoN on an NF. The NiMoN-NF700 (made at 700 °C) exhibited a good catalytic OER performance at an ~290 mV overpotential to achieve 50 mA cm^{-2}, compared to bare $NiMoO_4$ nanowires (~510 mV at 10 mA cm^{-2}) and other electrodes. It has been observed by DFT, that the density of states (DOS) distribution of the NiMoN structure is more delocalized near the Fermi surface, which helps to increase the conductivity and electrocatalytic performance. Through synergistic control of morphology and electronic conductivity features, ternary $Co_{1-x}V_xP$ nano-needle arrays exhibited a notable catalytic HER activity with low overpotentials of ~46 and ~226 mV *vs.* RHE at current densities of 10 and 400 mA cm^{-2}, respectively; a small Tafel slope and good stability were also achieved.[289] The NF@$Co_{1-x}V_x$-hydroxide needles revealed an excellent OER performance. In addition, the assembled Co-V based electrolyzer based on NF@$Co_{1-x}V_x$-hydroxide needles, as an anode, and NF@$Co_{1-x}V_xP$, as a cathode, can deliver lower overall water splitting-cell voltages of 1.58, 1.75, and 1.92 V at 10, 100, and 300 mA cm^{-2}, respectively. Due to its excellent conductive nature, a ternary $Fe_xCo_{1-x}P$ NWA/ CC exhibited an excellent HER activity, similar to Pt in an 0.5 M H_2SO_4 electrolyte.[290] As shown in **Figure 25(i)**, using a two-step growth method, metallic cobalt-nickel selenide nanorods on NF ($Co_{0.75}Ni_{0.25}Se$/NF) were prepared and used as a bi-functional electrocatalyst.[126] Due to its unique nanostructure, supportive bimetallic effects, and intrinsic metallic features, the $Co_{0.75}Ni_{0.25}Se$/NF electrode exhibited low overpotentials of ~269 mV (~50 mA cm^{-2}) for OER and ~106 mV (~10 mA cm^{-2}) for the HER. This binder-free electrocatalyst requires a cell voltage of 1.60 V to realize the overall water splitting current density of 10 mA cm^{-2}. Using DFT calculations, it was further revealed that the synergy between Co and Ni elements is favourable for improving the internal nanostructure of the catalyst to ensure excellent electrical conductivity and small HER Gibbs free energy.

One of the promising approaches to improve conductivity is doping, where synergistic coupling effects from multiple heteroatoms play a vital role; for example, cation and/or anion doping can optimize the electronic nature and increase the catalytic performance. Due to the high electronic conductivity and the synergistic coupling effect between Ni and MoO_2 interfaces, the Ni–MoO_2-450 NWs on CC exhibited an excellent platinum-like HER activity, with an almost zero onset overpotential and a reduced Tafel slope of ~30 mV dec^{-1}, which indicates that the fast charge recombination step is rate-limiting.[291] In addition, a facile chemical bath deposition (CBD) technique for phosphorization was employed to increase the overall water splitting performance of a

SS mesh (SSM), as shown in **Figure 25(ii)**.[292] As a result, due to electronic modification of the SSM by Ni and P, the Ni-P incorporated SSM can lead to an HER overpotential of 149 mV *vs*. RHE to reach 10 mA cm^{-2}. Similarly, the Mo-doped Ni_3S_2 grown on NF exhibited a superior HER/OER catalytic activity with overpotentials of ~61 and 213 mV to reach 10 mA cm^{-2}, respectively.[111] Furthermore, when used as both a cathode and anode for overall water splitting, a cell voltage of ~1.485 V was required to attain a current density of 10 mA cm^{-2} in an alkaline solution. In addition, due to the conductivity enhancement by W and Mo- doping, the W,Mo-NiCoP/NF required a overall water splitting cell voltage of 1.85 V to reach of 500 mA cm^{-2} with excellent stability over 50 h.[293] Recently, using a facile cation exchange reaction, a single atom of rhodium (Rh-SAC) modified CuO nanowire array on CF (Rh SAC–CuO NAs/CF) was prepared by Xu *et al*.[294] As shown in **Figure 26**, when the Rh SAC–CuO NAs/CF was used as an anode and a cathode for overall water splitting, the Rh SAC–CuO NAs/CF can attain a current density of ~10 mA cm^{-2} at ~1.51 V. Furthermore, DFT calculations indicate the high OER and HER intrinsic catalytic activities from the adequate adsorption energy of intermediates on Rh SAC.

In addition, CNF-based free-standing electrodes have shown significant OER activity as a result of their conductivity and synergistic coupling effects with heteroatoms (e.g., N, P, B, and S). Porous N and P co-doped CNF that were directly grown on a conductive carbon paper (CP) exhibited a high OER activity with a low overpotential of 310 mV at 10 mA cm^{-2}, with performance comparable to a benchmark of iridium oxide (IrO_2).[295] However, the self-supported catalyst revealed a small activity attenuation after 12 h continuous operation. DFT calculations indicated that the enhanced OER activity originated from the synergistic effect between the N, P dopants, and the carbon matrix. Due to the enhanced conductivity, the partially oxidized Ni supported on a Ni-N co-doped CNF exhibited excellent performance for overall water splitting.[296] Meanwhile, a series of phosphorus-doped Fe_7S_8 nanowires integrated within carbon (P-Fe_7S_8@C) were synthesized *via* a one-step phosphorization of one-dimensional (1D) Fe-based organic-inorganic nanowires.[297] The as-obtained P-Fe_7S_8@C catalysts with modified electronic configurations present a typical porous structure, providing a large number of active sites for rapid reaction kinetics. DFT calculations demonstrate that the doping of Fe_7S_8 with P can enhance the electron density of Fe_7S_8 near the Fermi level and weaken the Fe-H bonding, leading to a decrease in the adsorption free energy barrier on active sites. As a result, an optimal catalyst of P-Fe_7S_8-600@C exhibited a

relatively low overpotential of ~136 mV *vs*. RHE for the HER to achieve a current density of 10 mA cm^{-2} and a significantly low overpotential of ~210 mV for the OER at 20 mA cm^{-2} in alkaline media. The Cr-doped $NiCo_2O_4$ (Cr-$NiCo_2O_4$) nanoneedles (NNs) on NF performed as an excellent bi-functional electrocatalyst for both HER and OER.[298] It has been demonstrated that Cr-doping significantly increases the activity for HER and OER by increasing the conductivity of the NNs and allowing the exposed active sites on NNs to be electrochemically accessible. In the two-electrode cell, where FeOOH/Cr-$NiCo_2O_4$/NF was used both as a cathode and anode for overall water splitting, a cell voltage of only ~1.65 V was required to achieve an electrolysis current density of 100 mA cm^{-2}.

As a result of achieving an enhanced bi-functional electrocatalytic performance *via* an improved conductivity, substantial effort has been dedicated to studying the influence of heteroatom doping. It has been observed that the existence of two or more dopant elements also increases the potential to enhance the conductive nature, active sites, and the prospect of tuning the catalytic activity of the host material. For example, Fe-Ni incorporated conductive metal-organic framework (CMOF) nanowire arrays on CC,[299] Fe doped Ni_3S_2 NNs supported on NF,[300] Co-doped Ni-Mo phosphide nanorod arrays fabricated on NF,[301] ternary pyrite-type cobalt phosphosulfide (CoPS) on CFP,[302] vanadium doped CoP nanorods array catalyst grown on CC,[303] and electrodeposited Co–P on a CuO nanowire array on CF[304] have been realized as robust electrocatalysts for energy conversion.

6.1.3 Influence of heterostructure formation

Usually, the catalytic kinetics of 1D binder-free nanostructure can be improved by integrating one component with another to form heterojunctions, which leads to unique electronic properties at the interface, leading to interfacial charge polarization and bonding with reaction intermediates. In this regard, metallic nanostructured nickel sulfide/phosphide hybrids (NiS_xP_y) with 1D nanowires grown on 1D nanorods were prepared by Fu *et al*.[287] The resultant metallic hybrid NiS_xP_y on NF can accelerate the electron transfer process and expose abundant *in-situ* generated NiOOH species during the OER (NiS_xP_y–O). Consequently, the NiS_xP_y–O exhibited a low overpotential of 192 mV to attain a current density of 10 mA cm^{-2} and robust stability above 135 h without degradation. In the case of NiCoP nanowires decorated with CoP nanoparticles on NF (NiCoP–CoP/NF), the CoP nanoparticles were strongly interfaced with the NiCoP nanowires producing abundant electrocatalytic active sites for overall water splitting,

as seen in **Figure 27(i)**.[305] In addition, the NiS/Ni_2P/ CC requires low overpotentials of ~111 and ~265 mV for the HER and OER, respectively, to achieve a current density of ~20 mA cm^{-2}; this outperforms their counterparts such as Ni_2P and NiS under the same conditions.[306] The NiS/Ni_2P/CC electrode requires a cell voltage of 1.67 V to provide ~10 mA cm^{-2} in a two-electrode system, which is similar to the cell using a benchmark Pt/C||RuO_2 electrode. Recently, Yang *et al*.[307] prepared NiO_x@Co_3O_4/CC nanowires by plasma-enhanced ALD. The two transition metal oxides play a leading role in heterojunction formation, which eventually enhances the OER performance and stability. As a consequence, the free-standing electrode needed a low overpotential of ~360 mV for OER in an alkaline medium. Owing to the heterojunction feature, the CoMnFe hydroxysulfide nanowire (NW)@$Ni(OH)_2$ nanorod arrays exhibited superior catalytic performance in terms of a low overpotential of ~264 mV at 200 mA cm^{-2} for the OER, with a low Tafel slope of ~73 mV dec^{-1}, and long-term stability for at least 100 h in an alkaline electrolyte.[308] Hybrid nanorods of NiFeP-MoO_2 on NF can reach overall water splitting current densities of10 mA cm^{-2} and 100 mA cm^{-2} at 0.41 V and 1.65 V at 10 mA cm^{-2} and 100 mA cm^{-2}, respectively.[309] Dense nanowires (NWs) of Cu_xO were formed on a CF, which were comprised of mixed phases of Cu_2O and CuO as electrochemical active sites.[135] It has been observed that both Cu_2O and CuO served as an active center for HER and OER, respectively, and the *in-situ* heterojunction formation was favourable to the catalytic performance. In an alkaline solution, overpotentials of ~135 and 315 mV lead to a current density of 10 mA cm^{-2}, and small Tafel slopes of 135 and 63 mV dec^{-1} were achieved on the Cu_xO NWs/CF catalyst for HER and OER, respectively along with long-term stability. Moreover, the core-shell of Cu@WC nanowires exhibited an excellent HER performance in a pH-universal electrolyte.[310] This enhanced performance was attributed to the modified core-shell structure, which weakens the hydrogen bond during absorption.

Recently, Wang *et al*.[311] utilized the hydrothermal method followed by carbon deposition treatment to make a hierarchical nanowire array (NWA's) of heterostructured Mo_2C/Mo_3Co_3C bouquet-like on NF (Mo_2C/Mo_3Co_3C-NF). The NF acted as a current collector that eases the directional growth of the active phases and exposure of additional active sites for the HER. The addition of Co also leads to heterojunction formation; as a result, an intrinsic HER activity was promoted. Conversely, Ni_3S_2 is extremely active for OER, and it displays a reduced performance for overall water splitting due to an inadequate HER performance. As a result, the HER

activity and overall water splitting performance can be enhanced by its combination with MoS_2, which is highly active for HER.[312] As a consequence of the heterostructure interface and electronic effects, the N-doped Ni_3S_2/N-doped MoS_2 1D hetero-nanowires on NF (N-Ni_3S_2/N-MoS_2/NF) exhibited a high efficient electrocatalytic activity for both HER and OER under alkaline conditions.[313] Recent efforts have been devoted to integrating individual HER and OER electrocatalysts to advance heterojunction structures, which can stimulate the reaction kinetics on a variety of active sites and electron-reconfigured interfaces.[314, 315] A CNT@NiSe on SS serves as the robust free-standing electrode for overall water splitting in 1.0 M KOH, as seen in **Figure 27(ii)**.[316] In addition, N and Co decorated CNT films on CC,[317] and NiO_x@Co_3O_4/CC[307] have attracted attention due to variability in chemical composition, surface structure, and high activity.

6.1.4 Role of defects

The defect engineering of nanostructures is of significance since it can offer an approach to further improve catalytic activity, in particular for 1D nanostructures with a high surface to bulk ratio and the opportunity to engineer the defect structure along the longitudinal direction. As a result, the electronic structure of a nanomaterial can be fine-tuned while the defects, which often act as the catalytic active sites, can improve performance.[318, 319] As seen in **Figure 28**, it has been shown that boron (B) and oxygen (O) defects in a Co_3O_4 nanowire (NWs) grown on NF (V_OB-Co_3O_4/NF) electrode can modify their electronic structure, improve the electrical conductivity and produce a large number of electro-active sites.[320] The resultant self-supported V_OB-Co_3O_4/NF electrode can provide a current density of 50 mA cm^{-2} at low overpotentials of ~184 mV for HER and ~315 mV for OER in 1.0 M KOH with outstanding stability and durability. As a bi-functional catalyst, the V_OB-Co_3O_4/NF can act as both a cathode and anode and requires ~1.67 V to achieve a current density of 10 mA cm^{-2} for the overall water splitting reaction. Ding *et al*.[321] used a facile composition-engineering activation strategy to prepare Pt/FeMn- coral-like 1T-MoS_2 nanorods/NF with rich crystal defects. Significantly, it exhibited outstanding HER and OER activity and excellent stability in alkaline media. Moreover, the $NiCo_2O_4$ NWA's with rich oxygen deficiencies require a low HER overpotential of 104 mV to achieve 10 mA cm^{-2}; such catalysts also exhibit superior long-term durability for 24 h at 100 mA cm^{-2}.[322] Recently, an optimized oxygen vacancy (OV) content in self-supported OV-rich $NiCo_2O_4$ NWA's was found to exhibit a higher HER activity and improved stability in alkaline media compared to

its counterparts with lower OV contents.[323] Similarly, Ni_3S_2-Co_9S_8 heterostructure NWs supported on NF were fabricated by a two-step hydrothermal method.[324] The catalyst showed an excellent OER activity with an overpotential of ~294 mV at 20 mA cm^{-2}, which was attributed to the highly defective hetero-interfaces between the metallic Co_9S_8 and Ni_3S_2 grains. An O-doped Co_2P layer supported CuO NWs on a CF (O-doped Co_2P/CuO NWs/CF), was prepared by Doan *et al.*[139] Such a distinctive architecture was established to create a significant level of defects and controlled surface chemistry, with rich catalytic active sites and enhanced surface area with abundant channels for diffusion. Noticeably, the catalyst attained low overpotentials of ~101 and ~270 mV to achieve a current density of 10 mA cm^{-2} towards the alkaline HER and OER, respectively.

It is well known that electrocatalysts that are either entirely amorphous or amorphous with nanocrystalline grains are more active than highly crystalline grains due to their more coordinative unsaturated sites, surface defects, and locally disordered structures.[325, 326] Recently, 1D Fe_2B NW with mixed amorphous and crystalline phases were deposited onto NF through a chemical reduction method. The Fe_2B NWs/NF catalyst exhibited an overpotential of 276 mV for the OER at 10 mA cm^{-2} due to the presence of mixed phases.[327] A catalyst based on an amorphous $CoMoO_4$ nanowire array on Ti mesh ($CoMoO_4$ NWA/Ti) was synthesized by Zhao *et al.*[328] Due to amorphous structural features, the $CoMoO_4$ NWA/Ti exhibited higher catalytic activity in 1.0 M KOH in terms of low overpotentials of ~81 and 243 mV to attain current densities of 10 and 100 mA cm^{-2}, respectively with remarkable long-term durability. In addition, a hydrothermally prepared amorphous $FeMoS_4$ nanorod array on a CC ($FeMoS_4$ NRA/CC) demonstrated a superior catalytic activity and strong long-term electrochemical durability in 1.0 M PBS solution (pH ~7).[329] It required an overpotential of ~204 mV to achieve a current density of 10 mA cm^{-2}, which was ~450 mV lower than that for FeOOH NRA/CC.

6.1.5 Influence of porosity

Unusually, a mesoporous nature that increases the surface area and active sites are effective approaches to lower the overpotential and improve electrocatalytic performance.[330] For example, Xue *et al.*[331] prepared cobalt nitride porous nanowires (Co_4N NWs) with a length and diameter of ~7 μm and ~135 nm, respectively on a CC as a bi-functional electrocatalyst for overall water splitting. The porous Co_4N nanowires are composed of small-sized particles ranging from 5 to 20 nm, and the diameter of the

NW is ~135 nm as shown by the TEM image (**Figure 29**). Elemental mapping revealed that the Co and N elements were uniformly distributed throughout the porous NW. It has been proposed that an adequate space between the porous NW in the binder-free electrode aids in the rapid release of gas bubbles from the electrode surface during electrocatalysis, even at a high current density. As a result, the self-supported Co_4N NW/CC exhibited a current density of 10 mA cm^{-2} at low overpotentials of ~97 mV for HER and ~251 mV for OER in alkaline electrolyte. In addition, for overall water splitting, the self-supported porous Co_4N NW arrays/CC as a cathode and anode requires a cell voltage of ~1.587 V to attain a current density of 10 mA cm^{-2} and displayed long-term stability at a high current density of ~360 mA cm^{-2} over 37 h, which is comparable to the performance of commercial Pt and IrO_2. Recently, porous silicon nanowires (SiNWs) on a Si wafer have been produced by a metal-assisted anodic etching (MAAE) method.[332] Due to the nanowire features and its porous nature, the SiNWs generated hydrogen at a rate that was approximately ten times quicker than the rate reported for other Si nanostructures, such as nanoparticles in pH = 7 of acetone/H_2O or ethanol/H_2O solution. An electrodeposited CoP mesoporous nanorod array on NF exhibited mesoporosity and a high surface area (148 m^2 g^{-1}). This unique mesoporous NRA electrode exhibited an excellent electric interconnection and enhanced mass transport for both the HER and OER.[265] Finally, as an alkaline electrolyzer, it can provide a current density of 10 mA cm^{-2} at a voltage of ~1.62 V over the long term, which is better than Pt and IrO_2.

A nano-tubular mesoporous CoP electrocatalyst prepared by the Kirkendall effect provided a highly efficient HER.[333] Using a similar strategy, Ni_2P-nanorods/ NF was prepared by Wang *et al*.[99] and the resulting microporous structure featured a self-supported Ni_2P-NRs/Ni composite electrode with high electrochemical performance towards acidic HER. Similarly, Ren *et al*.[279] prepared porous WN nanowires arrays (NWs) on CC by N_2 plasma treatment of WO_x NWs for a small time period of 10 min. The WN NWs exhibited a high HER electrocatalytic activity and stability in both acidic and alkaline media. Their strategy suggests a facile way to construct highly porous, active, and stable catalysts for HER. Moreover, highly porous $NiCo_2O_4$ nanowires grown on FTO were found to be extremely active for catalytic water oxidation.[334] An interconnected porous Ni–Co disulfide network has been grown on CC ($(Ni_{0.33}Co_{0.67})S_2$ nanowires (NWs)/CC), which exhibited an outstanding HER/OER activity in terms of overpotentials of ~156 mV *vs*. RHE in 0.5 M H_2SO_4 solution and

~334 mV *vs*. RHE in 1.0 M KOH solution for HER for a current density of 100 mA cm^{-2}, respectively.[335] In addition, when used as an OER catalyst, the $(Ni_{0.33}Co_{0.67})S_2$ NWs/CC requires an overpotential of ~295 mV at ~100 mA cm^{-2} in 1.0 M KOH. The excellent electrochemical properties were related to the synergetic bimetallic effects and the porous network structure, which facilitated a high charge transfer rate.

6.1.6 Effect of catalysts processing temperatures

Thermal annealing is a standard process used for improving structural phase features, intrinsic stress relaxation, conductivity enhancement (including alloying), and surface roughness control in materials.[336, 337] As a qualitative approach, annealing modifies the surface morphology and active sites of materials with temperature and time, which in turn improves the catalytic activity intrinsically. Self-supported 1D nanomaterials, such as metal oxides, sulfides, phosphide, nitrides, and their composites were *in-situ* grown followed by thermal treatment on conductive substrates, have been widely exploited for robust HER and OER.[14, 338] In this regard, nanotubes of $NiCo_2O_4$/NF were obtained after calcining in the air at 400 °C for 3 h.[339] The $NiCo_2O_4$ porous nanotubes showed a superior low charge transfer resistance and more exposed active sites compared to $NiCo_2O_4$/NF with needle-like and rod-like structures. With these benefits, the $NiCo_2O_4$ porous nanotubes showed an exceptional electrocatalytic performance for overall water splitting and reached a low potential of ~1.63 V at ~10 mA cm^{-2}. In addition, there is no visible degradation after long-term testing for 12 h. In a similar approach, Chen *et al*.[340] prepared the Fe–Mo oxide hybrid nanorods (NRs)/NF through a hydrothermal method, which was followed by annealing at a high temperature of 450 °C for 2 h with a heating rate of 5 °C min^{-1} in a H_2/Ar atmosphere. As a result of conductivity and crystalline nature enhancement due to the thermal treatment, the Fe–Mo oxide hybrid NRs/NF showed excellent catalytic activity for the OER and HER in alkaline media and achieved a current density of 10 mA cm^{-2} at overpotentials of 200 and 66 mV, respectively. As a bi-functional electrode for overall water splitting, it achieved a current density of 10 mA cm^{-2} at a voltage of 1.52 V and sustained a current density of 60 mA cm^{-2} for 60 h. It has been observed that the unique surface morphology, with a self-supported structure, exposed more active sites to facilitate charge transfer, thereby leading to improved catalytic activity and stability.

MOF-derived 1D heterostructures are also of great interest. For example, Zhou *et al*.[341] prepared shish-kebab type $MnCo_2O_4$@Co_3O_4 nano-needle arrays from MnCo-

LDH@ZIF-67 by thermal annealing in the air *via* an improved MOF-template-directed strategy. As a consequence, the $MnCo_2O_4$@Co_3O_4 exhibited an improved electrocatalytic activity for the OER in an alkaline environment. As shown in **Figure 30(i)**, Xu *et al.*[342] prepared $Ni_{12}P_5$/Ni-Pi/NF electrodes through phosphitization at 350 °C for 1 h, with a heating rate of 2 °C min^{-1} in an N_2 atmosphere. As a result, the $Ni_{12}P_5$/Ni-Pi/NF displayed an excellent bi-functional electrocatalytic performance due to improved mass transport properties, conductivity, and mechanical robustness. In addition, it has been observed that the nanorod morphology of the $Ni_{12}P_5$/Ni-Pi/NF with a high surface-to-volume ratio not only provides a facile charge transport and improved electron transfer properties but can also afford more exposed active sites. Interestingly, reducing the Pt amount or loading level on electrocatalysts for HER is also of great interest for commercial applications. In this regard, Zhao *et al.*[343] prepared an ultra-small level of ~8.3 μg cm^{-2} Pt loaded on a free-standing mesoporous titanium nitride nanotube array (TiN NTAs) *via* electrodeposition. Initially, the mesoporous TiN NTAs were prepared by annealing TiO_2 NTAs in an NH_3 flow at 750 ℃ for 3 h. As a consequence, the Pt-TiN NTAs exhibited a 15-fold greater mass activity towards the HER compared to the benchmark of 20 wt.% Pt/C in acidic media, with a low overpotential of ~71 mV *vs*. RHE at a current density of ~10 mA cm^{-2}, a small Tafel slope value of ~ 46.4 mV dec^{-1}, and excellent stability; this can be seen in **Figure 30(ii)**.

6.1.7 Summary and perspective

The advancement of robust 1D nanomaterials with binder-free electrode features has led to significant advances in electrocatalytic water splitting. These binder-free electrocatalysts often possess a highly porous nature, which is advantageous for electrolyte permeation. Compared with binder-free planar film electrodes, binder-free 1D nanostructured electrodes exhibit not only superior electrocatalytic activity but also have improved stability due to the easy release of gas bubbles formed at the electrode surface. Notably, several 1D electrocatalysts such as metal chalcogenides, oxides/hydroxides, and metal nitrides have high electrical conductivities and robust performance in both acid and alkaline media. As a result of their unusual geometric and morphologic features, 1D binder-free nanostructures have additional distinctive properties, such as an accelerated charge transfer and inhibition of agglomeration. However, several bare 1D binder-free electrocatalysts often exhibit poor performance due to a limited number of exposed active sites, poor conductivity and some possess a high overpotential for both the HER and OER. For example, 1D binder-free

electrocatalysts based on MoS_2, CoPi, WN, Ni_3S_2, CoPi, NiPi, CoN, and NiCoS are more attractive candidates for electrochemical water splitting due to their excellent intrinsic conductivity, rich catalytic activity, porosity, and superior electrochemical stability when used for the HER/OER. Moreover, fine-tuning the chemical composition, porosity, and conductivity for bi-functional electrocatalysts across of range of nanostructures, such as nanotubes, nanorods, and nanowires, can improve the physical properties of the electrocatalysts by increasing the number of exposed active sites and assisting in the diffusion of reactants in the electrolyte. In particular, the meso-/macro-porous features of the catalysts can act as diffusion channels for the electrolyte to increase the active sites. In addition, it has been shown that the incorporation of two or more dopant elements can enhance the conductive nature and active sites to provide an exciting prospect of fine-tuning the catalytic activity of 1D binder-free electrode materials. Usually, the catalytic kinetics of 1D binder-free nanostructure can be greatly enriched by integrating one component with another component to develop heterojunctions, which can lead to unique electronic properties at the interface, initiating interfacial charge polarization and bonding with reaction intermediates. In addition, generating optimum defects on 1D nano- and micro-structures can improve HER/OER performance by providing a highly conductive nature and exposed active sites. Notably, the development of binder-free 1D nano- and micro-structure electrodes can improve the stability of the catalyst in all pH-based overall water splitting.

6.2 HER/OER performance on 2D nano- and micro-structured binder-free electrodes

To replace precious Pt, Ru- and Ir-based electrocatalysts, a number of self-supported nanostructures based on earth-abundant candidates have been developed. In this regard, significant effort has been devoted to developing alternative electrocatalysts based on earth-abundant self-supported 2D materials; these are summarised in **Table 3**.[344, 345] 2D nanomaterials can have a thickness of one atomic layer, with a thickness and dimensions on nano- and micro-scale. In contrast to bulk materials, these 2D nanomaterials have a high aspect ratio (surface-area-to-volume ratio) and have many atoms on their surface.[8, 318] These atoms have different functionalities compared to internal atoms, and the increase in the number of exposed surface atoms leads to a modification in the behaviour of 2D nanomaterials, especially for electrocatalysis.

6.2.1 Impact of exposed active sites

New insights into the nature of the catalytic active sites in catalysts for water splitting are needed for the improvement of high-performance binder-free electrocatalysts. In this regard, nickel (II) sulfide (NiS) NS with a thickness of 10 nm and a size of 200 nm were grown on SS (NiS@SLS) mesh and exhibited a superior catalytic activity toward the OER in an alkaline electrolyte in terms of low overpotential of ~297 mV at a current density of 10 mA cm^{-2}, with a small Tafel slope ~47 mV dec^{-1}; this system shows a competitive performance at high current densities due to more exposed active sites.[151] Ultrathin-sized $FeNiO_xH_y$ nanoflake arrays with ~4.5 nm thickness were prepared on NF *via* a facile hydrothermal reaction.[346] Under alkaline conditions (1.0 M KOH), the optimized $FeNiO_xH_y$/NF showed extremely small overpotentials of ~195 and 306 mV to attain current densities of 10 and 1000 mA cm^{-2}, respectively, and showed limited attenuation of performance during a 160 h of stability test, even at a current density of up to 1000 mA cm^{-2}, signifying excellent OER catalytic activity and durability. Notably, the FeOOH and NiOOH created from *in-situ* oxidation of the nickel surface atoms of the NF substrate formed active sites and were contributed to the high performance. In addition, due to the more exposed active sites, the FeNiOOH NS grown on a FeNi foam (FNF) *via in-situ* chemical oxidation provided an excellent OER performance by a small overpotential of ~252 mV at a current density of ~10 mA cm^{-2}, with a low Tafel slope of ~36.8 mV dec^{-1}, and outstanding operational stability for at least 50 h in an alkaline solution.[347]

Similarly, Liu *et al*.[348] prepared a $NiMo_xCo_{2-x}$ layered double hydroxide (LDH) on NF. The as-prepared NiMo-Co-LDH/NF catalyst retained an overpotential of ~123 mV for HER at 10 mA cm^{-2} and ~279 mV for OER at 20 mA cm^{-2}. As shown in **Figure 31**, Duan *et al*.[349] prepared a nickel-iron-based metal-organic framework array on a variety of substrates such as NF, SS mesh, and GC substrates by a dissolution–crystallization mechanism. The 2D NiFe-MOF nanosheets on NF exhibited interesting properties for alkaline HER and OER electrocatalysis, which included a small overpotential of ~134 mV for HER, compared to the other samples including Ni-MOF (~177 mV), bulk-sized NiFe-MOF (~196 mV), and calcined NiFe-MOF (~255 mV). The turnover frequency (TOF) of the NiFe-MOF for HER at an overpotential of 400 mV was 2.8 s^{-1}, which is better than that of Ni-MOF (0.91 s^{-1}), bulk NiFe-MOF (0.53 s^{-1}), and calcined NiFe-MOF (0.19 s^{-1}). It has been observed that NiFe-MOF offered exposed active molecular metal sites (Ni and Fe) that possessed a small thickness of the nanosheets, with enhanced electrical conductivity. In addition, it exhibited a higher electrocatalytic

performance towards OER, with a small overpotential of ~240 mV at 10 mA cm^{-2} and long-term operation for 20,000 s. Remarkably, the TOF of the electrode was ~ 3.8 s^{-1} at an overpotential of 400 mV. Recently, Tian *et al.*[227] used electric-field-assisted *in-situ* hydrolysis of two isomeric bulk MOFs (FJI-H25Fe and FJI-H25FeCo) into ultrathin FeCo-oxyhydroxide (FeCo-MOF-EH) nanosheets on CFP. Due to the metal oxyhydroxide nanosheets having high crystallinity, exposed active sites, and appropriate morphology, it displayed excellent OER performance with an extremely low overpotential of ~231 mV at ~10 mA cm^{-2} and long-term durability of at least 30 h in an alkaline solution. The TOF value at an overpotential of ~300 mV was 0.062 s^{-1} for FeCo-MOF-EH, which is noticeably higher than Fe-MOF-EH (0.0032 s^{-1}), FeCo-MOF-H (0.021 s^{-1}), and Fe-MOF-H (0.00017 s^{-1}), thereby validating the substantial OER activity of FeCo-MOF-EH. Due to more exposed active sites, vertically standing MoP nanosheet arrays on Mo substrate exhibited outstanding HER catalytic activity, which requires a small overpotential of ~95 and ~106 mV to attain 10 mA cm^{-2} in 0.5 M H_2SO_4 and 1 M KOH, respectively, and presents relatively a small Tafel slope of ~50.0 and 56.0 mV dec^{-1}.[350] Recently, Jian *et al.*[187] prepared 2D nickel-iron phosphide (NiFe-P) nanosheets on a porous 3DGF as NiFe-P@3DGF to design a bi-functional electrocatalyst with excellent catalytic activity towards OER and HER. Under alkaline conditions at a current density of 10 mA cm^{-2}, the NiFe-P@3DGF binder-free electrode offered overpotentials of 189 and 131 mV for OER and HER, respectively, and stabilities that exceed 50 h. Moreover, as a bi-functional catalyst, it exhibited an excellent water-splitting capability with a cell voltage of ~1.57 V at 10 mA cm^{-2}. The unique structure of the 3DGF substrate with its high surface area, extremely exposed active sites, a robust skeleton, and the unique core-shell structure of the NiFe (oxy)hydroxides/phosphide formed during the reaction led to the high activity of the electrocatalyst.

6.2.2 Effect of intrinsic conductivity enhancement

Usually, there are two strategies to increase the conductivity of any catalysts, (i) improving the intrinsic conductivity of the electrocatalysts by inducing dopants into the crystal lattice,[8, 351] and (ii) producing a highly-conductive support that retains a high specific surface area.[139] Significantly, most layered double hydroxide (LDH) materials display 2D-layered nanosheet structures on which metal cations can be located.[352, 353] In addition, such 2D nanosheet structures make the cations and anions in the host layers and interlayers tunable for the enhancement of conductivity, which offers new

opportunities for fabricating novel LDH electrocatalysts.[354, 355] In this regard, by changing the Ni/Cr ratios, Ye *et al*.[356] prepared a nickel-chromium layered double hydroxide (NiCr-LDH) nanosheet array on NF. The optimized Ni_2Cr_1-LDH showed extraordinary HER and OER activities with an ultra-low overpotential of ~138 mV at 100 mA cm^{-2} and ~319 mV at 100 mA cm^{-2}, respectively; outstanding durability at 1.55 V for 30 h at 10 mA cm^{-2} was also achieved for Ni_2Cr_1-LDH compared to other reported Ni-based LDHs. It has been suggested that the optimal metal concentration can enhance the catalytic performance of the catalysts. Both experimental and DFT calculations demonstrated that the Cr^{3+} ions within the LDH layer may act as charge transfer sites to effectually improve the intrinsic electrochemical activity. Zhou *et al*.[357] investigated the OER performance of self-supported NiFe LDH/NF through the effect of Ni and Fe ratio variations. It has been observed that both the Ni and Fe in the NiFe LDH nanoarray persist at a lower valence state due to reduction by the NF. Theoretical calculations demonstrate that a gradient effect can enhance the OH binding strength to the Ni sites, thus modifying O and OOH binding to the Fe sites, which can lower the absorption energy and decrease the overpotential required for the OER process. Ren *et al*.[358] fabricated a FeNiOH on NF through Fe doping for a free-standing bi-functional electrode formed via a hydrothermal method. The assimilated architecture by Fe doping is favourable for creating hierarchical pores, exposed catalytic active sites and providing appropriate structural and electrical properties, which improves the bi-functional electrocatalytic activity of the as-fabricated FeNiOH/NF. Consequently, as an electrocatalyst for OER, the FeNiOH/NF exhibited an outstanding activity with overpotentials of ~271 and ~318 mV at current densities of 20 and 100 mA cm^{-2}, respectively, with a small Tafel slope of 72 mV dec^{-1} in a 1.0 M KOH solution.

Wang *et al*.[218] prepared a self-standing bi-functional electrocatalyst consisting of Co-doped MoS_2 nanosheets on CFP *via* a hydrothermal method. Due to the conductive nature of the CFP substrate, more exposed active edges of the MoS_2 sheets, and the metallic nature due to Co-doping, the $Mo_xCo_{1-x}S_2$/CFP exhibited high bi-functional activity for the overall water splitting in a 1.0 M KOH electrolyte, which could generate a current density of 20 mA cm^{-2} at an overpotential of ~197 mV for HER and ~235 mV for OER. By nickel electroplating and an *in-situ* sulfurization route, a highly flexible Ni_3S_2@Ni/ CC electrode was prepared by Qian *et al*.[359] Due to the exposed active sites, the Ni_3S_2@Ni/CC electrode exhibited high activity for the OER to achieve a benchmark of 10 mA cm^{-2} at a low overpotential of ~290.9 mV with a Tafel slope of ~101.26 mV

dec^{-1}. Interestingly, when the electrode was tested under a bending angle of 180°, there were small increments of ~9.9 mV in η_{10} and ~6.55 mV dec^{-1} in the Tafel slope. In addition, it delivers excellent long-term durability for 30 h for OER in an alkaline. As shown in **Figure 32(i)**, ultrathin nanosheets of Fe/Ni metal-organic framework (MOF) grown on NF (NiFe-MS/MOF@NF) performed as a highly efficient bi-functional electrocatalyst.[360] It showed significant catalytic activity and stability toward both OER (~230 mV at 50 mA cm^{-2}) and HER (156 mV at 50 mA cm^{-2}) in an alkaline electrolyte and bi-functionally catalyzes overall alkaline water splitting at a current density of 50 mA cm^{-2} by a cell voltage of 1.74 V. The mechanism for improvement is attributed to the impregnated metal sulfide clusters in the nanosheets, which stimulates the formation of ultrathin nanosheets to significantly increase the surface area and leads to a high electric conductivity, and enlarges the catalytic reaction area to provide more exposed active sites for catalytic reaction. Iron-doped nickel MOF nanosheets *in-situ* grown on conductive NF (Fe-Ni MOF NSs/NF) provided a highly exposed surface area and abundant metal sites, which are beneficial to electrocatalytic OER performance.[361] Moreover, an ultra-small iron-rich Fe(Ni)-MOF cluster-decorated ultrathin Ni-rich Ni(Fe)-MOF nanosheets made from NiFe alloy foam have been used as a self-supported working electrode for the OER.[362] The structure can achieve current densities of 10 and 100 mA cm^{-2}, with small overpotentials of ~227 and ~253 mV, respectively, surpassing the benchmark of RuO_2. It was observed that the strong coupling effect between the Ni and Fe active sites is responsible for its excellent OER performance.

Recently, as shown in **Figure 32(ii**), Liu *et al.*[363] prepared various compositions of nickel or cobalt ions incorporated in WP_2 self-supporting nanosheet arrays on CC by *in-situ* phosphidation for acidic HER. Due to the conductive nature, the optimized catalyst of 1% Ni-WP_2 NS/CC showed a good electrocatalytic HER performance with an overpotential of ~110 mV at 10 mA cm^{-2} and a Tafel slope of ~65 mV dec^{-1} in an acid solution, which is higher than other Ni or Co incorporated WP_2/CC electrodes. Besides, the Ni-doped WP_2 exhibited a lower Gibbs free energy. Fe-doped Ni_2P nanosheets exhibited low overpotentials (η_{100}) of 213 and 210 mV for OER and HER, respectively.[364] In addition, a vertically aligned tungsten (W) doped VSe_2 nanoplate array on CC has been prepared by Kumar *et al.*[365] As a consequence, the optimal $W_xV_{1-x}Se_2$ nanoplate array exhibited a low overpotential of 173 mV to achieve a current density of ~10 mA cm^{-2} for HER in acidic conditions compared to pristine VSe_2 (280 mV). The Tafel slope values of the $W_xV_{1-x}Se_2$ nanoplates array were ~80

mV dec^{-1}. Due to the enriched active sites, the unique nanosheets of Fe,Rh-Ni_2P/NF reached the current density of 10 mA cm^{-2} at a low voltage of 1.62 V.[366] It has been realized that the self-driven charge transfer properties of P-CoFe-LDH@MXene/NF can enhance electron transport efficiency, resulting in excellent overall water splitting at a low cell voltage of 1.52 V.[367] Likewise, active sites enriched cobalt-molybdenum nitride nanosheet arrays grown on Ni foam ($CoMoN_x$ NSAs/NF) required the HER and OER overpotentials of 91 and 231 mV, respectively to reach the current density of 10 mA cm^{-2}.[368] In addition, when the $CoMoN_x$ NSAs/NF was used as a bi-functional electrode, it reached the current density of 10 mA cm^{-2} at a low cell voltage of 1.55 V.

6.2.3 Influence of heterostructure formation

Portable bi-functional water-splitting devices inspired by rechargeable metal-air batteries and fuel cells are gaining attention; however, their scalable usage is hindered by the lack of suitable bi-functional electrocatalysts. In this regard, highly efficient multifunctional heterojunction electrocatalysts have been developed and demonstrated; for example, a 2D nanosheet array of a heterostructure of Mo-doped $NiCo_2O_4$/$Co_{5.47}N$ deposited on NF (Mo-$NiCo_2O_4$/$Co_{5.47}N$/NF).[369] The positive effect of doping by a high-valence metal into a heterostructured nanosheet array provides a balanced electronic structure and greatly exposed active sites. As an example, a Mo-$NiCo_2O_4$/$Co_{5.47}N$/NF exhibited a high catalytic activity toward the OER and HER, with large current densities of 50 mA cm^{-2} at low overpotentials of ~310 mV for OER, and ~170 mV for HER, respectively in an alkaline condition. In addition, a low voltage of ~1.56 V was achieved for the Mo-$NiCo_2O_4$/$Co_{5.47}N$/NF-based water-splitting cell to attain a current density of 10 mA cm^{-2}, as shown in **Figure 33**. Interface-tailoring by adding sulfur on $NiCo_2O_4$@$NiMo_2S_4$ nanosheet on NF led to an excellent overall electrochemical activity with a low cell voltage of ~1.63 V at 50 mA cm^{-2} and stability for 13 h.[370] Due to interface rich nature, the nano-sheets of NiO/RuO_2/NF exhibited excellent HER and OER activity and stability, along with excellent overall water splitting, it only requires a low cell voltage of 1.44 V to reach 10 mA cm^{-2}.[371] In addition, nanosheets of IrNi-$FeNi_3$ on NF require a small cell voltage of 1.47 V to generate 10 mA cm^{-2}.[372]

A NiOOH-decorated α-FeOOH nanosheet array (ASF) has been fabricated on sintered 316L SS felt (SSF) as a substrate.[373] The 2D nanosheets provided a large specific surface area and active components of Fe and Ni elements, which were distributed uniformly on the α-FeOOH nanosheets, thereby providing adequate exposure of

electrochemical active sites and assisting in an effective contact between them and the electrolyte. As a result, the ASF exhibited an excellent OER in terms of low overpotential of ~256 mV at 10 mA cm^{-2}, with a low Tafel slope of 45 mV dec^{-1}. Hou *et al.*[374] prepared a ternary electrocatalyst of NiFe LDH anchored on $Co_{0.85}Se$ nanosheets located on an exfoliated graphene (EG) foil. Between these three constituents, the NiFe LDH with an intrinsically high OER catalytic activity provided a unique nanoarray structure to create $Co_{0.85}Se$ hybrids; the $Co_{0.85}Se$ nanosheets act to provide abundant positively charged active sites of Co^{2+} and Co^{3+}. The intrinsic advantages and strong coupling of these three components contributed to a greater catalytic activity in terms of overpotentials of 1.50 and 1.51 V to attain current densities of 150 and 250 mA cm^{-2}, respectively for the OER. A current density of 10 mA cm^{-2} can be reached at an overpotential of −0.26 V and resulted in excellent overall water splitting and excellent stability in a base solution. Due to the heterostructure feature, the N doped NiZnCu-layered double hydroxide with reduced graphene oxide on an NF (N–NiZnCu LDH/rGO) exhibited an excellent OER activity.[375] In addition, the heterostructure catalyst of 2D nanosheets of Co_9S_8/1D nanorod of Cu_2S on Cu foam (Co_9S_8/Cu_2S/CF) required a low HER and OER overpotentials of 165 mV and 195 mV to reach 10 mA cm^{-2}, respectively.[376] As a bi-functional water splitting electrode, it requires 1.6 V at 10 mA cm^{-2}.

6.2.4 Role of defects

The formation of defects on 2D materials at the atomic scale is another efficient approach to accelerate the electrocatalytic activity of binder-free trimetallic LDH catalysts.[377] In this regard, Xie *et al.*[378] formed Zn and Al sites into NiFe LDH to manufacture defect-rich NiFeZn and NiFeAl LDHs on NF by selective etching, In particular, producing Zn(II)/Al(III) sites in NiFe LDHs and selectively creating M(II)/M(III) defects on NiFe LDH. An Electron Paramagnetic Resonance (EPR) study was applied to investigate the paramagnetic defects in the materials, *i.e.*, exposure of the unsaturated Ni/Fe sites on NiFeAl LDHs/NF. As a consequence, the M(II) defect-rich NiFe LDHs reached an OER current density of 20 mA cm^{-2} at ~200 mV overpotential, which was greater than other bare materials. Furthermore, DFT calculations showed that the dangling Ni–Fe sites formed by defect engineering of a Ni–O–Fe site at the atomic scale lowered the Gibbs free energy of the oxygen evolution process. Xie *et al.*[379] formed partially amorphous NiFe LDH nanosheet arrays on NIF (NiFe alloy foam). This unique partially amorphous arrangement produced Ni^{3+} cations

and increased the concentration of high-valence active sites for OER, while the NiFe alloy foam with an optimized Ni:Fe ratio provided long-term stability in alkaline media toward the OER. In addition, it was shown that the enriched oxygen vacancies of 2D layered L-CoO nanosheets with a lamellar crystal structure grown on SS could provide long-term durability of over 1000 h in an alkaline OER.[380] Wang *et al.*[381] constructed a hybridization heterostructure that was organized by a CF, 1D $Cu_{2+1}O$ nanowires (NWs) with metal defects, and 2D Co_3O_4 nanosheets complete. It was observed that *in-situ* grown $Cu_{2+1}O$ NWs with abundant metal defects provided a high catalytic activity and dramatically shortened the diffusion pathway of ions and electrons. The interfaces created between the $Cu_{2+1}O$ and Co_3O_4 provided a highly electrochemically active surface area. As a result, $Cu@Cu_{2+1}O@Co_3O_4$ heterostructure delivered superior electrocatalytic OER. Fe-doped Ni-Co phosphide nanoplates on CC (Fe_x-NiCoP) were prepared by Guo *et al*.[382] Due to the hierarchical features, the 2D nanoplates are comprised of fine nanocrystals and planner defects due to the doping effects of Fe. Therefore, the Fe_x-NiCoP exhibited an excellent electrocatalytic performance for both the HER and OER, and the electrocatalytic performance was sensitive to the Fe content. By adjusting the Fe content, Fe_1-NiCoP attained a current density of 10 mA cm^{-2} at a low overpotential of ~60 mV for the HER, whereas Fe_2-NiCoP with a higher Fe doping content reached 50 mA cm^{-2} at ~293 mV for the OER, as seen in **Figure 34(i)**. This enhanced performance can be attributed to the increased exposure of active sites created by the planar defects. Due to rich oxygen vacancies, the hybrid nanosheets of Fe-Ni_5P_4/NiFeOH required low HER and OER overpotentials of 197 and 221 mV, respectively, along with a low voltage for overall water splitting of 1.55 V at 10 mA cm^{-2}.[383] In a similar approach, due to the increased oxygen vacancies, a self-activated, etched, and anodized SS (EASS) showed an extremely high surface area with excellent durability for 100 h at 100 mA cm^{-2} for the HER in a 1.0 M KOH solution.[384] An amorphous (Co-Mn)S tailored into nanosheets on SS substrates was prepared by Kale *et al*.[385] During fabrication, a stoichiometric composition was effectively tuned and greatly influenced the electrocatalytic OER activity by modification of the electronic structure and binding strength with intermediates. Defect-rich MoS_2 nanosheets vertically grown on graphene exhibited high activity for HER, with a low overpotential of ~140 mV at 10 mA cm^{-2}, a small Tafel slope of 42 mV dec^{-1}, a substantial increase in exchange current density of 63 μA cm^{-2}, and excellent stability compared to the bare catalysts.[386]

6.2.5 Effect of Porosity

It is well-known that textural properties such as specific surface area, pore size, and pore volume are also associated with high electrocatalytic activity.[387] In this regard, several researchers were focused on binder-free porous structures for enhanced bi-functional electrocatalytic water splitting.[388, 389] For example, Guo *et al*.[194] prepared a binder-free electrode of N and S doped graphene (SNG) on a conductive GF by drop-casting and *in-situ* annealing. As a result, during the OER, the SNG@GF exhibited a low overpotential of ~330 mV *vs*. RHE at 10 mA cm^{-2} with a Tafel slope of ~149 mV dec^{-1} in 1.0 M KOH, as shown in **Figure 35(i)**. This enhanced performance was attributed to its porous nature, which can provide a fast electron transfer rate and large electrolyte/electrode interfaces. A Ru-rich porous framework on NiFe-based ribbons with amorphous-nanocrystalline was prepared by a melt-spinning method.[390] A Ru-doped NiFe-based catalyst with a nanoporous surface (NP-Ru_x) exhibited an excellent OER activity, with an ultra-low overpotential of ~245 mV at 10 mA cm^{-2} and a small Tafel slope of ~15 mV dec^{-1} and low charge-transfer resistance under 1.0 M KOH. The enhanced performance may be due to the Ru-rich nanoporous architecture; it can provide a large number of active sites and facilitate mass transfer across the electrode/electrolyte interface. Recently, Zhou *et al*.[391] prepared porous NiCoSe NSA's from 2D MOFs on NF through a simple ion-exchange reaction, followed by a hydrothermal treatment using different amounts of Se powder. Due to the unique 2D multi-porous structure with high conductivity, high electrochemical active surface area, and open channels, the as-prepared NiCoSe NSA's/Ni arrays exhibited an excellent electrochemical HER activity with a low overpotential of ~170 mV to achieve 10 mA cm^{-2}, and for the OER it required a low overpotential of ~278 mV to achieve 20 mA cm^{-2} and possessed long-term stability. Moreover, when the NiCoSe nanosheet arrays were used as both an anode and cathode, the water splitting cell only required ~1.51 V to achieve a current density of 10 mA cm^{-2} and a durability of over 48 h in an alkaline medium; see **Figure 35(ii)**.

6.2.6 Effect of catalysts processing temperatures

Thermally treated heterostructures of 2D/1D have received much attention for their numerous catalytically active sites and low contact resistance due to the development of chemical bonds at the interface. In this regard, Liu *et al*.[392] prepared 2D ReS_2 nanosheet/1D CoS_2 nanowires on CC and ReS_2/CoP on CC as a robust heterostructure through sulfurization and phoshipidation reactions at 500 °C. The

terminal S^{2-} exposed on the surface of the CoS_2 nanowires acted not only as the nucleus for ReS_2 nanosheets but also as a channel to enhance electron transport efficiency. As a result, the ReS_2/CoS_2 heterostructure showed an outstanding HER compared to ReS_2/CoP on CC, as shown in **Figure 36**. Liu *et al*.[393] prepared self-supported WP_2 and WP nanosheet (NS) arrays *via* an *in-situ* solid-phase phosphidation of WO_3 nanosheet arrays on CC. Different phosphating temperatures (650, 700, 750, 800, 850, 900 °C) were employed to attain different WP_2 NS/CC and WP NS/CC catalysts. As a consequence, WP_2/CC (650 °C) and WP NS/CC (800 °C) arrays exhibited an excellent acidic HER activity in terms of low overpotentials of ~140 and ~175 mV at 10 mA cm^{-2} with a Tafel slope of ~ 85 and ~103 mV dec^{-1}, respectively. By simply tuning the reaction temperature, Yan *et al*.[394] reported binder-free porous Ni_2P-Ni_5P_4 heterostructured NSA's on CC, where Ni_2P, Ni_2P-Ni_5P_4, and Ni_5P_4 synthesized at 300, 330, and 350 °C, respectively. As a consequence of a thermal effect and phosphidation, the porous Ni_2P-Ni_5P_4 exhibited a higher alkaline OER and HER compared to other samples. After 200 °C for 2 h, the annealed 2D copper oxide (CuO) electrocatalyst on SS substrate formed *via* chemical bath deposition showed a better OER performance than the non-annealed sample.[395] Due to the 2D morphology and the optimized electronic properties by heat treatment, the catalyst can provide a stable current density of >10 mA cm^{-2} for over 10 h in an alkaline medium. Recently, Yang *et al*.[396] prepared a series of binder-free electrodes based on Co_3O_4@NF, Fe_2O_3@NF, and Co_3O_4/Fe_2O_3@NF by calcining the as–obtained precursor in the air at 350 °C for 2h. The heterostructure features and conductivity enhancement due to the heat treatment of a Co_3O_4/Fe_2O_3@NF electrode provided an excellent OER in an alkaline solution in terms of low overpotential of ~254 mV at 10 mA cm^{-2}, a small Tafel slope ~33 mV dec^{-1}, with robust stability of 24 h. Compared with bare Co_3O_4/Fe_2O_3 (η_{10} = 493 mV), Fe_2O_3@NF (η_{10} = 378 mV) and Co_3O_4@NF (η_{10} = 350 mV), the Co_3O_4/Fe_2O_3@NF electrode presented noticeably enhanced electrocatalytic performance.

6.2.7 Summary and perspective

As a result of the unique structural features and facile fabrication conditions, the development of 2D nano- and micro-structured binder-free electrodes has significantly expanded in the past decades. The family of available 2D nano- and micro-structured materials has rapidly expanded from graphene to carbon nitrides, transition metal oxides/hydroxides, metal dichalcogenides (TMDs), metal nitrides, MOFs, and their

hybrid composites on conductive substrates. Compared to their bulk counterparts and other forms of nanostructures, 2D nanomaterials with a thickness of just one or a few atomic layers on highly conductive support can provide unique electrical, chemical, physical and mechanical properties, leading to superior catalytic properties. Furthermore, 2D binder-free electrodes offer several unique structural and catalytic benefits as a result of the larger density of low-coordinated surface atoms, surface dangling bonds, large lattice distortions, and rich defects. These exceptional features provide abundant benefits for improving surface chemisorption, fine-tuning the surface electronic states, improving carrier mobility, facilitating fast reaction kinetics, and thereby increasing the overall water splitting performance. However, several 2D binder-free nano- and micro-structured materials are restricted to strong acidic or alkaline electrolytes for achieving higher overall water splitting activity. Therefore, effectively combining the diverse merits of nano-/micro-materials by the rational design of 2D structures for overall water splitting systems is crucial. Given the benefits of effectively combining multi-faceted nano- and micro-structures on a conductive substrate, the morphological, structural features, and electroactivities of the individual component can be tailored, and the synergistic effects between them can be exploited, which can influence overall water splitting performance. The lack of long-term stability and durability data has been improved by the hybridization of 2D nanomaterials; together, these binder-free features provide new openings to improve resistance against oxidation in air and electrocatalyst surface damage, which enables their large-scale practical application in water splitting.

6.3 HER/OER performance of 3D nano- and micro-structured binder-free electrodes

Three-dimensional (3D) nano- and micro-structured binder-free electrodes are composed of nano- and/or micrometer-sized grains or crystallites. Owing to the unique structure, chemical composition, and mesoporous nature, these fascinating materials have extraordinary properties that could be exploited to make next-generation binder-free electrocatalytic materials. The hierarchical 3D structure of these electrodes provides large electrochemical reaction areas and optimal H_2 and O_2 gas dissipation with controlled open space, resulting in excellent catalytic performance; these are summarised in **Table 4**. However, several strategies have been utilized to enhance the catalytic performance and will now be discussed.

6.3.1 Impact of exposed active sites

The utilization of highly exposed active sites on nano- and micro-structured binder-free electrodes is of great interest in practical applications. In this regard, 3D interconnected MoS_2 nanosheets on 316-type SS meshes with different mesh numbers were formed *via* a facile hydrothermal method.[397] Owing to the exposed active sites, the optimized MoS_2/SS electrocatalysts showed a higher electrocatalytic performance for HER with a low overpotential of ~160 mV at 10 mA cm^{-2} and a small Tafel slope of 61 mV dec^{-1} in an alkaline condition. Due to abundant active sites provided by MoS_2, the MoS_2/graphite hybrid rod exhibited an energetic electron transport with a resistance as low as ~1-5 Ω. As a consequence, the MoS_2/graphite hybrid rod offered excellent HER performance in acidic conditions.[192] Moreover, hydrothermally prepared 3D hierarchical MoS_2 micro-flowers on macroporous Ti mesh (MoS_2 MF-Ti) exhibited abundant active edges, good conductivity, and meso-/macro-porous structures; as a consequence, it exhibited an excellent acidic HER.[173] In addition, using an electrodeposition method, 3D nanocones of Ni-Co, Ni-Fe, and Ni-Co-Fe were prepared on a Cu substrate by Darband *et al*.[398] During HER and OER testing, compared to other binder-free electrodes, the Ni-Fe-Co nanostructured electrocatalyst exhibited excellent activity with a low overpotential of ~91 mV for the HER and ~316 mV for the OER to attain a current density of 10 mA cm^{-2}, where the low Tafel slope values of 86 and 43 mV dec^{-1} were realized for the HER and OER, respectively. In addition, as a bi-functional electrode, the Ni-Fe-Co nanostructured electrocatalyst can provide a current density of 10 mA cm^{-2} under a cell voltage of 1.6 V, with long-term durability. This enhanced activity was attributed to the high active surface area, more exposed active sites, and rapid separation of bubbles from the electrode surface. Zhang *et al*.[399] prepared a 3D binder-free electrode of interconnected Ni(Fe)O_xH_y NSA's on a SS mesh substrate (SSNNi) by a hydrothermal method. Due to the well-defined 3D architecture with highly exposed surface area and active sites, there was an enhanced electron and mass transport capacity due to facile electrolyte penetration. Significantly, the 3D binder-free electrode of interconnected Ni(Fe)O_xH_y NSA's/SSNNi electrode provided excellent OER performance compared to bare SS, and nitrogen treated SS (SSN) in terms of a low overpotential (~0.23 V *vs*. RHE), a small Tafel slope (~36 mV dec^{-1}), and long-term durability in an alkaline condition. As shown in **Figure 37,** a 3D hierarchical structure composed of homogeneously distributed Ni-Fe-P nanoparticles embedded in N-doped carbons on NF (labeled as Ni-Fe-P@NC/NF) was prepared by an anion exchange method and a low-temperature phosphidation of nano-tubular

Prussian blue analogue (PBA). This structure exhibited an excellent bi-functional electrocatalytic activity in terms of low cell voltage of ~1.47 V to achieve ~10 mA cm^{-2} with outstanding durability for 100 h when used as a practical electrolyzer.[400] The enhanced performance of Ni-Fe-P@NC/NF was accredited to the abundance of active sites formed by multiple components and its hierarchical porous nature.

6.3.2 Effect of intrinsic conductivity enhancement

A 3DGF provides an excellent porosity with a large surface area and stability; however, in a bare condition its electrocatalytic performance is poor due to the low electrical conductivity and limited electrocatalytic active sites. In order to enhance the electrocatalytic performance of 3DGF, several researchers have used a doping strategy.[186, 401, 402] In this regard, Zhou *et al*.[403] prepared Ar plasma pre-treated and N, S co-doped 3DGF (3DGF-Ar-NS). As a result, the HER improved due to the conductive nature of the material, the flexible 3D graphene skeleton, and the porous features that facilitated charge transportation. The Ar-plasma-pre-treated N, S co-doped 3DGF, exhibited improved HER performance due to its conductive nature, flexible 3D graphene skeleton, and porous features that facilitated charge transportation. The 3DGF-Ar-NS revealed a small Tafel value of ~75 mV dec^{-1} compared to bare 3DGF (~182 mV dec^{-1}) in 0.5 M H_2SO_4. The 3DGF-Ar-NS required a small overpotential of ~298 mV to attain a 10 mA cm^{-2}, considerably lower than the 3DGF-NS (~520 mV), 3DGF-Ar (~638 mV), and 3DGF (~769 mV). Compared with bare and Ar plasma pre-treatment graphene foams, the use of N and S co-doping further increased the HER activity *via* the improved conductivity of 3DGF. As shown in **Figure 38,** due to the high electrical conductivity and a robust skeleton that led to more active sites and faster electron and ion transport, the P doped Fe_3O_4 nanoflowers on 3D porous graphene (denoted as P–Fe_3O_4@3DG) provided enhanced performance for HER in 1.0 M KOH with a low overpotential of ~123 mV at 10 mA cm^{-2}, small Tafel slope of ~65 mV dec^{-1}, and outstanding durability beyond 50 h. It also exhibited substantial performance under neutral and acidic media.[404] It was also thought that P-doping could provide a low Gibbs free energy and binding of H^*. Recently, Zhang *et al*.[136] introduced a vapor ammonization-electroreduction approach to fabricate N-modified 3D CF (SN-CF). The SN-CF electrocatalyst displayed a high electrocatalytic HER activity in 1.0 M KOH, with low overpotentials of ~188 and ~377 mV to attain current densities of 10 and 100 mA cm^{-2}, respectively. In addition, the SN-CF showed good cycling stability of ~95% after 2000 cycles and long-term durability for ~12 h at a current density of

~10 mA cm^{-2}. Metals of Ni, Co, and Zn doped CuO@GCE modified electrodes have been fabricated by Rani *et al*.[405] As a consequence of their enhanced conductivity, compared to other electrocatalysts, the Co-doped CuO@GCE modified electrode displayed a current density of 4.41 mA g^{-1} at 2.1 V with a lower Tafel slope value of ~67 mV dec^{-1} with 24 h long-term durability. In addition, flower-like nanostructured multi-metallic compounds of nickel-iron-chromium compound/stainless steel foil (NICC/SSF) electrocatalyst require only a small HER and OER overpotentials of 85 mV and 274 mV at 10 mA cm^{-2}, respectively.[406] Notably, due to their high enhancement in intrinsic conductivity, it required a low cell voltage of 1.60 V to reach a overall water splitting current density of 10 mA cm^{-2}.

6.3.3 Influence of heterostructure formation

Electrochemical water splitting depends strongly on electronic conductivity, mass transport, and active sites; however, the difficulty in facilitating electronic conductivity, mass transport, and revealing adequate active sites is an obstacle for both HER and OER. To address these issues, several researchers have utilized heterostructure formation on binder-free electrodes.[407-409] For example, as shown in **Figure 39**, hydrothermally prepared 3D Hydrangea Macrophylla like Ni_2V-MOFs@NF requires relatively low overpotentials of ~244 and ~89 mV for the OER and HER, respectively, which accelerated the overall water splitting activity with ~1.55 V at 10 mA cm^{-2} and strong durability of 80 h.[410] The enhanced performance was attributed to the combination of 2D ultrathin NS self-assembling into a 3D nanoflower and the regulation of electronic structure resulting from the synergetic interaction between nickel (Ni) and vanadium (V), which has also been revealed by DFT calculations. Bimetallic sulfides of MoS_2-NiS_2 anchored 3D N-doped Graphene foam (MoS_2-NiS_2/NGF) were prepared by Kuang *et al*.[411] The strong interfaces between the MoS_2-NiS_2 nanoparticles and NGF with a 3D interconnected tubular hollow structure provided a superior performance towards HER and OER. Remarkably, during the HER and OER reactions, the overpotential and charge transfer resistance of the 3D MoS_2-NiS_2/NGF hybrid was much lower than the bare NGF, MoS_2/NGF, NiS_2/NGF, and physically mixed MoS_2-NiS_2+NGF. This was attributed to the abundant active sites and varied pathways for highly efficient charge transport. Interestingly, as a bi-functional catalyst, the MoS_2-NiS_2/NGF also exhibited an excellent overall water splitting of 10 mA cm^{-2} at 1.64 V with long-term durability in 1.0 M KOH. Due to the heterostructure formed, a hierarchical MoS_2/CoS_2 heterostructure array on CFP exhibited an excellent

HER performance in terms of a low onset potential of ~20 mV and an overpotential of ~125 mV at a current density of 100 mA cm^{-2} in 0.5 M H_2SO_4.[412] Furthermore, it exhibited excellent long-term durability compared with bare CoS_2 and MoS_2. Unusually, a hydrothermally prepared nanoflower-like VO_x/NiS/NF electrode can provide a high electrical conductivity and surface area, along with an amorphous VO_x feature.[413] Due to this exceptional combination of features, the VO_x/NiS/NF binder-free electrode showed an outstanding catalytic OER activity with a lower overpotential of ~330 mV at 50 mA cm^{-2}, smaller Tafel slope of ~121 mV dec^{-1}, and an inferior semicircle from electrochemical impedance spectroscopy (EIS) analysis compared to VO_x/NF in an alkaline solution. Due to the 3D hierarchical architecture with a high surface area, the 3D Cu@NiFe LDH electrode showed a small charge-transfer resistance of ~2.8 Ω, indicating facile electron transfer and electrocatalytic kinetics compared to bare samples.[414] As a bi-functional catalyst, the 3D Cu@NiFe LDH electrode realized a current density of 10 mA cm^{-2} at a voltage of 1.54 V, and 100 mA cm^{-2} at 1.69 V with excellent durability for overall water splitting, which was superior to the benchmark of IrO_2(+)//Pt(−) electrodes. Recently, Yang *et al*.[415] proposed a three-step hydrothermal method to effectively fine-tune the heterointerfaces of rectangular spongy-like core-shell NiS/CoS/CC-3 bi-functional electrocatalyst by adjusting the thickness of the NiS shell. Due to the unique rectangular spongy-like structural feature and the abundant heterointerfaces between the NiS and CoS, the NiS/CoS/CC-3 catalyst exhibited exceptional electrocatalytic activity and stability for both HER and OER. It required low overpotentials of ~102 and 290 mV to reach 10 mA cm^{-2} for HER and OER, respectively, in an alkaline solution. As a two-electrode electrolyzer, the NiS/CoS/CC-3 reached a current density of 10 mA cm^{-2} at a potential of 1.57 V, with outstanding durability over 72 h. Likewise, the MOF-$CoSe_2$@$MoSe_2$ core-shell requires a low cell voltage of 1.53 V for overall water splitting.[416] Due to the interface rich 3-dimensional (3D) hierarchical architecture, the Cu_3N@CoNiCHs@CF reached HER and OER current density of 10 mA cm^{-2} at 182 and 155 mV, respectively.[417] While the Cu_3N@CoNiCHs@CF requires a low cell voltage of 1.58 V for overall water splitting.

6.3.4 Role of defects

It is well-known that defect engineering has been utilized to introduce partial-metallicity into selected semiconductor electrocatalysts, thereby increasing their electrical conductivity, catalytic activity, and electrocatalytic performance. In this regard, as shown in **Figure 40(i),** Zhang *et al*.[418] prepared oxygen vacancies

intermediated NiO/Co_3O_4 heterostructures on NF using various ratios of Ni and Co. It was estimated that the oxygen vacancy ratio of NiO/Co_3O_4 is 28.4%, far beyond that of both the pristine NiO (6.3%) and Co_3O_4 (8.4%). The NiO/Co_3O_4 heterostructure further reduces the coordination number of the neighbouring metal atoms and leads to optimized energetics of the electrocatalytic reaction. The charge-transfer resistance (R_{ct}) of NiO/Co_3O_4 was only ~2.8 Ω, which was five times lower than NiO (~14.5 Ω) or Co_3O_4 (~22.6 Ω), indicating that a fast interface electronic transmission contributed to the improved conductivity *via* electronic interaction effects at the interface. Due to the heterointerface and improved oxygen vacancies at the interfaces, the NiO/Co_3O_4 heterostructure showed an overpotential of only ~262 mV at 10 mA cm^{-2} and a low Tafel slope of ~58 mV dec^{-1} for OER in alkaline medium. Moreover, by DFT analysis, it was found that the *d*-band centers of Co near the interface in NiO/Co_3O_4 remained far from the Fermi level, thus confirming a reduction of the unfavourable strong adsorption to oxo-intermediates during the OER process, which impacted on catalytic activity. As shown in **Figure 40(ii),** the defected Ru_1/D-NiFe LDH can surpass the Pt/C catalyst.[419] Significantly, as a bi-functional electrode, the Ru_1/D-NiFe LDH‖Ru_1/D-NiFe LDH electrodes delivered 10 mA cm^{-2} with long-term stability over 100 h representing good robustness. Kong *et al.*[420] introduced a defect engineering strategy to enhance the electrocatalytic activity of 3D hierarchical $NiMo_3S_4$ on CC. The incorporated Ni atoms play a vital role in creating $NiMo_3S_4$ nanostructures by creating significant defect sites, which provide an enlarged "*d*" spacing of the (002) crystal plane, leading to improved performance. In addition, the 3D hierarchical morphology of a defect-rich $NiMo_3S_4$/CC provided a large surface area, good electron transport, high ion-diffusion rates, and HER performance. Due to the defect-rich heterogeneous interface with a disordered structure, the MoS_2/NiS_2 on CC was used as both cathode and anode electrodes for overall water splitting. As a consequence of defects at the interfaces, the optimal MoS_2/NiS_2 heterostructure exhibited a voltage of 1.59 V at a current density of 10 mA cm^{-2} and good stability in 1.0 M KOH.[421] It was observed that rich defects and a disordered structure at the interfaces could modify the electronic interactions and ease electron transfer, which can benefit catalytic reactions. It was also revealed that sulfur defects could provide rich active sites and accelerate electron/mass transfer to improve catalytic performance.

6.3.5 Effect of Porosity

A hierarchical 3D structure can provide large reaction areas with a meso-/micro-porous nature and optimal gas dissipation with consistent open space, resulting in excellent electrocatalytic HER and OER performance. For example, Meng *et al.*[422] prepared a 3D interconnected nanosheets array of $MMoO_4$ on CC (whereas M = Co, Ni) as a binder-free electrode. Due to the synergistic effect of high surface area with a porous nature, fast charge, and mass transport, the $CoMoO_4$-CC electrode showed a low OER overpotential of ~290 mV to attain 10 mA cm^{-2} current density and a Tafel slope of ~94 mV dec^{-1} in an alkaline; this activity was higher than $NiMoO_4$-CC. Similarly, a hierarchical Co_3O_4-decorated CuO–Cu_2O nanorod core-shell assembly was *in-situ* grown on a CF (named as CuO_x@Co_3O_4 NRs/CF).[423] Due to its large electrochemical surface area and the synergetic effects between the CuO_x core and Co_3O_4 shell, the CuO_x@Co_3O_4 NRs/CF exhibited high overall water splitting catalytic activity in an alkaline medium. As a result, the CuO_x@Co_3O_4 NRs/CF resulted in a small overpotential of ~240 mV for OER and ~242 mV for HER at a current density of 50 mA cm^{-2}, with low Tafel slopes of ~46 and ~61 mV dec^{-1}, respectively. The CuO_x@Co_3O_4 NRs/CF can produce O_2 or H_2 for at least ~24 h with a small decay in catalytic activity with high faradaic efficiencies of 99.7% and 96.4% for the OER and HER, respectively. A 3D porous heterogeneous framework of "celosia-like" FeCo-LDH and P-MoO_3 grown MXene on NF (P-MoO_3 FCL MXene/NF), exhibits excellent activity HER and OER activity with a low overpotential of 118 mV and 179 mV at 10 mA cm^{-2}, respectively.[424] As a bi-functional electrode, it requires the overpotential of 1.53 V to reach 10 mA cm^{-2}. Due to the mesoporous nature, the 3D MoS_2-WS_2/graphene achieved a small overpotential of 110 mV at a current density of 10 mA cm^{-2} and a small Tafel slope of ~41 mV dec^{-1}, indicating a high HER activity compared to bare graphene and MoS_2.[425] In addition, using electrodeposition combined with a hydrothermal method, Liang *et al.*[426] prepared a porous 3D structured NiFe LDH, which was electrodeposited on Ni_3S_2 nanosheets on NF for OER. Compared with RuO_2, the Ni_3S_2 /NiFe (LDH)/NF exhibited enhanced performance in terms of a low overpotential of ~200 mV was required to reach a current density of 10 mA cm^{-2} in 1.0 M KOH. To date, a variety of porous natured catalysts have been reported, which include Co_3O_4,[427] Ni_3S_2,[428] Co_9S_8,[429] NiP,[430] $NiCoSe_2$,[431] CoNiLDH,[432] Ni-FeOOH,[433] FeCoP/C,[434] NiFe/$NiCo_2O_4$,[389] and Mn-doped FeP/$Co_3(PO_4)_2$/CC[435] to achieve an improved electrocatalytic HER and OER.

6.3.6 Effect of catalysts processing temperatures

Nanocomposites and carbon catalysts derived from a vertically aligned 3D self-branched porous/hollow MOF nanostructure on a flexible current collector are of great interest. In this regard, a 3D self-branched $ZnCo_2O_4$@NC hollow nanowall array grown on flexible carbon textiles (CT) was prepared by Kong *et al.*[436] through carbonization of ZnCo-MOF/CT at 700 °C in Ar for 2 h, followed by a heat treatment at 250° C for 1.5 h in air. During OER testing, the 3D self-branched $ZnCo_2O_4$@NC/CTs electrode exhibited excellent performance with a low onset potential of ~1.38 V *vs*. RHE and long-term electrochemical stability. In addition, a self-standing 3D core@shell Co@$CoMoO_4$ nanowire array (Co@$CoMoO_4$ NA) on an NF electrode was prepared by Xiang *et al.*[437] by various calcination temperatures (300, 400, and 500 °C) of a precursor of cobalt carbonate hydroxide@$CoMoO_4$ (CCH NA@$CoMoO_4$) under an H_2/N_2 atmosphere. As a consequence, in a 1.0 M KOH solution, the 400 °C calcined Co@$CoMoO_4$ NA electrode exhibited a remarkable activity with an extremely low HER overpotential of ~46 mV at 10 mA cm^{-2}, which is similar to commercial Pt/C, as seen in **Figure 41(i)**. The 3D intersectional architecture of the $Ni_xCo_{3-x}O_4$ nanoplates was prepared by annealing of Ni-Co PBA /NF at 350 °C for 2 h with a heating rate of 2 °C min^{-1} in air, which upon subsequent calcination in the air resulted in $Ni_xCo_{3-x}O_4$ nanoplate arrays with porous and hollow nanocubes.[438] During OER testing, the optimal $Ni_xCo_{3-x}O_4$/NF required an overpotential of ~287 mV to achieve a current density of 10 mA cm^{-2}. Interestingly, the optimal annealing temperature significantly improved the surface porosity with facile transport channels for the electrolyte. Hierarchically assembled Cu_2O@Fe_2O_3@CC-500 needs ultralow HER and OER overpotentials of 188 mV and 296 mV to afford 10 mA cm^{-2} in an alkaline medium, respectively.[439] As a bi-functional water electrolyzer, the Cu_2O@Fe_2O_3@CC-500 requires a cell voltage of 1.675 V at 10 mA cm^{-2} and exhibited excellent stability. Moreover, the Co-P@IC/(Co-Fe)P@CC was fabricated with a thermal phosphorization route and exhibited small overpotentials of ~174 and ~53 mV at 10 mA cm^{-2} for the OER and HER in an alkaline media, respectively, and exhibited an ultra-low operating cell voltage for overall water splitting of 1.46 V.[440] As shown in **Figure 41(ii),** a bi-functional catalyst of Co_2Cr_1-P@3DGF prepared by phosphorization at 300 °C at 4 h under Ar, achieved remarkable electrocatalytic HER and OER activities in 1.0 M KOH, with a low overpotential of ~118 and ~270 mV to reach 10 mA cm^{-2}, respectively.[441] In addition, when applying Co_2Cr_1-P@3DGF as overall water splitting catalytic electrode in an alkaline condition, the required cell voltage at ~10 mA cm^{-2} with ~1.56

V. The superior performance was mainly attributed to the incorporation of a Cr into CoP and the high conductivity of the 3D graphene network substrate formed by thermal phosphidation.

Fascinatingly, three kinds of porous $MoNi_4$ networks on NF formed by hydrothermal treatment, followed by annealing at 300, 450, and 600 °C, were prepared by Jin *et al*.[442] The resulting $MoNi_4$/NF-450 °C showed high activity for both HER and OER compared to other samples. The higher catalytic performance was credited to not only being fully reduced into $MoNi_4$ but also preserving the original morphology after annealing at 450 °C. As a consequence, it needed only ∼1.58 V to realize 10 mA cm^{-2} for overall water splitting and showed outstanding stability without loss of activity after 24 h. Adhikari *et al*.[443] utilized the electrodeposition of CoS followed by the calcination of Ni-Co hydroxide coated NF at 350 °C for 2 h. Using a calcination effect, they attained a 3D core-shell structured $NiCo_2O_4$@CoS/NF. Due to the synergistic effect of the 3D core-shell structure, the $NiCo_2O_4$@CoS/NF exhibited a superior activity towards OER in terms of a low overpotential of ~290 mV to reach 10 mA cm^{-2}, with high durability in an alkaline solution. Similarly, Zhang *et al*.[444] utilized the phosphidation of a NiFe-LDH precursor at 300 °C for 2 h under H_2/Ar to prepare the 3D hierarchical $NiFeO_x$/NiFeP binder-free electrocatalysts. An O_2 plasma treatment was adopted to create a 4-6 nm $NiFeO_x$ amorphous layer on the surface of the NiFeP at different time periods of 1, 2, 3, and 4 s. The molar ratio of Ni^{2+} to Fe^{3+} was varied (1:3, 1:1, and 3:1) to achieve $NiFeO_x$/NiFeP/NF. As a result, the $NiFeO_x$/NiFeP/NF prepared by 3 min in an O_2 plasma-treated electrocatalyst revealed an excellent OER in an alkaline medium. Similarly, Wang *et al*.[445] prepared a series of binder-free electrodes of Co_3O_4@$NiCo_2O_4$-6 h, Co_3O_4@$NiCo_2O_4$-8 h, and Co_3O_4@$NiCo_2O_4$-10 h by a hydrothermal method at different time periods of 6, 8, and 10 h respectively, at 180 °C. Furthermore, to improve the conductivity, all materials were calcined in air at 300 °C for 4 h. As a consequence of hydrothermal temperature and calcination of the Co_3O_4@$NiCo_2O_4$-8h catalyst enabled it to reach an OER current density of 50 mA cm^{-2}, with an overpotential of ~290 mV in a 1.0 M KOH solution; this performance was higher than all other materials.

6.3.7 Summary and Perspective

Self and directed assembly of 3D nano- and micro-structured materials on a conductive substrate has been of interest since a 3D shape avoids cracking or other forms of physical, chemical, and mechanical degradation of the material. In this fashion, rapid

progress has been made in the designing of bare or heterostructured nano- and micro-structured materials at length scales ranging from a few nanometers to 100's of nanometers on a variety of conductive substrates. In such cases, a variety of structural tuning approaches, such as *in-situ* and *ex-situ* methods, are being utilized to fabricate 3D nano- and micro-structured binder-free catalysts with a wide range of structural complexity. The prospect of fine-tuning 3D nano- and micro-structures for effective water-splitting depends on studying operating parameters such as fabrication conditions, including *in-situ* and *ex-situ* reaction temperature, pH, and reactor type. Hence, both theoretical and experimental studies are necessary for understanding the principle of water splitting using a range of 3D binder-free electrodes. Remarkably, much effort has been dedicated to realizing practical water splitting by the construction of self-supported 3D catalysts on the conductive electrodes to avoid the use of additives or binders and ensure good electronic contact between the water splitting 3D catalysts and the supportive electrode. Furthermore, numerous scalable strategies have been considered for preparing non-precious metal-based bi-functional binder-free 3D electrocatalysts for overall water splitting, creating potential directions for the scale-up of water electrolysis technology for real-world application.

6.4 Seawater splitting performance of 1D, 2D, and 3D nano- and micro-structured binder-free electrodes

Seawater electrolysis is highly promising for large-scale H_2 production, but challenging due to the complex composition of seawater, *i.e.,* the existence of dissolved ions such as Ca^{2+}, Mg^{2+}, Na^{+}, and Cl^{-}, microbial/bacteria, and other small undesired particulates. This can lead to interference of several competing reactions by blocking active sites, producing by-products, and poisoning and corrosion of electrodes, altering the pH of electrolyte, which ultimately lead to poor activity and stability.[446, 447] In this case, 1D, 2D, and 3D nano- and micro-structured binder-free electrodes have been regarded as attractive candidates for practical seawater electrolysis due to the tailored nano- and micro-structure morphologies with controlled electrocatalyst/substrate interface, fine-tuned electronic structure, enriched electronic conductivity, more exposed active sites, and optimized corrosion resistance and stability.[448-451] For example, a metal nitride of NiFeN nanoparticles decorated on NiMoN nanorods on NF performed as an active and durable OER catalyst for alkaline seawater electrolysis.[452] As a consequence of the binder-free features and highly conductive nature, it reached a current density of ~500

and ~1000 mA cm^{-2} at low voltages of ~1.608 and 1.709 V, respectively, for overall alkaline seawater splitting at 60 °C, with high durability over 100 h; see **Figure 42(i)**. In addition, due to the highly porous nature and good chlorine-corrosion resistance afforded by Ni_xP micro sheet arrays, the hierarchical sandwich-like catalyst (NiCoN|Ni_xP|NiCoN) on NF exhibited a long-term durability of 24 h in natural seawater.[453] As shown in **Figure 42(ii)**, due to the porosity and good hydrophilic features, the S-doped Ni/Fe (oxy)hydroxide catalysts on NF required low overpotentials of ~300 and 398 mV *vs.* RHE to deliver current densities of 100 and 500 mA cm^{-2}, respectively, when directly used as a binder-free OER catalyst in alkaline natural seawater electrolyte with durability over 100 h.[454] The Mo_2C/MoP hetero-nanoparticles within N, P co-doped carbon nanofibers can act as an anti-corrosion inherent and assist against corrosion and poisoning.[455] Apart from excellent HER activity in seawater, this hybrid binder-free catalyst can retain over 16 h at 10 mA cm^{-2} current density without any decay, signifying excellent durability for seawater splitting. An additional benefit is that, compared with conventional water electrolysis, seawater electrolysis technology can be used for both H_2 generation and desalination of seawater.[456, 457] Several other binder-free electrocatalysts such as Yolk-Shell Ni–Se,[458] NiFe-LDH,[459], and heterogeneous bimetallic phosphide of Ni_2P-Fe_2P[460] have evolved as possible alternatives for energetic seawater electrolysis.

6.5 Long-term durability of 1D, 2D, and 3D nano- and micro-structured binder-free electrodes

Long-term stability is essential for any catalysts to reach commercial-scale H_2 production via water splitting technology. In this regard, the importance of durability has also been considered in depth.[450, 461] In a binder-free electrode configuration, the interfacial adhesion between electrocatalysts and substrates plays an important role in the enhancement of catalytic activity and stability. For example, due to optimal interfacial adhesion, a Pt/Ni-Mo electrocatalyst results in the facile electrolytes mass transfer and removal of evolved gas bubbles on its surface. As a result, the Pt/Ni-Mo/NF electrode operated for ~140 h at 2000 mA cm^{-2} in a 1.0 M KOH electrolyte, with minor degradation.[448] During electrochemical reactions, the dissolution of components may lead to diminishing performance.[84] In this concern, Yang *et al*.[462] utilized CeO_2 to chemically stabilize a NiO/CC catalysts. As a result, the CeO_2 highly suppressed the leaching of active composition and promoted the homogenous distribution of

reconstructed catalytic NiOOH. In addition, nanosheets of FeNi LDH grown on a Fe foam maintained a constant current density of 1000 mA cm^{-2} for over 6000 h in 1.0 M KOH for OER.[463] Nanoparticles of Ni decorated V-doped NiFe LDH nanosheets/NF (denoted as P-V-NiFe LDH NSA) exhibited robust long-term durability for 1000 h at 10 mA cm^{-2} for overall water splitting.[464] Due to the effective interfaces of Ni-Fe-P with NC/NF, the Ni-Fe-P@NC/NF showed high durability for 100 h.[400] In addition, LiCoBPO/NF showed excellent durability over 40 days, signifying its potential for practical application.[465] Due to its super-hydrophilic and super-oleophobic features, the binder-free electrocatalyst of hierarchical $CoMoS_x$/NF exhibited rapid electrolyte accessibility and rapid release of gas bubbles, which resulted in a current density of 500 mA cm^{-2} at 1.89 V and sustained for 100 h without decay in 1.0 M KOH.[466] Moreover, due to the affinity of active components with the substrate, facile charge/mass transfer, rapid release of evolved gas, and optimized electrochemical active sites, several 1D, 2D, and 3D binder-free nano- and micro-structured materials have emerged for high current density water splitting and possess long-term stability and durability in harsh working conditions; these are indicated in **Table 2- Table 4.**

7. Applications Beyond

7.1 Binder-free electrodes for bi-functional solar photoelectrochemical (PEC) water splitting

In addition to electrocatalytic water splitting, photoelectrochemical (PEC) water splitting has attracted increasing research attention due to its potential to alleviate energy and environmental issues. PEC splitting of water into H_2 and O_2 is an intriguing method to directly convert solar energy into fuel.[2, 467, 468] The PEC cell contains a semiconducting anode/cathode that is immersed in a liquid electrolyte, leading to water oxidation/reduction through charge separation in the bulk of the electrode material by light absorption at the surface of the photoelectrode.[6, 469] In brief, the incident photons absorbed by the semiconductor generate electron-hole pairs, which are isolated by the built-in electric field inside the photoelectrode, completed in the semiconductor–liquid junction (SCLJ) by semiconductor and electrolyte Fermi level equilibration.[23, 470] In a photoanode, holes are driven to the photoelectrode surface to achieve the OER; meanwhile, electrons are collected by the back contact and close the circuit performing the proton reduction reaction in the counter electrode.[471-473] Similarly, if the semiconductor's built-in electric field drives electrons to the surface to realize the HER,

it is considered a photocathode.[474] Nano- and/or micro-structured electrodes provide numerous intriguing characteristics for PEC compared to other unadorned semiconductor materials.[475, 476] Due to the optimized bandgap, nano- and/or micro-structured electrodes may increase the reaction rate or enable the reaction to occur at a lower potential.[477] Moreover, a tailored nanostructure, conductivity optimization, and porous morphology will not only increase active sites but also contribute to a lower overpotential with high performance. Among the different PEC devices that could be established to realize efficient water splitting, tandem PEC cells show more flexibility and afford high theoretical conversion efficiency.[478, 479]

Expanding the real-world use of PEC systems for the collection of solar light will necessitate the manufacture of low-cost semiconductors composed of earth's abundant elements. Nano- and micro-structured semiconductors such as Si,[480] InP,[481] CdTe,[482] $CuInS_2$,[483] $CuGaSe_2$,[484] $CuGa_3Se_5$,[485] and $CuIn_xGa_{1-x}Se_2$[486] have been demonstrated as efficient photocathodes for PEC water reduction. However, for other binary and ternary semiconductor-based photocathodes, the improvement of the PEC performance has been impeded by many limitations, including low carrier mobility, Fermi level pinning induced by surface states, and difficulty in establishing high-quality heterojunctions.[487] In addition, the observed photocurrents for HER generated by these photocathodes remain relatively low. In addition, most photocathode materials were based on CdS,[488] MoS_2,[489] In_2S_3,[490] and Cu_2O.[491] Similarly, several kinds of most promising nano- and micro-structured semiconductors have been employed as photoanodes, which include TiO_2,[492] $BiVO_4$,[493], and Ta_3N_5(TaON).[494] Notably, for PEC-based OER reactions, bismuth (Bi)-containing semiconductors have been extensively applied.[495] However, substantial photo-corrosion has been observed on these photocathodes.[488]

Recently, bi-functional PEC water splitting has attracted attention, in which a single photocatalyst material endorses both HER and OER of PEC water splitting in the same electrolyte solution.[478, 496-498] Such bi-functionality could afford numerous practical advantages such as scalability, non-precious materials utilization, and system versatility, which will ultimately reduce the cost of the total system. In this regard, a bi-functional PEC–electrochemical (PEC–EC) system based on an improved perovskite-$BiVO_4$ tandem device was proposed by Pornrungroj *et al*.[499] As shown in **Figure 43(i)**, this system is based on an "artificial leaf" tandem PEC structure that comprises an inverse-structure lead halide perovskite sheltered by a graphite-epoxy/perylene-C

coating (exhibited 96 h stability of operation in water) and a porous $BiVO_4$ on FTO. The light-absorbers are interfaced with an H_2 evolution catalyst (Pt) and a Co-based water oxidation catalyst of amorphous $TiCoO_x$ (TiCo), respectively, (named as FTO|$BiVO_4$|TiCo) which can also be directly driven by electricity. Thus, the device can work in PEC mode during light irradiation and change to an electricity-powered mode in dark conditions. As a result, the bi-functional perovskite-based FTO|$BiVO_4$|TiCo tandem cells provide a solar-to-hydrogen efficiency of 1.3% under simulated solar irradiation and onset for water electrolysis at 1.8 V with long-term durability over 10 h in 0.1 M K_2SO_4 electrolyte. Recently, a tandem cell comprising of an *n*-type photoanode of n-Se/$BiVO_4$ and a *p*-type photocathode of *p*-Cr_2O_3/CuO:Ni could reach a photocurrent of ~0.04 mA cm^{-2} at zero bias.[500] Kim *et al*.[501] demonstrated a unique, flexible, and hybrid bi-functional multilayer PEC water splitting photoelectrode composed of nano-scale graphene oxide (nGO) and a terpyridine complex of ruthenium(II) (TPY_2Ru) on an ITO-coated PET substrate for overall water splitting reaction. To make an efficient PEC system for water splitting, they hosted a TPY_2Ru to harvest visible light to create more photo-induced electrons as well as nGO to afford photoactive sites for water splitting in the multilayer photoelectrode. Remarkably, during bi-functional PEC water splitting, this photoelectrode exhibited a photoanodic current density of ~4.28 μA cm^{-2} at 1.23 V *vs*. RHE and a photocathodic current density of 28.42 μA cm^{-2} at 0 V *vs.* RHE in a potassium phosphate buffer solution at pH ~7. Furthermore, it revealed remarkable retention of current density after a ~1000-cycle durability test. It has been disclosed that nanoscale-architecture-controlled engineering may efficiently enhance the performance of photoelectrodes. By taking advantage of MXenes (MXDs) and carbon quantum dots (CQDs), Nguyen *et al*.[502] demonstrated solar-assisted overall water splitting of core-shell structured MXene@carbon (MX@C) nanodot hybrids on a Mo-doped $BiVO_4$/FTO (named as BVO) substrate, see **Figure 43(ii)**. For the fabrication of MX@C hybrids, the bottom-up synthesis of CQDs and the top-down route of MXDs were joined through the facile one-pot method. By assimilating the cathode (MX@C on NF) with the photoanode (MX@C/Mo-BVO), the solar-assisted PEC water splitting was implemented by the two-electrode set-up in 0.1 M phosphate buffer electrolyte. As a consequence, the MX@C/BVO‖MX@C on the NF-based PEC cell reached a current density of ~1.23 mA cm^{-2} at 1.23 V, which was ~1.57 times higher than 0.78 mA cm^{-2} of the BVO‖NF cell. Furthermore, long-term stability over 8 h at 1.23 V toward solar-assisted overall water splitting was achieved

for MX@C/BVO)‖MX@C. This PEC improvement was accredited to the induced photon absorption of MX@C. Moreover, the high PEC activity was ascribed to the facile catalytic kinetics of the chemically and electronically integrated MX@C hybrid at the hetero-interface for both OER and HER.

Solar-driven water splitting to generate viable H_2 can be achieved through a modular photovoltaic–photoelectrochemical (PV–PEC) approach. Whereas PV–PEC operates the external bias provided by solar cells to drive a separate electrolyzer component, PEC employs charges generated *via* photo-excitation of semiconducting materials to directly split H_2O into H_2 and O_2. Recently, Kim *et al.*[503] prepared a non-precious metal of Co-based phosphide promoted $BiVO_4$ photoelectrode, as shown in **Figure 44(i)**. Initially, the Mo-doped $BiVO_4$ films on FTO substrate were prepared by a modified metal-organic decomposition method. Later, CoP and Co-Pi nanoparticles were prepared by chemical reduction followed by phosphidation, and were loaded onto Mo-$BiVO_4$-based photoelectrodes by drop-casting; the samples were named as CoP/1% Mo:$BiVO_4$ and Co-Pi/1% Mo:$BiVO_4$, respectively. For comparison, bare $BiVO_4$, Mo-doped $BiVO_4$ (1% Mo:$BiVO_4$), and hydrogen(H)-treated Mo:$BiVO_4$ (H, 1% Mo:$BiVO_4$) were prepared in a similar way. A tandem cell was constructed using the photoanode of CoP/hydrogen-treated, 1% Mo-doped $BiVO_4$/FTO, and a CoP/NF as the cathode and a sequence attached with a crystalline two junction Si solar cell (*i.e.*, two numbers of Si solar cells) as the bias power generator. The tandem device demonstrated stable unassisted water splitting with a solar-to-hydrogen conversion efficiency (STH) of 5.3% under simulated solar light. It has been observed that the oxygen vacancy defects observed in $BiVO_4$, and the CoP loaded on the $BiVO_4$ photoanode turn into amorphous CoO_x–HPO_y; these features played a major role in bias-free water splitting. Recently, as shown in **Figure 44(ii)**, Fan *et al.*[504] prepared a stable PV–PEC tandem device made by a dual Si photoelectrode of an n^+np^+-Si photocathode and p^+pn^+-Si photoanode and two series-connected ordinary Si PV cells. Further, a 10 nm Ni protective layer together with a bi-functional Ni–Mo catalyst for both the Si photocathode and photoanode has been employed. As a consequence of protective layers and tandem cell feature, the PV–PEC device can perform spontaneous bi-functional water splitting without any applied bias. A stable photocurrent density of 7.97 mA cm^{-2} was achieved at a zero bias voltage, a high STH of 9.8% with stability of over 100 h was attained in a 1.0 M KOH solution under 1 sun illumination. Other than making efforts on the unadorned photoelectrodes for bi-functional PEC water

splitting, exploring novel nano- and micro-structured semiconductors employed as photoanodes and photocathodes for overall water splitting can be a new direction of research.

7.2 Binder-free photoelectrodes for photocatalytic dye degradation

Photocatalysis is an attractive tool for green energy conversion and environmental decontamination. According to published research reports, over 10-12% of annual global dye production (~0.7 million tons) is released into industrial effluent.[505, 506] Industrial wastewater containing a variety of dyes such as Rose Bengal, Victoria blue, Thymol blue, Caramine, Indigo Red, Red 120, Rhodamine B, Methylene Blue, Eriochrome Black-T (EBT), inorganic (heavy metal ions, metal complexes, salts, etc.), nutrients and pathogens, are responsible for water pollution.[23, 506-511] Due to their carcinogenic behaviour, it can lead to severe environmental problems and impact human health. In addition, providing accessibility of clean and fresh water for human use is among the most important issues facing the world over the next 20-25 years.

The structural diversity of synthetic dyes facilitates their applications in a range of industries. Hence, the advance of environmentally friendly technologies to eradicate dyes from wastewater has become an urgent priority. Recently, photocatalytic dye degradation using engineered nano- and micro-structured binder-free electrode materials has emerged as potential schemes as effective solutions for water treatment. In this regard, Zhang *et al*.[512] prepared a heterostructure composite of 2D reduced graphene oxide (rGO) and g-C_3N_4 co-modified 3D TiO_2 nanotube array (rGO@g-C_3N_4/TNAs) photoelectrodes were fabricated on titanium sheets. The photocatalytic dye degradation activity of the photoelectrodes under tetracycline hydrochloride (TC) was evaluated, as shown in **Figure 45(i)**. Notably, the incorporation of g-C_3N_4 and rGO reduced the bandgap of the TNAs photoelectrode and encouraged the separation of photo-induced electron-hole pairs. As a consequence, the rGO@g-C_3N_4/TNAs photoelectrode exhibited a higher removal rate of TC of ~90% after 120 min. Zhao *et al*.[513] used a photoanode of $BiVO_4$ and a photocathode of Cu_2O/CuO to degrade phenol with instantaneous silver (Ag) recovery. Remarkably, within 4 h, *via* this system, 86.4% removal of phenol (~5 mg L^{-1}) and 100% recovery of Ag (~40 mg L^{-1}) was attained, which was highly efficient than a PFC system without the addition of Ag^+ ions. As a consequence, it has been observed that a high concentration of Ag^+ and low initial pH were favourable for efficient phenol removal.

Recently, as shown in **Figure 45(ii),** Zhang *et al.*[514] prepared Co_2P modified TiO_2 nanotubes arrays to degrade methylene blue. Due to the rapid hole transfer by a co-catalyst of Co_2P from the valence band of TiO_2, the Co_2P/TiO_2, and 1.5 wt.% Co_2P/TiO_2 NTAs revealed a degradation rate of 88.73% within 90 min, which was ~1.3 times higher than pure TiO_2. A netlike 3D Z-scheme photoelectrode has been introduced by Ma *et al.*[515] where g-C_3N_4 nanosheets decorated TiO_2 nanobelt-tubes (TNBTs) were fabricated. The photocatalytic decomposition of TC was investigated under light irradiation. Interestingly, due to stronger visible light absorption and reduced recombination of photogenerated electron-hole pairs, the g-C_3N_4/TNBTs exhibited excellent performance compared to bare TNBTs. Notably, the photocurrent response of g-C_3N_4/TNBTs was ~1.88 times higher than that of TNBTs. The photocatalytic degradation rate of g-C_3N_4/TNBTs for TC was considerably higher than that of TNBTs (0.017 min^{-1} *vs.* 0.007 min^{-1}). Moreover, it has been observed that the radicals of O_2^- and h^+ were the dominant oxidation species during the degradation of TC. Liu *et al.*[516] recognized that the highest TC degradation rate constant of 4.20×10^{-2} min^{-1} by the doping of I and P with TiO_2 (ITP-4 photoelectrode; P was 4 at.%) at pH 11 under visible light.

7.3 Summary and Perspective

Both water splitting and dye degradation efficiency and commercial prospects in photocatalytic reactions are highly dependent upon the properties of the photocatalyst, such as low cost, an appropriate bandgap, high stability, and high production ability. Significantly, compared to conventional bulk materials, 1D, 2D, and 3D nano- and micro-structured metal oxide and metal sulfide-based photocatalysts are extensively used as a result of their distinctive properties for photocatalysis; however, they are restricted due to their wide bandgap in the UV range and reduced diffusion lengths. These restrictions can be removed by doping, forming nanocomposites, co-catalysts decoration, structural modification during fabrication, and providing a protective layer coating to limit corrosion. Binder-free electrodes with these features can fine-tune the bandgap to harvest the complete solar spectrum. However, compared with conventional powder photocatalysts, nano- and micro-structured binder-free electrodes have gained significant attention due to their high catalytic activity, ease of desired structure fabrication/modification, *i.e.*, shape versatility, long-term durability, and low cost. Moreover, catalysts aggregation during photocatalytic testing has been prevented by using a binder-free electrode configuration, which can enhance the photocatalytic water

splitting performance and dye degradation efficiency. Integrated approaches such as PV–PEC, PEC-EC, and PV-EC strategies benefit from the ability to employ commercially accessible PV, laboratory-made EC or PEC electrolyzer units separately; these systems can provide a facile way for bi-functional water splitting. Such PV-PEC modular systems are still limited by the high cost and complexity of the construction of individual units. Nonetheless, it can be expected that 1D, 2D, and 3D nano- and micro-structured binder-free electrodes will soon move from the laboratory scale to the industrial scale for green and clean energy utilization.

8. Overall conclusions

The development of robust 1D, 2D, and 3D nano- and micro-structured binder-free electrodes with designed properties and architectures has led to significant advances in bi-functional electrocatalytic water splitting, Photoelectrochemical (PEC) water splitting, and photocatalysis. In this review, we have highlighted the state-of-the-art of binder-free nano- and micro-structures, from approaches based on rational and well-regulated fabrication to their successful application with regard to the electrocatalytic HER/OER and photocatalysis. Binder-free 1D, 2D, and 3D nano- and micro-structured materials exhibit distinct chemical and physical properties that are considerably different from bulk materials. Through single-step or multi-step fabrication methods, it is possible to achieve precise control over the 1D, 2D, and 3D morphology by control of the synthesis conditions, and the catalytic kinetic parameters can be optimized to enhance the properties of binder-free electrodes. Remarkably, several kinds of nano- and micro-structured materials have been considered in detail for electrocatalytic overall water splitting and enhanced performance; these include MoS_2, NiS_2 Ni_3S_2 pyrite-phase CoS_2, CoTe, NiTe, $FeCo_2S_4$, $NiCo_2S_4$, WN, CoP, FeP, WP_2, Cu_3P, $Co_{0.8}$-$Mn_{0.2}$-P, $Co_{1-x}V_xP$, Co(OH), NiCo(OH), NiMoN, $NiMoO_4$, and $Co_{0.75}Ni_{0.25}Se$ in 1D, 2D, and 3D arrangements. In addition, there are other promising materials such as SnS, Ta_2S, NbS_2, Co(OH), Ni(OH), MnS, Mn(OH), CoN, MoN, and their composites that remain to be fully explored. Moreover, CoMnS, MoWS, NiWS, CoWS, $BiMnO_4$, and their hybrid composites and alloys in binder-free electrode arrangements such as graphene foam (GF), highly oriented pyrolytic graphite (HOPG), Ti foil, stainless steel (SS), anodic aluminum foil (AAO), and indium or fluorine-doped tin oxide (ITO/FTO) are relatively immature in terms of preparation methods and optimizing their electrocatalytic/photocatalytic properties, and are worthy of future investigation. The advancement of 1D, 2D, and 3D nano- and micro-structured binder-free electrodes will

help expand green energy conversion technologies, and further research will create further insights that will benefit academia, industry, and society, as described below.

9 Fundamental Scientific Challenges and Future Perspectives

Recent research has used conductive substrate for in-situ growth of multi-dimensional nano- and micro-structured catalysts, These materials can accelerate facile charge transfer and effective mass diffusion, promote the high utilization of exposed active sites, enhance reaction kinetics, and stability, thus producing efficient catalysts. As a result, several nano- and micro-structured binder-free electrodes have realized high electrocatalytic and photocatalytic activity compared to their bulk counterparts, with some systems performing better than benchmark commercial catalysts. However, several of the reported electrocatalysts show good catalytic activity only at small current densities (from a few tens to a few hundreds of mA cm^{-2} and the yield of H_2 production is approximately of few tens to a few thousands of μL per gram) for a period of few tens of hours. This has yet to meet the requirements of practical industrial electrolyzers, while the industrial use requires several hundreds of current densities (>500 mA cm^{-2}) for thousands of hours. In this regard, the development of 1D, 2D, and 3D nano- and micro-structured binder-free materials for robust electrochemical water splitting reaction urgently requires further breakthroughs, which include **(Scheme 3)**,

(i) Typically, the electrocatalytic and photocatalytic reactions occur on the surface of the electrocatalyst, which is regulated by the optimum surface adsorption, effective charge transfer between interfaces, the intrinsic catalytic activity of the catalyst, its fine-tuned electronic structure, and high utilization of exposed active sites. To improve the water splitting performance, the development of electro- or photo-catalysts with multi-component nano- and micro-hybrid structures has been considered, in which the interface between multi-components in hybrid structures leads to the strong interaction of molecules and the catalyst. However, it is essential to realize new nano- and micro-structured materials using new systems and strategies; this can include using graphene, carbon nanotubes (CNTs), selective doping, reaction temperature control, nano-/micro-structural tuning, composition tuning, defect engineering, and enhanced surface area with meso-/macro-porosity and conductivity. These strategies could promote the exposure of real active sites, chemical/mechanical stability, and improve the kinetics of catalytic reactions, which can improve catalyst performance. Notably, in the 1D system, most studies have focused on arrays of nanowires, nanorods, and

nanotubes. For 2D systems, monolayers and few-layer nanosheets, platelets, and flakes have been considered. For 3D systems, most have focused on hierarchical flower-shaped and 3D branched hierarchical nanoarrays. In addition, the transparent conductive oxides (TCOs), and stainless steels substrates have rarely been used for nanostructure growth, since their flat surfaces reduce the section of appropriate synthesis methods. Thus, careful pre-treatments such as etching to produce a rough surface, and seed layer coating to grow 1D, 2D, and 3D nanostructures can be used. Furthermore, nano- and micro-structures can be modified through post-treatment methods, hydrothermal, and printing techniques. Accordingly, developing additional interesting nano- and micro-structures such as nanobelts, nanoribbons, nanodisks, nanocubes, hollow structures, and core-shell structures s on a suitable conductive substrate would be of interest to enhance water splitting performance. Such future research paths can widen the family of 1D, 2D, and 3D binder-free electrodes for both electrocatalytic and photocatalytic applications.

(ii) During electrocatalytic and photocatalytic testing, nano- and micro-structured materials can exhibit aggregation, dissolution, corrosion, and structural damage; this can be detrimental to the overall performance. Therefore, the use of carbon coating or an active layer of precious metal coating or decorations of nanoparticles or atoms is of interest. This provides opportunities to enhance intrinsic activity and longer-term stability against corrosion and oxidation. To validate the robustness of the catalyst, it is necessary to analyze the structural and chemical stability before and after electrocatalytic or photocatalytic reactions.

(iii) Early high-performance binder-free electrode fabrication methods often involved a limited number of materials, such as nickel foam, copper foam, titanium-foil, stainless steel, and carbon cloth. The choice of a suitable substrate is an important preliminary step in evaluating electrochemically active materials, including electrocatalysts and photoelectrodes. However, compared to these conductive substrates, the growth of 1D, 2D, and 3D nano- and micro-structures that has grown on other conductive substrates are relatively limited. Therefore, the production of 1D, 2D, and 3D electrocatalysts on other conductive substrates such as copper mesh, iron foam, graphene foam, highly oriented pyrolytic graphite (HOPG), aluminum foil, stainless steel, and ITO/FTO are worthy of future study.

(iv) Recent research has focused on the fabrication and modification of grown nanocatalysts, but there is less research on conductive substrates. For example, metal foams such as nickel foam, copper foam, iron foam, and transparent conductive oxides (TCOs) are highly conductive. However, their reduced mechanical strength limits a real long-term application at high current density and under harsh conditions. In addition, during fabrication at high–temperature (>400-500 °C), they can be fragile. Conductive substrates such as carbon cloth, and carbon fibers are alternatives to metal foams and TCOs. However, while they may possess high flexibility, elasticity, and high-temperature stability, their conductivity is lower than metal foams, which may limit their reaction kinetics. To improve the activity, strong affinity, and to remove the residual organic species, a pre-treatment in nitric acid is typically required for as-received commercial carbon cloth. Therefore, more effort should be devoted to optimizing advanced conductive substrates, since they can not only assist in enhancing electrocatalytic activity *via* facile charge transfer but also contributes to robust and long-term stability.

(v) To date, finding an optimal mass loading of active catalytic material grown on Ni foam, Cu foam, stainless steel, carbon cloth, and carbon fiber paper remains a challenge. When the active material loading is high and/or layers are thick, the catalysts can delaminate from the substrate, or dissolve in electrolyte solution during testing. Moreover, if the loading of the active material is small or thin active layers are used, it may possess low catalytic activity. Hence, there is a need to ensure that the active material is in good contact with the conductive substrate when stressed, such as during twisting, bending, and stretching during repeated catalytic processes. Therefore, determining the optimal amount of catalysts is essential for sustained water splitting. A greater understanding of the mechanical stresses in the catalytic coatings and substrates during in-service conditions would be beneficial.

(vi) In addition to high electrocatalytic activity, ex-situ methods have been widely employed to analyze surface/bulk structure, electronic changes, substrate-catalyst relation, interfacial structures, and their real active sites on the binder-free electrodes. Such methods cannot disclose all the necessary characterization information under real working conditions, such as the fundamental mechanism of coupling effects between the components of active materials, the interface

binding force between substrate and electrocatalyst, and the structural and mechanistic elucidation of solid-liquid-gas interfaces. Hence, advanced in-situ operando techniques such as microscopic techniques (in-situ TEM, STEM, and atomic force microscopy), and in-situ spectroscopic methods such as XPS, Raman, Mössbauer, FT-IR, XRD, XANES, should be used to achieve precise real-time observations and fully understand the binder-free electrocatalysis systems. This information can aid in the design of binder-free multidimensional nanocatalysts with high activity, stability, and selectivity expectations.

(vii) From a water-splitting viewpoint, while several binder-free electrodes are suitable for either HER or OER, few exhibit a robust activity in either alkaline or acidic, or neutral conditions. Thus, it is crucial to determine the optimal materials and structures for bi-functional reactions in all pH solutions and challenging conditions. In addition, for commercial-scale H_2 production via water electrolysis, a robust and long-term stability is essential. Currently, the few thousands of hours of durability (without any catalysts degradation) requirements is the main drawback between laboratory-scale into practical use. Thus, understanding the structural, chemical stability, and degradation mechanism in a wide-pH electrolyte is worthy of further investigation.

(viii) Catalytic activity is highly sensitive to the local reaction environment, and it is evaluated by the energy required for adsorption/desorption of reaction intermediates and the formation/rupture of chemical bonds. Hence, theoretical studies on the formation mechanism, interface reaction kinetics, and real catalytic active sites identification and charge density modulations on several 1D, 2D, and 3D structures and their structure-property relationships can be strengthened. There is a need to improve our understanding of the mechanisms of charge carrier's creation for effective bi-functional electrocatalysis and photocatalysis applications. This can build on the significant experimental effort that has been devoted to the controlled synthesis of a range of 1D, 2D, and 3D morphologies on conductive substrates and understanding the formation mechanism for effective electrocatalysis and photocatalysis application.

(ix) Recently, to realize electrocatalytic H_2 production at a large-scale, integrated approach such as photovoltaic-electrochemical (PV–EC) photovoltaic-photoelectrochemical (PV–PEC) and photoelectrochemical-electrochemical (PEC-EC) strategies have been used to combine commercially accessible PV and

lab-scale binder-free nano- and micro-structured electrodes based electrochemical and/or PEC electrolyzer units separately. However, many PV-based modular systems are limited by a low efficiency (< 12%), high cost, and complexity in terms of the construction of individual units. To achieve higher efficiencies, effort should seek to pair nano- and micro-sized materials with 1D, 2D, and 3D structural tuning for the construction of robust bi-functional electrocatalytic water splitting. In addition, fine-tuned appropriate bandgap energy, suitable band-edge positions, and adequate photon harvesting are needed for the design of highly efficient PEC cells.

(x) Due to complicated chemical compositions with abundant unknown ions, molecules, and bacteria/microbes, the direct electrolysis and photocatalysis of seawater are highly challenging. Thus, reported research has often utilized simulated seawater solution with well-defined pH value, concentration, and composition. Achieving a breakthrough in the direct electrolysis of natural seawater is of paramount importance, although it is motivated by the high performance and selectivity of advanced binder-free electrodes, however, major benefits are expected in terms of 1D, 2D, and 3D nanostructure tuning, robust stability and cost-effective. Through the optimization of electron transfer ability from active sites to substrates by means of regulating the interspace between electrocatalyst-substrate and creating conductive networks and integrated electrodes and electrocatalysts, the seawater splitting activity and durability of binder-free electrodes can also be improved.

Finally, many of the binder-free electrodes for bi-functional water splitting applications were proof-of-concept and laboratory scale. There is, therefore, a need to progress scale-up of the manufacture of 1D, 2D, and 3D binder-free electrodes for large-scale commercial applications using high-yield synthesis. Based on this overview, we believe that the engineering of 1D, 2D, and 3D nano- and micro-structured binder-free electrodes, and their hybrids, has opened a new research direction to achieve a fascinating combination of chemical, mechanical and physical properties for a wide range of commercial applications in electrocatalysis, photocatalysis and beyond.

Acknowledgment

This work was financially supported by the National Natural Science Foundation of China (22062005, U20A20128), Natural Science Foundation of Guangxi Province

(2019GXNSFFA245016, 2018GXNSFAA138108), Scientific Research Start-Up Project Program of Guilin University of Technology (RD2000002183), and National Research Foundation of Korea (NRF) grant funded by the Korea government (MSIT) (2020R1A4A4079954).

References

1. Wang, Y.; Wang, S.; Ma, Z.-L.; Yan, L.-T.; Zhao, X.-B.; Xue, Y.-Y.; Huo, J.-M.; Yuan, X.; Li, S.-N.; Zhai, Q.-G., *Advanced Materials* **2022,** *32*, 2107488. DOI https://doi.org/10.1002/adma.202107488.
2. Chandrasekaran, S.; Yao, L.; Deng, L.; Bowen, C.; Zhang, Y.; Chen, S.; Lin, Z.; Peng, F.; Zhang, P., *Chemical Society Reviews* **2019,** *48* (15), 4178-4280.
3. Sun, W.; Wang, F.; Zhang, B.; Zhang, M.; Küpers, V.; Ji, X.; Theile, C.; Bieker, P.; Xu, K.; Wang, C., *Science* **2021,** *371* (6524), 46-51.
4. Li, Q.; Li, H.; Xia, Q.; Hu, Z.; Zhu, Y.; Yan, S.; Ge, C.; Zhang, Q.; Wang, X.; Shang, X., *Nature Materials* **2021,** *20* (1), 76-83.
5. Huang, L.; Zaman, S.; Tian, X.; Wang, Z.; Fang, W.; Xia, B. Y., *Accounts of Chemical Research*, **2021,** 54(2), 311-322.
6. Younis, S. A.; Kwon, E. E.; Qasim, M.; Kim, K.-H.; Kim, T.; Kukkar, D.; Dou, X.; Ali, I., *Progress in Energy and Combustion Science* **2020,** *81*, 100870.
7. Zhu, J.; Roscow, J.; Chandrasekaran, S.; Deng, L.; Zhang, P.; He, T.; Wang, K.; Huang, L., *ChemSusChem* **2020,** *13* (6), 1275-1295.
8. Chandrasekaran, S.; Ma, D.; Ge, Y.; Deng, L.; Bowen, C.; Roscow, J.; Zhang, Y.; Lin, Z.; Misra, R.; Li, J., *Nano Energy* **2020**, 105080.
9. Wang, H.-F.; Chen, L.; Pang, H.; Kaskel, S.; Xu, Q., *Chemical Society Reviews* **2020,** *49* (5), 1414-1448.
10. Khalid, M.; Bhardwaj, P. A.; Honorato, A. M.; Varela, H., *Catalysis Science & Technology* **2020,** *10* (19), 6420-6448.
11. Chen, P.; McCreery, R. L., *Analytical Chemistry* **1996,** *68* (22), 3958-3965.
12. Xu, J.; Chen, Q.; Swain, G. M., *Analytical Chemistry* **1998,** *70* (15), 3146-3154.
13. Li, L.; Bu, L.; Huang, B.; Wang, P.; Shen, C.; Bai, S.; Chan, T.-S.; Shao, Q.; Hu, Z.; Huang, X., *Advanced Materials* **2021,** *33* (51), 2105308. DOI https://doi.org/10.1002/adma.202105308.
14. Song, J.; Huang, Z.-F.; Pan, L.; Li, K.; Zhang, X.; Wang, L.; Zou, J.-J., *Applied Catalysis B: Environmental* **2018,** *227*, 386-408.
15. Koper, M.; Sluyters, J., *Journal of Electroanalytical Chemistry* **1994,** *371* (1-2), 149-159.
16. Karthik, P. E.; Alessandri, I.; Sengeni, A., *Journal of the Electrochemical Society* **2020,** *167* (12), 125503.
17. Fang, Y.-H.; Liu, Z.-P., *ACS Catalysis* **2014,** *4* (12), 4364-4376.
18. Costentin, C.; Savéant, J.-M., *Nature Reviews Chemistry* **2017,** *1* (11), 1-8.
19. Zhu, S.; Ho, S.-H.; Jin, C.; Duan, X.; Wang, S., *Environmental Science: Nano* **2020,** *7* (2), 368-396.
20. Zaera, F., *Chemical Society Reviews* **2013,** *42* (7), 2746-2762.
21. Chen, S.; Cui, S.; Chandrasekaran, S.; Ke, C.; Li, Z.; Chen, P.; Zhang, C.; Jiang, Y., *Electrochimica Acta* **2020,** *341*, 135893.
22. Chen, S.; Chandrasekaran, S.; Cui, S.; Li, Z.; Deng, G.; Deng, L., *Journal of Electroanalytical Chemistry* **2019,** *846*, 113153.

23. Chandrasekaran, S.; Bowen, C.; Zhang, P.; Li, Z.; Yuan, Q.; Ren, X.; Deng, L., *Journal of Materials Chemistry A* **2018,** *6* (24), 11078-11104.
24. Nishimura, S.; Ebitani, K., *ChemCatChem* **2016,** *8* (14), 2303-2316.
25. Chandrasekaran, S.; Kim, E. J.; Chung, J. S.; Bowen, C. R.; Rajagopalan, B.; Adamaki, V.; Misra, R.; Hur, S. H., *Journal of Materials Chemistry A* **2016,** *4* (34), 13271-13279.
26. Chandrasekaran, S.; Hur, S. H., *Materials Research Bulletin* **2019,** *112*, 95-103.
27. Chandrasekaran, S.; Zhang, C.; Shu, Y.; Wang, H.; Chen, S.; Nesakumar Jebakumar Immanuel Edison, T.; Liu, Y.; Karthik, N.; Misra, R. D. K.; Deng, L.; Yin, P.; Ge, Y.; Al-Hartomy, O. A.; Al-Ghamdi, A.; Wageh, S.; Zhang, P.; Bowen, C.; Han, Z., *Coordination Chemistry Reviews* **2021,** *449*, 214209. DOI https://doi.org/10.1016/j.ccr.2021.214209.
28. Jin, T.; Han, Q.; Jiao, L., *Advanced Materials* **2020,** *32* (3), 1806304.
29. Li, Y.; Sun, Y.; Qin, Y.; Zhang, W.; Wang, L.; Luo, M.; Yang, H.; Guo, S., *Advanced Energy Materials* **2020,** *10* (11), 1903120.
30. Du, R.; Jin, X.; Hübner, R.; Fan, X.; Hu, Y.; Eychmüller, A., *Advanced Energy Materials* **2020,** *10* (11), 1901945.
31. Zhu, J.; Hu, L.; Zhao, P.; Lee, L. Y. S.; Wong, K.-Y., *Chemical Reviews* **2019,** *120* (2), 851-918.
32. Tang, C.; Titirici, M.-M.; Zhang, Q., *Journal of Energy Chemistry* **2017,** *26* (6), 1077-1093.
33. Ji, J.; Li, Y.; Peng, W.; Zhang, G.; Zhang, F.; Fan, X., *Advanced Materials* **2015,** *27* (36), 5264-5279.
34. Kumar, R.; Sahoo, S.; Joanni, E.; Singh, R. K.; Tan, W. K.; Kar, K. K.; Matsuda, A., *Progress in Energy and Combustion Science* **2019,** *75*, 100786.
35. Li, J.; Zheng, G., *Advanced Science* **2017,** *4* (3), 1600380.
36. Jin, H.; Joo, J.; Chaudhari, N. K.; Choi, S.-I.; Lee, K., *ChemElectroChem* **2019,** *6* (13), 3244-3253. DOI https://doi.org/10.1002/celc.201900507.
37. Skorokhod, V.; Uvarova, I.; Ragulya, A., *Kyiv: Academperiodica* **2001,** *1*, 180.
38. Pokropivny, V. V.; Skorokhod, V. V., *Materials Science and Engineering: C* **2007,** *27* (5), 990-993. DOI https://doi.org/10.1016/j.msec.2006.09.023.
39. Xia, Y.; Yang, P.; Sun, Y.; Wu, Y.; Mayers, B.; Gates, B.; Yin, Y.; Kim, F.; Yan, H., *Advanced Materials* **2003,** *15* (5), 353-389.
40. Zhang, X.; Jiang, J.; Shen, Z.; Dan, Z.; Li, M.; Lin, Y.; Nan, C. W.; Chen, L.; Shen, Y., *Advanced Materials* **2018,** *30* (16), 1707269.
41. Kruk, S.; Poddubny, A.; Smirnova, D.; Wang, L.; Slobozhanyuk, A.; Shorokhov, A.; Kravchenko, I.; Luther-Davies, B.; Kivshar, Y., *Nature Nanotechnology* **2019,** *14* (2), 126-130.
42. Chu, K.; Liu, F.; Zhu, J.; Fu, H.; Zhu, H.; Zhu, Y.; Zhang, Y.; Lai, F.; Liu, T., *Advanced Energy Materials* **2021,** *11* (11), 2003799. DOI https://doi.org/10.1002/aenm.202003799.
43. Zhu, J.; Xie, M.; Chen, Z.; Lyu, Z.; Chi, M.; Jin, W.; Xia, Y., *Advanced Energy Materials* **2020,** *10* (16), 1904114.
44. Tan, C.; Chen, J.; Wu, X.-J.; Zhang, H., *Nature Reviews Materials* **2018,** *3* (2), 1-13.
45. Cai, J.; Shen, J.; Zhang, X.; Ng, Y. H.; Huang, J.; Guo, W.; Lin, C.; Lai, Y., *Small Methods* **2019,** *3* (1), 1800184.
46. Sun, Y.; Wang, Y.; Chen, J. Y.; Fujisawa, K.; Holder, C. F.; Miller, J. T.; Crespi, V. H.; Terrones, M.; Schaak, R. E., *Nature Chemistry* **2020**, 1-10.

47. Li, L.; Wang, P.; Shao, Q.; Huang, X., *Chemical Society Reviews* **2020,** *49* (10), 3072-3106. DOI 10.1039/D0CS00013B.
48. Khandelwal, M.; Kumar, A., *Journal of Materials Chemistry A* **2015,** *3* (45), 22975-22988. DOI 10.1039/C5TA07603J.
49. Liu, Z.; Yuan, X.; Zhang, S.; Wang, J.; Huang, Q.; Yu, N.; Zhu, Y.; Fu, L.; Wang, F.; Chen, Y.; Wu, Y., *NPG Asia Materials* **2019,** *11* (1), 12. DOI 10.1038/s41427-019-0112-3.
50. Rodwihok, C.; Wongratanaphisan, D.; Thi Ngo, Y. L.; Khandelwal, M.; Hur, S. H.; Chung, J. S., *Nanomaterials (Basel)* **2019,** *9* (10). DOI 10.3390/nano9101441.
51. Ramanathan, S.; Gopinath, S. C. B.; Md. Arshad, M. K.; Poopalan, P., *Biosensors and Bioelectronics* **2019,** *141*, 111434. DOI https://doi.org/10.1016/j.bios.2019.111434.
52. Zhu, J.; Chen, Z.; Xie, M.; Lyu, Z.; Chi, M.; Mavrikakis, M.; Jin, W.; Xia, Y., *Angewandte Chemie International Edition* **2019,** *131* (22), 7322-7326.
53. Zhu, J.; Lyu, Z.; Chen, Z.; Xie, M.; Chi, M.; Jin, W.; Xia, Y., *Chemistry of Materials* **2019,** *31* (15), 5867-5875.
54. Qu, K.; Zheng, Y.; Jiao, Y.; Zhang, X.; Dai, S.; Qiao, S. Z., *Advanced Energy Materials* **2017,** *7* (9), 1602068.
55. Kwon, J.; Han, H.; Choi, S.; Park, K.; Jo, S.; Paik, U.; Song, T., *ChemCatChem* **2019,** *11* (24), 5898-5912. DOI https://doi.org/10.1002/cctc.201901638.
56. Ma, T. Y.; Dai, S.; Qiao, S. Z., *Materials Today* **2016,** *19* (5), 265-273. DOI https://doi.org/10.1016/j.mattod.2015.10.012.
57. Sun, H.; Yan, Z.; Liu, F.; Xu, W.; Cheng, F.; Chen, J., *Advanced Materials* **2020,** *32* (3), 1806326. DOI https://doi.org/10.1002/adma.201806326.
58. Liu, J.; Zhu, D.; Zheng, Y.; Vasileff, A.; Qiao, S.-Z., *ACS Catalysis* **2018,** *8* (7), 6707-6732. DOI 10.1021/acscatal.8b01715.
59. Ferrari, A. C.; Bonaccorso, F.; Fal'ko, V.; Novoselov, K. S.; Roche, S.; Bøggild, P.; Borini, S.; Koppens, F. H. L.; Palermo, V.; Pugno, N.; Garrido, J. A.; Sordan, R.; Bianco, A.; Ballerini, L.; Prato, M.; Lidorikis, E.; Kivioja, J.; Marinelli, C.; Ryhänen, T.; Morpurgo, A.; Coleman, J. N.; Nicolosi, V.; Colombo, L.; Fert, A.; Garcia-Hernandez, M.; Bachtold, A.; Schneider, G. F.; Guinea, F.; Dekker, C.; Barbone, M.; Sun, Z.; Galiotis, C.; Grigorenko, A. N.; Konstantatos, G.; Kis, A.; Katsnelson, M.; Vandersypen, L.; Loiseau, A.; Morandi, V.; Neumaier, D.; Treossi, E.; Pellegrini, V.; Polini, M.; Tredicucci, A.; Williams, G. M.; Hee Hong, B.; Ahn, J.-H.; Min Kim, J.; Zirath, H.; van Wees, B. J.; van der Zant, H.; Occhipinti, L.; Di Matteo, A.; Kinloch, I. A.; Seyller, T.; Quesnel, E.; Feng, X.; Teo, K.; Rupesinghe, N.; Hakonen, P.; Neil, S. R. T.; Tannock, Q.; Löfwander, T.; Kinaret, J., *Nanoscale* **2015,** *7* (11), 4598-4810. DOI 10.1039/C4NR01600A.
60. Khandelwal, M.; Chandrasekaran, S.; Hur, S. H.; Chung, J. S., *Journal of Power Sources* **2018,** *407*, 70-83. DOI https://doi.org/10.1016/j.jpowsour.2018.10.055.
61. Xu, R.; Du, L.; Adekoya, D.; Zhang, G.; Zhang, S.; Sun, S.; Lei, Y., *Advanced Energy Materials* **2020,** *n/a* (n/a), 2001537. DOI https://doi.org/10.1002/aenm.202001537.
62. Joy, J.; Mathew, J.; George, S. C., *International Journal of Hydrogen Energy* **2018,** *43* (10), 4804-4817. DOI https://doi.org/10.1016/j.ijhydene.2018.01.099.
63. Edison, T. N. J. I.; Atchudan, R.; Karthik, N.; Chandrasekaran, S.; Perumal, S.; Raja, P. B.; Perumal, V.; Lee, Y. R., *Fuel* **2021,** *297*, 120786. DOI https://doi.org/10.1016/j.fuel.2021.120786.
64. Yang, H.; Driess, M.; Menezes, P. W., *Advanced Energy Materials* **2021,** *11* (39), 2102074. DOI https://doi.org/10.1002/aenm.202102074.

65. Chandrasekaran, S.; Chung, J. S.; Kim, E. J.; Hur, S. H., *J Electrochem Sci Technol* **2016,** *7* (1), 1-12.
66. Zhu, J.; Xu, L.; Lyu, Z.; Xie, M.; Chen, R.; Jin, W.; Mavrikakis, M.; Xia, Y., *Angewandte Chemie International Edition* **2021,** *60* (18), 10384-10392. DOI https://doi.org/10.1002/anie.202102275.
67. Han, N.; Yang, K. R.; Lu, Z.; Li, Y.; Xu, W.; Gao, T.; Cai, Z.; Zhang, Y.; Batista, V. S.; Liu, W.; Sun, X., *Nature communications* **2018,** *9* (1), 924. DOI 10.1038/s41467-018-03429-z.
68. Wang, J.; Yang, H.; Li, F.; Li, L.; Wu, J.; Liu, S.; Cheng, T.; Xu, Y.; Shao, Q.; Huang, X., *Science Advances* **2022,** *8* (9), eabl9271.
69. Li, H.; Wen, P.; Li, Q.; Dun, C.; Xing, J.; Lu, C.; Adhikari, S.; Jiang, L.; Carroll, D. L.; Geyer, S. M., *Advanced Energy Materials* **2017,** *7* (17), 1700513.
70. Ali Shah, S.; Xu, L.; Sayyar, R.; Bian, T.; Liu, Z.; Yuan, A.; Shen, X.; Khan, I.; Ali Tahir, A.; Ullah, H., *Chemical Engineering Journal* **2022,** *428*, 132126. DOI https://doi.org/10.1016/j.cej.2021.132126.
71. Sun, L.; Luo, Q.; Dai, Z.; Ma, F., *Coordination Chemistry Reviews* **2021,** *444*, 214049. DOI https://doi.org/10.1016/j.ccr.2021.214049.
72. Liu, H.; He, Q.; Jiang, H.; Lin, Y.; Zhang, Y.; Habib, M.; Chen, S.; Song, L., *ACS Nano* **2017,** *11* (11), 11574-11583. DOI 10.1021/acsnano.7b06501.
73. Zhou, G.; Liu, G.; Liu, X.; Yu, Q.; Mao, H.; Xiao, Z.; Wang, L., *Advanced Functional Materials* **2022,** *32* (4), 2107608. DOI https://doi.org/10.1002/adfm.202107608.
74. Wang, M.; Wan, Z.; Meng, X.; Li, Z.; Ding, X.; Li, P.; Li, C.; Wang, J.-G.; Li, Z., *Applied Catalysis B: Environmental* **2022,** *309*, 121272. DOI https://doi.org/10.1016/j.apcatb.2022.121272.
75. Morales-Guio, C. G.; Stern, L.-A.; Hu, X., *Chemical Society Reviews* **2014,** *43* (18), 6555-6569. DOI 10.1039/c3cs60468c.
76. Wang, J.; Zang, N.; Xuan, C.; Jia, B.; Jin, W.; Ma, T., *Advanced Functional Materials* **2021,** *31* (43), 2104620. DOI https://doi.org/10.1002/adfm.202104620.
77. Cheng, N.; Stambula, S.; Wang, D.; Banis, M. N.; Liu, J.; Riese, A.; Xiao, B.; Li, R.; Sham, T.-K.; Liu, L.-M.; Botton, G. A.; Sun, X., *Nature Communications* **2016,** *7* (1), 13638. DOI 10.1038/ncomms13638.
78. Li, X.; Hao, X.; Abudula, A.; Guan, G., *Journal of Materials Chemistry A* **2016,** *4* (31), 11973-12000. DOI 10.1039/C6TA02334G.
79. Xu, Y.; Kraft, M.; Xu, R., *Chemical Society Reviews* **2016,** *45* (11), 3039-3052. DOI 10.1039/C5CS00729A.
80. Chen, S.; Chandrasekaran, S.; Cui, S.; Zhang, X., *Inorganic Chemistry Communications* **2020,** *120*, 108159. DOI https://doi.org/10.1016/j.inoche.2020.108159.
81. Chandrasekaran, S.; Li, N.; Zhuang, Y.; Sui, L.; Xiao, Z.; Fan, D.; Aravindan, V.; Bowen, C.; Lu, H.; Liu, Y., *Chemical Engineering Journal* **2022,** *431*, 134073. DOI https://doi.org/10.1016/j.cej.2021.134073.
82. Xu, Z. J., *Nano-Micro Letters* **2017,** *10* (1), 8. DOI 10.1007/s40820-017-0161-5.
83. Wang, P.; Wang, B., *ChemSusChem* **2020,** *13* (18), 4795-4811. DOI https://doi.org/10.1002/cssc.202001293.
84. Luo, Y.; Zhang, Z.; Chhowalla, M.; Liu, B., *Advanced Materials n/a* (n/a), 2108133. DOI https://doi.org/10.1002/adma.202108133.

85. Auer, A.; Sarabia, F. J.; Winkler, D.; Griesser, C.; Climent, V.; Feliu, J. M.; Kunze-Liebhäuser, J., *ACS Catalysis* **2021,** *11* (16), 10324-10332. DOI 10.1021/acscatal.1c02673.
86. Ledezma-Yanez, I.; Wallace, W. D. Z.; Sebastián-Pascual, P.; Climent, V.; Feliu, J. M.; Koper, M. T. M., *Nature Energy* **2017,** *2* (4), 17031. DOI 10.1038/nenergy.2017.31.
87. Zhu, W.; Zhang, R.; Qu, F.; Asiri, A. M.; Sun, X., *ChemCatChem* **2017,** *9* (10), 1721-1743. DOI https://doi.org/10.1002/cctc.201601607.
88. Chaudhari, N. K.; Jin, H.; Kim, B.; Lee, K., *Nanoscale* **2017,** *9* (34), 12231-12247. DOI 10.1039/C7NR04187J.
89. Yan, X.; Tian, L.; He, M.; Chen, X., *Nano Letters* **2015,** *15* (9), 6015-6021. DOI 10.1021/acs.nanolett.5b02205.
90. Ranaweera, C. K.; Zhang, C.; Bhoyate, S.; Kahol, P. K.; Ghimire, M.; Mishra, S. R.; Perez, F.; Gupta, B. K.; Gupta, R. K., *Materials Chemistry Frontiers* **2017,** *1* (8), 1580-1584. DOI 10.1039/C7QM00108H.
91. Zhang, L.; Liu, B.; Zhang, N.; Ma, M., *Nano Research* **2018,** *11* (1), 323-333. DOI 10.1007/s12274-017-1634-z.
92. Ouyang, C.; Wang, X.; Wang, C.; Zhang, X.; Wu, J.; Ma, Z.; Dou, S.; Wang, S., *Electrochimica Acta* **2015,** *174*, 297-301. DOI https://doi.org/10.1016/j.electacta.2015.05.186.
93. Cheng, N.; Liu, Q.; Asiri, A. M.; Xing, W.; Sun, X., *Journal of Materials Chemistry A* **2015,** *3* (46), 23207-23212. DOI 10.1039/C5TA06788J.
94. Shit, S.; Bolar, S.; Murmu, N. C.; Kuila, T., *ACS Sustainable Chemistry & Engineering* **2019,** *7* (21), 18015-18026. DOI 10.1021/acssuschemeng.9b04882.
95. Wang, S.; Xue, W.; Fang, Y.; Li, Y.; Yan, L.; Wang, W.; Zhao, R., *Journal of Colloid and Interface Science* **2020,** *573*, 150-157. DOI https://doi.org/10.1016/j.jcis.2020.03.098.
96. Chaudhari, N. K.; Oh, A.; Sa, Y. J.; Jin, H.; Baik, H.; Kim, S. G.; Lee, S. J.; Joo, S. H.; Lee, K., *Nano Convergence* **2017,** *4* (1), 7. DOI 10.1186/s40580-017-0101-6.
97. Zhou, H.; Wang, Y.; He, R.; Yu, F.; Sun, J.; Wang, F.; Lan, Y.; Ren, Z.; Chen, S., *Nano Energy* **2016,** *20*, 29-36. DOI https://doi.org/10.1016/j.nanoen.2015.12.008.
98. Xu, R.; Wu, R.; Shi, Y.; Zhang, J.; Zhang, B., *Nano Energy* **2016,** *24*, 103-110. DOI https://doi.org/10.1016/j.nanoen.2016.04.006.
99. Wang, X.; Kolen'ko, Y. V.; Liu, L., *Chemical Communications* **2015,** *51* (31), 6738-6741. DOI 10.1039/C5CC00370A.
100. Cheng, W.; Zhang, H.; Zhao, X.; Su, H.; Tang, F.; Tian, J.; Liu, Q., *Journal of Materials Chemistry A* **2018,** *6* (20), 9420-9427. DOI 10.1039/c8ta01662c.
101. Yang, L.; Guo, Z.; Huang, J.; Xi, Y.; Gao, R.; Su, G.; Wang, W.; Cao, L.; Dong, B., *Advanced Materials* **2017,** *29* (46), 1704574. DOI https://doi.org/10.1002/adma.201704574.
102. Sun, Z.; Yuan, M.; Lin, L.; Yang, H.; Li, H.; Sun, G.; Yang, X.; Ma, S., *Chemical Communications* **2019,** *55* (65), 9729-9732. DOI 10.1039/C9CC03929E.
103. Zhang, B.; Xiao, C.; Xie, S.; Liang, J.; Chen, X.; Tang, Y., *Chemistry of Materials* **2016,** *28* (19), 6934-6941.
104. Jiang, M.; Li, Y.; Lu, Z.; Sun, X.; Duan, X., *Inorganic Chemistry Frontiers* **2016,** *3* (5), 630-634. DOI 10.1039/C5QI00232J.
105. Li, S.; Sirisomboonchai, S.; Yoshida, A.; An, X.; Hao, X.; Abudula, A.; Guan, G., *Journal of Materials Chemistry A* **2018,** *6* (39), 19221-19230. DOI 10.1039/C8TA08223E.

106. Yuan, W.; Zhao, M.; Yuan, J.; Li, C. M., *Journal of Power Sources* **2016,** *319*, 159-167. DOI https://doi.org/10.1016/j.jpowsour.2016.04.044.
107. Lu, Y.; Chen, Y.; Srinivas, K.; Su, Z.; Wang, X.; Wang, B.; Yang, D., *Electrochimica Acta* **2020**, 136338.
108. Feng, L.-L.; Yu, G.; Wu, Y.; Li, G.-D.; Li, H.; Sun, Y.; Asefa, T.; Chen, W.; Zou, X., *Journal of the American Chemical Society* **2015,** *137* (44), 14023-14026. DOI 10.1021/jacs.5b08186.
109. Zhu, W.; Yue, X.; Zhang, W.; Yu, S.; Zhang, Y.; Wang, J.; Wang, J., *Chemical Communications* **2016,** *52* (7), 1486-1489. DOI 10.1039/C5CC08064A.
110. Shang, X.; Li, X.; Hu, W.-H.; Dong, B.; Liu, Y.-R.; Han, G.-Q.; Chai, Y.-M.; Liu, Y.-Q.; Liu, C.-G., *Applied Surface Science* **2016,** *378*, 15-21. DOI https://doi.org/10.1016/j.apsusc.2016.03.197.
111. Du, C.; Men, Y.; Hei, X.; Yu, J.; Cheng, G.; Luo, W., *ChemElectroChem* **2018,** *5* (18), 2564-2570.
112. Yu, H.; Quan, T.; Mei, S.; Kochovski, Z.; Huang, W.; Meng, H.; Lu, Y., *Nano-Micro Letters* **2019,** *11* (1), 41. DOI 10.1007/s40820-019-0269-x.
113. Chen, Q.; Fu, Y.; Jin, J.; Zang, W.; Liu, X.; Zhang, X.; Huang, W.; Kou, Z.; Wang, J.; Zhou, L., *Journal of Energy Chemistry* **2021,** *55*, 10-16.
114. Huang, C.; Zhong, Y.; Chen, J.; Li, J.; Zhang, W.; Zhou, J.; Zhang, Y.; Yu, L.; Yu, Y., *Chemical Engineering Journal* **2021,** *403*, 126304.
115. Liu, L.; Zhang, H.; Mu, Y.; Bai, Y.; Wang, Y., *Journal of Power Sources* **2016,** *327*, 599-609. DOI https://doi.org/10.1016/j.jpowsour.2016.07.104.
116. Liang, C.; Zou, P.; Nairan, A.; Zhang, Y.; Liu, J.; Liu, K.; Hu, S.; Kang, F.; Fan, H. J.; Yang, C., *Energy & Environmental Science* **2020,** *13* (1), 86-95.
117. Jiang, Y.; Lu, Y.; Lin, J.; Wang, X.; Shen, Z., *Small Methods* **2018,** *2* (5), 1700369. DOI https://doi.org/10.1002/smtd.201700369.
118. Du, C.; Shang, M.; Mao, J.; Song, W., *Journal of Materials Chemistry A* **2017,** *5* (30), 15940-15949. DOI 10.1039/C7TA03669H.
119. Xiao, C.; Zhang, B.; Li, D., *Electrochimica Acta* **2017,** *242*, 260-267. DOI https://doi.org/10.1016/j.electacta.2017.05.015.
120. Zhang, J.; Zhang, Z.; Ji, Y.; Yang, J.; Fan, K.; Ma, X.; Wang, C.; Shu, R.; Chen, Y., *Applied Catalysis B: Environmental* **2021,** *282*, 119609.
121. Duan, J.-J.; Zhang, R.-L.; Feng, J.-J.; Zhang, L.; Zhang, Q.-L.; Wang, A.-J., *Journal of Colloid and Interface Science* **2021,** *581*, 774-782.
122. Sirisomboonchai, S.; Li, S.; Yoshida, A.; Kongparakul, S.; Samart, C.; Kansha, Y.; Hao, X.; Abudula, A.; Guan, G., *Catalysis Science & Technology* **2019,** *9* (17), 4651-4658. DOI 10.1039/C9CY00964G.
123. Zhou, J.; Wang, Z.; Yang, D.; Qi, F.; Hao, X.; Zhang, W.; Chen, Y., *Nanoscale* **2020,** *12* (17), 9866-9872.
124. Ma, L.; Hu, Y.; Chen, R.; Zhu, G.; Chen, T.; Lv, H.; Wang, Y.; Liang, J.; Liu, H.; Yan, C.; Zhu, H.; Tie, Z.; Jin, Z.; Liu, J., *Nano Energy* **2016,** *24*, 139-147. DOI https://doi.org/10.1016/j.nanoen.2016.04.024.
125. Hu, J.; Ou, Y.; Li, Y.; Gao, D.; Zhang, Y.; Xiao, P., *ACS Sustainable Chemistry & Engineering* **2018,** *6* (9), 11724-11733. DOI 10.1021/acssuschemeng.8b01978.
126. Liu, S.; Jiang, Y.; Yang, M.; Zhang, M.; Guo, Q.; Shen, W.; He, R.; Li, M., *Nanoscale* **2019,** *11* (16), 7959-7966.
127. Yu, J.; Cheng, G.; Luo, W., *Nano Research* **2018,** *11* (4), 2149-2158. DOI 10.1007/s12274-017-1832-8.
128. Li, J.; Wei, G.; Zhu, Y.; Xi, Y.; Pan, X.; Ji, Y.; Zatovsky, I. V.; Han, W., *Journal of Materials Chemistry A* **2017,** *5* (28), 14828-14837. DOI 10.1039/C7TA03947F.

129. Li, W.; Gao, X.; Wang, X.; Xiong, D.; Huang, P.-P.; Song, W.-G.; Bao, X.; Liu, L., *Journal of Power Sources* **2016,** *330*, 156-166. DOI https://doi.org/10.1016/j.jpowsour.2016.08.126.
130. Yu, J.; Cheng, G.; Luo, W., *Journal of Materials Chemistry A* **2017,** *5* (22), 11229-11235. DOI 10.1039/C7TA02968C.
131. Sial, M. A. Z. G.; Lin, H.; Wang, X., *Nanoscale* **2018,** *10* (27), 12975-12980. DOI 10.1039/C8NR03350A.
132. Wang, Y.; Sun, Y.; Yan, F.; Zhu, C.; Gao, P.; Zhang, X.; Chen, Y., *Journal of Materials Chemistry A* **2018,** *6* (18), 8479-8487. DOI 10.1039/C8TA00517F.
133. Li, G.; Wu, X.; Guo, H.; Guo, Y.; Chen, H.; Wu, Y.; Zheng, J.; Li, X., *ACS Applied Materials & Interfaces* **2020,** *12* (5), 5951-5957.
134. Du, X.; Che, P.; Wang, Y.; Yuan, C.; Zhang, X., *International Journal of Hydrogen Energy* **2019,** *44* (41), 22955-22961.
135. Xing-Xing, M.; Li, C.; ZHANG, Z.; Ji-Lin, T., *Chinese Journal of Analytical Chemistry* **2020,** *48* (1), e20001-e20012.
136. Zhang, H.; Min, S.; Wang, F.; Zhang, Z., *International Journal of Hydrogen Energy* **2020,** *45* (4), 2808-2817.
137. Tian, J.; Liu, Q.; Cheng, N.; Asiri, A. M.; Sun, X., *Angewandte Chemie International Edition* **2014,** *53* (36), 9577-81. DOI 10.1002/anie.201403842.
138. Hou, C.-C.; Chen, Q.-Q.; Wang, C.-J.; Liang, F.; Lin, Z.; Fu, W.-F.; Chen, Y., *ACS Applied Materials & Interfaces* **2016,** *8* (35), 23037-23048. DOI 10.1021/acsami.6b06251.
139. Doan, T. L. L.; Tran, D. T.; Nguyen, D. C.; Le, H. T.; Kim, N. H.; Lee, J. H., *Applied Catalysis B: Environmental* **2020,** *261*, 118268.
140. Guan, C.; Liu, X.; Elshahawy, A. M.; Zhang, H.; Wu, H.; Pennycook, S. J.; Wang, J., *Nanoscale Horizons* **2017,** *2* (6), 342-348.
141. Shi, J.; Hu, J.; Luo, Y.; Sun, X.; Asiri, A. M., *Catalysis Science & Technology* **2015,** *5* (11), 4954-4958. DOI 10.1039/C5CY01121C.
142. Wu, X.; Lee, H.; Liu, H.; Lu, L.; Wu, X.; Sun, L., *International Journal of Hydrogen Energy* **2020,** *45* (41), 21354-21363.
143. Gao, D.; Liu, R.; Biskupek, J.; Kaiser, U.; Song, Y.-F.; Streb, C., *Angewandte Chemie International Edition* **2019,** *58* (14), 4644-4648. DOI https://doi.org/10.1002/anie.201900428.
144. Ma, X.; Chang, Y.; Zhang, Z.; Tang, J., *Journal of Materials Chemistry A* **2018,** *6* (5), 2100-2106. DOI 10.1039/C7TA09619D.
145. Shi, H.; Zhou, Y.-T.; Yao, R.-Q.; Wan, W.-B.; Ge, X.; Zhang, W.; Wen, Z.; Lang, X.-Y.; Zheng, W.-T.; Jiang, Q., *Nature Communications* **2020,** *11* (1), 2940. DOI 10.1038/s41467-020-16769-6.
146. Fan, M.; Gao, R.; Zou, Y.-C.; Wang, D.; Bai, N.; Li, G.-D.; Zou, X., *Electrochimica Acta* **2016,** *215*, 366-373. DOI https://doi.org/10.1016/j.electacta.2016.08.129.
147. Lu, C.; Wang, J.; Czioska, S.; Dong, H.; Chen, Z., *The Journal of Physical Chemistry C* **2017,** *121* (46), 25875-25881. DOI 10.1021/acs.jpcc.7b08365.
148. Huan, T. N.; Rousse, G.; Zanna, S.; Lucas, I. T.; Xu, X.; Menguy, N.; Mougel, V.; Fontecave, M., *Angewandte Chemie International Edition* **2017,** *56* (17), 4792-4796. DOI https://doi.org/10.1002/anie.201700388.
149. Zhou, X.; Qi, W.; Yin, K.; Zhang, N.; Gong, S.; Li, Z.; Li, Y., *Frontiers in Chemistry* **2020,** *7*, 900.
150. Todoroki, N.; Wadayama, T., *ACS Appl Mater Interfaces* **2019,** *11* (47), 44161-44169. DOI 10.1021/acsami.9b14213.

151. Chen, J. S.; Ren, J.; Shalom, M.; Fellinger, T.; Antonietti, M., *ACS Applied Materials & Interfaces* **2016,** *8* (8), 5509-5516.
152. Barauskienė, I.; Valatka, E., *Electrocatalysis* **2019,** *10* (1), 63-71. DOI 10.1007/s12678-018-0495-x.
153. Jadhav, H. S.; Roy, A.; Thorat, G. M.; Chung, W.-J.; Seo, J. G., *Journal of Industrial and Engineering Chemistry* **2019,** *71*, 452-459. DOI https://doi.org/10.1016/j.jiec.2018.12.002.
154. Zhang, H.; de Souza e Silva, J. M.; Lu, X.; de Oliveira, C. S.; Cui, B.; Li, X.; Lin, C.; Schweizer, S. L.; Maijenburg, A. W.; Bron, M.; Wehrspohn, R. B., *Advanced Materials Interfaces* **2019,** *6* (18), 1900774. DOI https://doi.org/10.1002/admi.201900774.
155. Yao, M.; Hu, H.; Wang, N.; Hu, W.; Komarneni, S., *Journal of Colloid and Interface Science* **2020,** *561*, 576-584. DOI https://doi.org/10.1016/j.jcis.2019.11.032.
156. Song, S.; Yu, L.; Xiao, X.; Qin, Z.; Zhang, W.; Wang, D.; Bao, J.; Zhou, H.; Zhang, Q.; Chen, S., *Materials Today Physics* **2020**, 100216.
157. Schäfer, H.; Chevrier, D. M.; Zhang, P.; Stangl, J.; Müller-Buschbaum, K.; Hardege, J. D.; Kuepper, K.; Wollschläger, J.; Krupp, U.; Dühnen, S.; Steinhart, M.; Walder, L.; Sadaf, S.; Schmidt, M., *Advanced Functional Materials* **2016,** *26* (35), 6402-6417. DOI https://doi.org/10.1002/adfm.201601581.
158. Anantharaj, S.; Venkatesh, M.; Salunke, A. S.; Simha, T. V. S. V.; Prabu, V.; Kundu, S., *ACS Sustainable Chemistry & Engineering* **2017,** *5* (11), 10072-10083. DOI 10.1021/acssuschemeng.7b02090.
159. Anantharaj, S.; Chatterjee, S.; Swaathini, K. C.; Amarnath, T. S.; Subhashini, E.; Pattanayak, D. K.; Kundu, S., *ACS Sustainable Chemistry & Engineering* **2018,** *6* (2), 2498-2509. DOI 10.1021/acssuschemeng.7b03964.
160. Liu, X.; You, B.; Sun, Y., *ACS Sustainable Chemistry & Engineering* **2017,** *5* (6), 4778-4784. DOI 10.1021/acssuschemeng.7b00182.
161. Huang, X.; Chang, S.; Lee, W. S. V.; Ding, J.; Xue, J. M., *Journal of Materials Chemistry A* **2017,** *5* (34), 18176-18182. DOI 10.1039/C7TA03023A.
162. Zhao, H.; Zhu, Y.-P.; Yuan, Z.-Y., *European Journal of Inorganic Chemistry* **2016,** *2016* (13-14), 1916-1923. DOI https://doi.org/10.1002/ejic.201501181.
163. Hou, C. C.; Fu, W. F.; Chen, Y., *ChemSusChem* **2016,** *9* (16), 2069-73. DOI 10.1002/cssc.201600592.
164. Arshad, F.; Munir, A.; Kashif, Q. Q.; Haq, T. u.; Iqbal, J.; Sher, F.; Hussain, I., *International Journal of Hydrogen Energy* **2020,** *45* (33), 16583-16590. DOI https://doi.org/10.1016/j.ijhydene.2020.04.152.
165. Wang, T.; Zhang, X.; Zhu, X.; Liu, Q.; Lu, S.; Asiri, A. M.; Luo, Y.; Sun, X., *Nanoscale* **2020,** *12* (9), 5359-5362.
166. Wei, X.; Chen, W.; Liu, N.; Fan, H., *Journal of Alloys and Compounds* **2020,** *830*, 154708. DOI https://doi.org/10.1016/j.jallcom.2020.154708.
167. Rodney, J. D.; Deepapriya, S.; Robinson, M. C.; Raj, C. J.; Perumal, S.; Kim, B. C.; Das, S. J., *International Journal of Hydrogen Energy* **2020,** *45* (46), 24684-24696.
168. Riyajuddin, S.; Tarik Aziz, S.; Kumar, S.; Nessim, G. D.; Ghosh, K., *ChemCatChem* **2020,** 12, 1394.
169. Pu, Z.; Luo, Y.; Asiri, A. M.; Sun, X., *ACS Applied Materials & Interfaces* **2016,** *8* (7), 4718-4723. DOI 10.1021/acsami.5b12143.
170. Liu, T.; Asiri, A. M.; Sun, X., *Nanoscale* **2016,** *8* (7), 3911-5. DOI 10.1039/c5nr07170d.
171. Liang, Y.; Liu, Q.; Luo, Y.; Sun, X.; He, Y.; Asiri, A. M., *Electrochimica Acta* **2016,** *190*, 360-364. DOI https://doi.org/10.1016/j.electacta.2015.12.153.

172. Liu, X.; Xi, W.; Li, C.; Li, X.; Shi, J.; Shen, Y.; He, J.; Zhang, L.; Xie, L.; Sun, X.; Wang, P.; Luo, J.; Liu, L.-M.; Ding, Y., *Nano Energy* **2018,** *44*, 371-377. DOI https://doi.org/10.1016/j.nanoen.2017.12.016.
173. Luo, S.; Lin, X.; Xu, L.; Guo, H.; Lai, J.; Wu, J.; Feng, Y.; Ma, L., *Colloids and Surfaces A: Physicochemical and Engineering Aspects* **2020,** *586*, 124186.
174. Gao, J. J.; Luo, P.; Qiu, H. J.; Wang, Y., *Nanotechnology* **2017,** *28* (10), 105705. DOI 10.1088/1361-6528/aa52d3.
175. Lu, W.; Liu, T.; Xie, L.; Tang, C.; Liu, D.; Hao, S.; Qu, F.; Du, G.; Ma, Y.; Asiri, A. M.; Sun, X., *Small* **2017,** *13* (32), 1700805. DOI https://doi.org/10.1002/smll.201700805.
176. Hong, W.; Jian, C.; Wang, G.; He, X.; Li, J.; Cai, Q.; Wen, Z.; Liu, W., *Applied Catalysis B: Environmental* **2019,** *251*, 213-219. DOI https://doi.org/10.1016/j.apcatb.2019.03.070.
177. Wang, Y.; Wang, J.; Xie, T.; Zhu, Q.; Zeng, D.; Li, R.; Zhang, X.; Liu, S., *Applied Surface Science* **2019,** *485*, 506-512. DOI https://doi.org/10.1016/j.apsusc.2019.04.240.
178. Dong, Z.; Ding, D.; Li, T.; Ning, C., *Applied Surface Science* **2018,** *443*, 321-328.
179. Su, S.; Zhou, Q.; Zeng, Z.; Hu, D.; Wang, X.; Jin, M.; Gao, X.; Nötzel, R.; Zhou, G.; Zhang, Z.; Liu, J., *ACS Applied Materials & Interfaces* **2018,** *10* (9), 8026-8035. DOI 10.1021/acsami.7b19197.
180. Yang, Y.; Zhou, K.; Ma, L.; Liang, Y.; Yang, X.; Cui, Z.; Zhu, S.; Li, Z., *Applied Surface Science* **2018,** *434*, 871-878. DOI https://doi.org/10.1016/j.apsusc.2017.10.049.
181. Wang, F.; Yu, Y.; Yin, X.; Tian, P.; Wang, X., *Journal of Materials Chemistry A* **2017,** *5* (19), 9060-9066. DOI 10.1039/C7TA01857F.
182. Ho, T. A.; Bae, C.; Nam, H.; Kim, E.; Lee, S. Y.; Park, J. H.; Shin, H., *ACS Applied Materials & Interfaces* **2018,** *10* (15), 12807-12815. DOI 10.1021/acsami.8b00813.
183. Cozzarini, L.; Bertolini, G.; Šuran-Brunelli, S. T.; Radivo, A.; Bracamonte, M. V.; Tavagnacco, C.; Goldoni, A., *International Journal of Hydrogen Energy* **2017,** *42* (30), 18763-18773. DOI https://doi.org/10.1016/j.ijhydene.2017.06.101.
184. Behranginia, A.; Asadi, M.; Liu, C.; Yasaei, P.; Kumar, B.; Phillips, P.; Foroozan, T.; Waranius, J. C.; Kim, K.; Abiade, J.; Klie, R. F.; Curtiss, L. A.; Salehi-Khojin, A., *Chemistry of Materials* **2016,** *28* (2), 549-555. DOI 10.1021/acs.chemmater.5b03997.
185. Zhu, Y.-P.; Ran, J.; Qiao, S.-Z., *ACS Applied Materials & Interfaces* **2017,** *9* (48), 41980-41987. DOI 10.1021/acsami.7b13836.
186. Liang, H.; Jiang, D.; Wei, S.; Cao, X.; Chen, T.; Huo, B.; Peng, Z.; Li, C.; Liu, J., *Journal of Materials Chemistry A* **2018,** *6* (33), 16235-16245.
187. Jian, X.; Li, S.; Liu, J.; Zhou, C.; Guo, S.; Zhang, P.; Yang, Y.; Chen, L., *ChemElectroChem* **2019,** *6* (21), 5407-5412. DOI https://doi.org/10.1002/celc.201901420.
188. Mai, N. T. L.; Bach, L. G.; Nhac-Vu, H. T.; Bui, Q. B., *Solid State Sciences* **2020,** *101*, 106143. DOI https://doi.org/10.1016/j.solidstatesciences.2020.106143.
189. Chen, L.; Zang, J.; Liu, X.; Zhang, Y.; Jia, S.; Tian, P.; Wang, Y., *Electrochimica Acta* **2018,** *281*, 386-393. DOI https://doi.org/10.1016/j.electacta.2018.05.193.
190. Chhetri, M.; Sultan, S.; Rao, C. N. R., *Proceedings of the National Academy of Sciences* **2017,** *114* (34), 8986. DOI 10.1073/pnas.1710443114.

191. Ye, Y.-J.; Zhang, N.; Liu, X.-X., *Journal of Materials Chemistry A* **2017,** *5* (46), 24208-24216. DOI 10.1039/C7TA06906E.
192. Sun, Z.; Yang, M.; Wang, Y.; Hu, Y. H., *ACS Applied Energy Materials* **2019,** *2* (2), 1102-1110.
193. Grigoriev, S. N.; Fominski, V. Y.; Nevolin, V. N.; Romanov, R. I.; Volosova, M. A.; Irzhak, A. V., *Inorganic Materials: Applied Research* **2016,** *7* (2), 285-291. DOI 10.1134/S2075113316020118.
194. Guo, X.; Duan, X.; Ji, J.; Fan, X.; Li, Y.; Zhang, F.; Zhang, G.; Zhu, Y.-A.; Peng, W.; Wang, S., *Journal of Colloid and Interface Science* **2021,** *583*, 139-148.
195. Kim, Y.; Hong, M.; Oh, H.; Kim, Y.; Suyama, H.; Nakanishi, S.; Byon, H. R., *The Journal of Physical Chemistry C* **2020,** *124* (37), 20135-20142.
196. Wang, K.; Chen, H.; Hua, Y.; Tong, Y.; Wang, Y.; Song, S., *Materials Today Energy* **2018,** *10*, 343-351. DOI https://doi.org/10.1016/j.mtener.2018.09.003.
197. Xia, L.; Song, H.; Li, X.; Zhang, X.; Gao, B.; Zheng, Y.; Huo, K.; Chu, P. K., *Frontiers in Chemistry* **2020,** *8*, 382.
198. Zhang, C.; Pu, Z.; Amiinu, I. S.; Zhao, Y.; Zhu, J.; Tang, Y.; Mu, S., *Nanoscale* **2018,** *10* (6), 2902-2907. DOI 10.1039/c7nr08148k.
199. Wang, Y.; Ni, Y.; Liu, B.; Shang, S.; Yang, S.; Cao, M.; Hu, C., *Electrochimica Acta* **2017,** *257*, 356-363. DOI https://doi.org/10.1016/j.electacta.2017.10.011.
200. Wang, M.; Fu, W.; Du, L.; Wei, Y.; Rao, P.; Wei, L.; Zhao, X.; Wang, Y.; Sun, S., *Applied Surface Science* **2020,** *515*, 146059. DOI https://doi.org/10.1016/j.apsusc.2020.146059.
201. Liu, Y.; Bai, Y.; Han, Y.; Yu, Z.; Zhang, S.; Wang, G.; Wei, J.; Wu, Q.; Sun, K., *ACS Applied Materials & Interfaces* **2017,** *9* (42), 36917-36926. DOI 10.1021/acsami.7b12474.
202. Liu, Y.; Ren, L.; Zhang, Z.; Qi, X.; Li, H.; Zhong, J., *Scientific Reports* **2016,** *6* (1), 22516. DOI 10.1038/srep22516.
203. Pu, Z.; Xue, Y.; Li, W.; Amiinu, I. S.; Mu, S., *New Journal of Chemistry* **2017,** *41* (5), 2154-2159. DOI 10.1039/c6nj03194c.
204. Ren, X.; Wu, D.; Ge, R.; Sun, X.; Ma, H.; Yan, T.; Zhang, Y.; Du, B.; Wei, Q.; Chen, L., *Nano Research* **2018,** *11* (4), 2024-2033. DOI 10.1007/s12274-017-1818-6.
205. Li, J.; Xia, Z.; Zhou, X.; Qin, Y.; Ma, Y.; Qu, Y., *Nano Research* **2017,** *10* (3), 814-825. DOI 10.1007/s12274-016-1335-z.
206. Surendran, S.; Selvan, R. K., *Advanced Materials Interfaces* **2018,** *5* (4), 1701056. DOI https://doi.org/10.1002/admi.201701056.
207. Liu, Z.; Tan, H.; Xin, J.; Duan, J.; Su, X.; Hao, P.; Xie, J.; Zhan, J.; Zhang, J.; Wang, J.-J.; Liu, H., *ACS Applied Materials & Interfaces* **2018,** *10* (4), 3699-3706. DOI 10.1021/acsami.7b18671.
208. Oh, I.; Youn, J.-S.; Park, Y.-K.; Jeon, K.-J., *Applied Surface Science* **2020,** *529*, 147089. DOI https://doi.org/10.1016/j.apsusc.2020.147089.
209. Hao, W.; Huang, H.; Chen, Z.; Wang, L.; Ma, X.; Huang, M.; Ou, X.; Guo, Y., *Electrochimica Acta* **2020,** *354*, 136645. DOI https://doi.org/10.1016/j.electacta.2020.136645.
210. Zhang, Y.; Qiu, Y.; Ji, X.; Ma, T.; Ma, Z.; Hu, P. A., *ChemSusChem* **2019,** *12* (16), 3792-3800. DOI https://doi.org/10.1002/cssc.201901628.
211. Hu, X.; Wang, R.; Sun, P.; Xiang, Z.; Wang, X., *ACS Sustainable Chemistry & Engineering* **2019,** *7* (24), 19426-19433.
212. Yu, C.; Liu, Z.; Han, X.; Huang, H.; Zhao, C.; Yang, J.; Qiu, J., *Carbon* **2016,** *110*, 1-7. DOI https://doi.org/10.1016/j.carbon.2016.08.020.

213. Huang, H.; Yu, C.; Han, X.; Li, S.; Cui, S.; Zhao, C.; Huang, H.; Qiu, J., *Industrial & Engineering Chemistry Research* **2017,** *56* (48), 14245-14251. DOI 10.1021/acs.iecr.7b03351.
214. Zhu, W.; Chen, R.; Yin, Y.; Zhang, J.; Wang, Q., *ChemistrySelect* **2018,** *3* (14), 3970-3974. DOI https://doi.org/10.1002/slct.201800247.
215. Guo, Y.; Guo, D.; Ye, F.; Wang, K.; Shi, Z.; Chen, X.; Zhao, C., *ACS Sustainable Chemistry & Engineering* **2018,** *6* (9), 11884-11891. DOI 10.1021/acssuschemeng.8b02164.
216. Liu, Y.; Wang, B.; Sun, Q.; Pan, Q.; Zhao, N.; Li, Z.; Yang, Y.; Sun, X., *ACS Applied Materials & Interfaces* **2020,** *12* (14), 16512-16520. DOI 10.1021/acsami.0c01603.
217. Wu, X.; Han, X.; Ma, X.; Zhang, W.; Deng, Y.; Zhong, C.; Hu, W., *ACS Applied Materials & Interfaces* **2017,** *9* (14), 12574-12583. DOI 10.1021/acsami.6b16602.
218. Wang, J.; He, Y.; Yang, Q.; Li, H.; Xie, Z.; Fan, Y.; Chen, J., *International Journal of Hydrogen Energy* **2019,** *44* (26), 13205-13213.
219. Zhou, Y.; Xiao, H.; Zhang, S.; Li, Y.; Wang, S.; Wang, Z.; An, C.; Zhang, J., *Electrochimica Acta* **2017,** *241*, 106-115. DOI https://doi.org/10.1016/j.electacta.2017.04.084.
220. Xie, Z.; Tang, H.; Wang, Y., *ChemElectroChem* **2019,** *6* (4), 1206-1212. DOI https://doi.org/10.1002/celc.201801106.
221. Zhai, L.; Mak, C. H.; Qian, J.; Lin, S.; Lau, S. P., *Electrochimica Acta* **2019,** *305*, 37-46. DOI https://doi.org/10.1016/j.electacta.2019.03.031.
222. Hu, Z.; Huang, J.; Luo, Y.; Liu, M.; Li, X.; Yan, M.; Ye, Z.; Chen, Z.; Feng, Z.; Huang, S., *Electrochimica Acta* **2019,** *319*, 293-301. DOI https://doi.org/10.1016/j.electacta.2019.06.178.
223. Ye, Z.; Li, T.; Ma, G.; Dong, Y.; Zhou, X., *Advanced Functional Materials* **2017,** *27* (44), 1704083. DOI https://doi.org/10.1002/adfm.201704083.
224. Yu, S. H.; Chua, D. H. C., *ACS Applied Materials & Interfaces* **2018,** *10* (17), 14777-14785. DOI 10.1021/acsami.8b02755.
225. Patel, M.; Ali, M.; Ahmad, J.; Dar, M.; Majid, K.; Lone, S.; Puthusseri, D.; Wahid, M., *Materials Letters* **2020,** *278*, 128456. DOI https://doi.org/10.1016/j.matlet.2020.128456.
226. Cheng, Y.; Guo, Y.; Zhang, N.; Tao, S.; Liao, Z.; Wang, Y.; Xiang, Z., *Nano Energy* **2019,** *63*, 103897. DOI https://doi.org/10.1016/j.nanoen.2019.103897.
227. Tian, J.; Jiang, F.; Yuan, D.; Zhang, L.; Chen, Q.; Hong, M., *Angewandte Chemie International Edition* **2020,** *59* (31), 13101-13108. DOI https://doi.org/10.1002/anie.202004420.
228. Chen, J.; Wang, J.; Chen, J.; Wang, L., *Journal of Materials Science* **2017,** *52* (22), 13064-13077. DOI 10.1007/s10853-017-1410-1.
229. Wan, M.; Li, J.; Li, T.; Zhu, H.; Wu, W.; Du, M., *Nanotechnology* **2018,** *29* (38), 385602. DOI 10.1088/1361-6528/aacfd7.
230. Gnanasekar, P.; Ranjith, K. S.; Manivel, P.; Han, Y.-K.; Kulandaivel, J., *ACS Applied Energy Materials* **2020,** *3* (7), 6717-6725. DOI 10.1021/acsaem.0c00856.
231. Chen, J.; Yu, D.; Liao, W.; Zheng, M.; Xiao, L.; Zhu, H.; Zhang, M.; Du, M.; Yao, J., *ACS Applied Materials & Interfaces* **2016,** *8* (28), 18132-18139. DOI 10.1021/acsami.6b05245.
232. Gu, H.; Fan, W.; Liu, T., *Nanoscale Horizons* **2017,** *2* (5), 277-283. DOI 10.1039/C7NH00066A.
233. Ji, D.; Peng, S.; Fan, L.; Li, L.; Qin, X.; Ramakrishna, S., *Journal of Materials Chemistry A* **2017,** *5* (45), 23898-23908. DOI 10.1039/c7ta08166a.

234. Zhang, Y.; Xia, X.; Cao, X.; Zhang, B.; Tiep, N. H.; He, H.; Chen, S.; Huang, Y.; Fan, H. J., *Advanced Energy Materials* **2017,** *7* (15), 1700220. DOI https://doi.org/10.1002/aenm.201700220.
235. Zhao, S.; Rasimick, B.; Mustain, W.; Xu, H., *Applied Catalysis B: Environmental* **2017,** *203*, 138-145. DOI https://doi.org/10.1016/j.apcatb.2016.09.048.
236. Wang, F.-f.; Xu, L.; Wang, P.; Zhang, Y., *Electrochimica Acta* **2019,** *306*, 437-445. DOI https://doi.org/10.1016/j.electacta.2019.03.091.
237. Kong, D.; Wang, Y.; Huang, S.; Lim, Y. V.; Wang, M.; Xu, T.; Zang, J.; Li, X.; Yang, H. Y., *Journal of Colloid and Interface Science* **2022,** *607*, 1876-1887. DOI https://doi.org/10.1016/j.jcis.2021.10.020.
238. Song, J.; Wei, C.; Huang, Z.-F.; Liu, C.; Zeng, L.; Wang, X.; Xu, Z. J., *Chemical Society Reviews* **2020,** *49* (7), 2196-2214. DOI 10.1039/C9CS00607A.
239. Demuru, S.; Nela, L.; Marchack, N.; Holmes, S. J.; Farmer, D. B.; Tulevski, G. S.; Lin, Q.; Deligianni, H., *ACS sensors* **2018,** *3* (4), 799-805.
240. Salimi, A.; Hallaj, R.; Soltanian, S., *Electroanalysis: An International Journal Devoted to Fundamental and Practical Aspects of Electroanalysis* **2009,** *21* (24), 2693-2700.
241. Shu, H.; Cao, L.; Chang, G.; He, H.; Zhang, Y.; He, Y., *Electrochimica Acta* **2014,** *132*, 524-532.
242. Sakita, A. M.; Della Noce, R.; Vallés, E.; Benedetti, A. V., *Applied Surface Science* **2018,** *434*, 1153-1160.
243. Hasan, M. M.; Rakib, R. H.; Hasnat, M. A.; Nagao, Y., *ACS Applied Energy Materials* **2020,** *3* (3), 2907-2915.
244. Shervedani, R. K.; Amini, A.; Sedeh, N. M., *International Journal of Hydrogen Energy* **2016,** *41* (31), 13459-13468.
245. Noorbakhsh, A.; Mirkalaei, M. M.; Yousefi, M. H.; Manochehri, S., *Electroanalysis* **2014,** *26* (12), 2716-2726.
246. Zhao, S.; Wangstrom, A. E.; Liu, Y.; Rigdon, W. A.; Mustain, W. E., *Electrochimica Acta* **2015,** *157*, 175-182. DOI https://doi.org/10.1016/j.electacta.2015.01.030.
247. Ting, C.-C.; Chao, C.-H.; Tsai, C. Y.; Cheng, I. K.; Pan, F.-M., *Applied Surface Science* **2017,** *416*, 365-370. DOI https://doi.org/10.1016/j.apsusc.2017.04.156.
248. Li, S.; Chen, H.; Liu, J.; Deng, Y.; Han, X.; Hu, W.; Zhong, C., *ACS Applied Materials & Interfaces* **2017,** *9* (33), 27765-27772. DOI 10.1021/acsami.7b08604.
249. Na, H.; Choi, H.; Oh, J.-W.; Jung, Y. S.; Cho, Y. S., *ACS Applied Materials & Interfaces* **2019,** *11* (28), 25179-25185. DOI 10.1021/acsami.9b06159.
250. Lebedev, D.; Copéret, C., *ACS Applied Energy Materials* **2019,** *2* (1), 196-200. DOI 10.1021/acsaem.8b01724.
251. Kölbach, M.; Fiechter, S.; van de Krol, R.; Bogdanoff, P., *Catalysis Today* **2017,** *290*, 2-9. DOI https://doi.org/10.1016/j.cattod.2017.03.030.
252. Menezes, P. W.; Panda, C.; Loos, S.; Bunschei-Bruns, F.; Walter, C.; Schwarze, M.; Deng, X.; Dau, H.; Driess, M., *Energy & Environmental Science* **2018,** *11* (5), 1287-1298. DOI 10.1039/C7EE03619A.
253. Jeong, J.-H.; Kunwar, S.; Pandit, S.; Lee, J., *ACS Applied Nano Materials* **2020,** *3* (7), 6507-6515. DOI 10.1021/acsanm.0c00983.
254. Tahira, A.; Ibupoto, Z. H.; Vagin, M.; Aftab, U.; Abro, M. I.; Willander, M.; Nur, O., *Catalysis Science & Technology* **2019,** *9* (11), 2879-2887. DOI 10.1039/C9CY00351G.
255. Li, Y.; Dong, Z.; Jiao, L., *Advanced Energy Materials* **2020,** *10* (11), 1902104.

256. Li, Y.; Li, R.; Wang, D.; Xu, H.; Meng, F.; Dong, D.; Jiang, J.; Zhang, J.; An, M.; Yang, P., *International Journal of Hydrogen Energy* **2020,** 46(7), 5131-5149.
257. Xue, Z.; Li, X.; Liu, Q.; Cai, M.; Liu, K.; Liu, M.; Ke, Z.; Liu, X.; Li, G., *Advanced Materials* **2019,** *31* (21), 1900430.
258. Xu, Q.; Jiang, H.; Zhang, H.; Hu, Y.; Li, C., *Applied Catalysis B: Environmental* **2019,** *242*, 60-66.
259. Jia, Y.; Jiang, K.; Wang, H.; Yao, X., *Chem* **2019,** *5* (6), 1371-1397. DOI https://doi.org/10.1016/j.chempr.2019.02.008.
260. Ray, C.; Lee, S. C.; Sankar, K. V.; Jin, B.; Lee, J.; Park, J. H.; Jun, S. C., *ACS Applied Materials & Interfaces* **2017,** *9* (43), 37739-37749. DOI 10.1021/acsami.7b11192.
261. Yu, X.; Hua, T.; Liu, X.; Yan, Z.; Xu, P.; Du, P., *ACS Applied Materials & Interfaces* **2014,** *6* (17), 15395-15402.
262. Babar, P.; Lokhande, A.; Gang, M.; Pawar, B.; Pawar, S.; Kim, J. H., *Journal of Industrial and Engineering Chemistry* **2018,** *60*, 493-497.
263. Wei, C.; Liu, C.; Gao, L.; Sun, Y.; Liu, Q.; Zhang, X.; Guo, J., *Journal of Alloys and Compounds* **2019,** *796*, 86-92.
264. Zhu, S.; Lei, J.; Zhang, L.; He, J., *International Journal of Hydrogen Energy* **2020,** *45* (15), 8031-8040.
265. Zhu, Y. P.; Liu, Y. P.; Ren, T. Z.; Yuan, Z. Y., *Advanced Functional Materials* **2015,** *25* (47), 7337-7347.
266. Wang, Y.; Ge, Z.; Li, X.; Zhao, J.; Ma, B.; Chen, Y., *Journal of Colloid and Interface Science* **2020,** *567*, 308-315.
267. Dong, B.; Yan, K.-L.; Liu, Z.-Z.; Chi, J.-Q.; Gao, W.-K.; Lin, J.-H.; Dai, F.-N.; Chai, Y.-M.; Liu, C.-G., *Journal of the Electrochemical Society* **2018,** *165* (3), H102.
268. Luo, X.; Ji, P.; Wang, P.; Cheng, R.; Chen, D.; Lin, C.; Zhang, J.; He, J.; Shi, Z.; Li, N., *Advanced Energy Materials* **2020,** *10* (17), 1903891.
269. Yan, K.-L.; Qin, J.-F.; Liu, Z.-Z.; Dong, B.; Chi, J.-Q.; Gao, W.-K.; Lin, J.-H.; Chai, Y.-M.; Liu, C.-G., *Chemical Engineering Journal* **2018,** *334*, 922-931.
270. Yang, Y.; Yao, H.; Yu, Z.; Islam, S. M.; He, H.; Yuan, M.; Yue, Y.; Xu, K.; Hao, W.; Sun, G.; Li, H.; Ma, S.; Zapol, P.; Kanatzidis, M. G., *Journal of the American Chemical Society* **2019,** *141* (26), 10417-10430. DOI 10.1021/jacs.9b04492.
271. Guo, Y.; Guo, D.; Ye, F.; Wang, K.; Shi, Z., *International Journal of Hydrogen Energy* **2017,** *42* (27), 17038-17048.
272. Zhang, D.; Li, J.; Luo, J.; Xu, P.; Wei, L.; Zhou, D.; Xu, W.; Yuan, D., *Nanotechnology* **2018,** *29* (24), 245402.
273. Ling, C.; Ouyang, Y.; Shi, L.; Yuan, S.; Chen, Q.; Wang, J., *ACS Catalysis* **2017,** *7* (8), 5097-5102.
274. Faber, M. S.; Lukowski, M. A.; Ding, Q.; Kaiser, N. S.; Jin, S., *The Journal of Physical Chemistry C* **2014,** *118* (37), 21347-21356.
275. Faber, M. S.; Dziedzic, R.; Lukowski, M. A.; Kaiser, N. S.; Ding, Q.; Jin, S., *Journal of the American Chemical Society* **2014,** *136* (28), 10053-10061.
276. Boppella, R.; Tan, J.; Yun, J.; Manorama, S. V.; Moon, J., *Coordination Chemistry Reviews* **2021,** *427*, 213552.
277. Chang, S.; Huang, X.; Ong, C. Y. A.; Zhao, L.; Li, L.; Wang, X.; Ding, J., *Journal of Materials Chemistry A* **2019,** *7* (31), 18338-18347.
278. Zuo, Y.; Liu, Y.; Li, J.; Du, R.; Han, X.; Zhang, T.; Arbiol, J.; Divins, N. r. J.; Llorca, J.; Guijarro, N. s., *Chemistry of Materials* **2019,** *31* (18), 7732-7743.
279. Ren, B.; Li, D.; Jin, Q.; Cui, H.; Wang, C., *Journal of Materials Chemistry A* **2017,** *5* (36), 19072-19078.

280. Yang, L.; Xu, H.; Liu, H.; Cheng, D.; Cao, D., *Small Methods* **2019,** *3* (5), 1900113.
281. Tao, J.; Zhang, Y.; Wang, S.; Wang, G.; Hu, F.; Yan, X.; Hao, L.; Zuo, Z.; Yang, X., *ACS Applied Materials & Interfaces* **2019,** *11* (20), 18342-18348.
282. Zheng, J.; Wu, A.; Chen, H.; Lv, X.; Xu, A.; Li, X., *International Journal of Hydrogen Energy* **2021,** *46* (2), 2026-2035.
283. Yang, X.; Lu, A.-Y.; Zhu, Y.; Hedhili, M. N.; Min, S.; Huang, K.-W.; Han, Y.; Li, L.-J., *Nano Energy* **2015,** *15*, 634-641.
284. Jiang, P.; Liu, Q.; Liang, Y.; Tian, J.; Asiri, A. M.; Sun, X., *Angewandte Chemie* **2014,** *126* (47), 13069-13073.
285. Du, X.; Fang, Y.; Guan, J.; Zhang, T.; Yi, L.; Wang, L.; Zhang, M., *International Journal of Hydrogen Energy* **2020,** 45(38), 18976-18984.
286. Koenigsmann, C.; Wong, S. S., *Energy & Environmental Science* **2011,** *4* (4), 1161-1176.
287. Fu, H. Q.; Zhang, L.; Wang, C. W.; Zheng, L. R.; Liu, P. F.; Yang, H. G., *ACS Energy Letters* **2018,** *3* (9), 2021-2029.
288. Chang, B.; Yang, J.; Shao, Y.; Zhang, L.; Fan, W.; Huang, B.; Wu, Y.; Hao, X., *ChemSusChem* **2018,** *11* (18), 3198-3207.
289. Yang, M.; Shang, C.; Li, F.; Liu, C.; Wang, Z.; Gu, S.; Liu, D.; Cao, L.; Zhang, J.; Lu, Z., *Science China Materials* **2020**, 1-12.
290. Tang, C.; Gan, L.; Zhang, R.; Lu, W.; Jiang, X.; Asiri, A. M.; Sun, X.; Wang, J.; Chen, L., *Nano Letters* **2016,** *16* (10), 6617-6621.
291. Ren, B.; Li, D.; Jin, Q.; Cui, H.; Wang, C., *Journal of Materials Chemistry A* **2017,** *5* (46), 24453-24461.
292. Gao, Y.; Xiong, T.; Li, Y.; Huang, Y.; Li, Y.; Balogun, M.-S. J. T., *ACS Omega* **2019,** *4* (14), 16130-16138.
293. Guo, X.; Li, M.; He, L.; Geng, S.; Tian, F.; Song, Y.; Yang, W.; Yu, Y., *Nanoscale* **2021,** *13* (33), 14179-14185. DOI 10.1039/d1nr03186d.
294. Xu, H.; Liu, T.; Bai, S.; Li, L.; Zhu, Y.; Wang, J.; Yang, S.; Li, Y.; Shao, Q.; Huang, X., *Nano Letters* **2020,** 20(7), 5482-5489.
295. Zhu, Y. P.; Jing, Y.; Vasileff, A.; Heine, T.; Qiao, S. Z., *Advanced Energy Materials* **2017,** *7* (14), 1602928.
296. Wu, Z.-Y.; Ji, W.-B.; Hu, B.-C.; Liang, H.-W.; Xu, X.-X.; Yu, Z.-L.; Li, B.-Y.; Yu, S.-H., *Nano Energy* **2018,** *51*, 286-293.
297. Le, T.-T.; Liu, X.; Xin, P.; Wang, Q.; Gao, C.; Wu, Y.; Jiang, Y.; Hu, Z.; Huang, S.; Chen, Z., *Journal of Materials Science & Technology* **2021,** *74*, 168-175. DOI https://doi.org/10.1016/j.jmst.2020.08.060.
298. Liu, T.; Diao, P., *Nano Research* **2020,** *13* (12), 3299-3309.
299. Li, W.-H.; Lv, J.; Li, Q.; Xie, J.; Ogiwara, N.; Huang, Y.; Jiang, H.; Kitagawa, H.; Xu, G.; Wang, Y., *Journal of Materials Chemistry A* **2019,** *7* (17), 10431-10438.
300. Lim, D.; Oh, E.; Lim, C.; Shim, S. E.; Baeck, S.-H., *Electrochimica Acta* **2020,** *361*, 137080.
301. Xie, H.; Lan, C.; Chen, B.; Wang, F.; Liu, T., *Nano Research* **2020,** *13* (12), 3321-3329.
302. Cabán-Acevedo, M.; Stone, M. L.; Schmidt, J.; Thomas, J. G.; Ding, Q.; Chang, H.-C.; Tsai, M.-L.; He, J.-H.; Jin, S., *Nature Materials* **2015,** *14* (12), 1245-1251.
303. Du, X.; Fang, Y.; Guan, J.; Li, S.; Wang, L.; Zhang, M., *International Journal of Hydrogen Energy* **2021,** 46(1), 599-608.
304. Chang, B.; Yang, Y.; Ye, Z.; Liu, S., *Dalton Transactions* **2019,** *48* (3), 891-897.

305. Liu, H.; Ma, X.; Hu, H.; Pan, Y.; Zhao, W.; Liu, J.; Zhao, X.; Wang, J.; Yang, Z.; Zhao, Q., *ACS Applied Materials & Interfaces* **2019,** *11* (17), 15528-15536.
306. Xiao, X.; Huang, D.; Fu, Y.; Wen, M.; Jiang, X.; Lv, X.; Li, M.; Gao, L.; Liu, S.; Wang, M., *ACS Applied Materials & Interfaces* **2018,** *10* (5), 4689-4696.
307. Yang, G.; Xiang, H.; Rauf, M.; Mi, H.; Ren, X.; Zhang, P.; Li, Y., *Journal of Power Sources* **2021,** *481*, 228925.
308. Guo, M.; He, M.; Li, X.; Zheng, Q.; Xie, F.; Xu, C.; Lin, D., *Electrochimica Acta* **2020,** *356*, 136793.
309. Wu, X.; Li, J.; Li, Y.; Wen, Z., *Chemical Engineering Journal* **2021,** *409*, 128161. DOI https://doi.org/10.1016/j.cej.2020.128161.
310. Yao, M.; Wang, B.; Sun, B.; Luo, L.; Chen, Y.; Wang, J.; Wang, N.; Komarneni, S.; Niu, X.; Hu, W., *Applied Catalysis B: Environmental* **2020,** *280*, 119451.
311. Wang, Y.-Q.; Xie, Y.; Zhao, L.; Sui, X.-L.; Gu, D.-M.; Wang, Z.-B., *ACS Sustainable Chemistry & Engineering* **2019,** *7* (7), 7294-7303.
312. Cao, J.; Zhou, J.; Zhang, Y.; Wang, Y.; Liu, X., *ACS Applied Materials & Interfaces* **2018,** *10* (2), 1752-1760.
313. Xu, Y.; Chai, X.; Ren, T.; Yu, H.; Yin, S.; Wang, Z.; Li, X.; Wang, L.; Wang, H., *Chemistry–A European Journal* **2019,** *25* (70), 16074-16080.
314. Zhai, Z.; Li, C.; Zhang, L.; Wu, H.-C.; Tang, N.; Wang, W.; Gong, J., *Journal of Materials Chemistry A* **2018,** *6* (21), 9833-9838.
315. Czioska, S.; Wang, J.; Teng, X.; Chen, Z., *ACS Sustainable Chemistry & Engineering* **2018,** *6* (9), 11877-11883.
316. Chen, T.-Y.; Vedhanarayanan, B.; Lin, S.-Y.; Shao, L.-D.; Sofer, Z.; Lin, J.-Y.; Lin, T.-W., *Journal of Colloid and Interface Science* **2020,** 574, 300-311.
317. Jin, Q.; Ren, B.; Cui, H.; Wang, C., *Applied Catalysis B: Environmental* **2021,** *283*, 119643.
318. Chandrasekaran, S.; Chung, J. S.; Kim, E. J.; Hur, S. H., *Chemical Engineering Journal* **2016,** *290*, 465-476.
319. Zhang, M.; Ci, S.; Li, H.; Cai, P.; Xu, H.; Wen, Z., *International Journal of Hydrogen Energy* **2017,** *42* (49), 29080-29090.
320. Yuan, H.; Wang, S.; Ma, Z.; Kundu, M.; Tang, B.; Li, J.; Wang, X., *Chemical Engineering Journal* **2021,** *404*, 126474.
321. Ding, X.; Li, X.; Lv, X.; Zheng, Y.-Z.; Wu, Q.; Ding, H.; Wu, J.; Li, R.; Tao, X., *Energy Technology* **2020,** 8(7), 2000268.
322. Wei, B.; Wu, J.; Mei, G.; Qi, Z.; Hu, W.; Wang, Z., *International Journal of Hydrogen Energy* **2019,** *44* (13), 6612-6617.
323. Liu, D.; Zhang, C.; Yu, Y.; Shi, Y.; Yu, Y.; Niu, Z.; Zhang, B., *Nano Research* **2018,** *11* (2), 603-613.
324. Zhang, R.; Cheng, L.; Wang, Z.; Kong, F.; Tsegazab, Y.; Lv, W.; Wang, W., *Applied Surface Science* **2020**, 146753.
325. Lassalle-Kaiser, B.; Zitolo, A.; Fonda, E.; Robert, M.; Anxolabehere-Mallart, E., *ACS Energy Letters* **2017,** *2* (11), 2545-2551.
326. Zhang, D.; Shi, J.; Qi, Y.; Wang, X.; Wang, H.; Li, M.; Liu, S.; Li, C., *Advanced Science* **2018,** *5* (12), 1801216.
327. Liu, Q.; Zhao, H.; Jiang, M.; Kang, Q.; Zhou, W.; Wang, P.; Zhou, F., *Journal of Materials Chemistry A* **2020,** *8* (27), 13638-13645.
328. Zhao, J.; Ren, X.; Ma, H.; Sun, X.; Zhang, Y.; Yan, T.; Wei, Q.; Wu, D., *ACS Sustainable Chemistry & Engineering* **2017,** *5* (11), 10093-10098.
329. Ren, X.; Wang, W.; Ge, R.; Hao, S.; Qu, F.; Du, G.; Asiri, A. M.; Wei, Q.; Chen, L.; Sun, X., *Chemical Communications* **2017,** *53* (64), 9000-9003.

330. Guan, C.; Wu, H.; Ren, W.; Yang, C.; Liu, X.; Ouyang, X.; Song, Z.; Zhang, Y.; Pennycook, S. J.; Cheng, C.; Wang, J., *Journal of Materials Chemistry A* **2018,** *6* (19), 9009-9018. DOI 10.1039/c8ta02528b.
331. Xue, Z.; Kang, J.; Guo, D.; Zhu, C.; Li, C.; Zhang, X.; Chen, Y., *Electrochimica Acta* **2018,** *273*, 229-238.
332. Ning, R.; Jiang, Y.; Zeng, Y.; Gong, H.; Zhao, J.; Weisse, J.; Shi, X.; Gill, T. M.; Zheng, X., *Nano Research* **2020**, 1-6.
333. Miao, Y.-E.; Li, F.; Zhou, Y.; Lai, F.; Lu, H.; Liu, T., *Nanoscale* **2017,** *9* (42), 16313-16320.
334. Yu, X.; Sun, Z.; Yan, Z.; Xiang, B.; Liu, X.; Du, P., *Journal of Materials Chemistry A* **2014,** *2* (48), 20823-20831.
335. Zhang, Q.; Ye, C.; Li, X. L.; Deng, Y. H.; Tao, B. X.; Xiao, W.; Li, L. J.; Li, N. B.; Luo, H. Q., *ACS Applied Materials & Interfaces* **2018,** *10* (33), 27723-27733.
336. Nai, J.; Xu, X.; Xie, Q.; Lu, G.; Wang, Y.; Luan, D.; Tao, X.; Lou, X. W., *Advanced Materials* **2022,** 34(4), 2104405. DOI https://doi.org/10.1002/adma.202104405.
337. Anantharaj, S.; Aravindan, V., *Advanced Energy Materials* **2020,** *10* (1), 1902666. DOI https://doi.org/10.1002/aenm.201902666.
338. Zhang, B.; Wang, H.; Zuo, Z.; Wang, H.; Zhang, J., *Journal of Materials Chemistry A* **2018,** *6* (32), 15728-15737.
339. Zhang, L.; Li, Y.; Peng, J.; Peng, K., *Electrochimica Acta* **2019,** *318*, 762-769.
340. Chen, W.; Qian, G.; Xu, Q.; Yu, C.; Yu, M.; Xia, Y.; Yin, S., *Nanoscale* **2020,** *12* (13), 7116-7123.
341. Zhou, J.-J.; Han, X.; Tao, K.; Li, Q.; Li, Y.-L.; Chen, C.; Han, L., *Chemical Engineering Journal* **2018,** *354*, 875-884.
342. Xu, X.; Du, P.; Guo, T.; Zhao, B.; Wang, H.; Huang, M., *ACS Sustainable Chemistry & Engineering* **2020,** *8* (19), 7463-7471.
343. Zhao, J.; Zeng, Y.; Wang, J.; Xu, Q.; Chen, R.; Ni, H.; Cheng, G. J., *Nanoscale* **2020,** *12* (28), 15393-15401.
344. Kong, X.; Xu, K.; Zhang, C.; Dai, J.; Norooz Oliaee, S.; Li, L.; Zeng, X.; Wu, C.; Peng, Z., *ACS Catalysis* **2016,** *6* (3), 1487-1492.
345. Li, Y.; Hu, L.; Zheng, W.; Peng, X.; Liu, M.; Chu, P. K.; Lee, L. Y. S., *Nano Energy* **2018,** *52*, 360-368.
346. Hu, H. S.; Si, S.; Liu, R. J.; Wang, C. B.; Feng, Y. Y., *International Journal of Energy Research* **2020,** *44* (11), 9222-9232.
347. Wang, Z.; Lei, Q.; Wang, Z.; Yuan, H.; Cao, L.; Qin, N.; Lu, Z.; Xiao, J.; Liu, J., *Chemical Engineering Journal* **2020**, 125180.
348. Liu, H.; Zhao, D.; Liu, Y.; Tong, Y.; Wu, X.; Shen, G., *Science China Materials* **2020**, 1-11.
349. Duan, J.; Chen, S.; Zhao, C., *Nature Communications* **2017,** *8* (1), 1-7.
350. Guo, Y.; Fu, X.; Zhang, B.; Peng, Z., *Journal of Alloys and Compounds* **2019,** *792*, 732-741.
351. Pei, L.; Zhong, J.; Li, T.; Bai, W.; Wu, S.; Yuan, Y.; Chen, Y.; Yu, Z.; Yan, S.; Zou, Z., *Journal of Materials Chemistry A* **2020,** *8* (14), 6795-6803.
352. Wang, Q.; O'Hare, D., *Chemical reviews* **2012,** *112* (7), 4124-4155.
353. Jian, J.; Yuan, L.; Qi, H.; Sun, X.; Zhang, L.; Li, H.; Yuan, H.; Feng, S., *ACS Applied Materials & Interfaces* **2018,** *10* (47), 40568-40576.
354. Wang, Y.; Zhang, Y.; Liu, Z.; Xie, C.; Feng, S.; Liu, D.; Shao, M.; Wang, S., *Angewandte Chemie International Edition* **2017,** *56* (21), 5867-5871.

355. Yu, J.; Wang, Q.; O'Hare, D.; Sun, L., *Chemical Society Reviews* **2017,** *46* (19), 5950-5974.
356. Ye, W.; Fang, X.; Chen, X.; Yan, D., *Nanoscale* **2018,** *10* (41), 19484-19491.
357. Zhou, D.; Jia, Y.; Duan, X.; Tang, J.; Xu, J.; Liu, D.; Xiong, X.; Zhang, J.; Luo, J.; Zheng, L., *Nano Energy* **2019,** *60*, 661-666.
358. Ren, J.-T.; Yuan, G.-G.; Weng, C.-C.; Chen, L.; Yuan, Z.-Y., *Nanoscale* **2018,** *10* (22), 10620-10628.
359. Qian, H.; Wu, B.; Nie, Z.; Liu, T.; Liu, P.; He, H.; Wu, J.; Chen, Z.; Chen, S., *Chemical Engineering Journal* **2020**, 127646.
360. Zhao, M.; Li, W.; Li, J.; Hu, W.; Li, C. M., *Advanced Science* **2020,** *7* (20), 2001965.
361. Pan, C.; Liu, Z.; Huang, M., *Applied Surface Science* **2020,** *529*, 147201.
362. Cao, C.; Ma, D. D.; Xu, Q.; Wu, X. T.; Zhu, Q. L., *Advanced Functional Materials* **2019,** *29* (6), 1807418.
363. Liu, W.; Geng, P.; Li, S.; Liu, W.; Fan, D.; Lu, H.; Lu, Z.; Liu, Y., *Journal of Energy Chemistry* **2022,** *55*, 17-24.
364. Li, M.; Wang, J.; Guo, X.; Li, J.; Huang, Y.; Geng, S.; Yu, Y.; Liu, Y.; Yang, W., *Applied Surface Science* **2021,** *536*, 147909.
365. Kumar, G. M.; Cho, H.; Ilanchezhiyan, P.; Lee, D.; Jeon, H.; Walke, P. D.; Kim, D.; Kang, T., *Applied Surface Science* **2021,** *540*, 148297.
366. Chen, M.-T.; Duan, J.-J.; Feng, J.-J.; Mei, L.-P.; Jiao, Y.; Zhang, L.; Wang, A.-J., *Journal of Colloid and Interface Science* **2022,** *605*, 888-896. DOI https://doi.org/10.1016/j.jcis.2021.07.101.
367. Deng, L.; Zhang, K.; Shi, D.; Liu, S.; Xu, D.; Shao, Y.; Shen, J.; Wu, Y.; Hao, X., *Applied Catalysis B: Environmental* **2021,** *299*, 120660. DOI https://doi.org/10.1016/j.apcatb.2021.120660.
368. Lu, Y.; Li, Z.; Xu, Y.; Tang, L.; Xu, S.; Li, D.; Zhu, J.; Jiang, D., *Chemical Engineering Journal* **2021,** *411*, 128433. DOI https://doi.org/10.1016/j.cej.2021.128433.
369. Liu, W.; Yu, L.; Yin, R.; Xu, X.; Feng, J.; Jiang, X.; Zheng, D.; Gao, X.; Gao, X.; Que, W., *Small* **2020,** *16* (10), 1906775.
370. Zhao, D.; Dai, M.; Liu, H.; Chen, K.; Zhu, X.; Xue, D.; Wu, X.; Liu, J., *Advanced Materials Interfaces* **2019,** *6* (21), 1901308.
371. Yu, T.; Xu, Q.; Luo, L.; Liu, C.; Yin, S., *Chemical Engineering Journal* **2022,** *430*, 133117. DOI https://doi.org/10.1016/j.cej.2021.133117.
372. Wang, Y.; Qian, G.; Xu, Q.; Zhang, H.; Shen, F.; Luo, L.; Yin, S., *Applied Catalysis B: Environmental* **2021,** *286*, 119881. DOI https://doi.org/10.1016/j.apcatb.2021.119881.
373. Zhang, D.; Kong, X.; Jiang, M.; Lei, D.; Lei, X., *ACS Sustainable Chemistry & Engineering* **2019,** *7* (4), 4420-4428.
374. Hou, Y.; Lohe, M. R.; Zhang, J.; Liu, S.; Zhuang, X.; Feng, X., *Energy & Environmental Science* **2016,** *9* (2), 478-483.
375. Hu, S.; Tan, Y.; Feng, C.; Wu, H.; Zhang, J.; Mei, H., *Journal of Power Sources* **2020,** *453*, 227872.
376. Zang, Z.; Wang, X.; Li, X.; Zhao, Q.; Li, L.; Yang, X.; Yu, X.; Zhang, X.; Lu, Z., *ACS Applied Materials & Interfaces* **2021,** *13* (8), 9865-9874. DOI 10.1021/acsami.0c20820.
377. Zhang, W.-D.; Yu, H.; Li, T.; Hu, Q.-T.; Gong, Y.; Zhang, D.-Y.; Liu, Y.; Fu, Q.-T.; Zhu, H.-Y.; Yan, X., *Applied Catalysis B: Environmental* **2020,** *264*, 118532.

378. Xie, Q.; Cai, Z.; Li, P.; Zhou, D.; Bi, Y.; Xiong, X.; Hu, E.; Li, Y.; Kuang, Y.; Sun, X., *Nano Research* **2018,** *11* (9), 4524-4534.
379. Xie, J.; Qu, H.; Lei, F.; Peng, X.; Liu, W.; Gao, L.; Hao, P.; Cui, G.; Tang, B., *Journal of Materials Chemistry A* **2018,** *6* (33), 16121-16129.
380. Wu, M.; Zhang, G.; Tong, H.; Liu, X.; Du, L.; Chen, N.; Wang, J.; Sun, T.; Regier, T.; Sun, S., *Nano Energy* **2021,** *79*, 105409.
381. Wang, C.; Wang, F.; Zhang, L.-S.; Qiu, S.-Y.; Gu, L.-L.; Wang, K.-X.; Zuo, P.-J.; Sun, K.-N.; Zhu, X.-D., *Chemical Engineering Journal 405*, 126699.
382. Guo, M.; Song, S.; Zhang, S.; Yan, Y.; Zhan, K.; Yang, J.; Zhao, B., *ACS Sustainable Chemistry & Engineering* **2020,** *8* (19), 7436-7444.
383. Li, C.-F.; Zhao, J.-W.; Xie, L.-J.; Wu, J.-Q.; Li, G.-R., *Applied Catalysis B: Environmental* **2021,** *291*, 119987. DOI https://doi.org/10.1016/j.apcatb.2021.119987.
384. Kim, M.; Ha, J.; Shin, N.; Kim, Y.-T.; Choi, J., *Electrochimica Acta* **2020,** *364*, 137315.
385. Kale, S. B.; Bhardwaj, A.; Lokhande, V. C.; Lee, D.-M.; Kang, S.-H.; Kim, J.-H.; Lokhande, C. D., *Chemical Engineering Journal* **2021,** *405*, 126993.
386. Zhu, P.; Chen, Y.; Zhou, Y.; Yang, Z.; Wu, D.; Xiong, X.; Ouyang, F., *International Journal of Hydrogen Energy* **2018,** *43* (31), 14087-14095.
387. White, R. J.; Luque, R.; Budarin, V. L.; Clark, J. H.; Macquarrie, D. J., *Chemical Society Reviews* **2009,** *38* (2), 481-494.
388. Hu, Q.; Li, G.; Liu, X.; Zhu, B.; Chai, X.; Zhang, Q.; Liu, J.; He, C., *Angew Chem Int Ed* **2019,** *131* (13), 4362-4366.
389. Xiao, C.; Li, Y.; Lu, X.; Zhao, C., *Advanced Functional Materials* **2016,** *26* (20), 3515-3523.
390. Xi, G.; Zuo, L.; Li, X.; Jin, Y.; Li, R.; Zhang, T., *Journal of Materials Science & Technology* **2021,** *70*, 197-204.
391. Zhou, Y.; Chen, Y.; Wei, M.; Fan, H.; Liu, X.; Liu, Q.; Liu, Y.; Cao, J.; Yang, L., *CrystEngComm* **2020,** *23*(1), 69-81.
392. Liu, Y.; Li, J.; Huang, W.; Zhang, Y.; Wang, M.; Gao, X.; Wang, X.; Jin, M.; Hou, Z.; Zhou, G., *ACS Applied Materials & Interfaces* **2020,** *12* (30), 33586-33594.
393. Liu, W.; Geng, P.; Li, S.; Zhu, R.; Liu, W.; Lu, H.; Chandrasekaran, S.; Pang, Y.; Fan, D.; Liu, Y., *International Journal of Hydrogen Energy* **2020,** *45* (53), 28576-28585.
394. Yan, Y.; Lin, J.; Bao, K.; Xu, T.; Qi, J.; Cao, J.; Zhong, Z.; Fei, W.; Feng, J., *Journal of Colloid and Interface Science* **2019,** *552*, 332-336.
395. Pawar, S. M.; Pawar, B. S.; Hou, B.; Kim, J.; Ahmed, A. T. A.; Chavan, H. S.; Jo, Y.; Cho, S.; Inamdar, A. I.; Gunjakar, J. L., *Journal of Materials Chemistry A* **2017,** *5* (25), 12747-12751.
396. Yang, Y.; Zhu, C.; Zhang, Y.; Xie, Y.; Lv, L.; Chen, W.; He, Y.; Hu, Z., *Journal of Physics and Chemistry of Solids* **2021,** *148*, 109680.
397. Zhang, K.; Liu, Y.; Wang, B.; Yu, F.; Yang, Y.; Xing, L.; Hao, J.; Zeng, J.; Mao, B.; Shi, W., *International Journal of Hydrogen Energy* **2019,** *44* (3), 1555-1564.
398. Darband, G. B.; Aliofkhazraei, M.; Rouhaghdam, A. S., *Journal of Colloid and Interface Science* **2019,** *547*, 407-420.
399. Zhang, Q.; Zhong, H.; Meng, F.; Bao, D.; Zhang, X.; Wei, X., *Nano Research* **2018,** *11* (3), 1294-1300.
400. Wang, Y.; Zhao, S.; Zhu, Y.; Qiu, R.; Gengenbach, T.; Liu, Y.; Zu, L.; Mao, H.; Wang, H.; Tang, J., *Iscience* **2020,** *23* (1), 100761.
401. Li, R.-Q.; Wang, B.-L.; Gao, T.; Zhang, R.; Xu, C.; Jiang, X.; Zeng, J.; Bando, Y.; Hu, P.; Li, Y., *Nano Energy* **2019,** *58*, 870-876.

402. Tsai, H.-C.; Vedhanarayanan, B.; Lin, T.-W., *ACS Applied Energy Materials* **2019,** *2* (5), 3708-3716.
403. Zhou, J.; Yue, H.; Qi, F.; Wang, H.; Chen, Y., *International Journal of Hydrogen Energy* **2017,** *42* (44), 27004-27012.
404. Li, S.; Jian, X.; Liu, J.; Guo, S.; Zhou, C.; Zhang, P.; Yang, Y.; Chen, L., *International Journal of Hydrogen Energy* **2020,** *45* (7), 4435-4443.
405. Rani, B. J.; Ravi, G.; Yuvakkumar, R.; Hasan, Z. M.; Ravichandran, S.; Hong, S., *Materials Chemistry and Physics* **2020,** *239*, 122321.
406. Zhou, C.; Gao, T.; Tan, J.; Luo, Z.; Mutallip, L.; Xiao, D., *Sustainable Energy & Fuels* **2021,** *5* (10), 2649-2659. DOI 10.1039/d1se00002k.
407. Liu, G.; Song, X.-Z.; Zhang, S.; Chen, X.; Liu, S.; Meng, Y.; Tan, Z., *Journal of Power Sources* **2020,** *465*, 228239.
408. Sun, Y.; Zhou, Y.; Zhu, Y.; Shen, Y.; Xie, A., *ACS Sustainable Chemistry & Engineering* **2019,** *7* (10), 9153-9163.
409. Zhang, H.; Maijenburg, A. W.; Li, X.; Schweizer, S. L.; Wehrspohn, R. B., *Advanced functional materials* **2020,** *30* (34), 2003261.
410. Lv, J.; Liu, P.; Yang, F.; Xing, L.; Wang, D.; Chen, X.; Gao, H.; Huang, X.; Lu, Y.; Wang, G., *ACS Applied Materials & Interfaces* **2020,** *12* (43), 48495-48510.
411. Kuang, P.; He, M.; Zou, H.; Yu, J.; Fan, K., *Applied Catalysis B: Environmental* **2019,** *254*, 15-25.
412. Ouyang, C.; Feng, S.; Huo, J.; Wang, S., *Green Energy & Environment* **2017,** *2* (2), 134-141.
413. Chai, Y.-M.; Zhang, X.-Y.; Lin, J.-H.; Qin, J.-F.; Liu, Z.-Z.; Xie, J.-Y.; Guo, B.-Y.; Yang, Z.; Dong, B., *International Journal of Hydrogen Energy* **2019,** *44* (21), 10156-10162.
414. Yu, L.; Zhou, H.; Sun, J.; Qin, F.; Yu, F.; Bao, J.; Yu, Y.; Chen, S.; Ren, Z., *Energy & Environmental Science* **2017,** *10* (8), 1820-1827.
415. Yang, Y.; Meng, H.; Zhang, Y.; Li, Z.; Zhang, Z.; Hu, Z., *Colloids and Surfaces A: Physicochemical and Engineering Aspects* **2020,** *607*, 125452. DOI https://doi.org/10.1016/j.colsurfa.2020.125452.
416. Patil, S. J.; Chodankar, N. R.; Hwang, S.-K.; Shinde, P. A.; Seeta Rama Raju, G.; Shanmugam Ranjith, K.; Huh, Y. S.; Han, Y.-K., *Chemical Engineering Journal* **2022,** *429*, 132379. DOI https://doi.org/10.1016/j.cej.2021.132379.
417. Liu, S.-Q.; Gao, M.-R.; Liu, S.; Luo, J.-L., *Applied Catalysis B: Environmental* **2021,** *292*, 120148. DOI https://doi.org/10.1016/j.apcatb.2021.120148.
418. Zhang, J.; Qian, J.; Ran, J.; Xi, P.; Yang, L.; Gao, D., *ACS Catalysis* **2020,** *10* (21), 12376-12384.
419. Zhai, P.; Xia, M.; Wu, Y.; Zhang, G.; Gao, J.; Zhang, B.; Cao, S.; Zhang, Y.; Li, Z.; Fan, Z.; Wang, C.; Zhang, X.; Miller, J. T.; Sun, L.; Hou, J., *Nature Communications* **2021,** *12* (1), 4587. DOI 10.1038/s41467-021-24828-9.
420. Kong, D.; Wang, Y.; Von Lim, Y.; Huang, S.; Zhang, J.; Liu, B.; Chen, T.; Yang, H. Y., *Nano Energy* **2018,** *49*, 460-470.
421. Lin, J.; Wang, P.; Wang, H.; Li, C.; Si, X.; Qi, J.; Cao, J.; Zhong, Z.; Fei, W.; Feng, J., *Advanced Science* **2019,** *6* (14), 1900246.
422. Meng, J.; Fu, J.; Yang, X.; Wei, M.; Liang, S.; Zang, H.-Y.; Tan, H.; Wang, Y.; Li, Y., *Inorganic Chemistry Frontiers* **2017,** *4* (11), 1791-1797.
423. Zhou, Q.; Li, T.-T.; Qian, J.; Hu, Y.; Guo, F.; Zheng, Y.-Q., *Journal of Materials Chemistry A* **2018,** *6* (29), 14431-14439.

424. Li, M.; Sun, R.; Li, Y.; Jiang, J.; Xu, W.; Cong, H.; Han, S., *Chemical Engineering Journal* **2022,** *431*, 133941. DOI https://doi.org/10.1016/j.cej.2021.133941.
425. Lonkar, S. P.; Pillai, V. V.; Alhassan, S. M., *International Journal of Hydrogen Energy* **2020,** *45* (17), 10475-10485.
426. Liang, Z.; Zhou, P.; Wang, Z.; Wang, P.; Liu, Y.; Qin, X.; Zhang, X.; Dai, Y.; Zheng, Z.; Huang, B., *International Journal of Hydrogen Energy* **2020,** *45* (15), 8659-8666.
427. Wang, X.; Li, T.-T.; Zheng, Y.-Q., *International Journal of Hydrogen Energy* **2018,** *43* (4), 2009-2017.
428. Yao, M.; Sun, B.; He, L.; Wang, N.; Hu, W.; Komarneni, S., *ACS Sustainable Chemistry & Engineering* **2019,** *7* (5), 5430-5439.
429. Liu, H.; Ma, F.-X.; Xu, C.-Y.; Yang, L.; Du, Y.; Wang, P.-P.; Yang, S.; Zhen, L., *ACS Applied Materials & Interfaces* **2017,** *9* (13), 11634-11641.
430. Jin, X.; Li, J.; Cui, Y.; Liu, X.; Wang, K.; Zhou, Y.; Yang, W.; Zhang, X.; Zhang, C.; Jiang, X., *International Journal of Hydrogen Energy* **2019,** *44* (12), 5739-5747.
431. Wang, X.; Zheng, Y.; Yuan, J.; Shen, J.; Hu, J.; Wang, A.-j.; Wu, L.; Niu, L., *Electrochimica Acta* **2017,** *225*, 503-513.
432. Feng, Y.; Wang, X.; Huang, J.; Dong, P.; Ji, J.; Li, J.; Cao, L.; Feng, L.; Jin, P.; Wang, C., *Chemical Engineering Journal* **2020,** *390*, 124525.
433. Suryawanshi, M. P.; Ghorpade, U. V.; Shin, S. W.; Suryawanshi, U. P.; Jo, E.; Kim, J. H., *ACS Catalysis* **2019,** *9* (6), 5025-5034.
434. Xiang, R.; Duan, Y.; Tong, C.; Peng, L.; Wang, J.; Shah, S. S. A.; Najam, T.; Huang, X.; Wei, Z., *Electrochimica Acta* **2019,** *302*, 45-55.
435. Liu, H.; Peng, X.; Liu, X.; Qi, G.; Luo, J., *ChemSusChem* **2019,** *12* (7), 1334-1341.
436. Kong, D.; Wang, Y.; Huang, S.; Hu, J.; Von Lim, Y.; Liu, B.; Fan, S.; Shi, Y.; Yang, H. Y., *Energy Storage Materials* **2019,** *23*, 653-663.
437. Xiang, R.; Duan, Y.; Peng, L.; Wang, Y.; Tong, C.; Zhang, L.; Wei, Z., *Applied Catalysis B: Environmental* **2019,** *246*, 41-49.
438. Shen, Y.; Guo, S.-G.; Du, F.; Yuan, X.-B.; Zhang, Y.; Hu, J.; Shen, Q.; Luo, W.; Alsaedi, A.; Hayat, T., *Nanoscale* **2019,** *11* (24), 11765-11773.
439. Zhang, N.; Zhang, Q.; Xu, C.; Li, Y.; Zhang, J.-Y.; Wu, L.; Liu, Y.; Fang, Y.-Z.; Liu, Z., *Chemical Engineering Journal* **2021,** *426*, 131192. DOI https://doi.org/10.1016/j.cej.2021.131192.
440. Zhu, Y.; Zhang, L.; Zhang, X.; Li, Z.; Zha, M.; Li, M.; Hu, G., *Chemical Engineering Journal* **2021,** *405*, 127002.
441. Li, K.; Jian, X.; Li, S.; Wang, W.; Lei, Y.; Zhang, P.; Liu, J.; Zhou, C.; Chen, L., *Inorganic Chemistry Frontiers* **2020,** *7*(24), 4913-4923.
442. Jin, Y.; Yue, X.; Shu, C.; Huang, S.; Shen, P. K., *Journal of Materials Chemistry A* **2017,** *5* (6), 2508-2513.
443. Adhikari, S.; Kwon, Y.; Kim, D.-H., *Chemical Engineering Journal* **2020,** *402*, 126192.
444. Zhang, C.; Gong, N.; Ding, C.; Li, Y.; Peng, W.; Zhang, G.; Zhang, F.; Fan, X., *International Journal of Hydrogen Energy* **2019,** *44* (48), 26118-26127.
445. Wang, Y.; Che, P.; Du, X.; Zhang, X., *International Journal of Hydrogen Energy* **2020,** *45* (53), 28598-28606.
446. Zhao, Y.; Jin, B.; Zheng, Y.; Jin, H.; Jiao, Y.; Qiao, S.-Z., *Advanced Energy Materials* **2018,** *8* (29), 1801926. DOI https://doi.org/10.1002/aenm.201801926.

447. Jadhav, A. R.; Kumar, A.; Lee, J.; Yang, T.; Na, S.; Lee, J.; Luo, Y.; Liu, X.; Hwang, Y.; Liu, Y.; Lee, H., *Journal of Materials Chemistry A* **2020,** *8* (46), 24501-24514. DOI 10.1039/d0ta08543j.
448. Yang, F.; Luo, Y.; Yu, Q.; Zhang, Z.; Zhang, S.; Liu, Z.; Ren, W.; Cheng, H.-M.; Li, J.; Liu, B., *Advanced Functional Materials* **2021,** *31* (21), 2010367. DOI https://doi.org/10.1002/adfm.202010367.
449. Wen, Q.; Yang, K.; Huang, D.; Cheng, G.; Ai, X.; Liu, Y.; Fang, J.; Li, H.; Yu, L.; Zhai, T., *Advanced Energy Materials* **2021,** *11* (46), 2102353. DOI https://doi.org/10.1002/aenm.202102353.
450. Duan, S.; Liu, Z.; Zhuo, H.; Wang, T.; Liu, J.; Wang, L.; Liang, J.; Han, J.; Huang, Y.; Li, Q., *Nanoscale* **2020,** *12* (42), 21743-21749. DOI 10.1039/d0nr05458e.
451. Gao, X.; Chen, Y.; Sun, T.; Huang, J.; Zhang, W.; Wang, Q.; Cao, R., *Energy & Environmental Science* **2020,** *13* (1), 174-182. DOI 10.1039/c9ee02380a.
452. Yu, L.; Zhu, Q.; Song, S.; McElhenny, B.; Wang, D.; Wu, C.; Qin, Z.; Bao, J.; Yu, Y.; Chen, S., *Nature Communications* **2019,** *10* (1), 1-10.
453. Yu, L.; Wu, L.; Song, S.; McElhenny, B.; Zhang, F.; Chen, S.; Ren, Z., *ACS Energy Letters* **2020,** *5* (8), 2681-2689.
454. Yu, L.; Wu, L.; McElhenny, B.; Song, S.; Luo, D.; Zhang, F.; Yu, Y.; Chen, S.; Ren, Z., *Energy & Environmental Science* **2020,** *13*(10), 3439-3446.
455. Liu, T.; Liu, H.; Wu, X.; Niu, Y.; Feng, B.; Li, W.; Hu, W.; Li, C. M., *Electrochimica Acta* **2018,** *281*, 710-716. DOI https://doi.org/10.1016/j.electacta.2018.06.018.
456. Liu, G.; Xu, Y.; Yang, T.; Jiang, L., *Nano Materials Science* **2020**. DOI:10.1016/j.nanoms.2020.12.003
457. Zhang, J.; Hu, W.; Cao, S.; Piao, L., *Nano Research* **2020**, 1-10.
458. Huang, Z.-D.; Feng, C.; Sun, J.-P.; Xu, B.; Huang, T.-X.; Wang, X.-K.; Dai, F.-N.; Sun, D.-F., *CCS Chemistry* **2020,** *3*(11), 2696-2711.
459. Dresp, S.; Thanh, T. N.; Klingenhof, M.; Brueckner, S.; Hauke, P.; Strasser, P., *Energy & Environmental Science* **2020,** *13*(6), 1725-1729.
460. Wu, L.; Yu, L.; Zhang, F.; McElhenny, B.; Luo, D.; Karim, A.; Chen, S.; Ren, Z., *Advanced Functional Materials* **2021,** *31* (1), 2006484.
461. Li, H.; Tang, Q.; He, B.; Yang, P., *Journal of Materials Chemistry A* **2016,** *4* (17), 6513-6520.
462. Yang, H.; Dai, G.; Chen, Z.; Wu, J.; Huang, H.; Liu, Y.; Shao, M.; Kang, Z., *Small* **2021,** *17* (32), 2101727. DOI https://doi.org/10.1002/smll.202101727.
463. Liu, Y.; Liang, X.; Gu, L.; Zhang, Y.; Li, G.-D.; Zou, X.; Chen, J.-S., *Nature Communications* **2018,** *9* (1), 2609. DOI 10.1038/s41467-018-05019-5.
464. Tang, Y.; Liu, Q.; Dong, L.; Wu, H. B.; Yu, X.-Y., *Applied Catalysis B: Environmental* **2020,** *266*, 118627. DOI https://doi.org/10.1016/j.apcatb.2020.118627.
465. Menezes, P. W.; Indra, A.; Zaharieva, I.; Walter, C.; Loos, S.; Hoffmann, S.; Schlögl, R.; Dau, H.; Driess, M., *Energy & Environmental Science* **2019,** *12* (3), 988-999. DOI 10.1039/c8ee01669k.
466. Shan, X.; Liu, J.; Mu, H.; Xiao, Y.; Mei, B.; Liu, W.; Lin, G.; Jiang, Z.; Wen, L.; Jiang, L., *Angewandte Chemie International Edition* **2020,** *59* (4), 1659-1665. DOI https://doi.org/10.1002/anie.201911617.
467. Chandrasekaran, S.; Choi, W. M.; Chung, J. S.; Hur, S. H.; Kim, E. J., *Materials Letters* **2014,** *136*, 118-121.
468. Chandrasekaran, S.; Kim, E. J.; Chung, J. S.; Yoo, I.-K.; Senthilkumar, V.; Kim, Y. S.; Bowen, C. R.; Adamaki, V.; Hur, S. H., *Chemical Engineering Journal* **2017,** *309*, 682-690.

469. Yang, W.; Prabhakar, R. R.; Tan, J.; Tilley, S. D.; Moon, J., *Chemical Society Reviews* **2019,** *48* (19), 4979-5015.
470. Chandrasekaran, S.; Ngo, Y.-L. T.; Sui, L.; Kim, E. J.; Dang, D. K.; Chung, J. S.; Hur, S. H., *Dalton Transactions* **2017,** *46* (40), 13912-13919.
471. Lin, J.; Liu, Y.; Liu, Y.; Huang, C.; Liu, W.; Mi, X.; Fan, D.; Fan, F.; Lu, H.; Chen, X., *ChemSusChem* **2019,** *12* (5), 961-967.
472. Lu, H.; Yan, Y.; Zhang, M.; Tan, H.; Geng, P.; Le, S.; Yang, Z.; Liu, Y., *Journal of Solid State Electrochemistry* **2018,** *22* (7), 2169-2181.
473. Chandrasekaran, S.; Hur, S. H.; Choi, W. M.; Chung, J. S.; Kim, E. J., *Materials Letters* **2015,** *160*, 92-95.
474. Chen, D.; Liu, Z.; Guo, Z.; Yan, W.; Ruan, M., *Chemical Engineering Journal* **2020,** *381*, 122655.
475. Liang, X.; Wang, P.; Tong, F.; Liu, X.; Wang, C.; Wang, M.; Zhang, Q.; Wang, Z.; Liu, Y.; Zheng, Z., *Advanced Functional Materials* **2020**, 2008656.
476. Chandrasekaran, S.; Hur, S. H.; Kim, E. J.; Rajagopalan, B.; Babu, K. F.; Senthilkumar, V.; Chung, J. S.; Choi, W. M.; Kim, Y. S., *RSC Advances* **2015,** *5* (37), 29159-29166.
477. Pan, L.; Liu, Y.; Yao, L.; Ren, D.; Sivula, K.; Grätzel, M.; Hagfeldt, A., *Nature Communications* **2020,** *11* (1), 1-10.
478. Chen, Y.; Feng, X.; Liu, Y.; Guan, X.; Burda, C.; Guo, L., *ACS Energy Letters* **2020,** *5* (3), 844-866.
479. Wang, Y.; Shi, H.; Cui, K.; Zhang, L.; Ge, S.; Jinghua, Y., *Applied Catalysis B: Environmental* **2020**, 119094.
480. Bae, D.; Pedersen, T.; Seger, B.; Malizia, M.; Kuznetsov, A.; Hansen, O.; Chorkendorff, I.; Vesborg, P. C., *Energy & Environmental Science* **2015,** *8* (2), 650-660.
481. Gao, L.; Cui, Y.; Vervuurt, R. H.; van Dam, D.; van Veldhoven, R. P.; Hofmann, J. P.; Bol, A. A.; Haverkort, J. E.; Notten, P. H.; Bakkers, E. P., *Advanced Functional Materials* **2016,** *26* (5), 679-686.
482. Su, J.; Minegishi, T.; Domen, K., *Journal of Materials Chemistry A* **2017,** *5* (25), 13154-13160.
483. Liu, Z.; Zhou, M., *ACS Sustainable Chemistry & Engineering* **2019,** *8* (1), 512-519.
484. Mahmoudi, B.; Caddeo, F.; Lindenberg, T.; Schneider, T.; Hölscher, T.; Scheer, R.; Maijenburg, A. W., *Electrochimica Acta* **2020,** *367*, 137183.
485. Palm, D. W.; Muzzillo, C. P.; Ben-Naim, M.; Khan, I.; Gaillard, N.; Jaramillo, T. F., *Sustainable Energy & Fuels* **2021,** *5*(2), 384-390.
486. Jacobsson, T. J.; Platzer-Björkman, C.; Edoff, M.; Edvinsson, T., *International Journal of Hydrogen Energy* **2013,** *38* (35), 15027-15035.
487. Pan, L.; Kim, J. H.; Mayer, M. T.; Son, M.-K.; Ummadisingu, A.; Lee, J. S.; Hagfeldt, A.; Luo, J.; Grätzel, M., *Nature Catalysis* **2018,** *1* (6), 412-420.
488. Wang, Y.; Wang, W.; Fu, J.; Liang, Y.; Yao, L.; Zhu, T., *Renewable Energy* **2020**.
489. Seo, D.-B.; Trung, T. N.; Kim, D.-O.; Duc, D. V.; Hong, S.; Sohn, Y.; Jeong, J.-R.; Kim, E.-T., *Nano-Micro Letters* **2020,** *12* (1), 1-14.
490. Tian, W.; Chen, C.; Meng, L.; Xu, W.; Cao, F.; Li, L., *Advanced Energy Materials* **2020,** *10* (18), 1903951.
491. Alizadeh, M.; Tong, G. B.; Qadir, K. W.; Mehmood, M. S.; Rasuli, R., *Renewable Energy* **2020,** *156*, 602-609.

492. Franz, S.; Arab, H.; Chiarello, G. L.; Bestetti, M.; Selli, E., *Advanced Energy Materials* **2020**, 2000652.
493. Kölbach, M.; Harbauer, K.; Ellmer, K.; van de Krol, R., *The Journal of Physical Chemistry C* **2020,** *124* (8), 4438-4447.
494. Higashi, M.; Domen, K.; Abe, R., *Energy & Environmental Science* **2011,** *4* (10), 4138-4147.
495. Tayebi, M.; Lee, B.-K., *Renewable and Sustainable Energy Reviews* **2019,** *111*, 332-343.
496. Song, H.; Oh, S.; Yoon, H.; Kim, K.-H.; Ryu, S.; Oh, J., *Nano Energy* **2017,** *42*, 1-7.
497. Qiu, Y.; Liu, W.; Chen, W.; Zhou, G.; Hsu, P.-C.; Zhang, R.; Liang, Z.; Fan, S.; Zhang, Y.; Cui, Y., *Science Advances* **2016,** *2* (6), e1501764.
498. Ding, C.; Qin, W.; Wang, N.; Liu, G.; Wang, Z.; Yan, P.; Shi, J.; Li, C., *Physical Chemistry Chemical Physics* **2014,** *16* (29), 15608-15614.
499. Pornrungroj, C.; Andrei, V.; Rahaman, M.; Uswachoke, C.; Joyce, H. J.; Wright, D. S.; Reisner, E., *Advanced Functional Materials* **2020**, 2008182.
500. Nasir, S. N. F. M.; Mat-Teridi, M. A., *Journal of Sol-Gel Science and Technology* **2020,** *93* (1), 1-5.
501. Kim, D.; Gu, M.; Choi, Y.; Kim, H.; Ryu, J.; Kim, B.-S., *ACS Applied Energy Materials* **2020,** *3* (7), 7103-7112.
502. Nguyen, D. N.; Gund, G. S.; Jung, M. G.; Roh, S. H.; Park, J.; Kim, J. K.; Park, H. S., *ACS Nano* **2020,** *14*(12), 17615-17625.
503. Kim, J. H.; Han, S.; Jo, Y. H.; Bak, Y.; Lee, J. S., *Journal of Materials Chemistry A* **2018,** *6* (3), 1266-1274.
504. Fan, R.; Cheng, S.; Huang, G.; Wang, Y.; Zhang, Y.; Vanka, S.; Botton, G. A.; Mi, Z.; Shen, M., *Journal of Materials Chemistry A* **2019,** *7* (5), 2200-2209.
505. Wang, C.-C.; Li, J.-R.; Lv, X.-L.; Zhang, Y.-Q.; Guo, G., *Energy & Environmental Science* **2014,** *7* (9), 2831-2867.
506. Rauf, M.; Ashraf, S. S., *Chemical Engineering Journal* **2009,** *151* (1-3), 10-18.
507. Sharma, S.; Dutta, V.; Singh, P.; Raizada, P.; Rahmani-Sani, A.; Hosseini-Bandegharaei, A.; Thakur, V. K., *Journal of Cleaner Production* **2019,** *228*, 755-769.
508. Samadi, M.; Zirak, M.; Naseri, A.; Kheirabadi, M.; Ebrahimi, M.; Moshfegh, A. Z., *Research on Chemical Intermediates* **2019,** *45* (4), 2197-2254.
509. Liu, Y.; Mi, X.; Wang, J.; Li, M.; Fan, D.; Lu, H.; Chen, X., *Inorganic Chemistry Frontiers* **2019,** *6* (4), 948-954.
510. Dang, D. K.; Sundaram, C.; Ngo, Y.-L. T.; Chung, J. S.; Kim, E. J.; Hur, S. H., *Sensors and Actuators B: Chemical* **2018,** *255*, 3284-3291.
511. Dang, D. K.; Sundaram, C.; Ngo, Y.-L. T.; Choi, W. M.; Chung, J. S.; Kim, E. J.; Hur, S. H., *Dyes and Pigments* **2019,** *165*, 327-334.
512. Zhang, B.; Ma, X.; Ma, J.; Zhou, Y.; Liu, G.; Ma, D.; Deng, Z.; Luo, M.; Xin, Y., *Journal of Colloid and Interface Science* **2020,** *577*, 75-85.
513. Zhao, X.; Li, X.; Wang, Y.; Lin, J.; Liu, J.; Shao, H., *Environmental Science: Water Research & Technology* **2020,** *6*(7), 1869-1879.
514. Zhang, X.; Fan, X.; Wang, X.; Deng, T.; Liu, E.; Bo, C., *Colloids and Surfaces A: Physicochemical and Engineering Aspects* **2020**, 124875.
515. Ma, X.; Chen, Q.; Liu, G.; Zhou, Y.; Ma, D.; Xin, S.; Yu, C.; Zhang, B.; Xin, Y., *Chemical Engineering Science* **2020**, 115844.
516. Liu, D.; Li, H.; Gao, R.; Zhao, Q.; Yang, Z.; Gao, X.; Wang, Z.; Zhang, F.; Wu, W., *Journal of Hazardous Materials* **2020**, 124309.

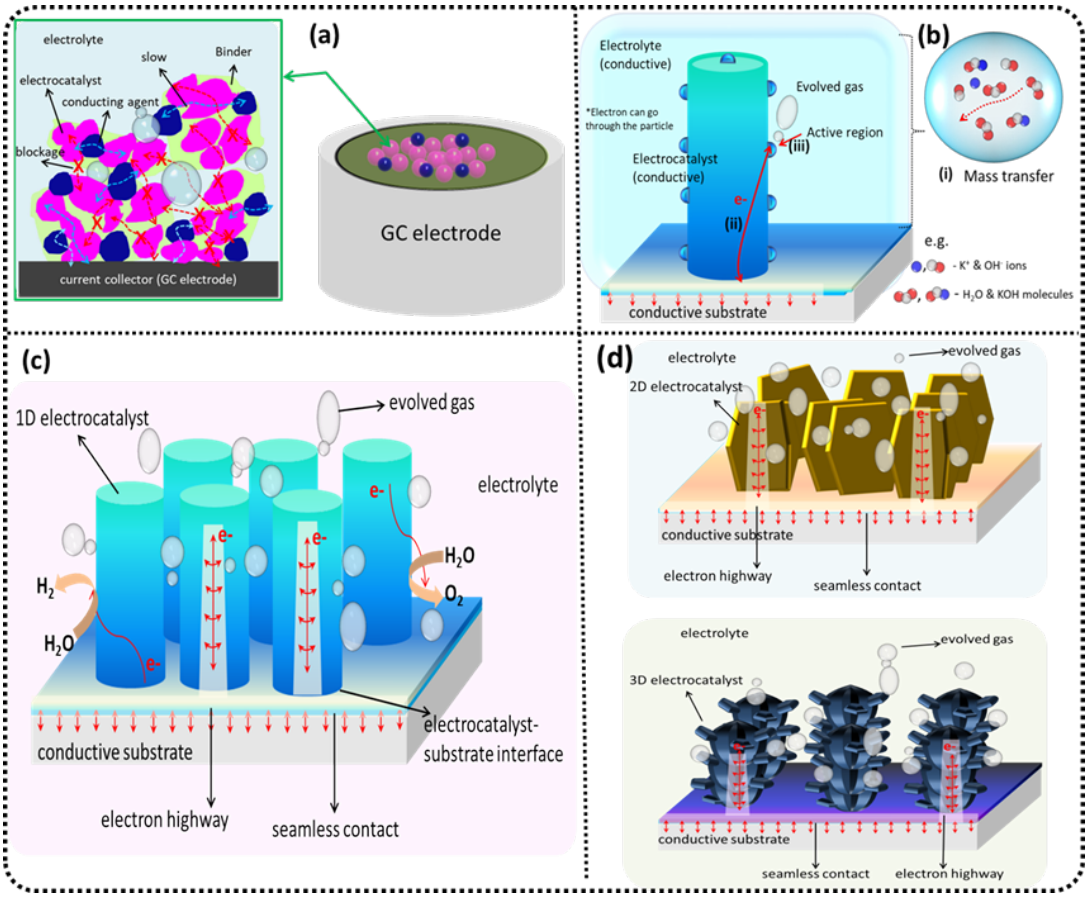

Figure 1 Schematic representation of structural and gas-involved electrochemical features of: (a) conventional powder based catalysts coated on glassy carbon (GC; as a current collector) with binders and conductive additives. (b) Electrochemical reactions on nano- and micro-structured binder-free electrodes and the three main reaction steps: (i) mass transfer process; (ii) electron transfer; and (iii) surface reaction to realize robust activity. Physical models of binder-free electrodes with *in-situ* grown (c) 1D, and (d) 2D and 3D nano- and-micro structured catalysts on the conductive substrates, represent the feasibility of more exposed active sites and facile charge transport to reach outstanding water splitting performance.

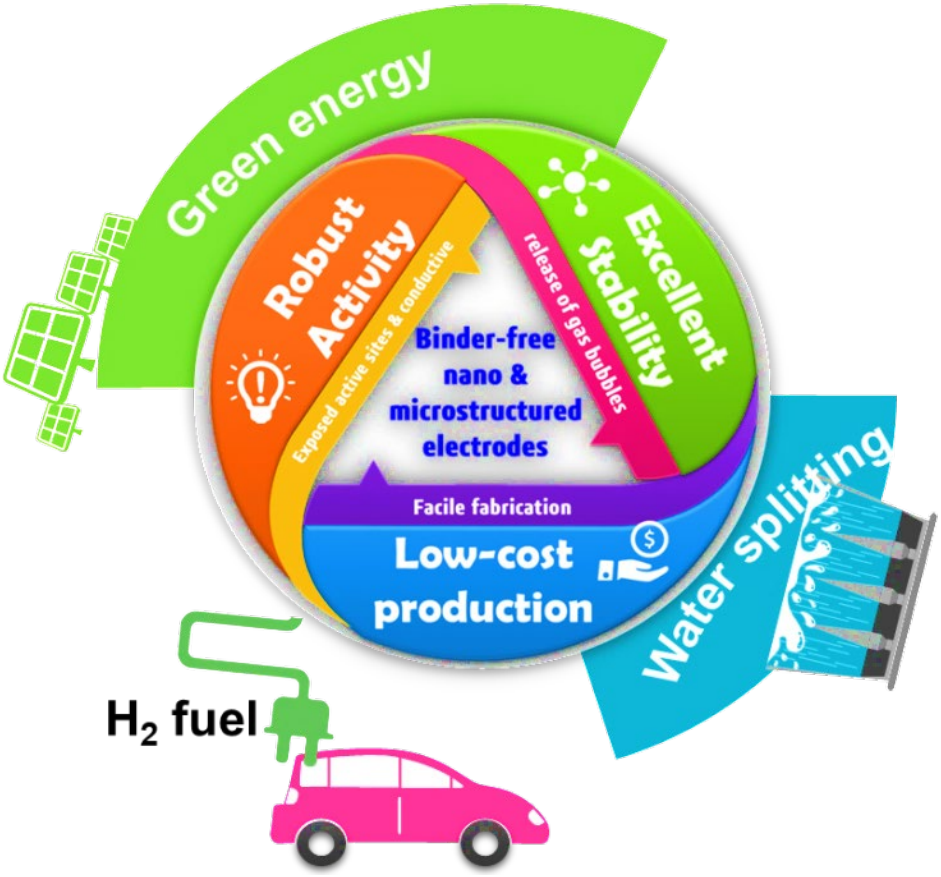

Scheme 1 Key properties of binder-free electrodes for overall water splitting

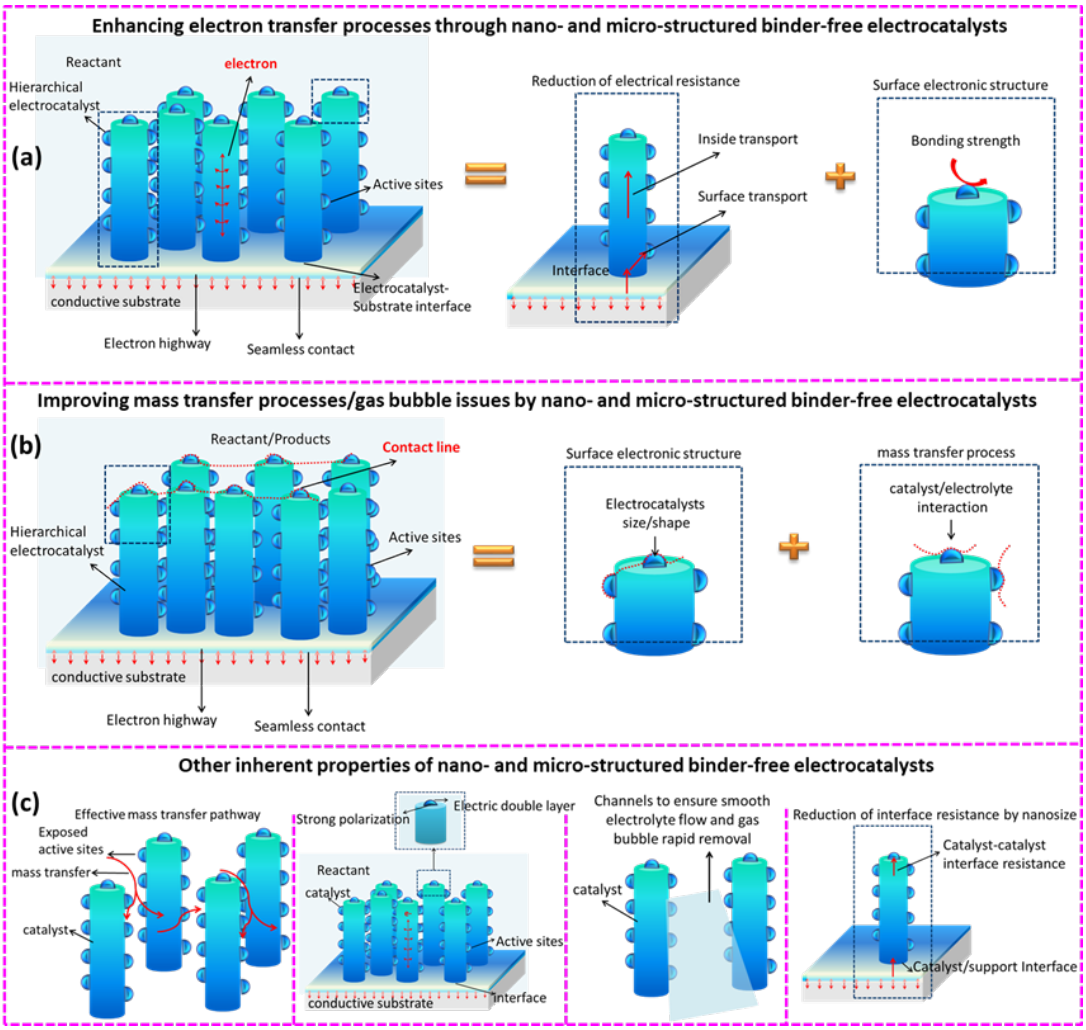

Figure 2 Schematics of several main inherent principles of in-situ grown binder-free electrocatalysts/support by engineering nano- and micro-structures. Modulation of electrochemical reactions and performances through (a) electron transfer, and (b) mass transfer processes. (c) Other key prospects of nano- and micro-structured binder-free electrodes for bi-functional water splitting including effective mass transfer pathway through nanoscale catalyst morphology, charge transfer through the electric double layer and strong polarization through low overpotential, the channel for catalyst-electrolyte interplay, and the bi-functional electrocatalytic performance enhancement through interface resistance reduction using nanoscale engineering.

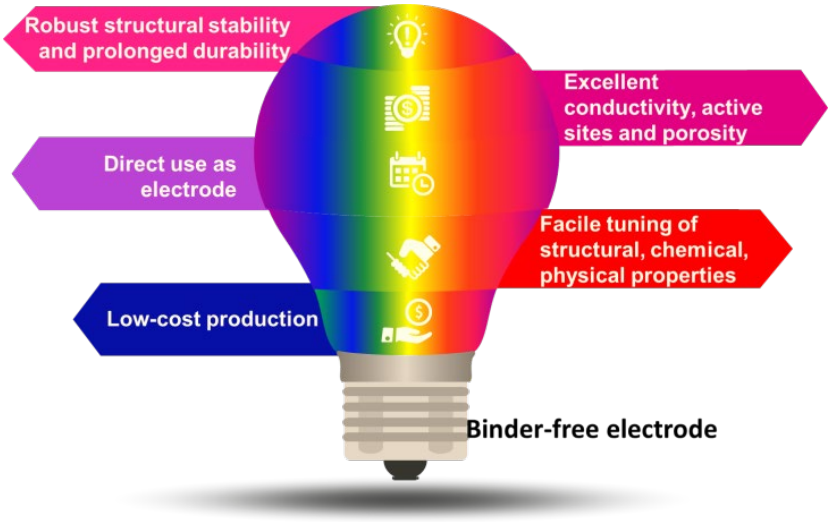

Scheme 2. Main features of binder-free electrodes

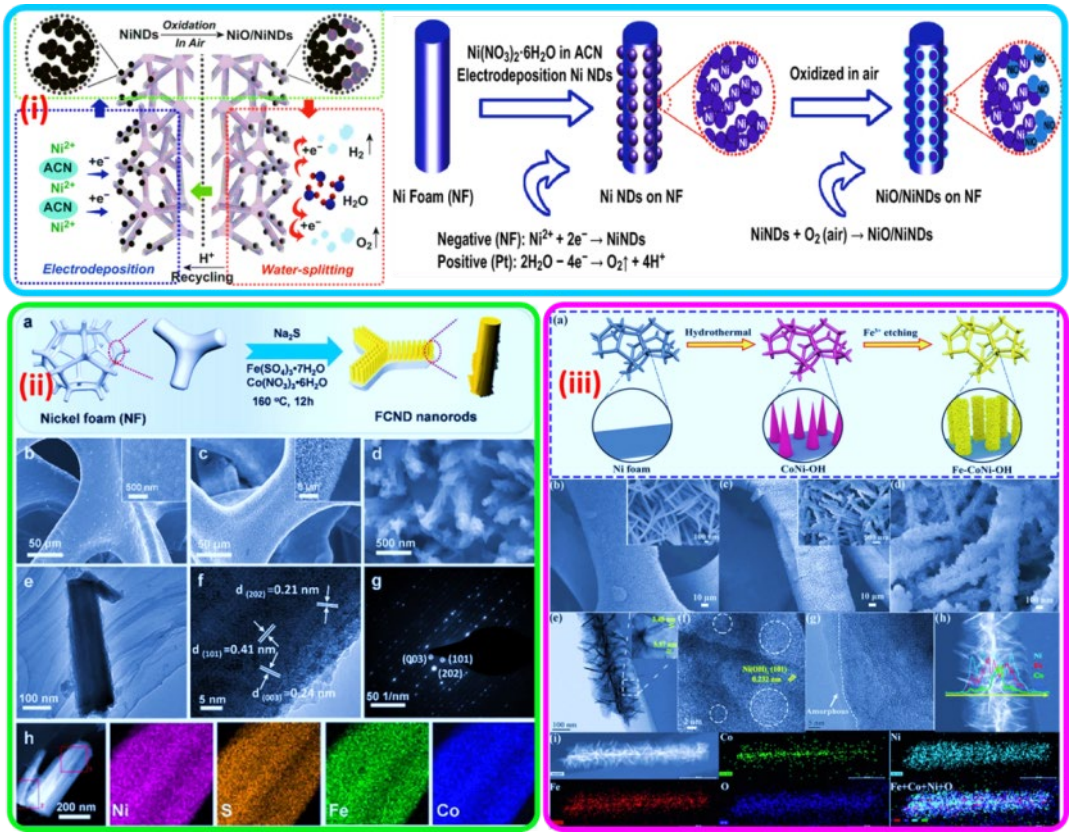

Figure 3 (i) Schematic of the fabrication process of NiO/NiND composite on Nickel foam (NF). Reproduced from ref[112] with permission from Springer, copyright 2019. (ii) (a) Schematic of the synthesis process for free-standing Fe, Co, and Ni ternary transition metal dichalcogenide (FCND) on NF, (b) SEM images of the ND nanoparticles (c-f). SEM, TEM, and HR-TEM images of the as-prepared FCND nanorod array at different magnifications, and (g-h) SAED pattern and elemental mapping of the FCND nanorod. Reproduced from ref[113] with permission from Elsevier, copyright 2021. (iii) (a) Schematic of the synthesis of Fe-CoNi-OH. SEM images of (b) CoNi-OH and (c, d) Fe-CoNi-OH at different magnifications (e) TEM image, (f, g) HRTEM images, (h) EDS line scan, and (i) Dark-field TEM (DF-TEM) with the elemental mapping of Fe-CoNi-OH. Reproduced from ref[114] with permission from Elsevier, copyright 2021.

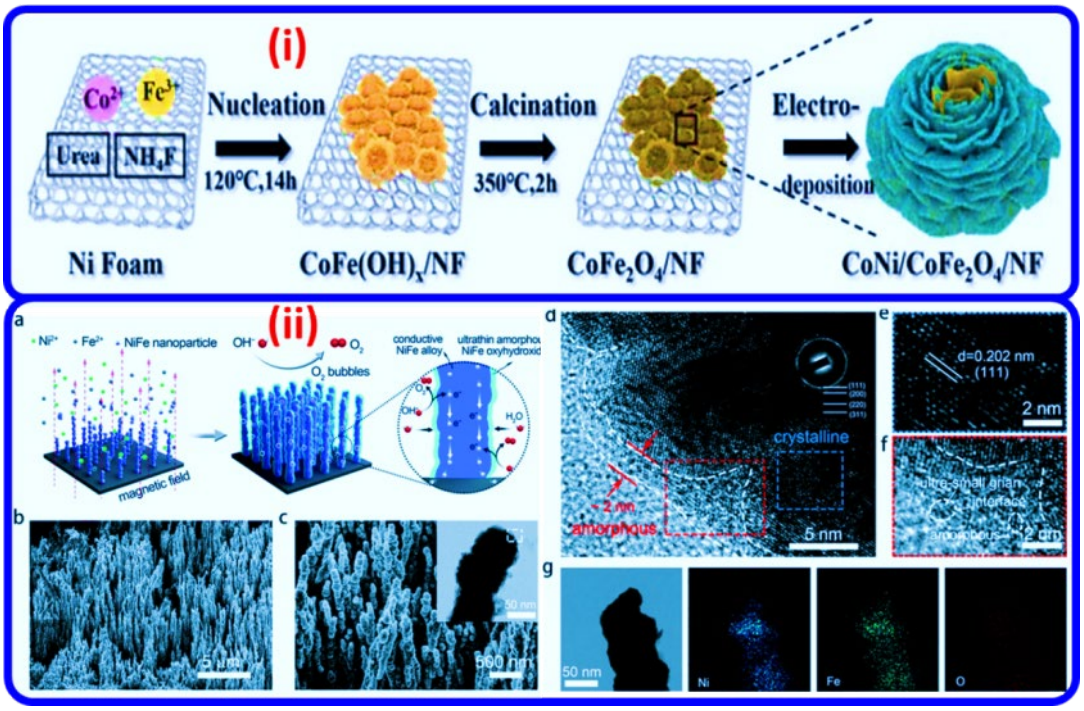

Figure 4 (i) Schematic of the formation process of the porous CoNi/$CoFe_2O_4$/NF composite electrode. Reproduced from ref[105] with permission from RSC, copyright 2018. (ii) (a) Schematic of the synthesis of the Ni_xFe_{1-x}–AHNA nanowire array and its catalytic role for the OER. (b-f) Microscopic images of Ni_xFe_{1-x}–AHNAs at different magnifications, and (g) EDX mapping of Ni, Fe, and O elements. Reproduced from ref[116] with permission from RSC, copyright 2020.

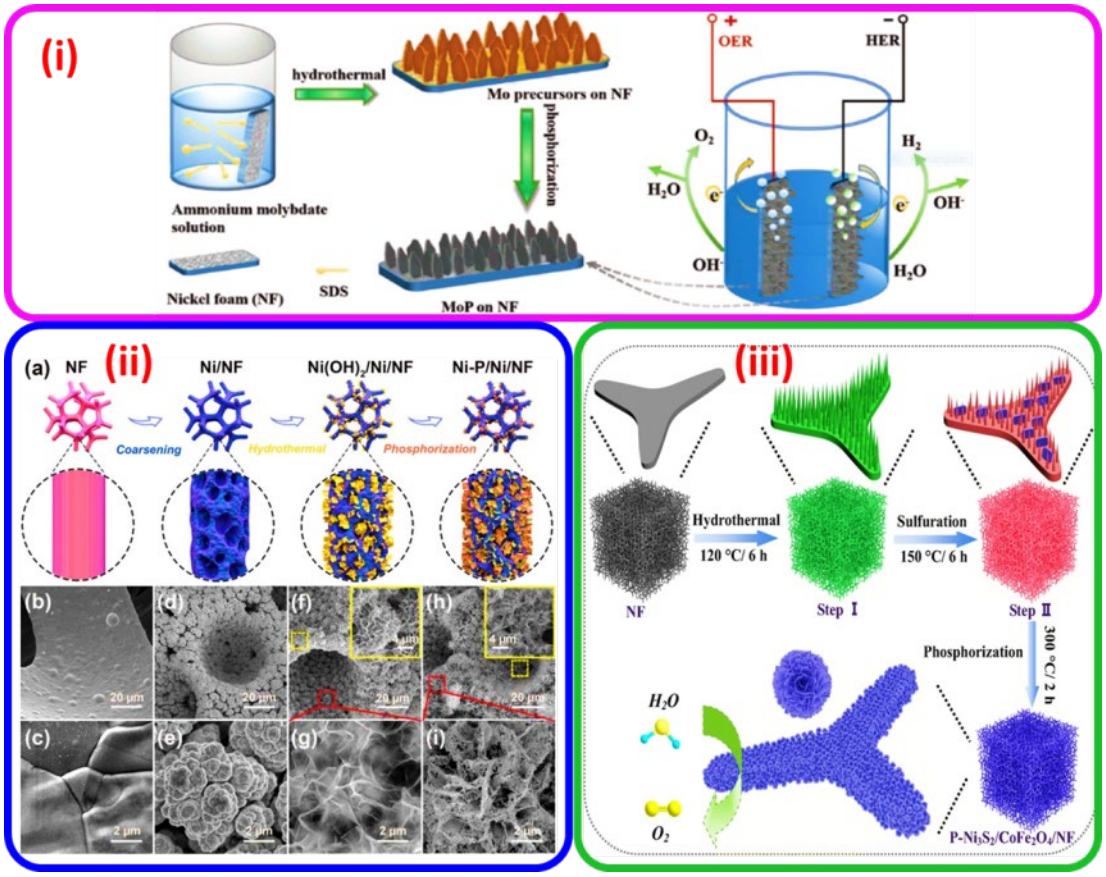

Figure 5 (i) Schematic of two step-syntheses of porous MoP nanosheet arrays on NF. Reproduced from ref[117] with permission from Wiley, copyright 2018, (ii) (a) Schematic of the synthetic route for Ni-P/Ni/NF; SEM images of NF (b, c), Ni/NF (d, e), $Ni(OH)_2$/Ni/NF (f, g) and Ni-P/Ni/NF (h, i) at different magnifications. Reproduced from ref[120] with permission from Elsevier, copyright 2021, and (iii) Scheme of constructing P-Ni_3S_2/$CoFe_2O_4$/NF electrode. Reproduced from ref[121] with permission from Elsevier, copyright 2021.

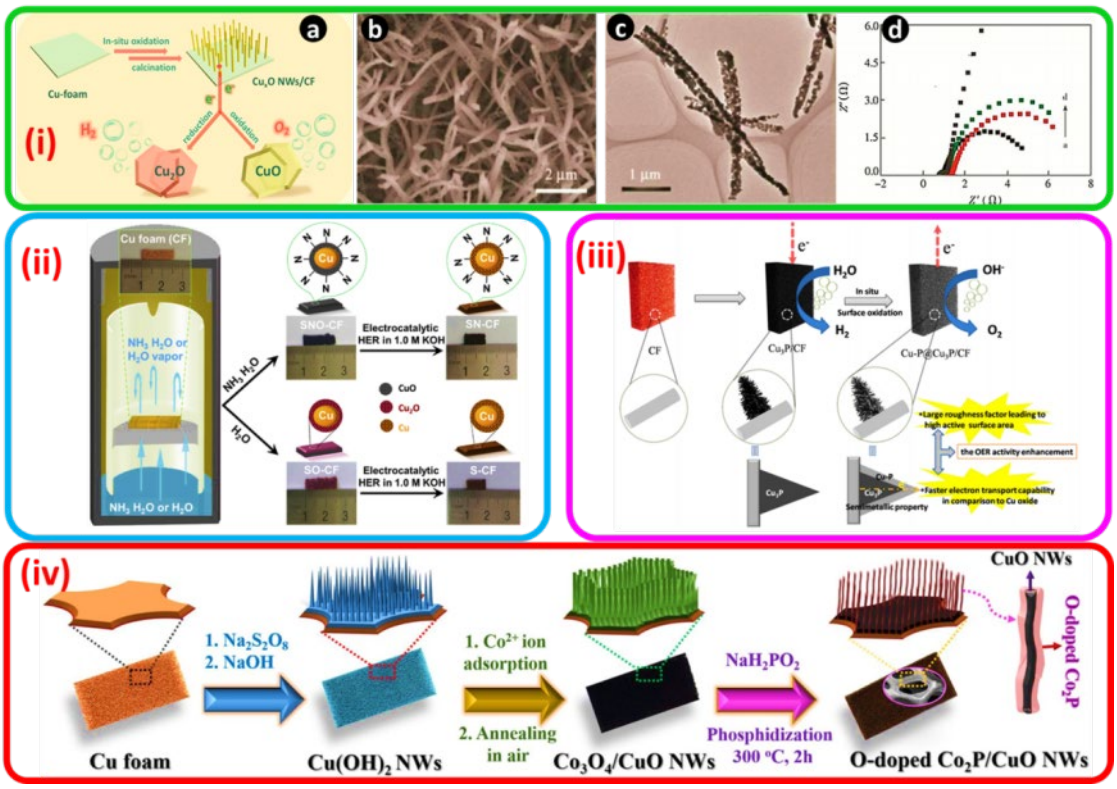

Figure 6 (i) (a) Schematic of *in-situ* fabrication of Cu_xO nanowires array consisting of CuO and Cu_2O on Cu foam (Cu_xO NWs/CF) and (b-d) microscopic images and EIS Nyquist plots at 0.135 V for Cu_xO NWs/CF. Reproduced from ref[135] with permission from Elsevier, copyright 2020. (ii) Schematic of the preparation process of the SN-CF electrode *via* vapor ammoniation followed by *in-situ* electrocatalytic reduction. Reproduced from ref[136] with permission from Elsevier, copyright 2020. (iii) Schematic of preparation of cedarlike Cu_3P/CF as a 3D cathode for water reduction and nanohybrid of Cu-P@Cu_3P/CF by *in-situ* surface oxidation and its water splitting mechanism. Reproduced from ref[138] with permission from ACS, copyright 2016, and (iv) Schematic of preparation of O-doped Co_2P/CuO NWs. Reproduced from ref[139] with permission from Elsevier, copyright 2020.

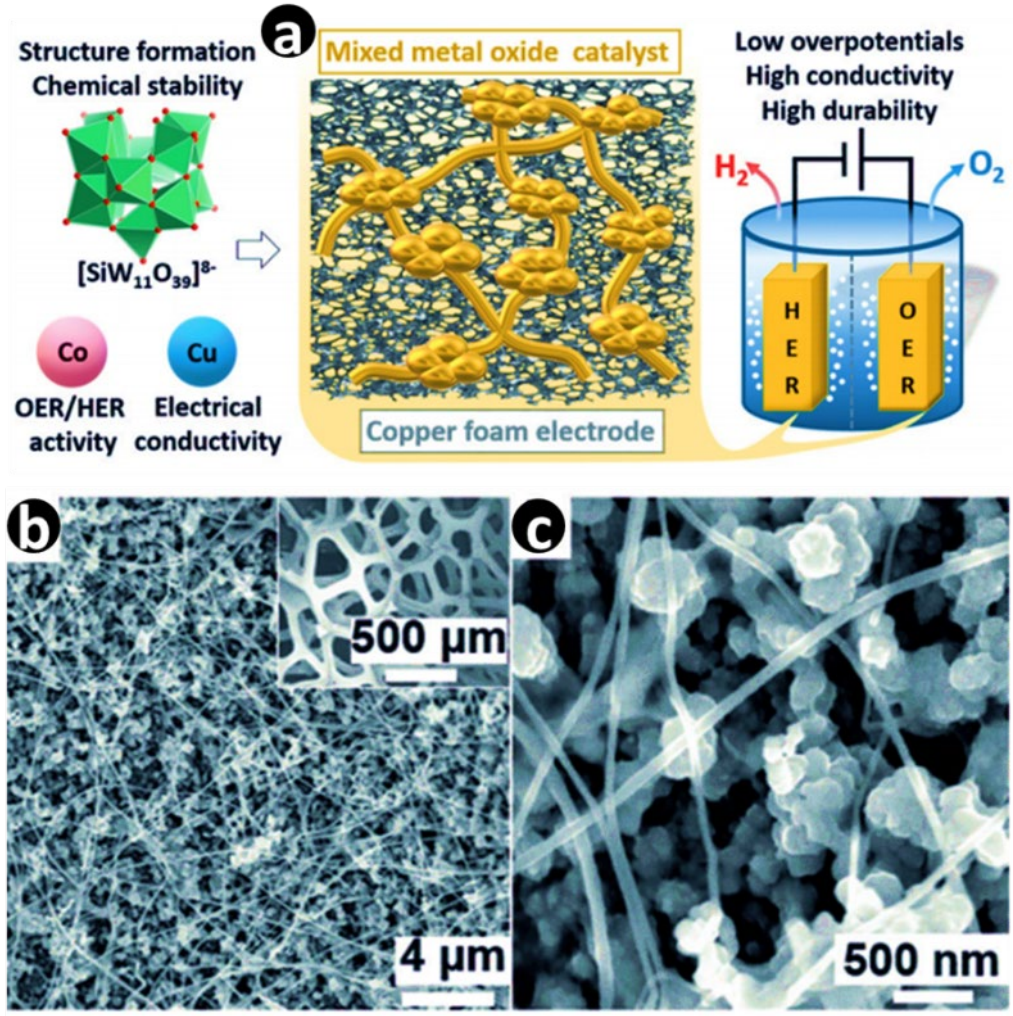

Figure 7 (a) Schematic of hydrothermal deposition of cobalt, copper, and tungsten oxide precursors on Cu foam electrode and (b-c) Microscopic images of nanowire structured Co-Cu-W oxide catalyst. Reproduced from ref[143] with permission from Wiley, copyright 2019.

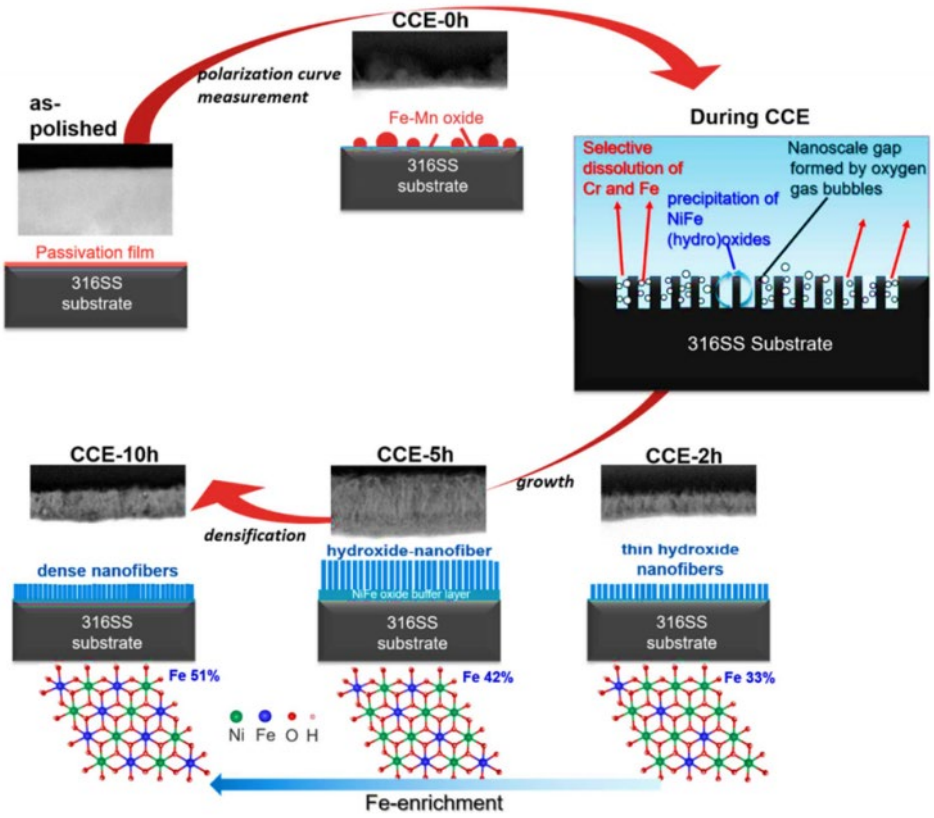

Figure 8 Schematic of time evolutions of the hetero-layered nanostructures prepared on constant current density electrolysis (CCE). Reproduced from ref[150] with permission from ACS, copyright 2019.

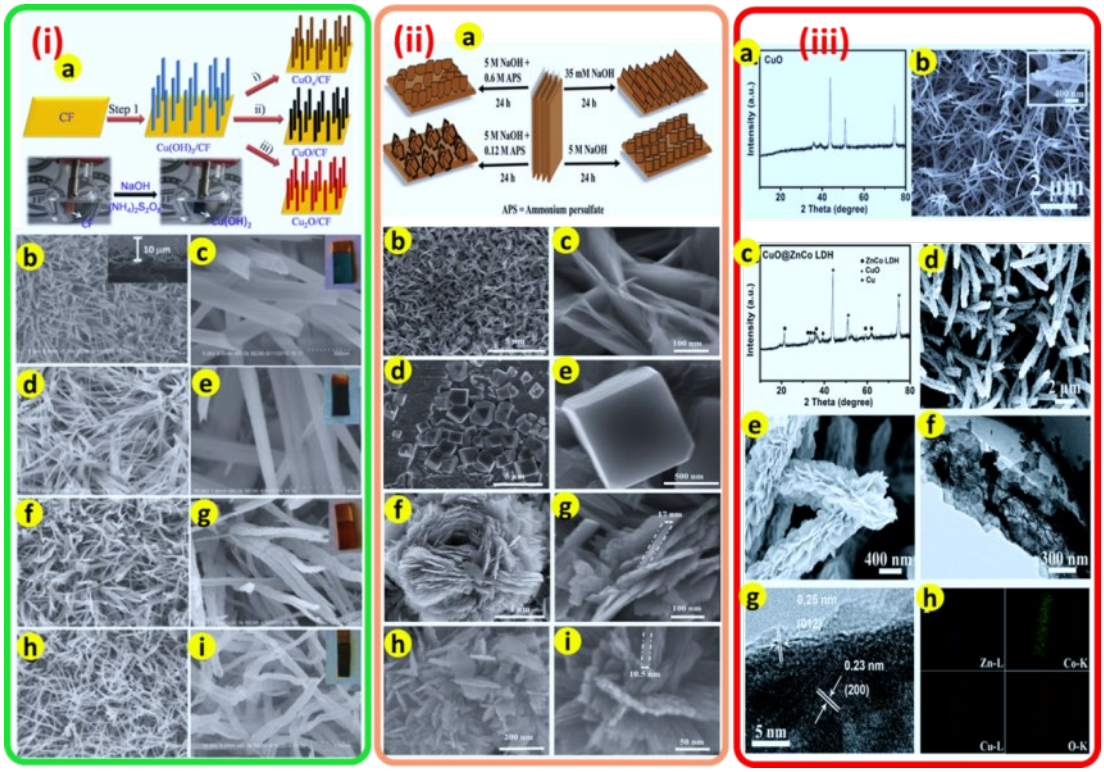

Figure 9 (i) (a) Illustration of the *in-situ* fabrication of Cu-based nanowire arrays on the CF surface, with photographs of CF before and after oxidation treatment in an aqueous solution of NaOH and $(NH_4)_2S_2O_8$ for 18 min. SEM images of (b,c) the as-prepared $Cu(OH)_2$/CF (inset: cross-section), (d,e) CuO/CF, (f,g) Cu_2O/CF, and (h,i) CuO_x/CF films. Inset: photographs of the corresponding Cu-based films. Reproduced from ref[163] with permission from Wiley, copyright 2016. (ii) Schematic of fabrication of various CuO nanostructures on Cu foil, (b,c), (d,e), (f,g), and (h,i) are the SEM images (lower and higher resolution) of CuO nanosheets, nanocubes, nanoflowers, and nano leaves respectively. Reproduced from ref[164] with permission from Elsevier, copyright 2020, and (iii) XRD pattern and SEM of hydrothermally grown CuO/CF (c-h) XRD pattern, microscopic images, and (f) EDX elemental mapping of Zn, Co, Cu, and O for CuO@ZnCo LDH/CF. Reproduced from ref[165] with permission from RSC, copyright 2020.

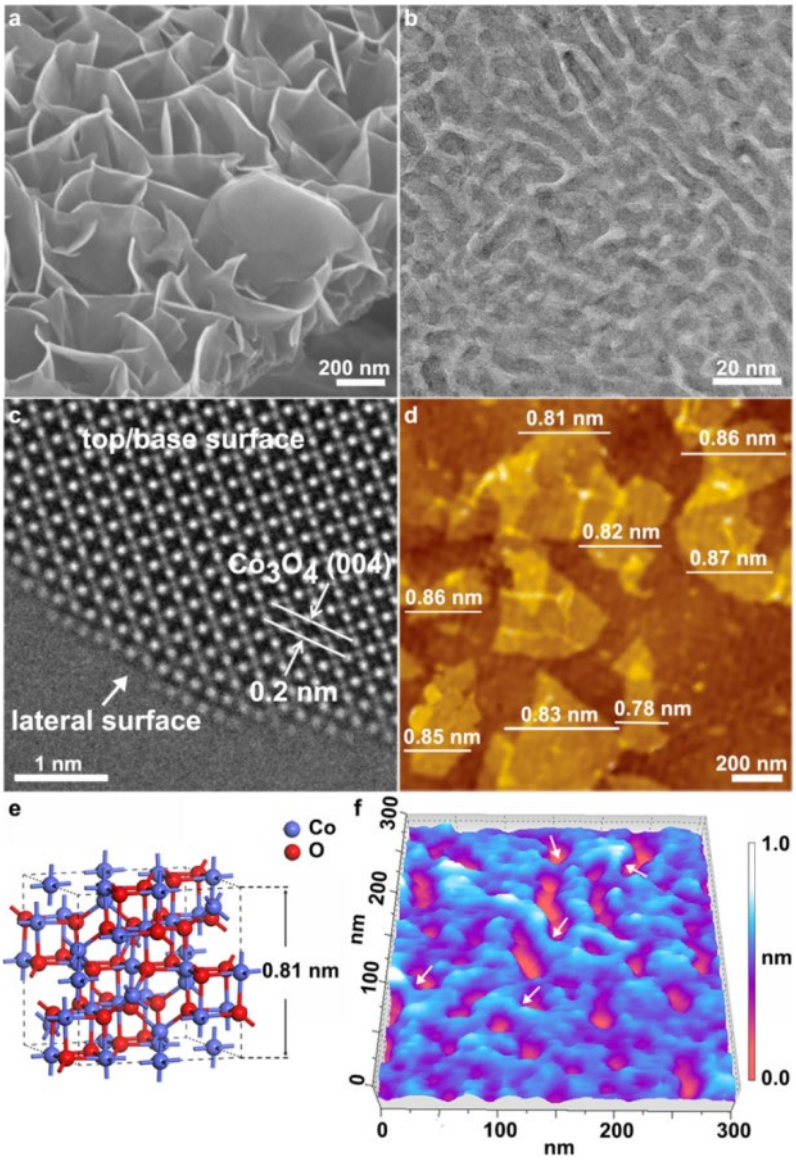

Figure 10 (a) SEM image of an NPCoO-UCS array, (b,c) Low-magnification and high-resolution TEM images of NPCoO-UCSs, (d) Top-view AFM image of NPCoO-UCSs, (e) 3D model of the standard unit cell of Co_3O_4, defined by six (001) facets, and (f) 3D AFM image of an NPCoO-UCS. Arrows indicate several typical ligaments with lateral surfaces. Reproduced from ref[172] with permission from Elsevier, copyright 2018.

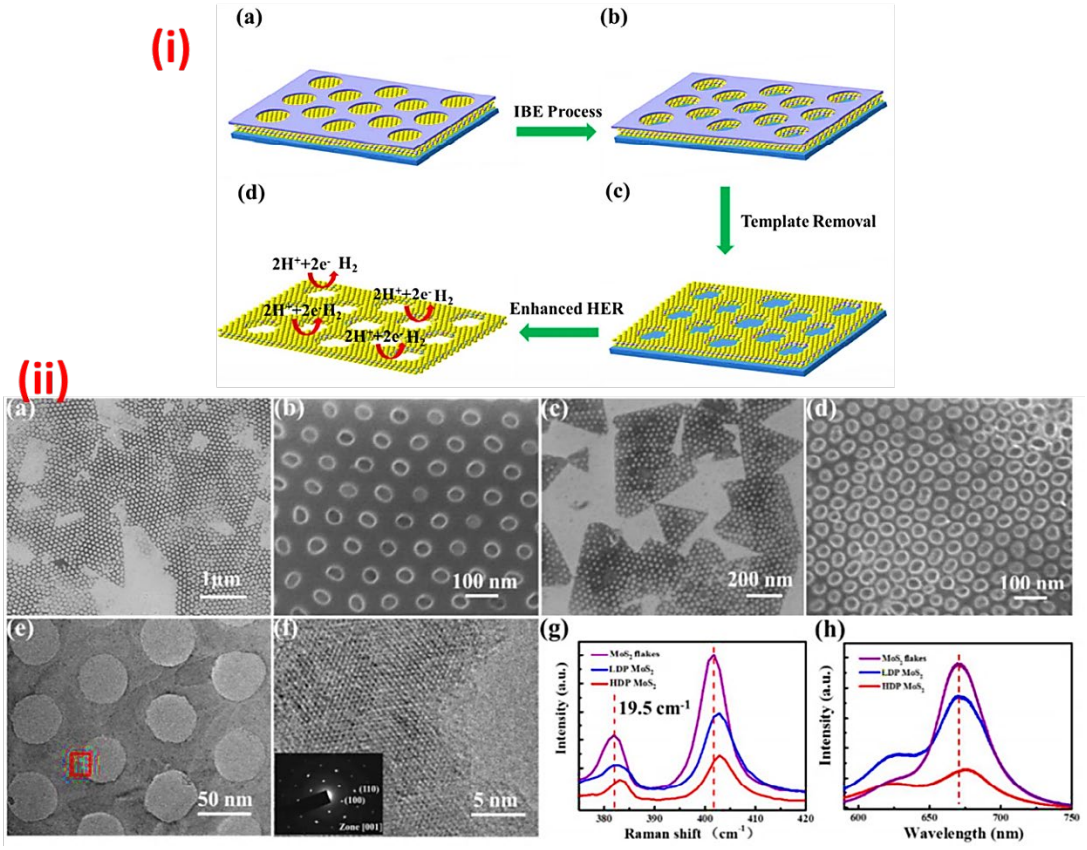

Figure 11 (i) (a) Monolayer MoS_2 by CVD growth covered with UTAM, (b) Nanopatterning by the UTAM-assisted IBE process, (c) Nanopore arrays of patterned monolayer MoS_2 after the removal of UTAM. (d) Schematic illustration of enhanced HER performance. (ii) (a,c) SEM images of low density porous (LDP) and high density porous (HDP) monolayer 2H MoS_2 flakes, and (b,d) the corresponding magnified SEM images. (e)TEM image of the LDP monolayer 2H MoS_2 formed by UTAM-assisted IBE, and (f) High-resolution HR-TEM image of the pore edge (marked in (e)), the inset shows the corresponding SAED pattern. (g) Raman and (h) PL spectra of LDP, HDP, and pristine monolayer 2H MoS_2 flake. Reproduced from ref[179] with permission from ACS, copyright 2018.

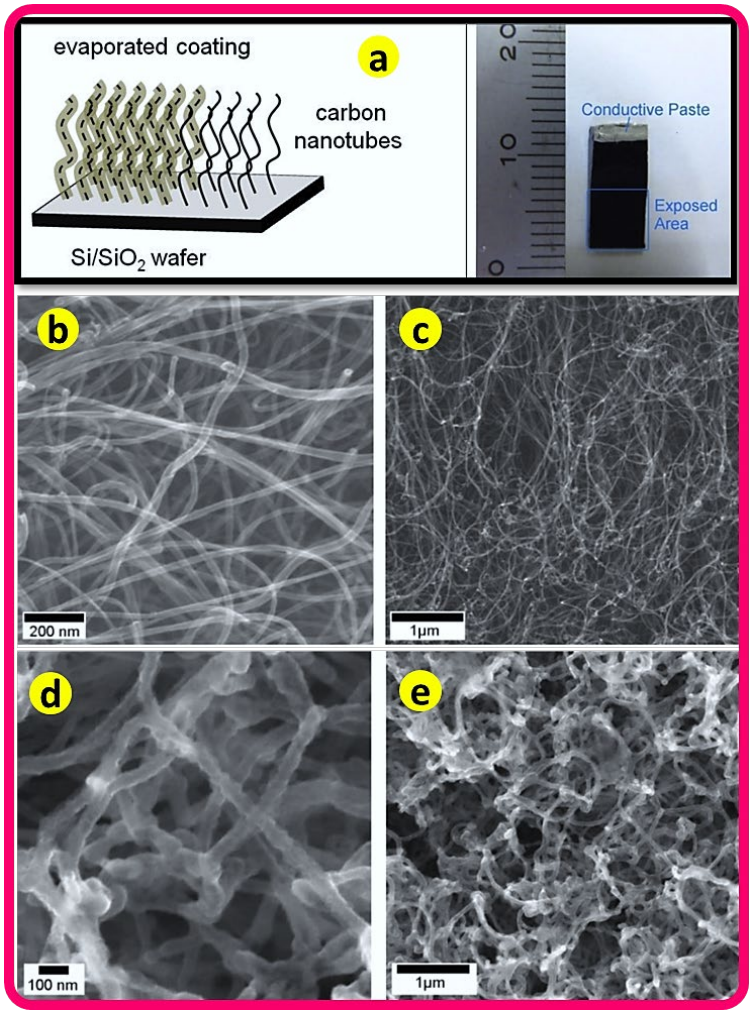

Figure 12 (a) Schematic of CNT/metal electrode; (right) photo of a final electrode. Ruler scale bar is in mm, SEM images of pristine CNTs (b-c), and (d-e) CNT/Co at different magnifications. Reproduced from ref[183] with permission from Elsevier, copyright 2017.

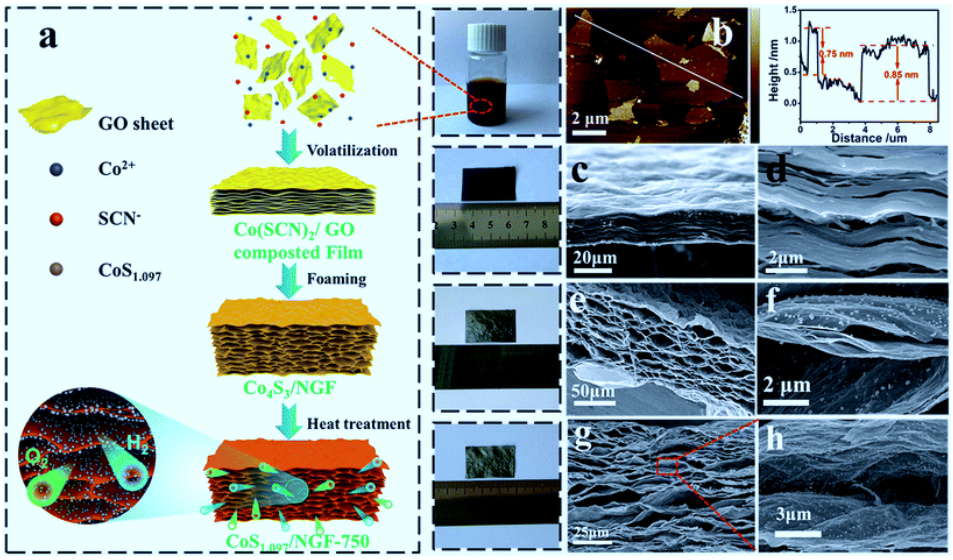

Figure 13 (a) Schematic for the stepwise fabrication of $CoS_{1.097}$/NGF-750, and (b) AFM image and the thickness of graphene oxide (GO) sheets. Cross-sectional SEM images of the $Co(SCN)_2$/GO composite film (c and d); Co_4S_3/NGF (e and f); and $CoS_{1.097}$/NGF-750 (g and h), respectively. Reproduced from ref[186]with permission from RSC, copyright 2018.

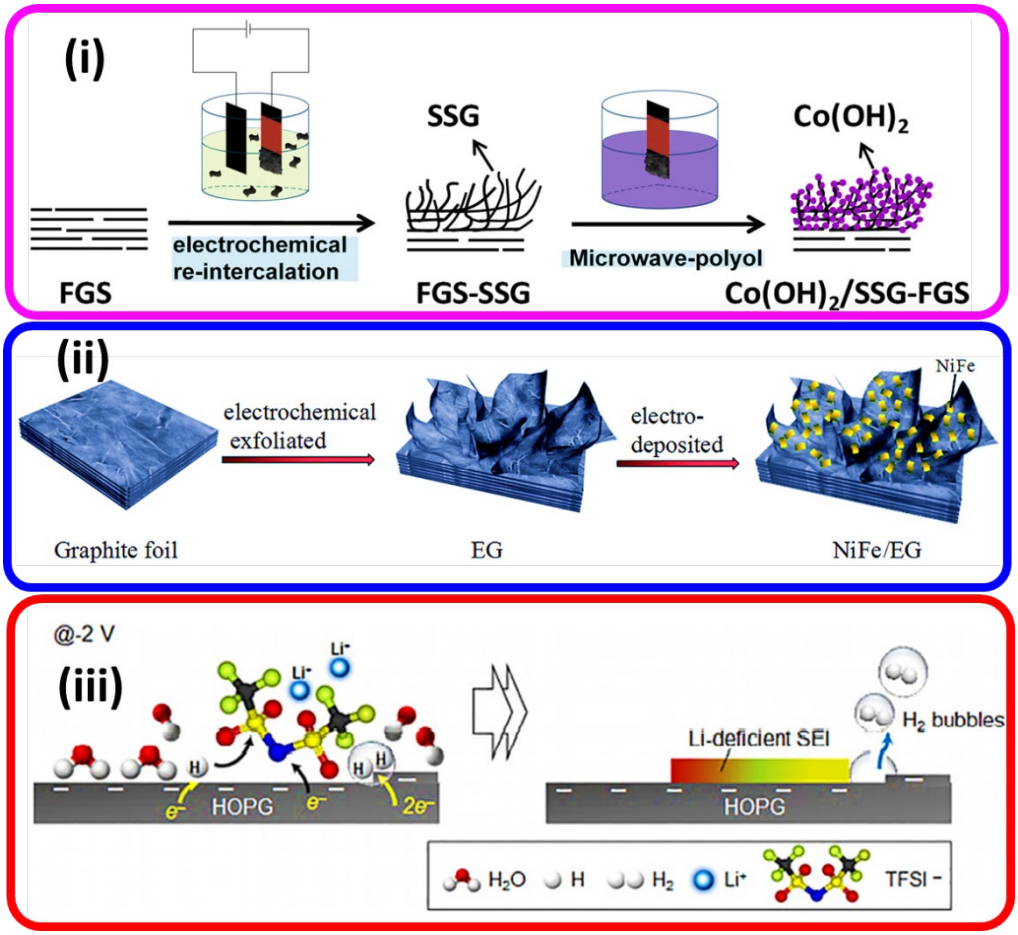

Figure 14 (i) Schematic for the preparation of $Co(OH)_2$/SSG-FGS. Reproduced from ref[189] with permission from Elsevier, copyright 2018. (ii) Fabrication process of the NiFe/EG electrode. Reproduced from ref[191] with permission from RSC, copyright 2017, and (iii) SEI formation process at −2 V. Reproduced from ref[195] with permission from ACS, copyright 2020.

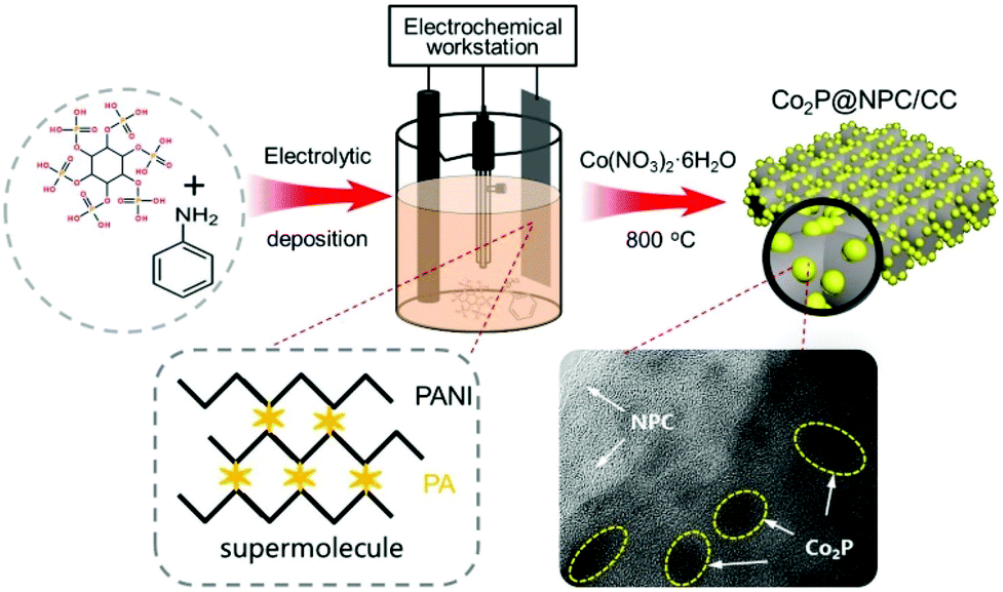

Figure 15 Schematic of the preparation of Co_2P@NPC. Reproduced from ref[198] with permission from RSC, copyright 2018.

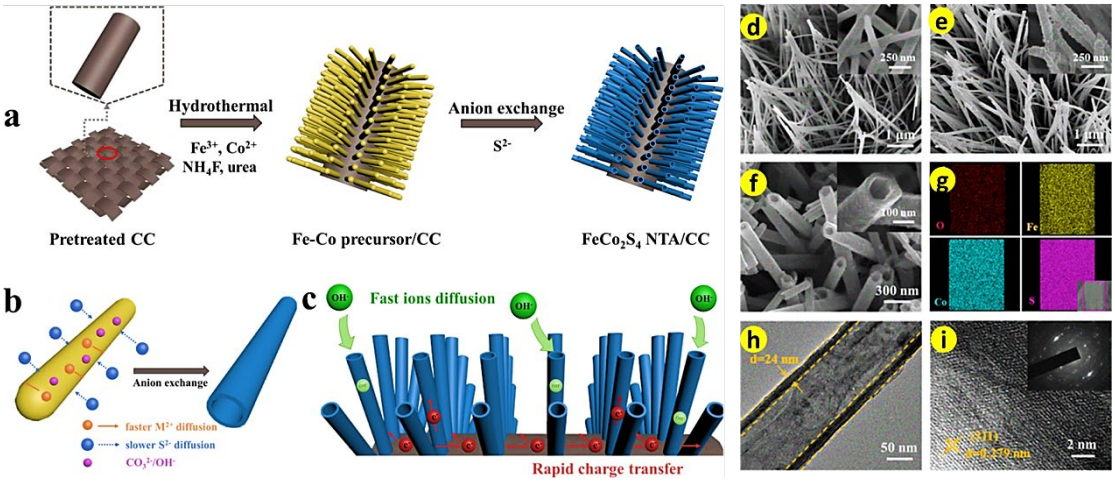

Figure 16 (a-b) Schematic of the synthesis of the $FeCo_2S_4$ nanotube arrays (NTA's) on CC through a two-step method by anion exchange reactions; (c) Schematic of the rapid electrons/ions transportation within the $FeCo_2S_4$ NTA/CC electrode during the OER process. SEM images of (d) Fe–Co precursor NWA/CC and (e,f) $FeCo_2S_4$ NTA/CC. (g) EDS elemental mapping images of $FeCo_2S_4$ NTA/CC and the inset is the corresponding SEM image. (e) TEM and (f) HRTEM image of $FeCo_2S_4$ NTA/CC, and the inset in (f) is the SAED pattern. Reproduced from ref[211] with permission from ACS, copyright 2019.

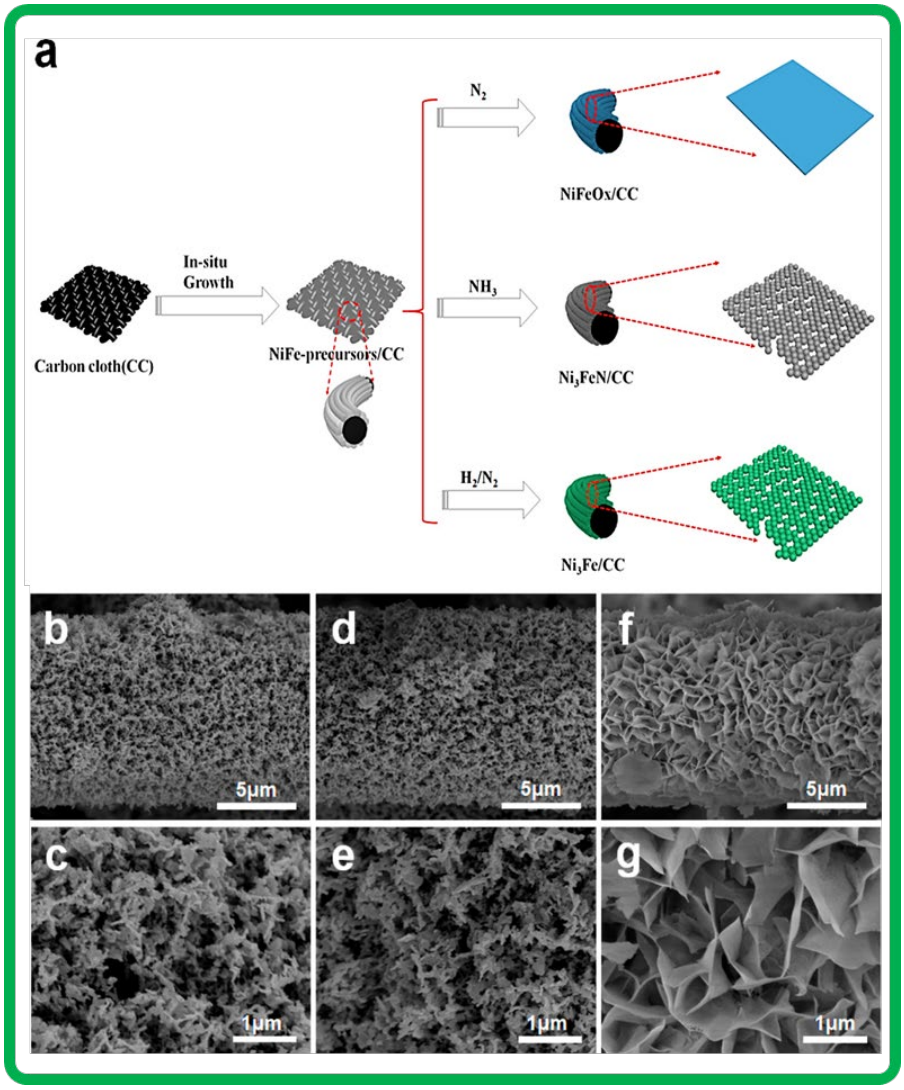

Figure 17 (a) Schematic of process for fabrication of NiFe based binder free electrodes at various conditions. SEM of (b,c) Ni_3FeN/CC, (d,e) Ni_3Fe/CC, and (f,g) $NiFeO_x$/CC. Reproduced from ref[207] with permission from ACS, copyright 2018.

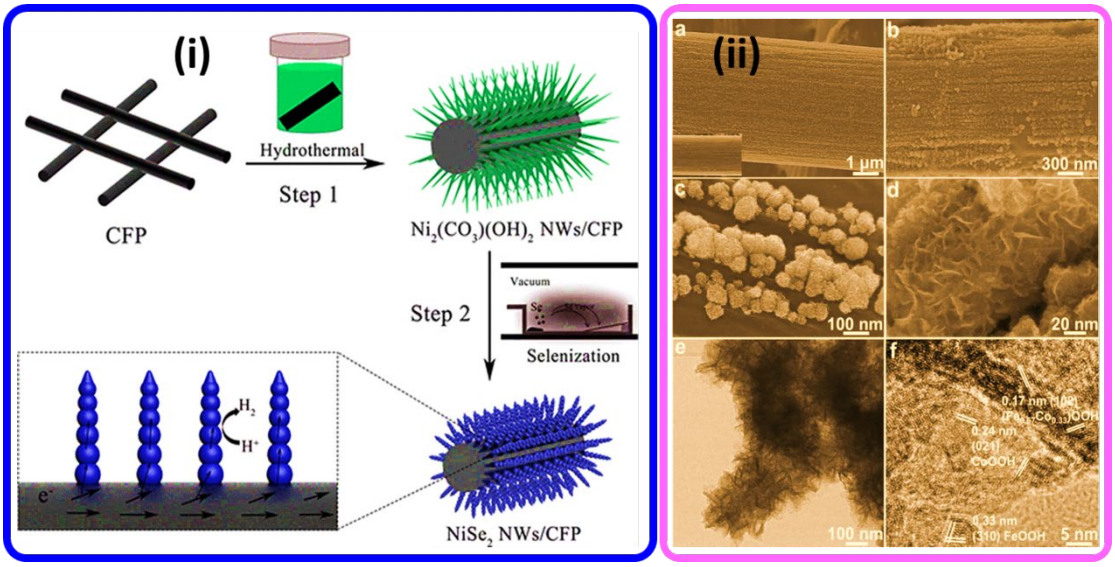

Figure 18 (i) Schematic of synthesizing $NiSe_2$ NW arrays on carbon fiber paper (CFP) *via* hydrothermal reaction followed by selenization. Reproduced from ref[215] with permission from ACS, copyright 2018. (ii) (a-d) FE-SEM, (e) TEM and (f) HR-TEM image of FeCo-MOF-EH. Inset of (a) SEM image of pure CFP. Reproduced from ref[227] with permission from Wiley, copyright 2020.

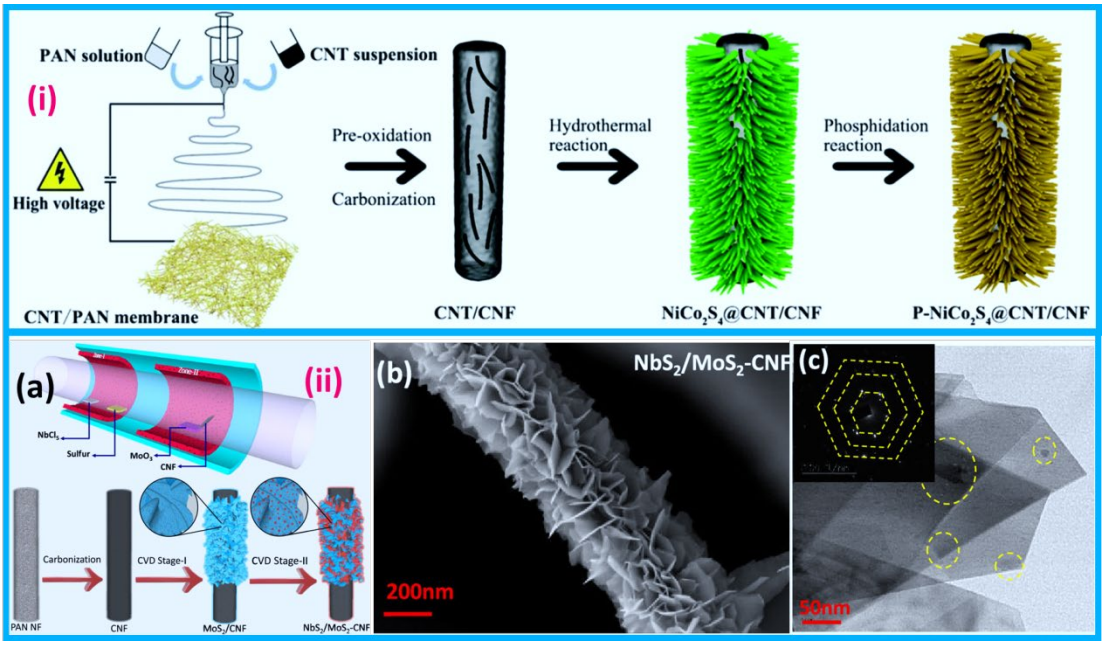

Figure 19 (i) Schematic of the preparation of P-$NiCo_2S_4$@CNT/CNF hybrid *via* a multi-step method. Reproduced from ref[232] with permission from RSC, copyright 2017. (ii) Schematic of one-step CVD synthesis of NbS_2/MoS_2-CNF heterostructure and (b-c) their microscopic images, inset is the SAED pattern of NbS_2/MoS_2. Reproduced from ref[230] with permission from ACS, copyright 2020.

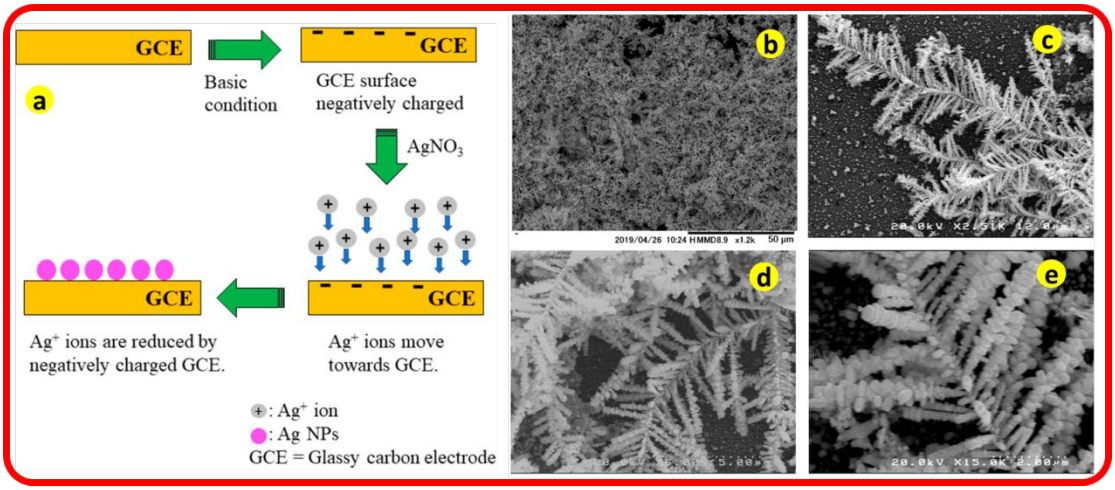

Figure 20 (a) Electroless deposition mechanism of silver particles onto a GCE and SEM images of the silver dendrite structure onto the GCE surface (b-e). Reproduced from ref[243] with permission from ACS, copyright 2020.

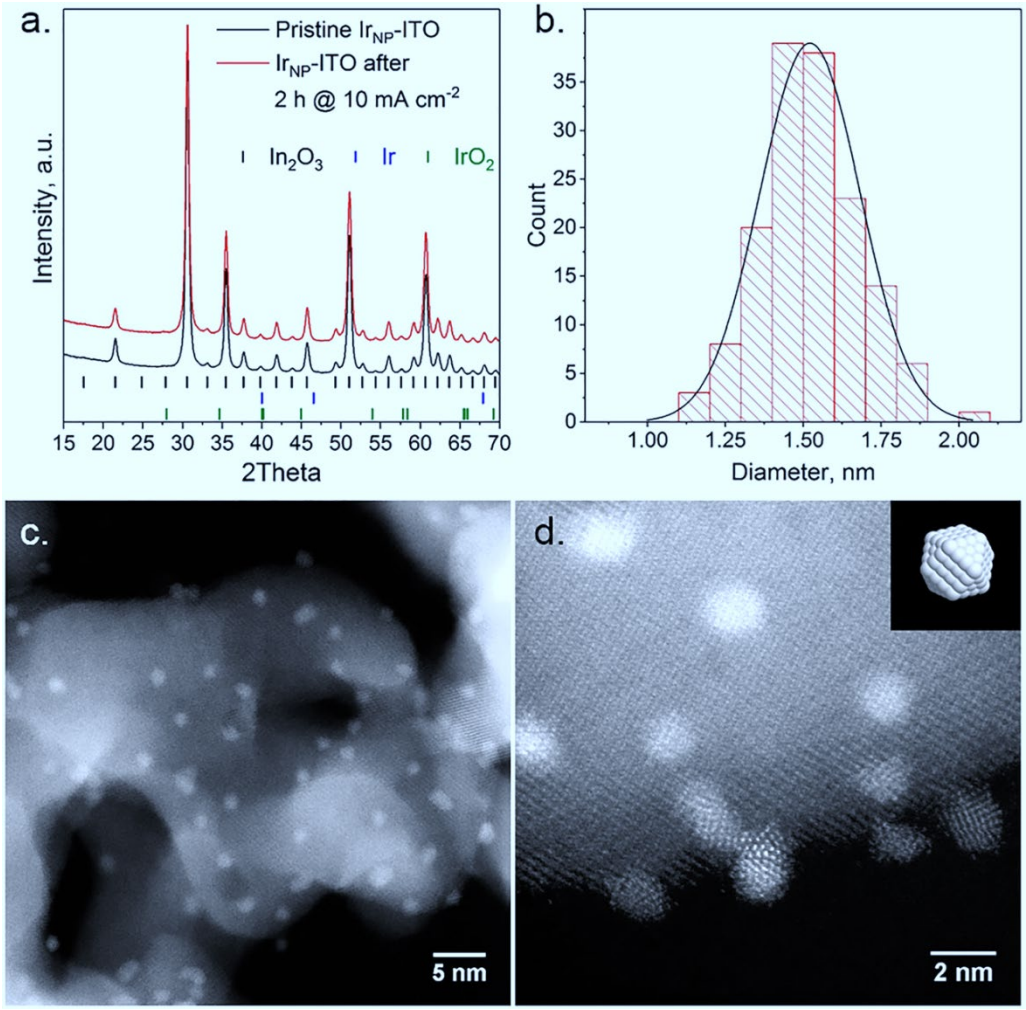

Figure 21 (a) XRD pattern of IrNP–ITO before (black line) and after 2 h at 10 mA cm^{-2} (red line). (b) Ir particle size distribution with the mean diameter of 1.5 ± 0.2 nm. (c, d) HAADF–STEM images of the pristine IrNP–ITO. Inset: 1.5 nm Ir particle of cuboctahedron shape. Reproduced from ref[250] with permission from ACS, copyright 2019.

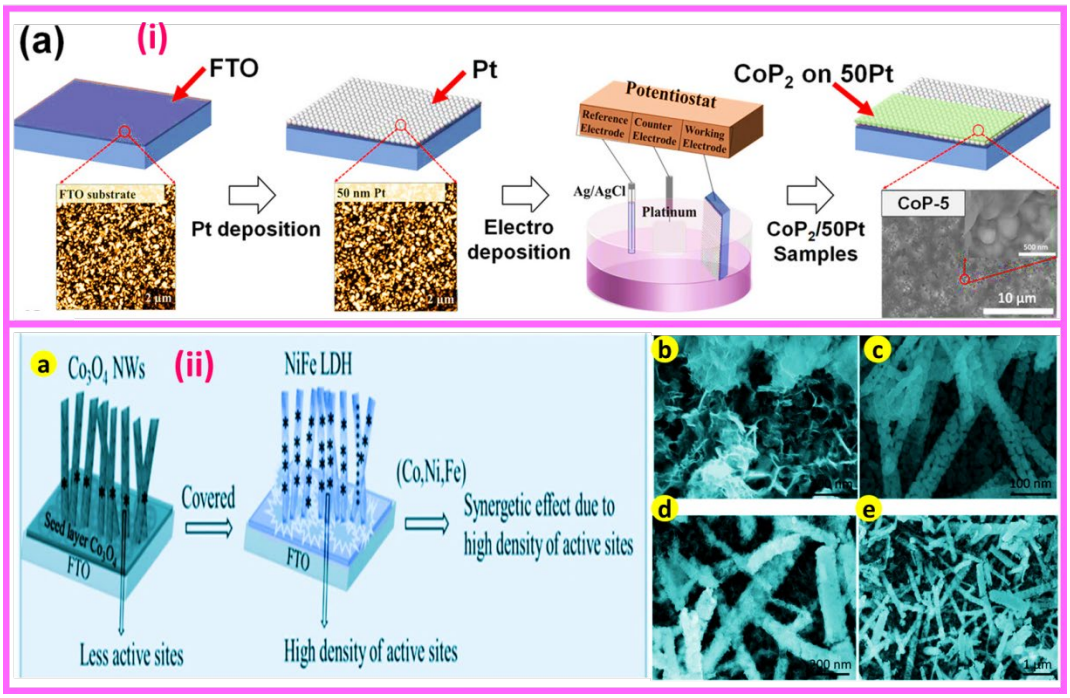

Figure 22 (i) (a) Schematic of the bi-functional CoP_2/Pt hybrid electrode fabrication process and SEM image of 50 nm Pt deposition on an FTO substrate (50 Pt), 5-cycle of CoP_2 synthesis directly on an FTO (CoP-5). Reproduced from ref[253] with permission from ACS, copyright 2020. (ii) Schematic showing the way to enrich active sites on NiFeLDH/ Co_3O_4 nanowires on FTO, and SEM images, (b) pure NiFeLDH, (c) pure Co_3O_4, and (c,d) NiFeLDH functionalized Co_3O_4 nanowires. Reproduced from ref[254] with permission from RSC, copyright 2019.

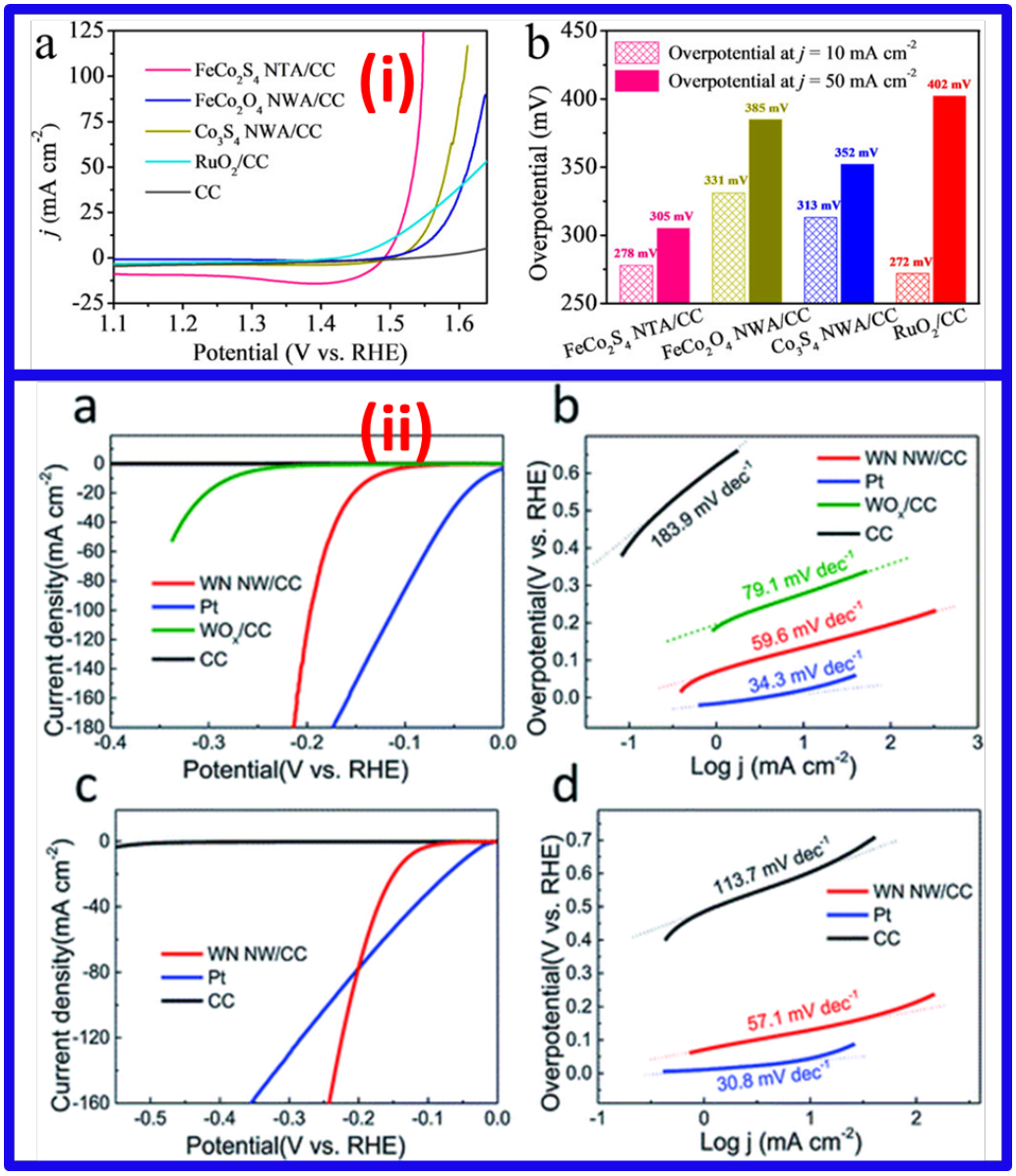

Figure 23 (i) (a) OER LSV polarization curves, and (b) Overpotentials at 10 and 50 mA cm^{-2}, in 1.0 M KOH at 25 °C. Reproduced from ref[211] with permission from ACS, copyright 2019. (ii) IR corrected LSV polarization curves, and (b) Corresponding Tafel plots of WN NW/CC in comparison with those of Pt, WO_x/CC, and CC in 0.5 M H_2SO_4, at a scan rate of 2 mV s^{-1}. (c) IR corrected LSV polarization curves and (d) Corresponding Tafel plots of WN NW/CC in comparison with Pt and CC in 1.0 M KOH. Reproduced from ref[279] with permission from RSC, copyright 2017.

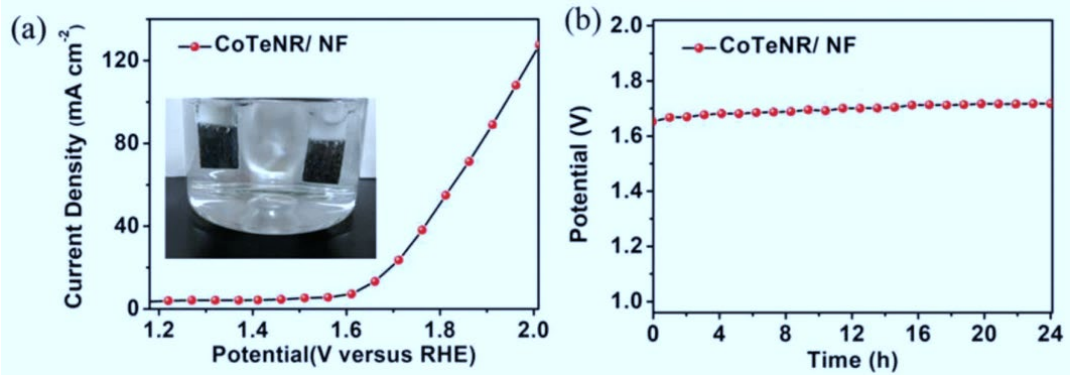

Figure 24 (a) LSV polarization curve of bi-functional CoTeNR/NF in 1.0 M KOH for overall water splitting at a scan rate of 5 mV s^{-1}. The inset is an image of overall water splitting. (b) Stability of overall water splitting at a current density of 10 mA cm^{-2}. Reproduced from ref[280] with permission from Wiley, copyright 2019.

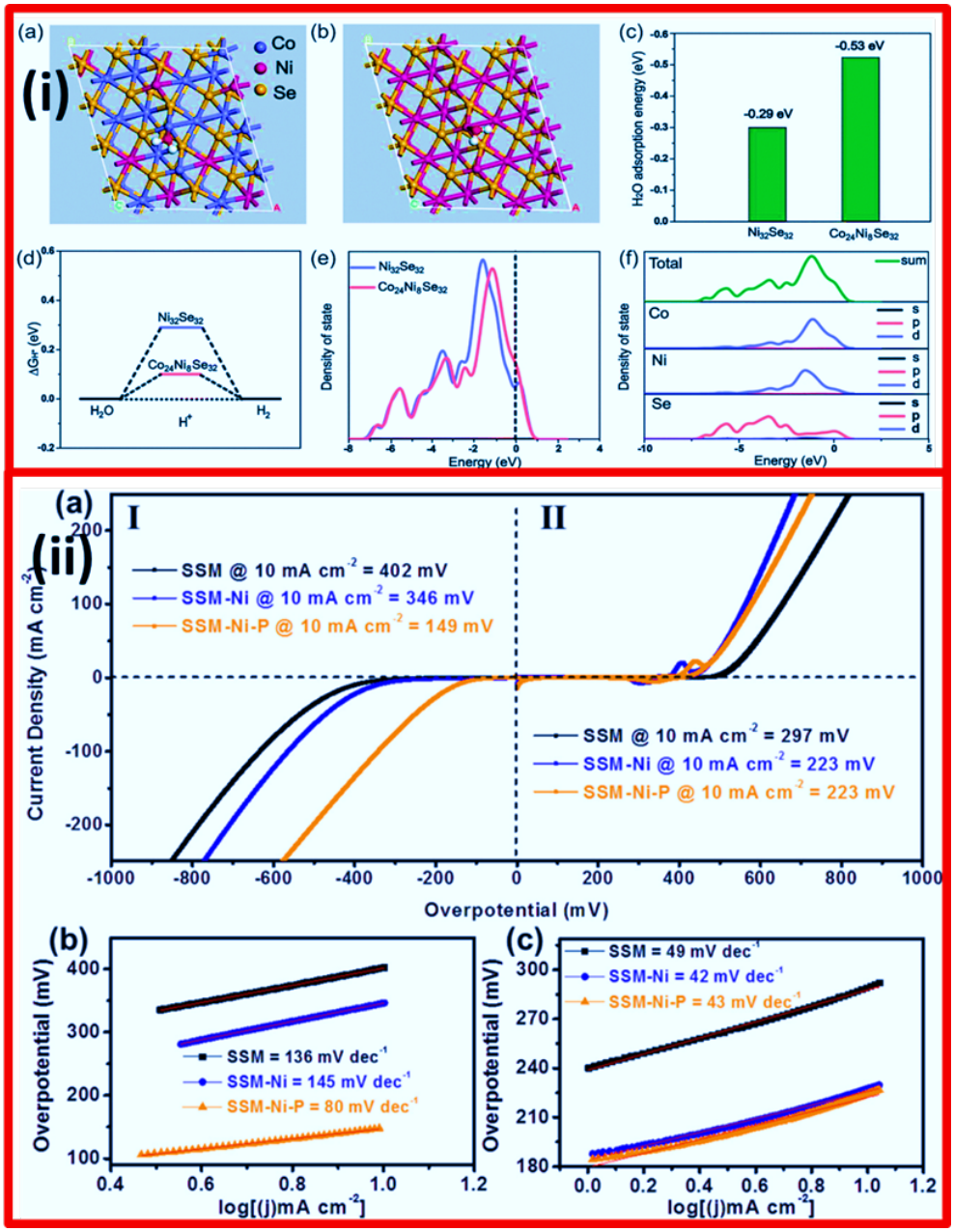

Figure 25 (i) (a–b) Top-view schematic models showing the H_2O molecule adsorbed on $Co_{24}Ni_8Se_{32}$ and $Ni_{32}Se_{32}$ surfaces. (c) DFT-calculated water adsorption energy and (d) HER free-energy for the $Co_{24}Ni_8Se_{32}$ and $Ni_{32}Se_{32}$ products. (e) Calculated density of states for $Co_{24}Ni_8Se_{32}$ and $Ni_{32}Se_{32}$ and (f) Total and partial density of states for $Co_{24}Ni_8Se_{32}$. Reproduced from ref[126] with permission from RSC, copyright 2019. (ii) Electrocatalytic (a-I) HER and (a-II) OER LSV curves of SSM, SSM-Ni, and SSM-Ni-P. (b) HER and (c) OER Tafel plots of SSM, SSM-Ni, and SSM-Ni-P electrocatalysts. Reproduced from ref[292] with permission from ACS, copyright 2019.

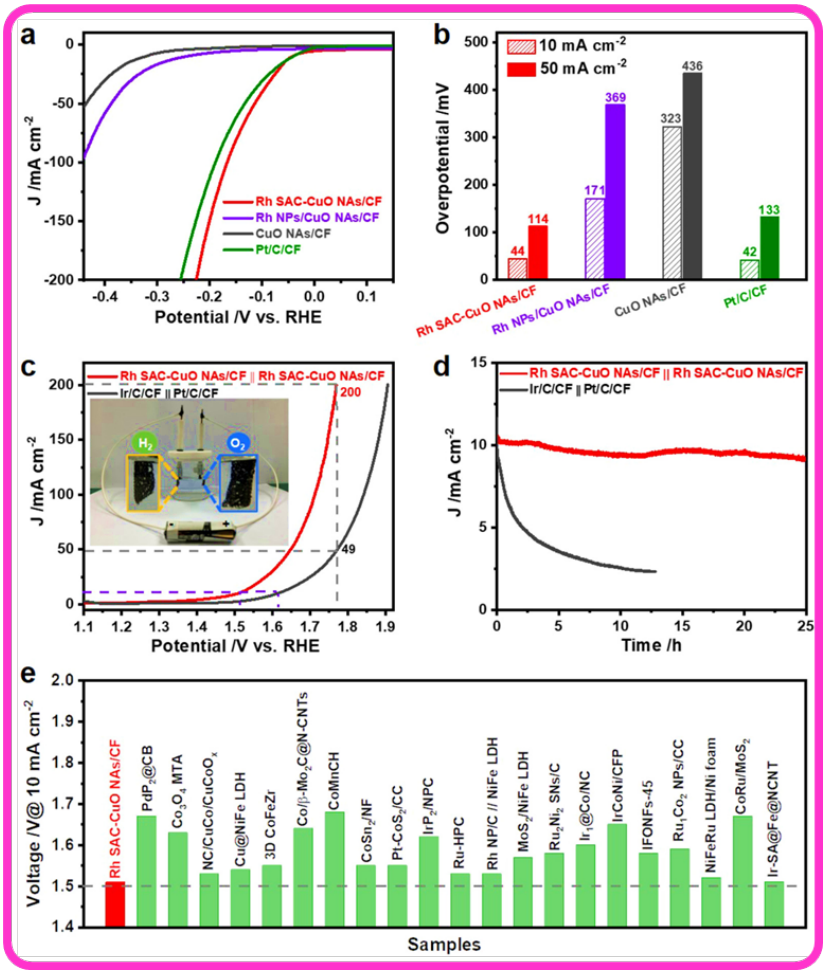

Figure 26 (a) HER polarization curves and (b) Overpotentials at 10 and 50 mA cm^{-2} of Rh SAC–CuO NAs/CF, Rh NPs/CuO NAs/CF, CuO NAs/CF, and Pt/C/CF. (c) Overall water splitting polarization curves. Inset image: setup for overall water splitting of Rh SAC–CuO NAs/CF ‖ Rh SAC–CuO NAs/CF powered by a commercial AA battery (1.5 V). (d) Time-dependent current density curves for the overall water splitting test at 10 mA cm^{-2}. (e) Comparison of the cell potentials and previously reported overall water splitting electrocatalysts at 10 mA cm^{-2}. Reproduced from ref[294] with permission from ACS, copyright 2020.

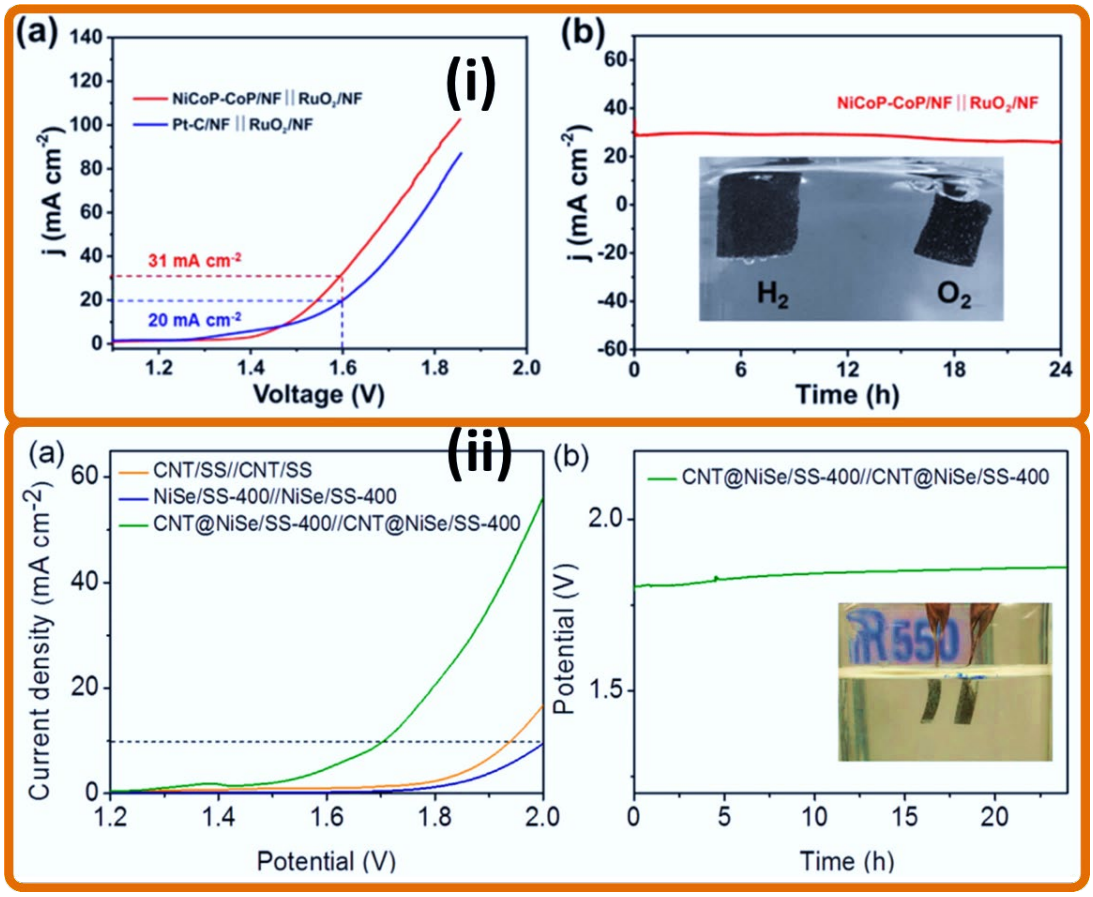

Figure 27 (i) (a) Linear sweep polarization curves of the NiCoP−CoP/NF||RuO_2/NF and Pt−C/NF||RuO_2/NF electrodes for the overall water-splitting system. (b) Chronoamperometric test under a static overpotential of 1.60 V of the NiCoP−CoP/NF||RuO_2/NF two-electrode cell. Inset in (b) shows the generation of H_2 and O_2 bubbles on the NiCoP−CoP/NF||RuO_2/NF two-electrode cell. Reproduced from ref[305] with permission from ACS, copyright 2019. (ii) Two-electrode configuration measurements. (a) LSV curves of different configurations at a scan rate of 3 mV s^{-1}, and (b) Chronopotentiometry curve of CNT@NiSe/SS-400//CNT@NiSe/SS-400 at a current density of 20 mA cm^{-2}. The inset of (b) shows an image of the couples of CNT@NiSe/SS-400, where generation of H_2 and O_2 bubbles is observed. Reproduced from ref[316] with permission from Elsevier, copyright 2020.

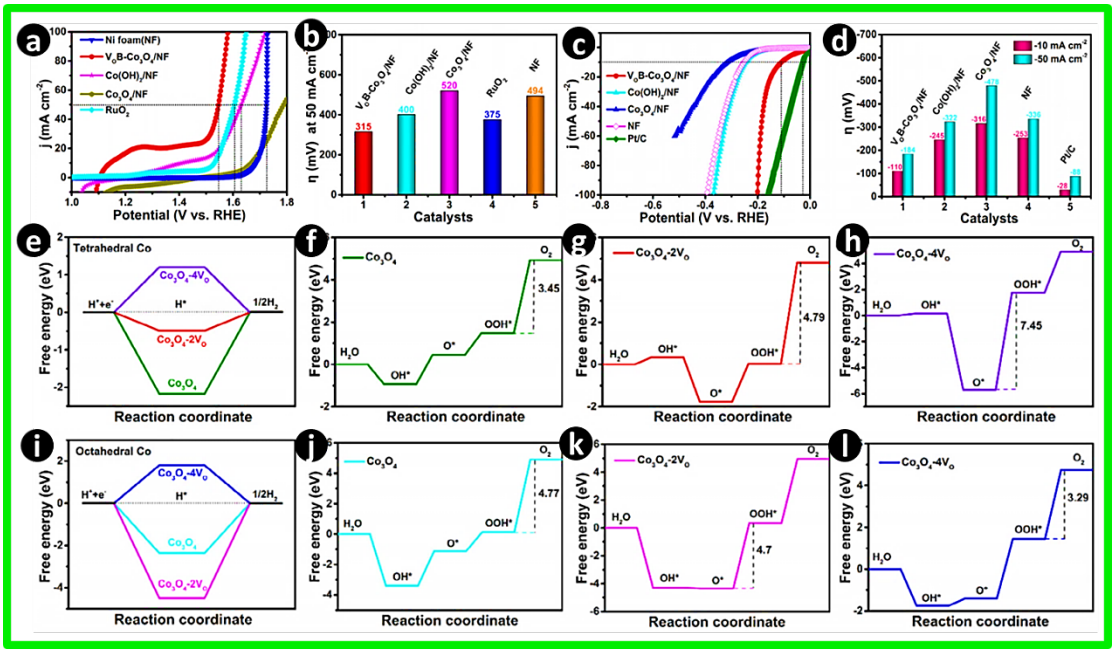

Figure 28 (a-d) Electrocatalytic OER and HER activities, and their corresponding overpotentials. Free energy diagrams of HER and OER on (e–h) tetrahedral Co^{2+} and (i-l) octahedral Co^{3+} sites of (0 0 1) plane with different oxygen vacancies. Reproduced from ref[320] with permission from Elsevier, copyright 2021.

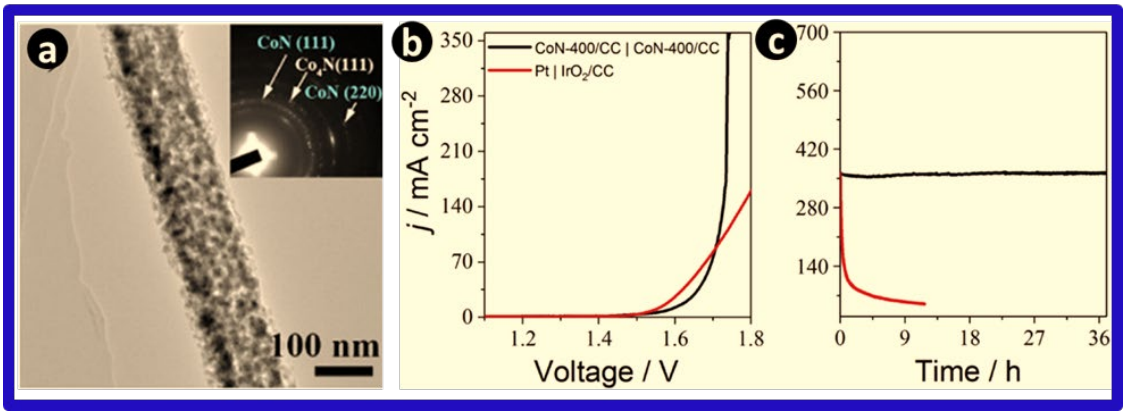

Figure 29 (a) TEM image and SAED pattern of the porous CoN-400/CC electrode, (b) Polarization curves of CoN-400/CC|CoN-400/CC and Pt|IrO_2/CC for overall water splitting in 1.0 M KOH. (c) Time-dependent current density curves for Pt|IrO_2/CC and CoN-400/CC|CoN-400/CC. The CoN-400/CC|CoN-400/CC couple was tested at a cell voltage of 1.74 V over 37 h. Reproduced from ref[331] with permission from Elsevier, copyright 2018.

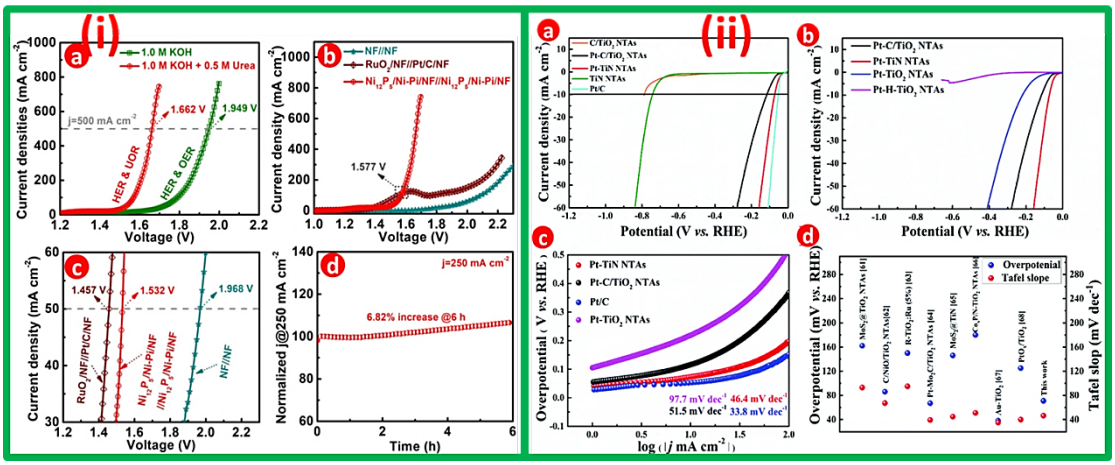

Figure 30 (i) (a) LSV curves for the $Ni_{12}P_5$/Ni-Pi/NF//Ni_{12}P5/Ni-Pi/NF couple in 1.0 M KOH with and without 0.5 M urea. (b,c) LSV curves for the couple of bare NF//NF, RuO_2/NF//Pt/C/NF, and $Ni_{12}P_5$/Ni-Pi/NF//$Ni_{12}P_5$/Ni-Pi/NF in 1.0 M KOH with 0.5 M urea. (d) Time-dependent potential curve of the $Ni_{12}P_5$/Ni-Pi/NF//$Ni_{12}P_5$/Ni-Pi/NF couple with a constant current density of 250 mA cm^{-2} for 6 h. Reproduced from ref[342] with permission from ACS, copyright 2020. (ii) Polarization curves of (a) Pt/C, C/TiO_2 NTAs, Pt–C/TiO_2 NTAs, TiN NTAs, and Pt-TiN NTAs. Polarization curves (b) and Tafel plots (c) of samples deposited on different substrates with Pt. (d) Comparison of the overpotentials and the Tafel slopes of TiO_2-based catalysts. Reproduced from ref[343] with permission from RSC, copyright 2020.

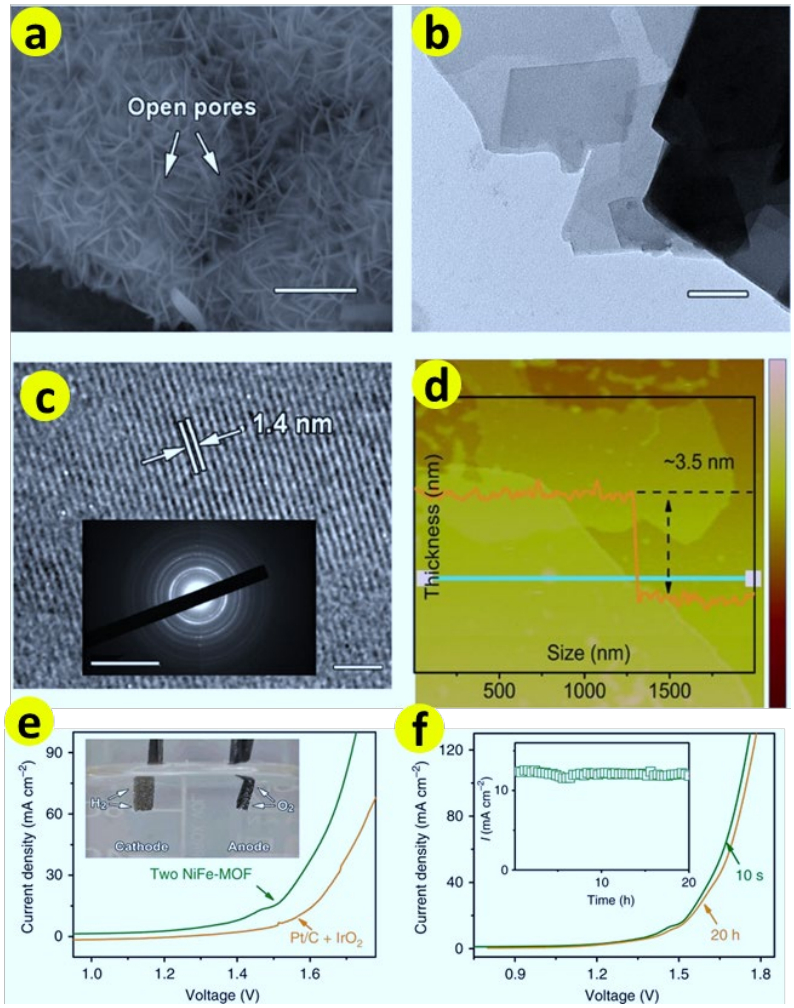

Figure 31 (a-d) SEM, HR-TEM, SAED pattern, and AFM image of NiFe-MOF. (e) Comparison of overall water splitting LSV plots using two NiFe-MOF electrodes and Pt/C cathode and an IrO_2 anode in 0.1 M KOH; the inset shows the evolution of H_2 and O_2 gas bubbles at the NiFe-MOF electrodes at a cell voltage of 1.6 V (d) LSV plots of overall water splitting of NiFe-MOF electrodes before and after 20 h chronoamperometric tests at 1.5 V; the inset displays resultant chronoamperometric plot. Reproduced from ref[337] with permission from Springer Nature, copyright 2017.

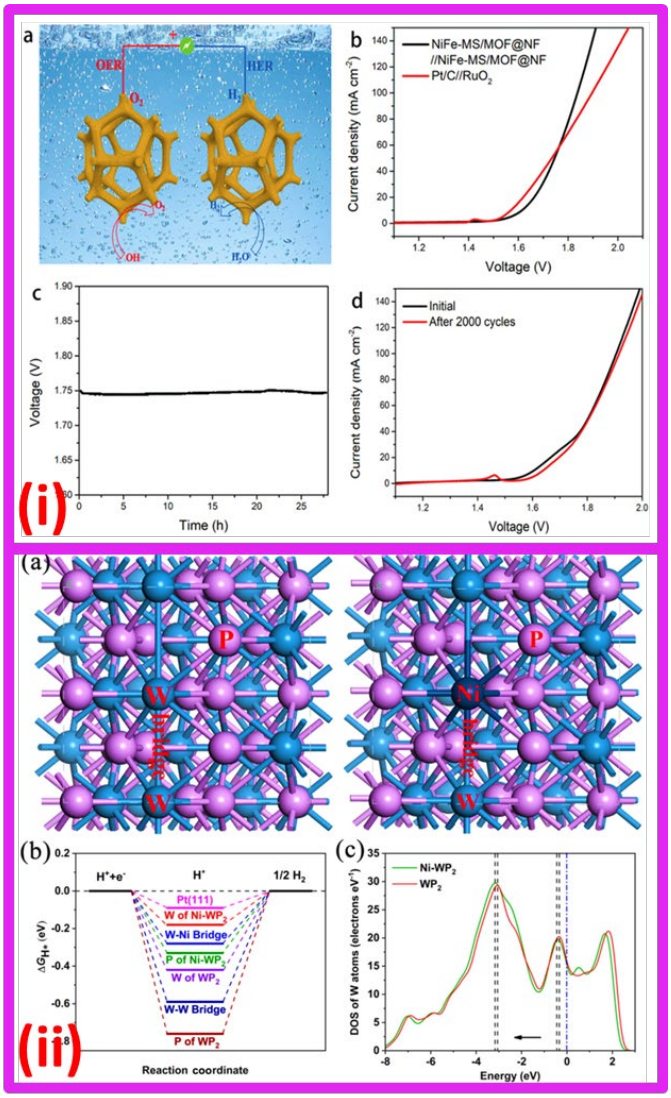

Figure 32 (i) (a) Schematic of the electrolyzer using NiFe-MS/MOF@NF as bi-functional electrocatalysts, (b) Polarization curves (without iR compensation) of NiFe-MS/MOF@NF-based and Pt/C-RuO_2-based electrolyzers, scan rate 2 mV s^{-1} (c) Voltage-time curve at a constant current density of 50 mA cm^{-2} and (d) Polarization curves before and after 2000 cycles between 1–2 V at a scan rate of 50 mV s^{-1} of NiFe-MS/MOF@NF-based electrolyzer. Reproduced from ref[360] with permission from Wiley, copyright 2020. (ii) (a) The slab models of WP_2 and Ni-WP_2 are used for geometry optimization. (b) Calculated hydrogen adsorption Gibbs free energy diagram for WP_2 and Ni-WP_2 on different sites. (c) d-orbital partial density of states (d-DOS) of W atoms, the vertical blue dash-dot line shows the position of the Fermi level. (Dark cyan, pink, and dark blue balls represent W, P, and Ni atoms, respectively). Reproduced from ref[363] with permission from Elsevier, copyright 2021.

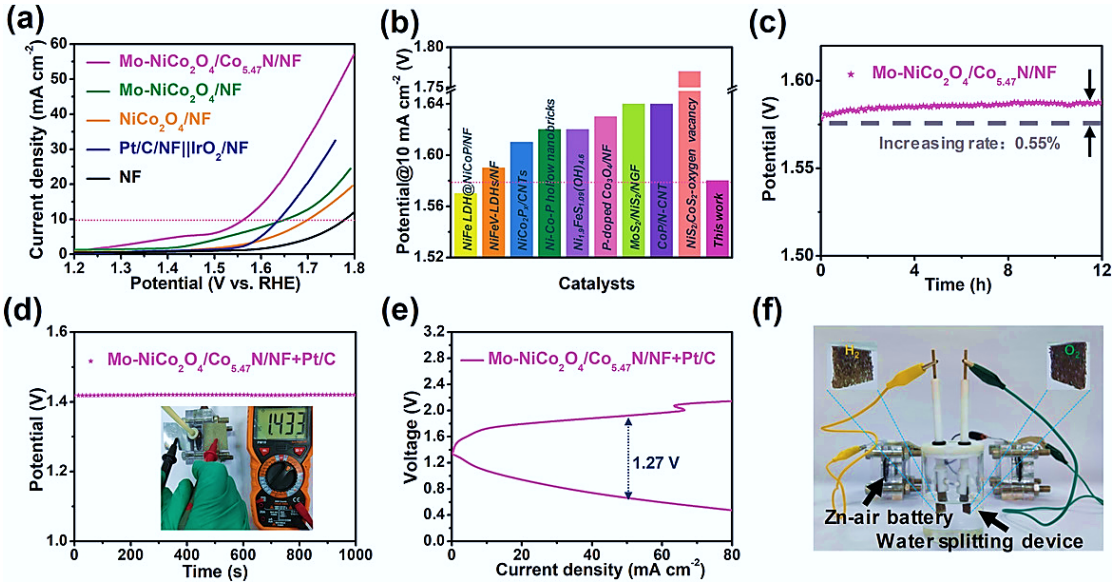

Figure 33 (a) LSV polarization curves of the prepared Mo-$NiCo_2O_4$/$Co_{5.47}$N/NF and other catalysts for overall water splitting in 1.0 M KOH. b) Comparison of cell voltage of the catalysts at the current density of 10 mA cm^{-2} (c) Stability of the Mo-$NiCo_2O_4$/$Co_{5.47}$N/NF||Mo-$NiCo_2O_4$/$Co_{5.47}$N/NF electrolyzer at 10 mA cm^{-2} (d) Open-circuit voltage, and (e) Charge-discharge polarization curves of the Mo-$NiCo_2O_4$/$Co_{5.47}$N/NF-based Zn–air battery. (f) Image of an overall water-splitting device driven by two Zn–air batteries connected in series. Reproduced from ref[369] with permission from Wiley, copyright 2020.

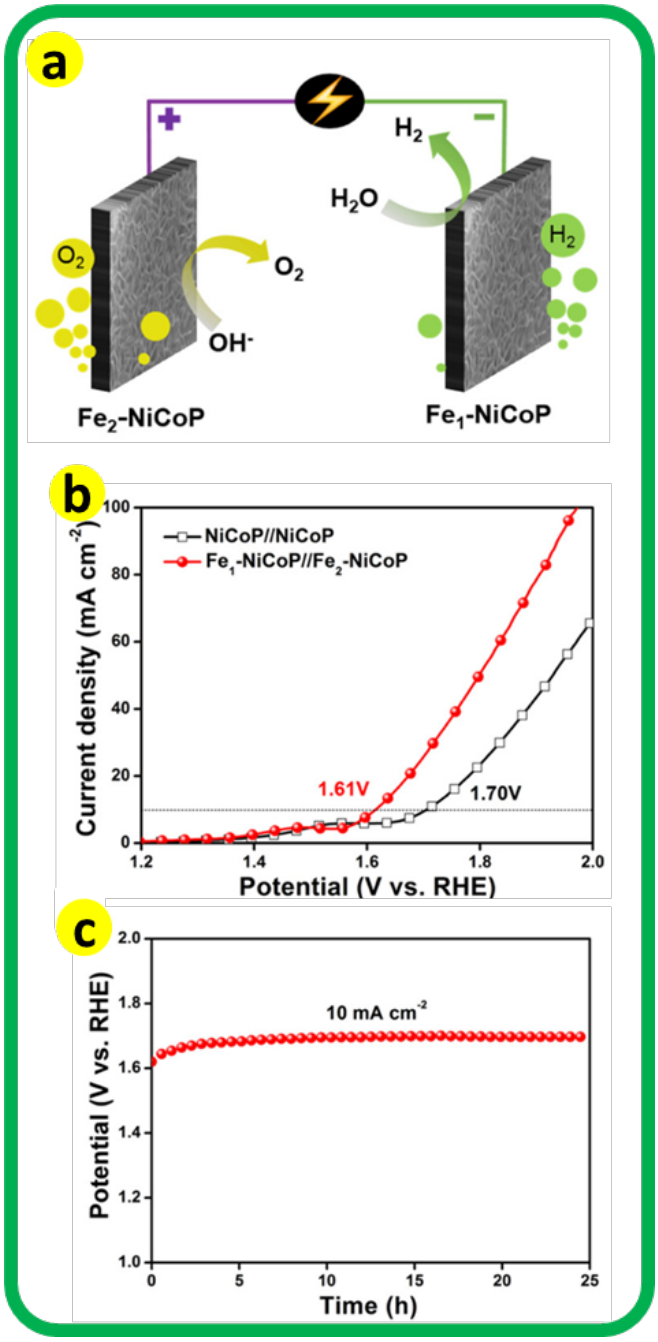

Figure 34 (i) (a) Schematic of water electrolyzer for overall water splitting. (b) Polarization curves for Fe1-NiCoP‖Fe2-NiCoP and NiCoP‖NiCoP catalysts in a two-electrode system under 1.0 M KOH electrolyte without iR-correction and (c) Chronopotentiometry curves of the Fe1-NiCoP‖Fe2-NiCoP electrolyzer at a current density of 10 mA cm^{-2}. Reproduced from ref[382] with permission from ACS, copyright 2020.

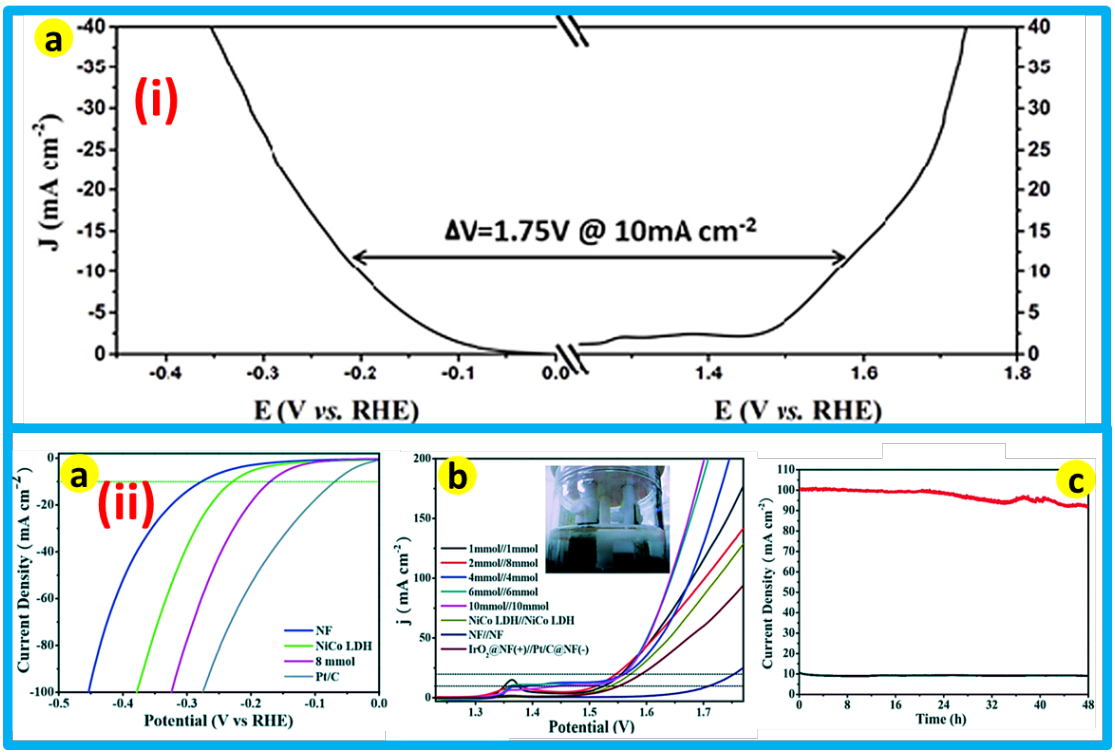

Figure 35 (i) (a) Polarization curves of the SNG@GF electrodes in 1.0 M KOH for HER and OER. Reproduced from ref[194] with permission from Elsevier, copyright 2021. (ii) (a) LSV curves and of NiCoSe (8 mmol), NF, NiCo LDH, and Pt/C for the HER. (b) LSV curves of NiCoSe (1 mmol)‖NiCoSe (1 mmol), NiCoSe (2 mmol)‖NiCoSe (8 mmol), NiCoSe (4 mmol)‖NiCoSe (4 mmol), NiCoSe (6 mmol)‖NiCoSe (6 mmol), NiCoSe (10 mmol)‖NiCoSe (10 mmol), NiCo LDH‖NiCo LDH, NF‖NF and IrO_2@NF(+)‖Pt/C@NF(−) for overall water splitting; (c) Chronopotentiometry (*i*–*t*) curves of the overall water splitting at 10 mA cm^{-2} and 100 mA cm^{-2}. Reproduced from ref[391] with permission from RSC, copyright 2020.

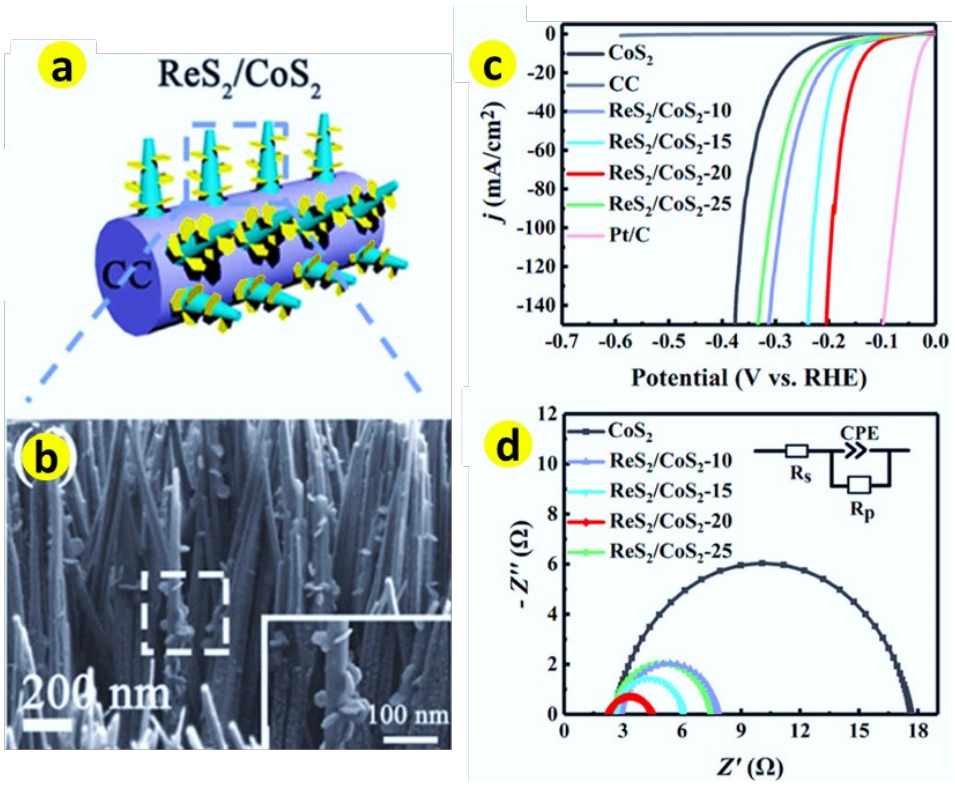

Figure 36 (a) Schematic of hetero-structured ReS_2/CoS_2 on CC by CVD.(b) SEM images of ReS_2/CoS_2, (c) HER polarization curves of CC, CoS_2, ReS_2/CoS_2-10, ReS_2/CoS_2-15, ReS_2/CoS_2-20, ReS_2/CoS_2-25, and Pt/C electrodes in 0.5 M H_2SO_4 with a potential sweep rate of 5 mV sec^{-1} and (d) Nyquist plots of CoS_2, ReS_2/CoS_2-10, ReS_2/CoS_2-15, ReS_2/CoS_2-20, and ReS_2/CoS_2-25 electrodes. Reproduced from ref[392] with permission from ACS, copyright 2020.

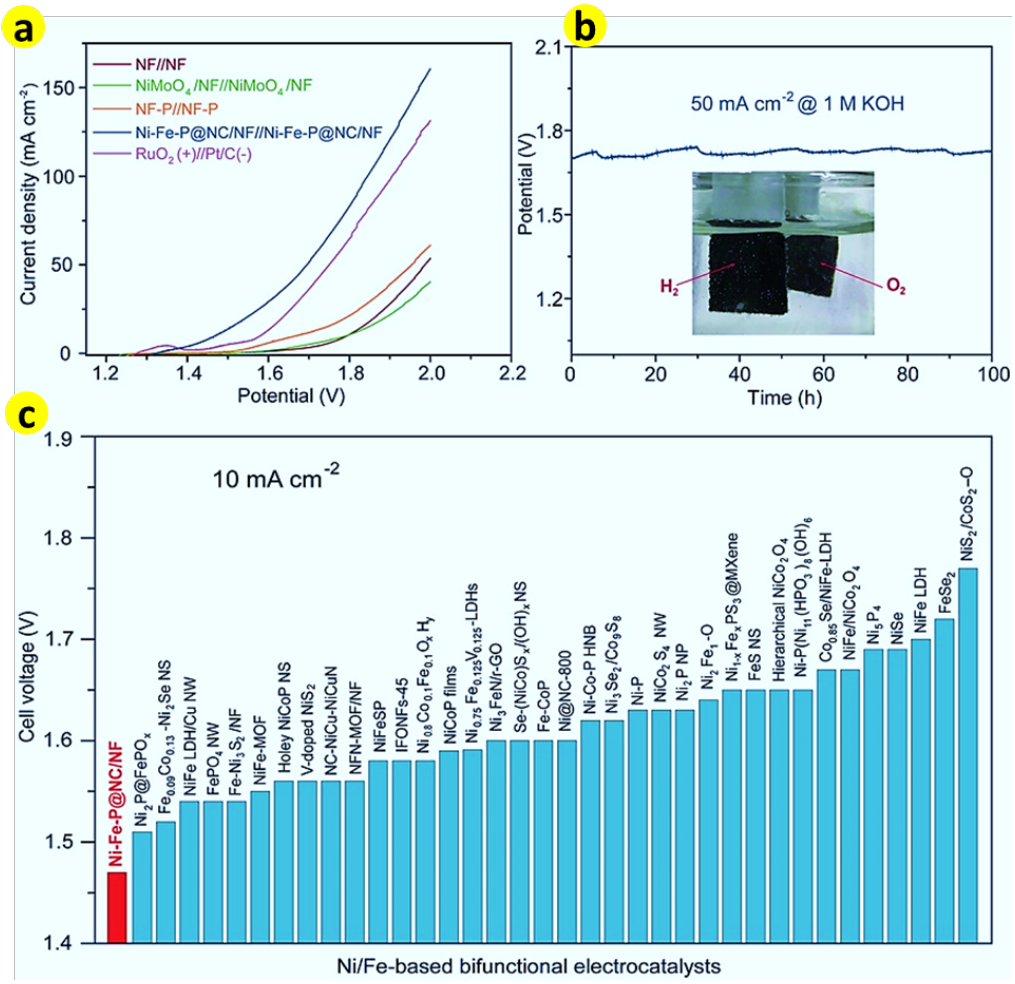

Figure 37 (a) Polarization curves of Ni-Fe-P/NF//Ni-Fe-P/NF for overall water splitting at a scan rate of 5 mV s^{-1} (b) Chronopotentiometry curve of water electrolysis using Ni-Fe-P@NC/NF as both the anode and cathode at a constant current density of 50 mA cm^{-2} for 100 h. (c) Comparison of cell voltage to achieve 10 mA cm^{-2} among previously reported excellent Ni/Fe-based electrolyzers. Reproduced from ref[400] with permission from Elsevier, copyright 2020.

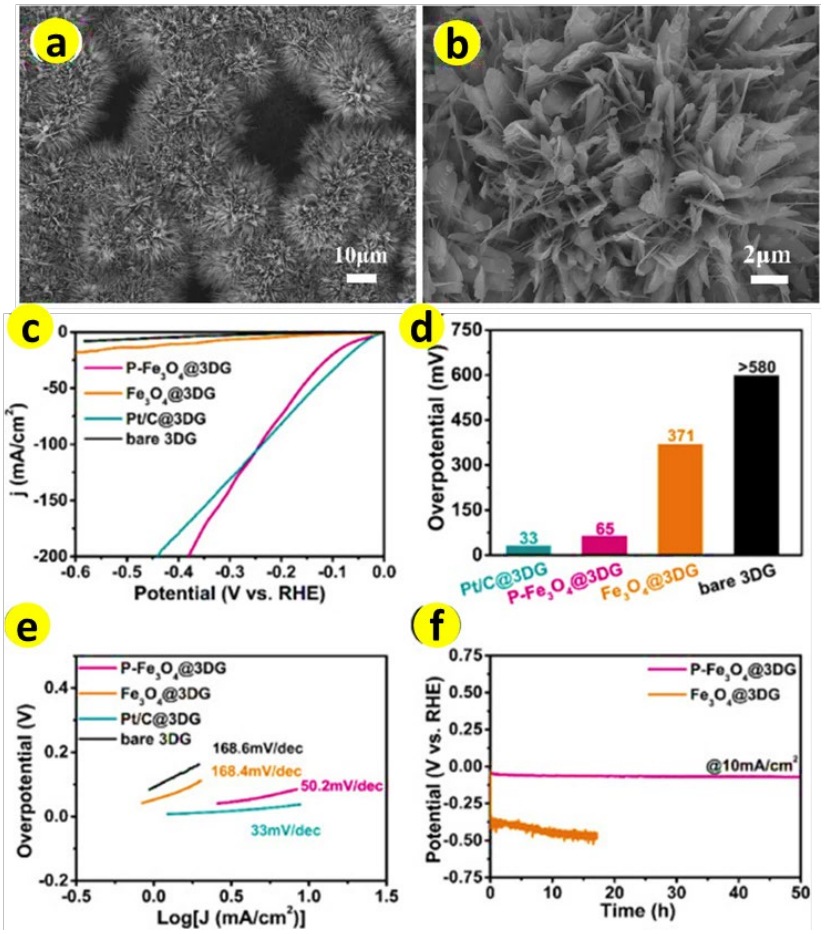

Figure 38 (a,b) FE-SEM images of P–Fe_3O_4@3DG hybrid composite. (c) LSV polarization curves of P–Fe_3O_4@3DG, Fe_3O_4@3DG, Pt/C@3DG, and bare 3DG in 0.5 M H_2SO_4 (d) Overpotentials of various electrodes at the current density of 10 mA cm^{-2} (e) Tafel slopes for the 3DG based electrodes and (f) Long-term stability of P–Fe_3O_4@3DG and Fe_3O_4@3DG electrode at 10 mA cm^{-2}. Reproduced from ref[404] with permission from Elsevier, copyright 2020.

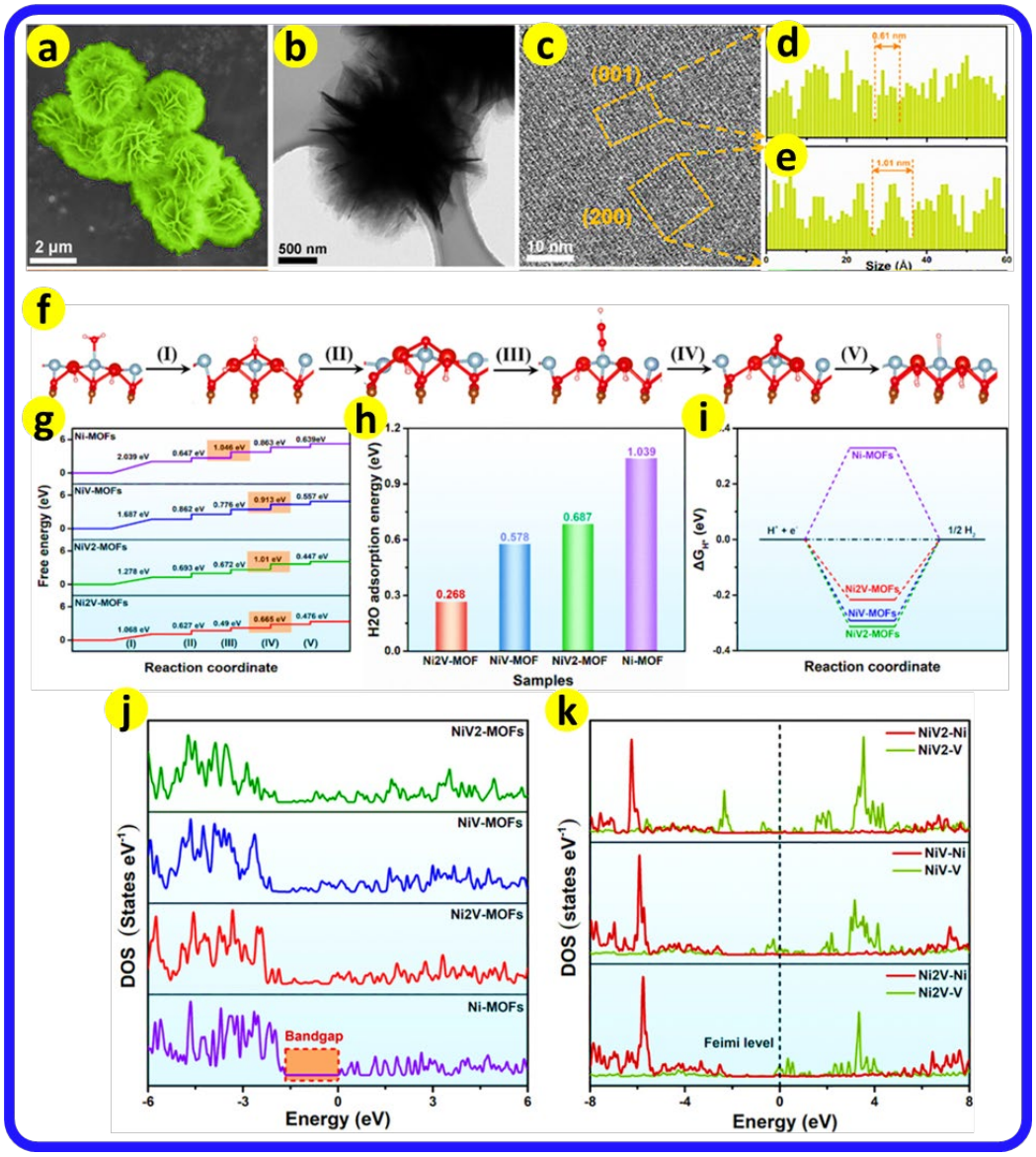

Figure 39 (a,b) SEM, TEM images of Ni_2V-MOFs scraped from Ni_2V-MOFs@NF (c) HR-TEM of nanosheet edge and the corresponding interplanar spacing (d, e). (f) $4e^-$-OERmechanism OER and corresponding H_2O adsorption process on Ni_2V-MOFs for DFT simulations and the active site is Ni ion (*) in the (001) crystal plane. Calculated free energy diagram for the OER (g), H_2O adsorption energy (h), and the DFT-calculated adsorption energy of H^+ for the HER (i) on the surfaces of Ni_2V-MOFs, NiV-MOFs, NiV_2-MOFs, and Ni-MOFs (j) Total electronic density of states (TDOS) calculated for Ni_2V-MOFs, NiV-MOFs, NiV_2-MOFs, and Ni-MOFs (k) Local electronic density of states (LDOS) calculated for Ni_2V-MOFs, NiV-MOFs, and NiV_2-MOFs. Reproduced from ref[410] with permission from ACS, copyright 2020.

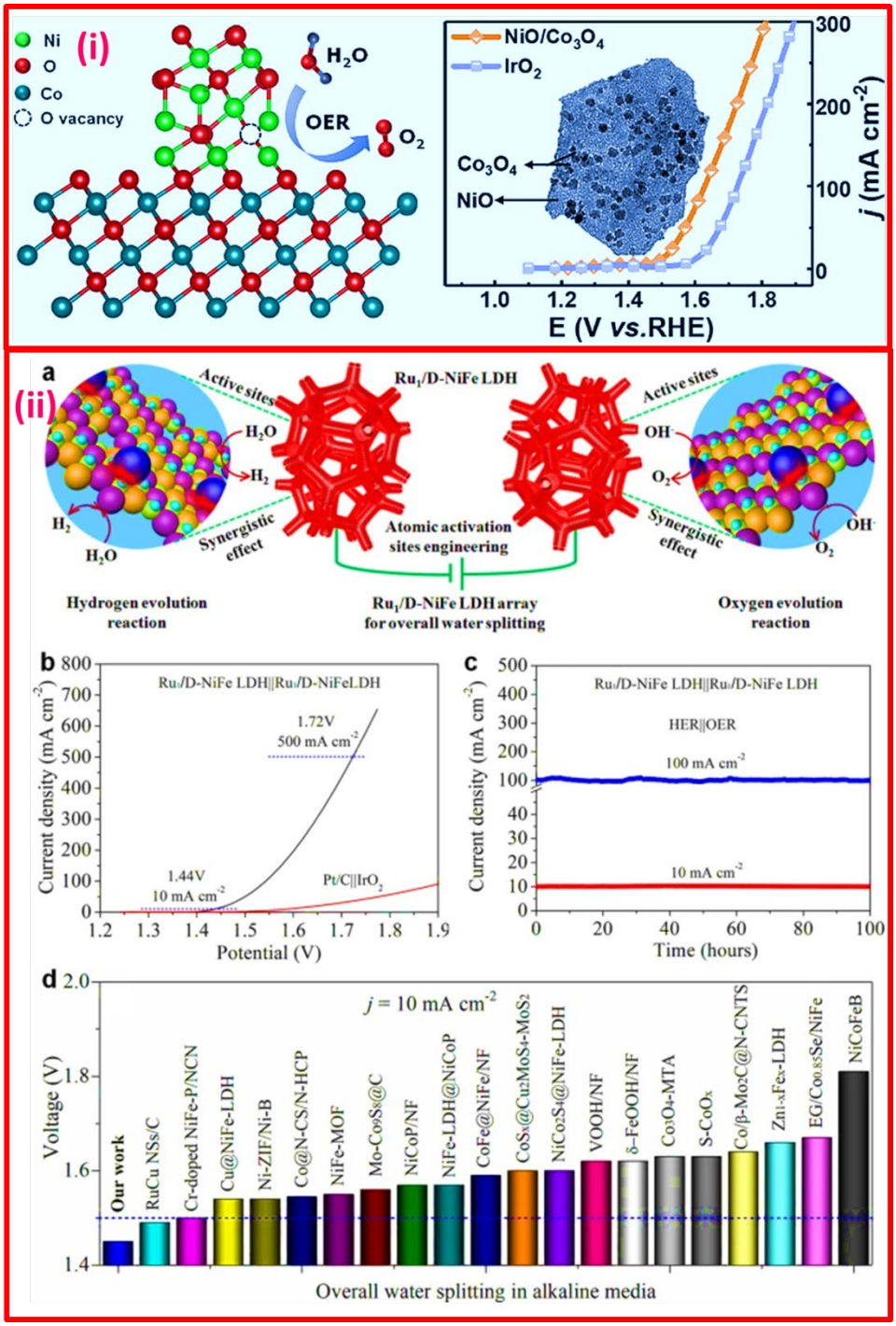

Figure 40 (i) (a,b) Schematic and oxygen evolution reaction in $NiO/Co_3O_4/NF$ hybrids. Reproduced from ref[418] with permission from ACS, copyright 2020. (ii) (a) Schematic diagram of water splitting in a two Ru_1/D-NiFe LDH-electrode arrangement, (b) Overall water splitting LSV curves, (c) chronoamperometric test of Ru_1/D-NiFe LDH at 1.44 (10 mA cm^{-2}) and 1.54 V (100 mA cm^{-2}), and (d) Performance comparison of Ru_1/D-NiFe LDH with reported bi-functional electrocatalysts. Reproduced from ref[419] with permission from Springer Nature, copyright 2021.

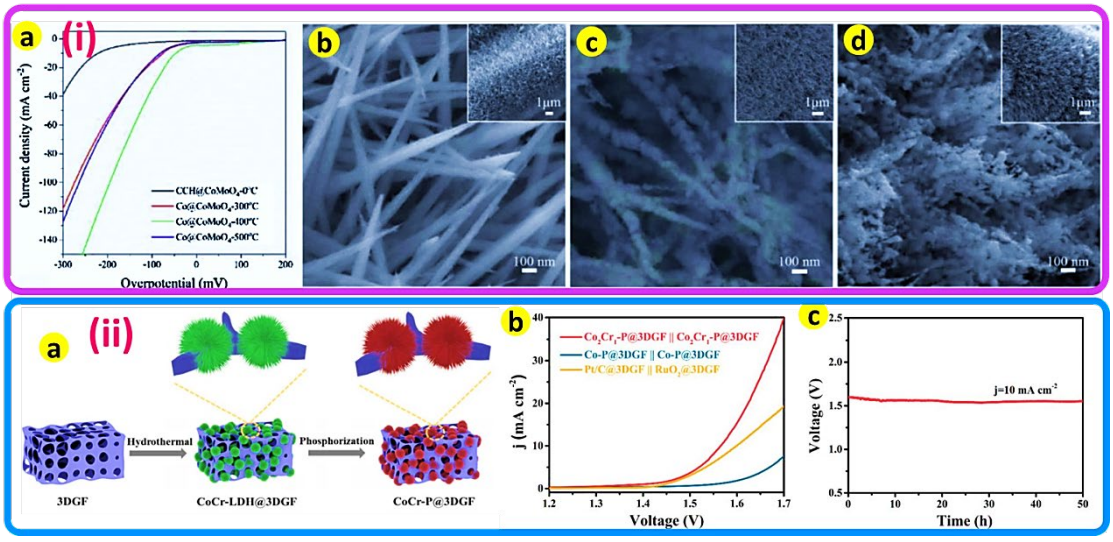

Figure 41 (i) (a) LSV curves of $Co@CoMoO_4$ electrodes in 1.0 M KOH solution (b) SEM of $Co@CoMoO_4$-300 °C (c) SEM of $Co@CoMoO_4$-400 °C (d) SEM of $Co@CoMoO_4$-500 °C. Reproduced from ref[437] with permission from Elsevier, copyright 2019. (ii) (a) Schematic of the formation of Co_2Cr_1-P@3DGF (b) Polarization curves of Co_2Cr_1-P@3DGF||Co_2Cr_1-P@3DGF, Co-P@3DGF||CoP@3DGF, and Pt/C||RuO_2@3DGF for overall water splitting (c) Stability test result over 50 h for Co_2Cr_1-P@3DGF||Co_2Cr_1-P@3DGF. Reproduced from ref[441] with permission from RSC, copyright 2020.

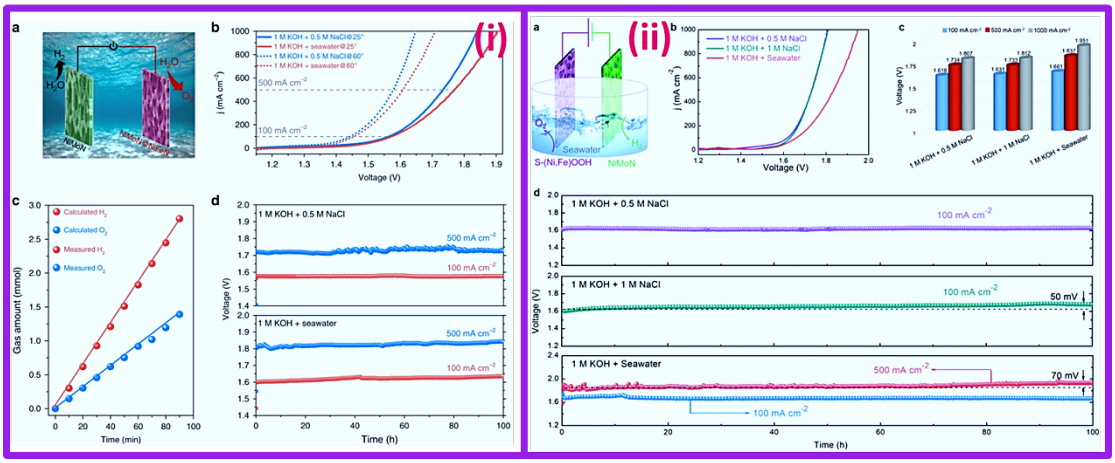

Figure 42 (i) (a) Schematic of overall seawater splitting electrolyzer with NiMoN and NiMoN@NiFeN as the cathode and anode, respectively. (b) Polarization curves after iR compensation of NiMoN and NiMoN@NiFeN coupled catalysts in a two-electrode electrolyzer tested in alkaline simulated (1 M KOH + 0.5 M NaCl, resistance: ~1.1 Ω) and natural seawater (1 M KOH + seawater, resistance: ~1.2 Ω) electrolytes under different temperatures. (c) Comparison between the amount of collected and theoretical gaseous products (H_2 and O_2) by the two-electrode electrolyzer at a constant current density of 100 mA cm^{-2} in 1.0 M KOH + 0.5 M NaCl at 25 °C. (d) Durability tests of the electrolyzer at constant current densities of 100 and 500 mA cm^{-2} in different electrolytes at 25 °C. Reproduced from ref[452] with permission from Springer Nature, copyright 2019. (ii) (a) Schematic of electrolyzer using NiMoN and S-(Ni,Fe)OOH as the cathode and the anode, respectively. (b) Polarization curves, and (c) Comparison of the required voltages at current densities of 100, 500, and 1000 mA cm^{-2} for the NiMoN‖S-(Ni,Fe)OOH electrolyzer in different electrolytes. (d) Long-term stability tests were conducted at constant current densities of 100 and 500 mA cm^{-2} in different electrolytes. Reproduced from ref[454] with permission from RSC, copyright 2020.

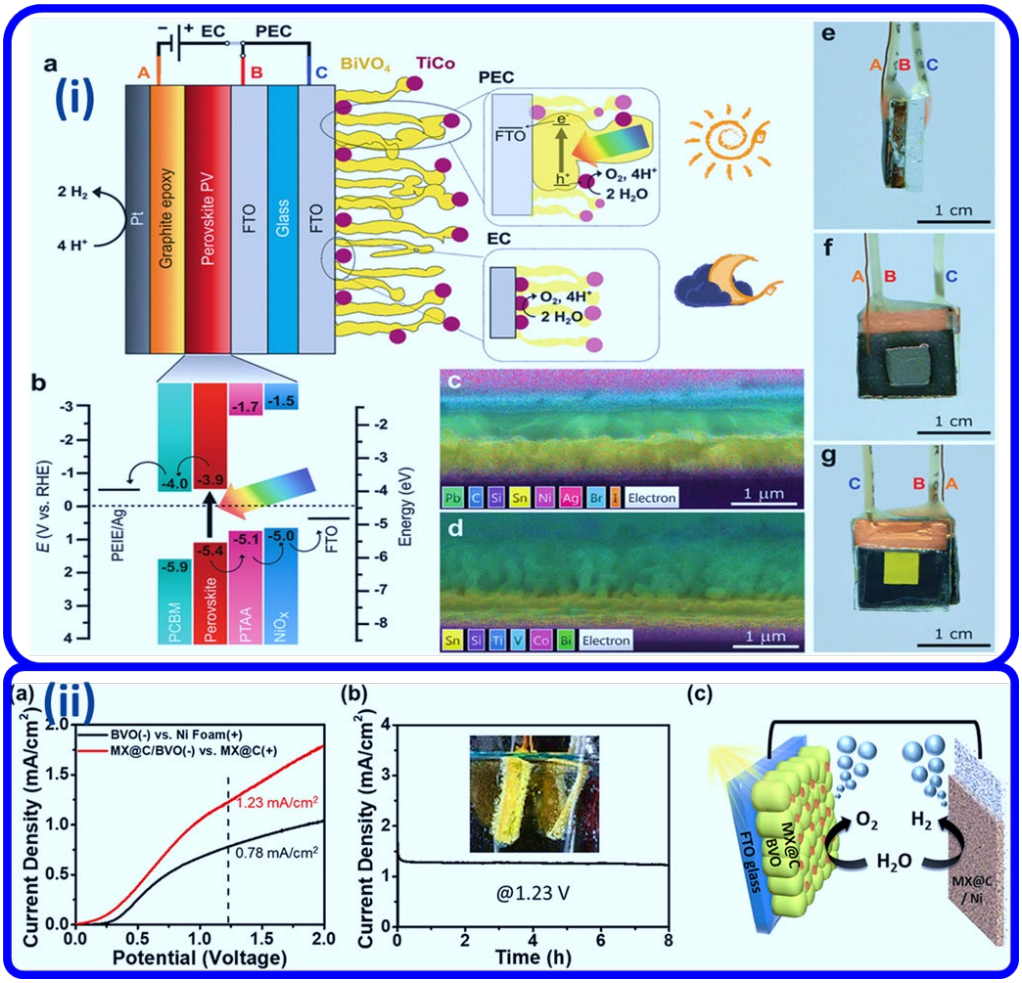

Figure 43 (i) Design of the bi-functional PEC–EC device for non-stop solar water splitting. (a) Schematic of the device operating via three wires: wire A is connecting to the graphite paste, B to the CsFAMA triple cation perovskite photocathode, and C to the FTO contact of the $BiVO_4$ photoanode, with a two-way electrical switch to select between PEC (daytime) and EC (dark) operation. (b) Energy diagram of the perovskite architecture, based on reported values.(c) EDX mapping of a perovskite PV cell and (d) $BiVO_4$ (photo)anode. (e–g) Photographs of the PEC–EC bi-functional device in an "artificial leaf" configuration: side view (e), perovskite side (f), $BiVO_4$ side (g). The wire notation corresponds to panel a. Reproduced from ref[499] with permission from Wiley, copyright 2020. (ii) (a) J–V curves of solar-assisted overall water splitting cells under AM 1.5 G 1 sun illumination of BVO (−) *vs.* Ni foam (+) and MX@C/BVO (−) *vs.* MX@C (on Ni foam, +). (b) Long-term stability (current density to time curve) and (c) Schematic mechanism of solar water splitting cells based on MX@C/BVO (−) *vs.* MX@C (on Ni foam, +) under AM 1.5 G 1 sun illumination. Inset shows a photograph of cell configuration for solar-assisted overall water splitting in the 0.1 M PBS electrolyte. Reproduced from ref[502] with permission from ACS, copyright 2020.

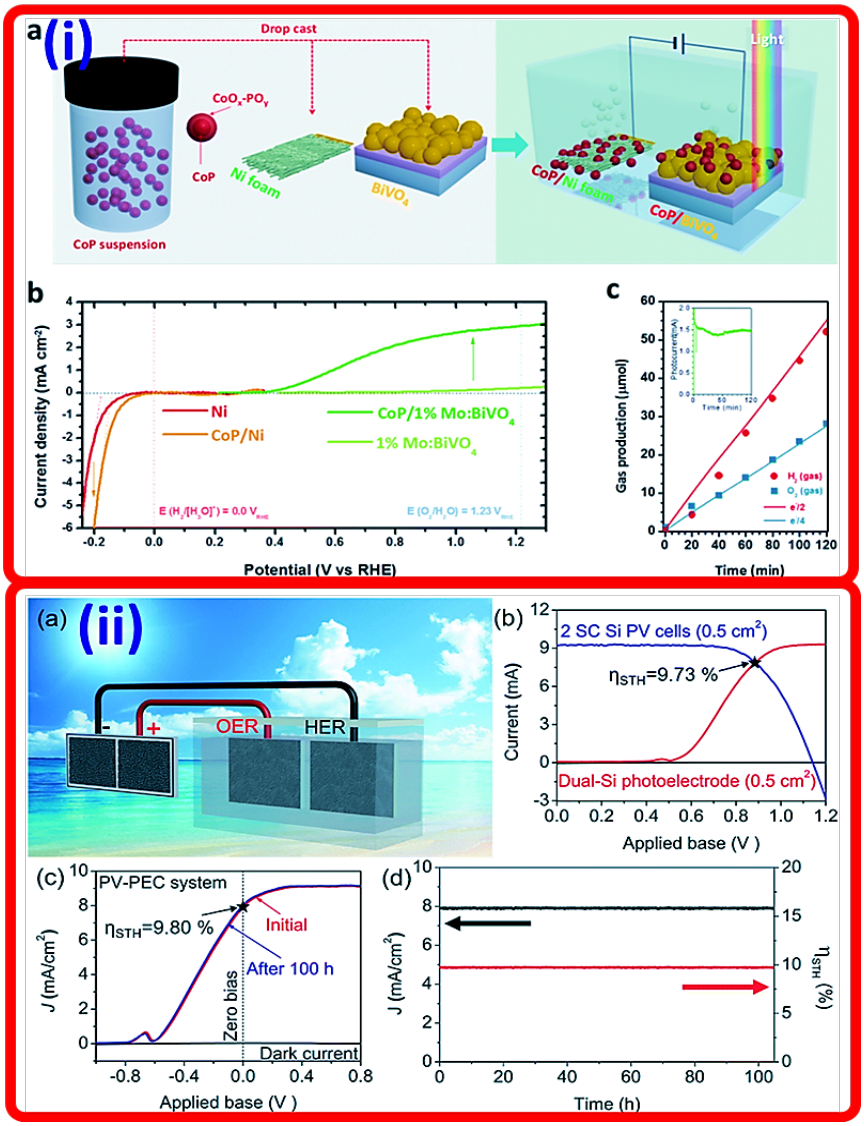

Figure 44 (i) (a) Schematic of CoP loading on the photoanode (Mo:$BiVO_4$) and cathode (NF) by drop-casting of a CoP suspension (left) and a PEC cell made from them. (b) I-V curves for a PEC water splitting system with the CoP loaded photoanode and cathode. (c) Gas evolution from the PEC cell under 1 sun irradiation at an applied bias of 1.0 VRHE in 0.5 M KPi (pH ~ 7.0). Cathode area = 2.0 cm^2 and photoanode area = 0.5 cm^2. Lines indicate expected gas evolution from measured photocurrents in the inset. Reproduced from ref[503] with permission from RSC, copyright 2018. (ii) (a) Schematic of the unassisted water splitting by combined PV–PEC system. (b) Two-electrode LSV curves of the dual-Si photoelectrode under dark (black) and AM 1.5G 1 sun illumination conditions (red). Also shown are the LSV curves of 2 SC Si PV cells under AM 1.5G 1 sun illumination (blue). The estimated η_{STH} for the combined PV–PEC system is marked at the crossing point. (c) Two-electrode LSV curves of the combined PV–PEC

system before and after over 100 h continuous unassisted solar water splitting. (d) Long-term J–t test and the corresponding η_{STH} for the combined PV–PEC system during continuous unassisted solar water splitting for over 100 h. Reproduced from ref[504] with permission from RSC, copyright 2019.

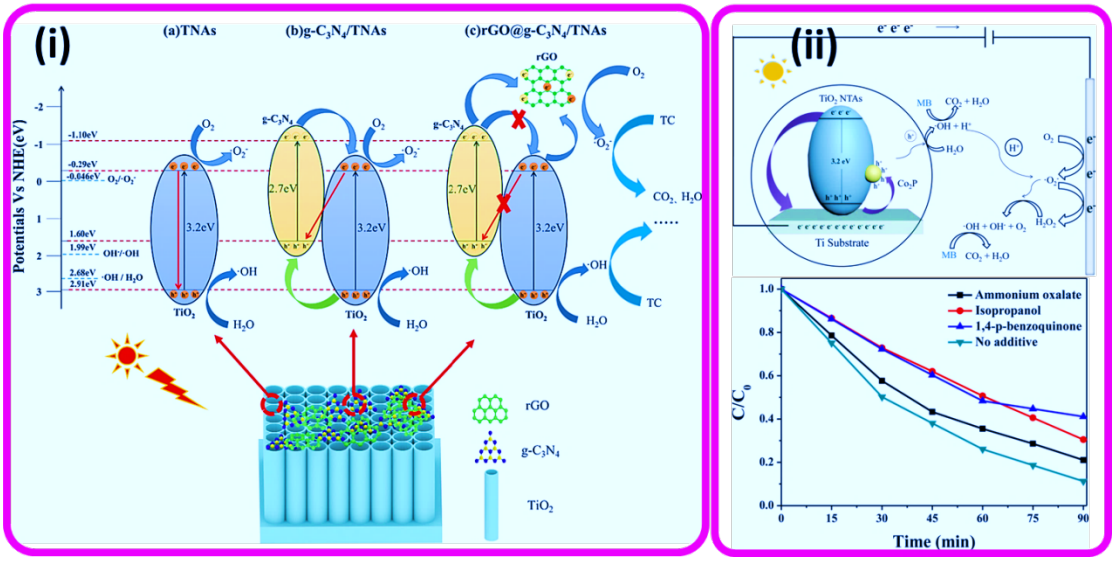

Figure 45 (i) Schematic of photocatalytic mechanism of (a) TNAs, (b) g-C_3N_4/TNAs, and (c) rGO@g-C_3N_4/TNAs photoelectrodes. Reproduced from ref[512] with permission from Elsevier, copyright 2020. (ii) Mechanism of PEC MB degradation by Co_2P/TiO_2 NTAs and the PEC degradation of MB by 1.5-Co_2P/TiO_2 NTAs with the addition of h^+, radical $.OH^-$ and radical $.O_2^-$ scavengers. Reproduced from ref[514] with permission from Elsevier, copyright 2020.

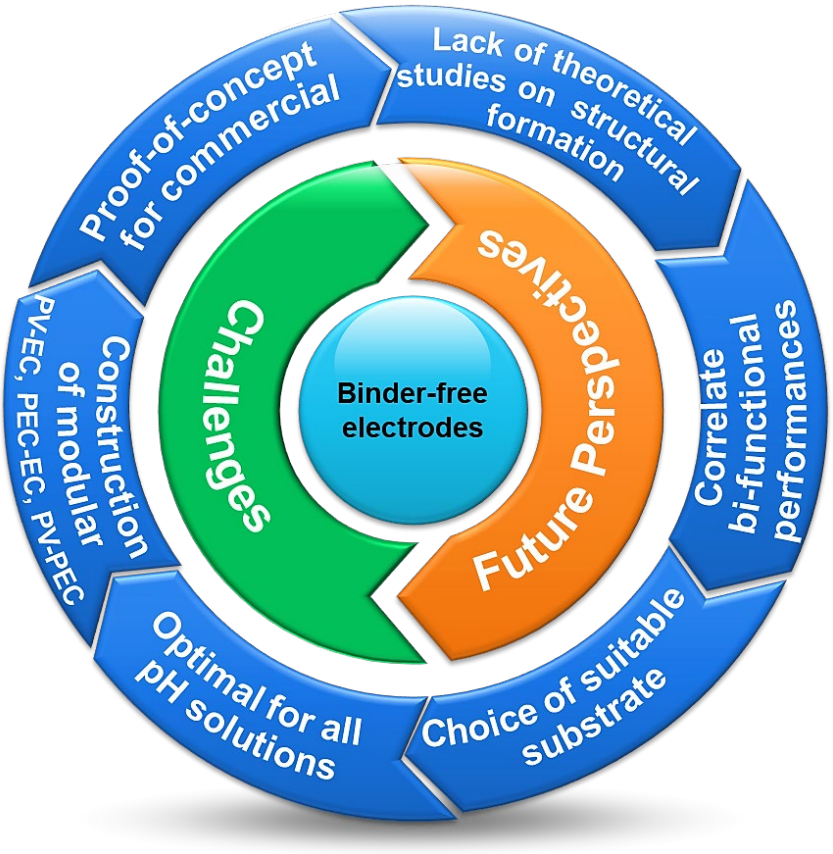

Scheme 3 Challenges and future perspectives of binder-free electrode materials to enhance energy conversion and storage performance.

Table 1 Summary of fabrication conditions for 1D, 2D, and 3D nano- and micro-structured robust binder-free electrocatalysts

Catalyst	Support	Fabrication method (precursor)	Features	Reference
Mo-doped Ni_3S_2 Nanowires	Ni foam	Hydrothermal and sulfidization process using $Ni(NO_3)_2·6H_2O$, $Na_2MoO_4·2H_2O$ and Na_2S	Nanowire array	[111]
Ni_xFe_{1-x} alloy	Ni foam	Chemical-deposition method under uniform electromagnetic field using $NiCl_2$ $FeCl_2$, and $Na_3C_6H_5O_7$	Nanowire array	[116]
CoNi (oxy)hydroxide	Ni foam	Hydrothermal processes using $Co(NO_3)_2·6H_2O$, $Ni(NO_3)_2·6H_2O$, NH_4F, and $(NH_2)_2CO$	Nanorod	[114]
NiTe nanowire NiTe/NiS	Ni foam	Etching of Ni foam, followed by hydrothermal and sulfidation	Nanowire Heterojunction by coupling with NiS nanodots	[257]
$Ni(OH)_2/Ni_3S_2$	Ni foam	Electrodeposition using $NiCl_2·6H_2O$, $CS(NH_2)_2$ and NaCl at a pH = 2.5	Nanoforest	[258]
Ni_3S_2 $Ni_3S_2@Co(OH)_2$	Ni foam Ni foam	In-situ hydrothermal using NF as Ni source In-situ hydrothermal using NF and $CoCl_2$	Nanowires Heterostructured NWA's	[134]
$Sn–Ni_3S_2$		Hydrothermal using NF as a Ni source $CS(NH_2)_2$ and $Na_2SnO_3·3H_2O$	Ultrathin nanosheets	[353]
$NiCoO_2/CoO/Ni_3N$	Ni foam	Hydrothermal reaction followed by annealing in ammonia	Nanosheets	[345]
$Ni(OH)_2$/Ni/NF $Ni_{12}P_5$-Ni_2P	Ni foam	Template-free electrodeposition using $NiCl_2$ and NH_4Cl	Nanosheets	[120]
$CoNi/CoFe_2O_4$ $CoNi/CoFe_2O_4$	Ni foam	Hydrothermal using $Co(NO_3)_2·6H_2O$, $Fe(NO_3)_2·9H_2O$, NH_4F, and $Co(NH_2)_2$ Hydrotheramal, followed by electrodeposition using $NiCl_2·6H_2O$ and $CoCl_2·6H_2O$	Nanoflowers Nanoflowers	[105]
MoP	Ni foam	MoO_2 on Ni foam and then further phosphorization treatment	Nanoflakes	[117]
NiFe LDHs Fe_2Ni_2N	Ni foam Ni foam	Hydrothermal method using $Ni(NO_3)_2·6H_2O$, $Fe(NO_3)_3·9H_2O$, $Co(NH_2)_2$ Nitridation of hydrothermally prepared NiFe LDHs nanoplates	Nanoplates array Nanoplates array	[104]
CoS_2@NGC	Ni foam	Template assisted method	Nanorod with an ultrathin carbon shell layer	[351]
CuO@Cu_2O	Cu foam	Chemical oxidation of a Cu foam with NaOH and $(NH_4)_2S_2O$, followed by annealing	Nanowires array	[135]
$Cu(OH)_2$ Cu_3P	Cu foam Cu foam	Wet-chemical route using APS and NaOH Phosphidation of $Cu(OH)_2$	Nanowires array Nanowires array	[137]

O-doped Co_2P layer supported CuO	Cu foam	Solution method followed by phosphidation of Co_3O_4/CuO NWs	Nanowire array	[139]
$Cu@CoS_x$	Cu foam	Solution method using Cu foam as a Cu source, $CoCl_2·6H_2O$ and thioacetamide	Macroporous amorphous	[140]
Ni_3Se_2	Cu foam	Electrochemical deposition using nickel acetate tetrahydrate, and selenium dioxide	Mesoporous nanocrystals	[141]
$Cu(OH)_2$ nanowires NiCo-LDH@$Cu(OH)_2$ NiCoP@Cu_3P	Cu foam Cu foam Cu foam	Chemical oxidation of Cu foam Hydrothermal method Phosphidation	Nanowires Nanosheets Forest-like nanosheets	[144]
Ni–Fe LDH	SS substrate	Anodization	Nanofiberlike	[150]
NiFeSe	SS substrate	Solution method followed by annealing and selenization	Nanoparticles	[156]
$Cu(OH)_2$ CuO_x	Cu foil Cu foil	Chemical oxidation of Cu foil with NaOH and $(NH_4)_2S_2O_8$ Annealing of $Cu(OH)_2$	Nanowire arrays Nanowire arrays	[163]
CuO nanostructures	Cu foil	Chemically controlled solution growth	Nanosheets (NSs), Nanocubes (NCs), Nanoflowers (NFs), and Nanoleaves (NLs)	[164]
$Cu(OH)_2$ CuO@ZnCo LDH	Cu foil	Solution method followed by thermal annealing Hydrothermal method using $Co(NO_3)_2·6H_2O$, $Zn(NO_3)_2·6H_2O$, NH_4F and of urea with CuO NW	Nanowire arrays Hierarchical arrays	[165]
Ni-Fe, Ni-Co, Ni-Fe-Co alloy	Cu foil	Electrodeposition using $NiCl_2·6H_2O$, $CoCl_2·6H_2O$, $FeCl_2·4H_2O$ H_3BO_3 and $C_2H_{10}Cl_2N_2$	Nanocones	[398]
$NiSe_2$	Ti plate	Electrodeposition using $NiCl_2.6H_2O$ and SeO_2 and LiCl	Nanoparticles	[169]
$Co_{0.13}Ni_{0.87}Se_2$	Ti plate	Electrodeposition using $Ni(CH_3COO)_2·4H_2O$, $Co(CH_3COO)_2·4H_2O$, SeO_2 and LiCl	Nanoparticles	[170]
MoS_2	Ti mesh	Template-free hydrothermal method	Microflowers	[173]
FeP	Ti plate	Hydrothermal method followed by phosphidation	Porous nanorods	[174]
Zn-doped Co_3O_4	Ti plate	Hydrothermal method followed by chemical reduction	Nanosheets	[172]
Ni-doped TiO_2 nanotubes	Ti plate	Anodization using EG, NH_4F and H_2O	Nanotubes	[178]
rGO@g-C_3N_4/TNAs	Ti plate	Anodization	3D Nanotube arrays	[512]
MoS_2	Al foil	CVD growth	Monolayer porous nanosheets	[179]
NiWP	Al foil	Anodic aluminum oxide (AAO) Template method	Nanoparticles	[180]

Ni_3S_2	SiO_2 substrate	Atomic layer deposition (ALD)	Metallic Nanoparticles	[182]
CoO	Si wafer	Ionic layer epitaxy (ILE) method	Nanosheets	[181]
M-CNT (M= Pd, Ni and Co)	Si wafer	Thermal evaporation	Nanotube	[183]
$CoS_{1.097}$ NPs on 3D N-doped graphene	graphene foam	Hydrazine assisted solution method followed by thermal-treatment process	3D porous structures	[186]
P–Fe_3O_4	graphene foam	Hydrothermal method, followed by phosphidation	Nanoflowers	[187]
MoS_2-NiS_2	graphene foam	CVD technique	3D interconnected tubular hollow structure	[411]
amorphous NiFe	exfoliated graphite foil (EG)	Electrodeposition using $Ni(NO_3)_2{\cdot}6H_2O$, $Fe(NO_3)_3{\cdot}9H_2O$ and CH_3COONH_4	Nanosheets	[379]
WC_x	CC	Electrodeposition followed by CVD technique using $Ar/H_2/CH_4$	Layer-stacking structure	[196]
$Ni(OH)_2$ NiP_2	CC	Hydrothermal Phosphidation	Nanosheets	[203]
Co_2P QDs integrated with N, P co-doped carbon	CC	Phosphidation	Nanosheets	[198]
$CoMoS_4$ nanosheet	CC	Topotactic conversion of a Co(OH)F nanosheet array on CC (Co(OH)F NS/CC) in a $(NH_4)_2MoS_4$ solution *via* an anion exchange reaction	Nanosheets	[204]
0D-2D $CoSe_2/MoSe_2$	CC	Selenization of $CoMoO_4$ nanosheets integrated on CC	Nanosheets	[197]
$FeCo_2S_4$ NTA	CC	Two-step hydrothermal method followed by sulfidation, whereas, the Co/Fe ratio and concentration have been varied	Nanotube arrays	[211]
NiCoPS	CC	Three-step process, hydrothermal treatment followed by sulfidation of $NiCo_2O_4$, then phosphorization of NiCoS NWs.	Nanowire arrays	[205]
Ni_3FeN sheets	CC	Electrodeposition followed by ammonization	Flower-like hierarchical nanoflakes	[207]
CNTs@$CoS_xSe_{2(1-x)}$	CC	CVD method followed by sulfurization/selenization reactions at different molar ratios	Porous tube-like	[210]
NiS/CoS	CC	Three-step hydrothermal method	Rectangular spongy-like	[415]
$Ni_2(CO_3)(OH)_2$	CC	Hydrothermal treatment of $Ni(NO_3)_2.6H_2O$ and $Co(NH_2)_2$	Nanowire arrays	[271]

FeCo-MOF FeCo-oxyhydroxides	CC	Electric-field assisted *in-situ* hydrolysis of two isomeric bulk MOFs	Nanosheets	[227]
$Co_{1-x}S$ nanosheet	CC	One-step electrodeposition	Nanosheets	[214]
metal-ion (Fe, V, Co, and Ni)-doped MnO_2	CC	Anodic co-electrodeposition	Ultrathin nanosheets	[223]
Zn-Co-S	CC	Two-step wet chemical method	Nanosheets, Nanoplates, and Nanoneedles	[217]
$Mo_{1-x}Co_xS_2$	CC	Hydrothermal method using $NaMoO_4 \cdot 2H_2O$, $CoCl_2 \cdot 6H_2O$, and thiourea	Nanosheets	[218]
P-$NiCo_2S_4$@CNT	CNF	Electrospinning of the polyacrylonitrile (PAN) and CNT dispersion, followed by peroxidation and carbonization	Nanofiber	[232]
$ZnCo_2O_4$@NC	CNF	Carbonization of ZnCo-MOF/CT at 700 °C	Hollow nanowall arrays	[436]
CoNC@MoS_2	CNF	Electrospinnig technique	Flakes	[411]

Table 2 Performance of recent binder-free 1D Nanoarrays for the water splitting

Catalyst	Electrolyte	HER overpotential (η_{10} in mV *vs.* RHE)	Tafel slope (mV dec^{-1})	Durability	OER overpotential (η_{10} in mV)	Tafel slope (mV dec^{-1})	Durability	Overpotential (η_{10} in V) for overall water splitting with durability	Reference
NiS_2 NWA's/CFP	1.0 M KOH	165	134	20 h	246	94.5	20 h	1.59 (20 h)	[271]
Ni_3S_2 NWA's/NF	1.0 M KOH	81	135	10 h	317	84.8	10 h	1.63 (30 h)	[272]
Co_3O_4 NTA's/CC CoS_2 NTA's/CC	1.0 M KOH 1.0 M KOH	278 193	90 88	- -	350 276	77 81	20 h 20 h	1.67 (20 h)	[140]
CoTeNR/NF NiTeNR/NF	1.0 M KOH 1.0 M KOH	202 248	115 185	12 h 12 h	350 (η_{100}) 610 (η_{100})	75 122	12 h 12 h	1.64 (24 h)	[280]
Fe@Ni nanofibers	1.0 M KOH	55	53.5	10 h	230	37.8	10 h	1.53 (20 h)	[281]
$Co_{1-x}V_xP$/NF	1.0 M KOH	46	58	24 h	-	-	-	1.58 (20 h)	[289]
$Co_{0.75}Ni_{0.25}Se$/NF	1.0 M KOH	106	58	16 h	269 (η_{50})	74	40 h	1.60 (22 h)	[126]
Rh SAC–CuO NAs/CF	1.0 M KOH	44	-	-	197	71.7	-	1.51 (25 h)	[294]
FeOOH/Cr-$NiCo_2O_4$/NF	1.0 M KOH	104	63	20 h	217	31	20 h	1.65	[298]
NiS_xP_y–O/NF	1.0 M KOH	-	-	-	340	95	135 h	-	[287]
NiS/Ni_2P/CC	1.0 M KOH	111 (η_{20})	78.1	25 h	265 (η_{20})	41.3	25 h	1.67 (10 h)	[306]
CoMnFe HS@$Ni(OH)_2$ /NF	1.0 M KOH	-	-	-	264(η_{200})	73	100 h	-	[308]
CNT@NiSe/SS	1.0 M KOH	174	135	-	258(η_{30})	37	-	1.71 (24 h)	[316]
V_OB-Co_3O_4/NF	1.0 M KOH	111	60.7	-	315(η_{50})	112.5	20 h	1.67 (20 h)	[320]
O- Co_2P/CuO NWs/CF	1.0 M KOH	101	69.4	30 h	270	74.7	30 h	1.54 (10 h)	[139]
CoN-400/CC	1.0 M KOH	97	93.9	35 h	251	75.4	35 h	1.587 (37 h)	[331]
$(Ni_{0.33}Co_{0.67})S_2$ NWs/CC	0.5 M H_2SO_4 1.0 M KOH	81 156	60 127	24 h 24 h	- 216(η_{20})	- 78	- 24 h	- 1.57 (30 h)	[335]
$NiCo_2O_4$/NF	1.0 M KOH	106.5	76.4	12 h	264(η_{20})	89.8	12 h	1.63 (12 h)	[339]

Fe–Mo oxide hybrid/NF	1.0 M KOH	66	68.73	85 h	200	70.3	85 h	1.52 (60 h)	[340]
NiFeP-MoO_2	1.0 M KOH	56	80.5	100 h	143	29	100 h	1.41 (500 h)	[309]
W,Mo-NiCoP/NF	1.0 M KOH	55	42.3	30 h	283(η_{20})	73	20 h	1.73 (12 h)	[293]
N-WC /CF	0.5 M H_2SO_4	89	75	24 h	-	-	-	1.40	[67]
NiMoN@NiFeN	1.0 M KOH	84	50.7	48 h	277(η_{100})	-	48 h	-	[452]
NiMoN || NiMoN@NiFeN	1 M KOH + 0.5 NaCl	-	-	-	-	-	-	1.564 (η_{100} & 100 h)	
	1 M KOH + Seawater	-	-	-	-	-	-	1.581 (η_{100} & 100 h)	

Table 3 Performance of recent binder-free 2D nano- and micro-structured catalysts for water splitting

Catalyst	**Electrolyte**	**HER overpotential (η_{10} in mV *vs.* RHE)**	**Tafel slope (mV dec^{-1})**	**Durability**	**OER overpotential (η_{10} in mV)**	**Tafel slope (mV dec^{-1})**	**Durability**	**Overpotential (η_{10} in V) for overall water splitting with durability**	**Reference**
$NiMo_xCo_{2-x}$ LDH/NF	1.0 M KOH	123	67.39	14 h	279 (η_{20})	77.99	14 h	1.71(η_{20} & 14 h)	[348]
NiFe-MOF/NF	0.1 M KOH	134	-	2,000 s	240	34	20,000 s	1.55 (20 h)	[349]
NiFe-P@3DGF	1.0 M KOH	131	45.1	50 h	189	46.1	50 h	1.57 (50 h)	[187]
Ni_2Cr_1-LDH/NF	1.0 M KOH	67	61.5	30 h	319 (η_{100})	22.9	30 h	1.55 (30 h)	[356]
$Mo_xCo_{1-x}S_2$/CFP	1.0 M KOH	197 (η_{20})	74	48 h	235 (η_{20})	78	48 h	-	[218]
P-CoMoS	1.0 M KOH 0.5 M H_2SO_4 1.0 M PBS	66 52 104	60.1 - -	24 h - -	260 345 361	70.2 - -	24 h - -	1.54 (100 h) - 1.601 (100 h)	[260]
$NiAl_\delta P$/NF	1.0 M KOH 0.5 M H_2SO_4 1.0 M Na_2SO_4	80 35 100	52 38 93	- - -	242 256 400	65 76 103	- - -	1.55 (20 h) 1.52 (20 h) 1.73 (20 h)	[100]

NiFe-MS/MOF@NF	1.0 M KOH	156(η_{50})	82	28 h	230 (η_{50})	32	17 h	1.61 (27 h)	[360]
Mo-$NiCo_2O_4$/$Co_{5.47}$N/NF	1.0 M KOH	81	116.7	36 h	310 (η_{50})	55.1	36 h	1.56 (12 h)	[369]
$NiCo_2O_4$@$NiMo_2S_4$ /NF	1.0 M KOH	159	53.1	14 h	310 (η_{20})	94.5	13 h	1.63(η_{50} & 13 h)	[370]
EG/$Co_{0.85}$Se/NiFe-LDH	1.0 M KOH	260	160	10 h	270 (η_{150})	57	10 h	1.71(η_{20} & 14 h)	[374]
Ni_2P-Ni_5P_4/CC	1.0 M KOH 1.0 M PBS	102 -	83 69	40 h 40 h	290 (η_{20}) -	109 -	48 h -	1.69 (24 h) -	[394]
Sn–Ni_3S_2	1.0 M KOH	170 (η_{100})	55.6	60 h	270 (η_{100})	52.7	60 h	1.46 (45 h)	[353]
IrNi-$FeNi_3$	1.0 M KOH	31.1	66.95	120 h	240 (η_{20})	36.01	120 h	1.47 (100 h; 6.0 M KOH)	[372]
Fe,Rh-Ni_2P/NF	1.0 M KOH	73	117.3	24 h	226 (η_{30})	52.7	24 h	1.62 (50 h)	[366]
$CoMoN_x$ NSAs/NF	1.0 M KOH	91	76.3	100 h	231	50.6	100 h	1.55 (100 h)	[368]
P-CoFe-LDH@MXene/NF	1.0 M KOH	85	98.59	25 h	252 (η_{200})	83.19	25 h	1.52 (100 h)	[367]
Fe-Ni_5P_4/NiFeOH	1.0 M KOH	197	94	30 h	221	35	80 h	1.55 (20 h)	[383]
NiO/RuO_2	1.0 M KOH	20	42	72 h	250 (η_{50})	68.7	72 h	1.44 (72 h; 6.0 M KOH)	[371]
Co_9S_8/Cu_2S/CF	1.0 M KOH	165	80.2	24 h	195	78.8	24 h	1.6 (8 h)	[376]
Ni_2P-Fe_2P/NF	1.0 M KOH 1.0 M KOH + Seawater	225 (η_{100}) -	86 -	24 h -	261 (η_{100}) -	58 -	- -	1.682 (48 h) 1.811 (48 h)	[460]
Mn-Doped FeP/$Co_3(PO_4)_2$ / CC	1.0 M KOH 0.5 M H_2SO_4 1.0 M PBS	85 27 117	96 44 81	10,000 CV 10,000 CV 10,000 CV	166 228 405	49 472 301	10,000 CV 10,000 CV 10,000 CV	1.61 (10,000 CV) 1.75 (10,000 CV) 1.82 (10,000 CV)	[435]
HCl-c-NiFe	1.0 M KOH	172 (η_{100}) 175 (η_{100})	77 -	- -	1.408 1.408	27 -	1000 h -	1.62 (η_{100} & 1000 h) 1.62 (η_{100} & 300 h)	[450]

	1.0 M KOH + 0.5 M NaCl								

Table 4 Performance of recent binder-free 3D nano- and micro-structured catalysts for water splitting

Catalyst	Electrolyte	HER overpotential (η_{10} in mV *vs.* RHE)	Tafel slope (mV dec^{-1})	Durability	OER overpotential (η_{10} in mV)	Tafel slope (mV dec^{-1})	Durability	Overpotential (η_{10} in V) for overall water splitting with durability	Reference
Ni-Co-Fe/CF	1.0 M KOH	91	86	30,000 s	316	43	18,000 s	1.6 (24 h)	[398]
Ni-Fe-P@NC/NF	1.0 M KOH	66	81	24 h	140	84.6	24 h	1.47 (100 h)	[400]
Ni_2V-MOFs/NF	1.0 M KOH	89	98.3	80 h	244	38.1	80 h	1.55 (80 h)	[410]
MoS_2-NiS_2/NGF	1.0 M KOH	172	70	12 h	370	-	12 h	1.64 (24 h)	[411]
Cu@NiFe LDH/CF	1.0 M KOH	116	58.9	48 h	199	27.8	48 h	1.54 (48 h)	[414]
NiS/CoS/CC-3	1.0 M KOH	102	114	72 h	290	86	72 h	1.57 (72 h)	[415]
MoS_2/NiS_2/CC	1.0 M KOH	62	50.1	24 h	278	91.7	24 h	1.59 (24 h)	[421]
CuO_x@Co_3O_4/CF	1.0 M KOH	242 (η_{50})	69	24 h	240 (η_{50})	46	24 h	-	[423]
Co-P@IC/(Co-Fe)P@CC	1.0 M KOH	53	88	24 h	174	18	24 h	1.46 (24 h)	[440]
Co_2Cr_1-P@3DGF	1.0 M KOH	118	71.12	50 h	270	79.4	50 h	1.56 (50 h)	[441]
$MoNi_4$/NF	1.0 M KOH	28	36	24 h	280	79	24 h	1.58 (24 h)	[442]
Ru_1/D-NiFe LDH	1.0 M KOH	18	29	24 h	189	31	24 h	1.44 (100 h)	[419]
$NiMo_3S_4$/CT	1.0 M KOH	155.6	89.6	72 h	126.2	78.2	72 h	1.55 (80 h)	[237]
P-MoO_3 FCL MXene/NF	1.0 M KOH	118	105	42 h	179	40.44	42 h	1.53 (42 h)	[424]
Cu_2O@Fe_2O_3@CC	1.0 M KOH	188	59	-	296	66	20 h	1.675 (20 h)	[439]
NICC/SSF	1.0 M KOH	85	85	24 h	274	42	24 h	1.56 (24 h)	[406]

Cu_3N@CoNiCHs@CF	1.0 M KOH	182	134	24 h	155	96	24 h	1.58 (48 h)	[417]
$MoS_2/Co_9S_8/Ni_3S_2$/NF (3:1)	1.0 M KOH 0.5 M H_2SO_4 1.0 M PBS	113 103 117	85 55 56	- - -	166 255 405	58 78 71	- - -	1.54 (24 h) 1.45 (80 h) 1.80 (20 h)	[270]
NC-CNT/CoP/CC	1.0 M KOH 0.5 M H_2SO_4 1.0 M PBS	120 62 45	73 39 77	20 h 20 h 20 h	240 - 420	76 - -	- - -	1.63 (20 h) 1.66 (20 h) 1.69 (20 h)	[330]
GO@Fe@Ni-Co/NF	1.0 M KOH + 0.5 M NaCl	150	-	-	247 (η_{50})	59	-	1.59 (η_{20} & 300 h)	[447]
3D karst NF	1.0 M PBS Seawater (pH~8)	110 -	- -	- -	432 -	- -	- -	1.88 (24 h) 1.79(24 h)	[451]

Table of Content (ToC)

The development of robust 1D, 2D, and 3D structured binder-free electrodes with designed properties and architectures has led to significant advances in bi-functional electrocatalytic water splitting, PEC water splitting, and photocatalysis. In this review, we have highlighted the state-of-the-art of binder-free nano- and micro-structures, from approaches based on rational and well-regulated fabrication to their successful application with regard to electrocatalytic HER/OER and photocatalysis.

Sundaram Chandrasekaran[a]*, Mahima Khandelwal[b], Fan Dayong[a], Lijun Sui[c], Jin Suk Chung[d], RDK Misra[e], Peng Yin[f], Eui Jung Kim[d], Woong Kim[b], Aravindan Vanchiappan[g], Yongping Liu[a]*, Seung Hyun Hur[d]*, Han Zhang[f] and Chris Bowen[h]*

Title: Developments and perspectives on robust nano- and micro-structured binder-free electrodes for bi-functional water electrolysis and beyond

ToC figure ((Please choose one size: 55 mm broad × 50 mm high **or** 110 mm broad × 20 mm high. Please do not use any other dimensions))

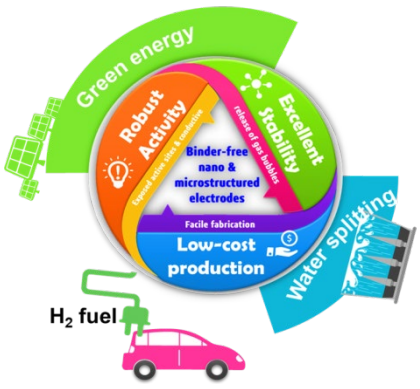

ToC figure